

Air Force Institute of Technology

AFIT Scholar

Theses and Dissertations

Student Graduate Works

12-1995

Experimental Investigation of a Supersonic Boundary Layer Including Favorable Pressure Gradient Effects

Joel J. Luker

Follow this and additional works at: <https://scholar.afit.edu/etd>



Part of the [Aerospace Engineering Commons](#)

Recommended Citation

Luker, Joel J., "Experimental Investigation of a Supersonic Boundary Layer Including Favorable Pressure Gradient Effects" (1995). *Theses and Dissertations*. 6101.

<https://scholar.afit.edu/etd/6101>

This Thesis is brought to you for free and open access by the Student Graduate Works at AFIT Scholar. It has been accepted for inclusion in Theses and Dissertations by an authorized administrator of AFIT Scholar. For more information, please contact AFIT.ENWL.Repository@us.af.mil.



DISTRIBUTION STATEMENT A

Approved for public release;
Distribution Unlimited

EXPERIMENTAL INVESTIGATION
OF A SUPERSONIC BOUNDARY LAYER
INCLUDING
FAVORABLE PRESSURE GRADIENT EFFECTS

THESIS

Joel J. Luker
Second Lieutenant, USAF

AFIT/GAE/ENY/95D-16

19960410 024

DEPARTMENT OF THE AIR FORCE
AIR UNIVERSITY
AIR FORCE INSTITUTE OF TECHNOLOGY

Wright-Patterson Air Force Base, Ohio

DTIC QUALITY INSPECTED 1

EXPERIMENTAL INVESTIGATION
OF A SUPERSONIC BOUNDARY LAYER
INCLUDING
FAVORABLE PRESSURE GRADIENT EFFECTS

THESIS

Joel J. Luker
Second Lieutenant, USAF

AFIT/GAE/ENY/95D-16

The views expressed in this thesis are those of the author and do not reflect the official policy or position of the Department of Defense or the United States Government.

EXPERIMENTAL INVESTIGATION
OF A SUPERSONIC BOUNDARY LAYER
INCLUDING
FAVORABLE PRESSURE GRADIENT EFFECTS

THESIS

Presented to the Faculty of the School of Engineering
of the Air Force Institute of Technology
Air University
In Partial Fulfillment of the
Requirements for the Degree of
Master of Science in Aeronautical Engineering

Joel J. Luker, B.S.
Second Lieutenant, USAF

December 19, 1995

Approved for public release; distribution unlimited

Acknowledgments

I would like to take this opportunity to thank everyone who lent me support during these last few grueling months. I must begin by thanking my advisor, Dr. Rodney Bowersox, whose experience and seemingly endless knowledge in every aspect of aerospace engineering, fluid mechanics, and especially turbulent flows made my life easier than it could have been during the last six months. Every time my train of thought seemed to be running off the tracks he was there to stop it before it crashed. I would also like to thank all the lab technicians at AFIT for putting up with the endless demands placed on them throughout the summer. In particular, I would like to thank Jay Anderson, who is bound to have a heart attack within the next five years unless he has learned not to put all the second lieutenants together in one lab. Last, but nowhere near least, I would like to thank my parents, Ron and Judy, for providing me with the discipline necessary to complete a project of this magnitude and for having the patience to realize that yes, I would call sometime within the next month.

Joel Jeffery Luker

Table of Contents

Acknowledgments	ii
Table of Contents	iii
List of Figures	xi
List of Tables	xv
List of Symbols	xvi
List of Abbreviations	xx
Abstract.....	xxi
1. Introduction.....	1-1
1.1 Motivation	1-1
1.2 Current Turbulence Models.....	1-2
1.3 Status of Current Turbulence Database	1-3
1.4 Overview of Current Experiment	1-4
1.5 Advantages of LDV	1-5
1.6 Objectives	1-6
1.7 Synopsis and Methodology of Current Research	1-7

2.	Development of Governing Equations	2-1
2.1	Compressible Navier-Stokes Equations.....	2-1
2.2	Time Averaging of the Governing Equations.....	2-2
2.2.1	Reynolds Averaging.....	2-3
2.2.2	Favré Averaging.....	2-4
2.3	Comments on the RANS, FANS, and Variable Definitions.....	2-5
2.4	Hot-Wire and CFD Results vs. LDV Measurements	2-7
2.4.1	Hot-Wire.....	2-7
2.4.2	CFD.....	2-7
2.5	Comments on Coordinate System Labeling	2-8
2.5.1	Wind Tunnel Coordinate System	2-8
2.5.2	Test Section Coordinate System.....	2-8
2.5.3	Traverse Coordinate System.....	2-8
2.5.4	Body-Intrinsic Coordinate System.....	2-9
3.	Principles of Laser Doppler Velocimetry	3-1
3.1	Laser Interference in the Measurement Control Volume	3-1
3.2	Velocity Calculation.....	3-3
3.3	Particle Validation.....	3-4
3.3.1	Fringe Count.....	3-5
3.3.2	Acceleration Detection.....	3-5
3.3.3	Local Maxima Check.....	3-6
3.3.4	Envelope, Pedestal, and Quality Factor	3-7
3.4	Directional Ambiguity and Frequency Shift	3-8
3.5	Particle Correlation and Coincidence Window.....	3-8

3.6	Angular Bias of Turbulence Measurements.....	3-9
3.7	Intensity Pattern of Scattered Light.....	3-11
3.8	Seeding the Flow: Intrusive Aspects of LDV and the Problem of Velocity Slip	3-13
3.8.1	Injector Design	3-13
3.8.2	Particle Sizing	3-14
3.8.3	Particle Material Considerations	3-14
4.	Equipment Description	4-1
4.1	Wind Tunnel Facilities	4-1
4.1.1	High-Pressure Air Supply	4-1
4.1.2	Vacuum System.....	4-2
4.1.3	Wind Tunnel Operation	4-2
4.1.4	Test Section	4-2
4.1.4.1	Model Design.....	4-3
4.1.4.2	Window Placement	4-4
4.2	LDV System.....	4-5
4.2.1	Laser Optics.....	4-5
4.2.2	Data Acquisition Equipment	4-8
4.2.3	Traverse.....	4-9
4.2.4	Seeding Apparatus.....	4-9
4.2.4.1	Atomizer.....	4-9
4.2.4.2	Seeding Material	4-9
4.2.4.3	Injector Design.....	4-11
4.3	Flow Visualization Equipment.....	4-11

5. Experimental Procedures	5-1
5.1 Wind Tunnel Operation	5-1
5.2 LDV System Preparation	5-1
5.2.1 Traverse Alignment, Laser Orientation and Origin Placement	5-2
5.2.1.1 Traverse Alignment	5-2
5.2.1.2 Origin Placement and Angular Streamwise Alignment	5-5
5.2.2 Alignment of Receiving Optics	5-5
5.2.3 Software Settings	5-6
5.2.3.1 Fixed Settings	5-6
5.2.3.2 Adjustable Settings	5-8
5.3 Data Collection Techniques	5-9
5.3.1 Traverse Path Across the Boundary Layer	5-9
5.3.2 Wall Proximity Limitations	5-9
5.3.3 Finite-Difference Grid	5-10
5.3.4 Atomizer Pressure	5-11
5.4 Coincidence Filtering	5-11
5.5 Flow Visualization	5-12
5.5.1 Shadowgraph Alignment	5-12
5.5.2 Schlieren Alignment	5-12
6. Data Reduction Procedures	6-1
6.1 Velocity Calculation	6-1
6.2 Separation of the Mean and Turbulent Mach Numbers	6-2
6.3 Mach Number Calculation	6-4
6.4 Density and Temperature Calculation	6-6

6.4.1	Flat Plate	6-6
6.4.2	FPG Region	6-6
6.5	Boundary Layer, Displacement and Momentum Thickness Calculations	6-8
6.6	Turbulence Statistics	6-9
6.7	Wall Shear Stress	6-12
6.8	Van Driest Velocity Profile	6-12
6.9	Turbulent Kinetic Energy	6-14
6.10	Strain Rate Calculation	6-14
6.11	Streamwise Pressure Gradient	6-16
7.	Results and Discussion	7-1
7.1	Pressure and Temperature Measurements	7-1
7.2	Flow Visualization	7-3
7.3	Flat Plate Results	7-5
7.3.1	Mean Flow Characteristics	7-5
7.3.1.1	Velocity Profiles and Boundary Layer Thicknesses	7-5
7.3.1.2	Mach Number	7-7
7.3.1.3	Density	7-8
7.3.1.4	Integral Momentum Thicknesses	7-9
7.3.2	Turbulence Intensities	7-10
7.3.3	Fluctuating Mach Number	7-12
7.3.4	Wall Shear Stress	7-13
7.3.5	“Incompressible” Reynolds Stresses	7-14
7.3.6	Van Driest Velocity Profile	7-18
7.3.7	Turbulence Statistics	7-19

7.3.7.1	Skewness, Flatness and Intermittency.....	7-19
7.3.7.2	Correlation Coefficient.....	7-21
7.3.7.3	Turbulent Kinetic Energy.....	7-23
7.4	FPG Results.....	7-24
7.4.1	Mean Flow Characteristics.....	7-24
7.4.1.1	Velocity.....	7-24
7.4.1.2	Mach Number and Density.....	7-25
7.4.1.3	Integral Momentum Thicknesses.....	7-26
7.4.2	Turbulence Intensities.....	7-27
7.4.3	Fluctuating Mach Number.....	7-27
7.4.4	Wall Shear Stress.....	7-28
7.4.5	“Incompressible” Reynolds Shear Stresses.....	7-29
7.4.6	Van Driest Velocity Profile.....	7-31
7.4.7	Turbulence Statistics.....	7-32
7.4.7.1	Skewness, Flatness and Intermittency.....	7-32
7.4.7.2	Correlation Coefficient.....	7-35
7.4.7.3	Turbulent Kinetic Energy.....	7-35
7.5	Strain Rate Profiles.....	7-37
7.6	Progression of Turbulent Quantities in FPG Test Section.....	7-41
8.	Summary, Conclusions and Recommendations.....	8-1
8.1	Summary and Conclusions.....	8-1
8.2	Recommendations.....	8-2

A. Factors Affecting LDV Results	A-1
A.1 Variation of Testing Parameters	A-1
A.1.1 Record Length	A-1
A.1.2 Seeding Density	A-3
A.1.3 Coincidence Window	A-3
A.2 Raw vs. Coincident Data	A-4
 B. Error Analysis	 B-1
B.1 Traverse Location Error	B-2
B.2 Origin Placement and Probe Angle Alignment Error	B-3
B.3 Velocity Measurement Error	B-4
B.3.1 Biasing Errors	B-4
B.3.2 Random Errors	B-5
B.3.2.1 Error from BSA Calculations	B-5
B.3.2.2 Repeatability	B-5
B.3.2.3 Traverse Location Error	B-6
B.3.2.4 Streamwise Angular Alignment Error	B-6
B.4 Total Pressure and Temperature	B-8
B.5 Mach Number, Temperature, Pressure and Density Error	B-9
B.6 Boundary Layer Thickness Error	B-10
B.7 Wall Shear Stress Error	B-11
B.8 Van Driest Velocity Error	B-12
B.9 Turbulence Statistics Error	B-12
B.10 Strain Rate Error	B-13
B.11 Error Summary	B-14

C. Compliance With Criteria of Settles and DodsonC-1

 C.1 Repeatability..... C-1

 C.2 Two-Dimensionality CheckC-4

 C.3 Tabulated Data C-4

Bibliography..... BIB-1

Vita..... VITA-1

List of Figures

Figure 1.1:	Sketch of FPG Test Section.....	1-5
Figure 2.1:	Time Scales for Averaging of Turbulent Variables	2-3
Figure 2.2:	Wind Tunnel and Test Section Coordinate Systems	2-8
Figure 2.3:	Traverse and Body-Intrinsic Coordinate Systems	2-9
Figure 3.1:	Typical Doppler Burst	3-2
Figure 3.2:	Fringe Disks and Measurement Volume.....	3-2
Figure 3.3:	Doppler and Sampling Times	3-3
Figure 3.4:	“Good” vs. “Bad” Particles	3-5
Figure 3.5:	Burst Pattern From Two Nearly-Coincident Bursts.....	3-6
Figure 3.6:	Local Maxima Validation.....	3-6
Figure 3.7:	Envelope and Pedestal Generation	3-7
Figure 3.8:	Turbulence Effect on Particle Direction	3-10
Figure 3.9:	Intensity of Scattered Light	3-12
Figure 3.10:	Magnitude of Intensity of Scattered Light.....	3-12
Figure 4.1:	Schematic of Wind Tunnel Facilities	4-1
Figure 4.2:	Scale Schematic of Test Section Ceiling	4-3
Figure 4.3:	Optical Window Placement Schematic.....	4-4
Figure 4.4:	Optical Window Test Section Coverage.....	4-5
Figure 4.5:	Laser and Transmitter	4-7
Figure 4.6:	Optic Probe (Receiving Optics)	4-7
Figure 4.7:	Beam Separation on Face of Receiving Optics	4-8
Figure 4.8:	Six-Jet Atomizer	4-10

Figure 4.9:	Injector Design and Location in Wind Tunnel	4-11
Figure 5.1:	Traverse and Laser Alignment Relative to the Wind Tunnel	5-2
Figure 5.2:	Traverse Aligned with Wind Tunnel	5-3
Figure 5.3:	Scattered Light Intensity Received by Optics	5-4
Figure 5.4:	Wall-Proximity Limitation for Two-Component Measurements	5-10
Figure 5.5:	Finite-Difference Grid	5-10
Figure 5.6:	Shadowgraph Alignment	5-13
Figure 5.7:	Schlieren Alignment	5-13
Figure 6.1:	Finite-Difference Grid Notation	6-15
Figure 7.1:	Pressure Distribution Along Wall and Boundary Layer Edge	7-2
Figure 7.2:	Shadowgraph of FPG Region	7-4
Figure 7.3:	Schlieren (Horizontal Knife Edge) in FPG Region	7-4
Figure 7.4:	Schlieren (Vertical Knife Edge) in FPG Region	7-4
Figure 7.5:	Flat Plate Velocity Profile vs. Distance From the Wall	7-6
Figure 7.6:	Flat Plate Mean Velocity Profile	7-7
Figure 7.7:	Flat Plate Mach Number Profile	7-8
Figure 7.8:	Flat Plate Non-Dimensional Density Profile	7-9
Figure 7.9:	Flat Plate u -Turbulence Intensity Profile	7-10
Figure 7.10:	Flat Plate v -Turbulence Intensity Profile	7-11
Figure 7.11:	Turbulence Intensity Data from Ref. [26] vs. Present LDV Measurements	7-12
Figure 7.12:	Fluctuating Mach Number over Flat Plate	7-13
Figure 7.13:	Incompressible Reynolds Shear Stress Scaled by Wall Shear Stress	7-14

Figure 7.14: Incompressible Reynolds Shear Stress Scaled by Extrapolated Wall Shear Stress.....	7-16
Figure 7.15: Incompressible Reynolds Shear Stress Scaled by Local Quantities	7-17
Figure 7.16: Flat Plate van Driest Velocity Profile.....	7-18
Figure 7.17: Skewness of Velocity Components in Flat Plate Flow	7-20
Figure 7.18: Flatness of Velocity Components in Flat Plate Flow.....	7-21
Figure 7.19: Flat Plate Intermittency Function Profile.....	7-22
Figure 7.20: Flat Plate Correlation Coefficient	7-22
Figure 7.21: Flat Plate TKE Profile	7-23
Figure 7.22: FPG Velocity Profile in Non-Dimensional Coordinates	7-24
Figure 7.23: FPG Mach Number Profile	7-25
Figure 7.24: FPG Non-Dimensional Density Profile	7-26
Figure 7.25: FPG vs. ZPG Turbulence Intensity Comparison	7-27
Figure 7.26: FPG Fluctuating Mach Number	7-28
Figure 7.27: FPG Incompressible Reynolds Stresses Scaled by Wall Shear Stress.....	7-29
Figure 7.28: FPG vs. ZPG Incompressible Reynolds Shear Stress Scaled by Local Quantities	7-30
Figure 7.29: FPG van Driest Velocity Profile.....	7-32
Figure 7.30: FPG vs. ZPG Skewness Comparison.....	7-33
Figure 7.31: u -Component Flatness Comparison	7-34
Figure 7.32: v -Component Flatness Comparison.....	7-34
Figure 7.33: Intermittency Function Comparison.....	7-35
Figure 7.34: FPG and ZPG Correlation Coefficient Comparison.....	7-36

Figure 7.35: FPG TKE Profile.....	7-36
Figure 7.36: $\partial\bar{u}/\partial x$ Strain Rates Over Flat Plate and in FPG Test Section.....	7-38
Figure 7.37: $\partial\bar{u}/\partial y$ Strain Rates Over Flat Plate and in FPG Test Section.....	7-38
Figure 7.38: $\partial\bar{v}/\partial x$ Strain Rates Over Flat Plate and in FPG Test Section.....	7-39
Figure 7.39: $\partial\bar{v}/\partial y$ Strain Rates Over Flat Plate and in FPG Test Section.....	7-39
Figure 7.40: $\partial\bar{u}/\partial z$ Strain Rates in FPG Test Section.....	7-40
Figure 7.41: $\partial\bar{v}/\partial z$ Strain Rates in FPG Test Section.....	7-40
Figure 7.42: Progression of u Turbulence Intensity Through Boundary Layer.....	7-41
Figure 7.43: Progression of Incompressible Reynolds Shear Stress Through FPG Test Section.....	7-42
Figure A.1: 8-Sample vs. 16-Sample Turbulence Intensity Data Over a Flat Plate.....	A-2
Figure A.2: 8-Sample vs. 16-Sample Second-Order Correlation Over a Flat Plate.....	A-2
Figure A.3: Effects of Seeding Density on Second-Order Correlation in FPG Test Section.....	A-4
Figure A.4: Raw vs. Coincident Mean Velocity Profiles.....	A-5
Figure A.5: Raw vs. Coincident Turbulence Intensity Profiles.....	A-5
Figure A.6: Possible Biasing Due to Length of Record Interval.....	A-6
Figure A.7: Number of Coincident Bursts Produced by Single Particle.....	A-8
Figure A.8: 8-Sample Raw and Coincident Turbulence Intensity Profiles.....	A-9
Figure B.1: Probe Angle Alignment Error.....	B-3
Figure B.2: Velocity Error Due to Angular Misalignment.....	B-6
Figure B.3: Graphical Derivation of $\Delta\delta$	B-11
Figure C.1: Repeatability of Second-Order Correlation Over a Flat Plate.....	C-3
Figure C.2: Velocity Comparison for Two-Dimensionality Check.....	C-4

List of Tables

Table 4.1:	Test Section Curve Coefficients	4-3
Table 5.1:	“Quick” Menu Constant Software Settings	5-7
Table 5.2:	“Soft” Menu Constant Software Settings	5-7
Table 5.3:	“BSA Program” Menu Constant Software Settings	5-7
Table 7.1:	Wall Pressure Measurements In the FPG Test Section	7-3
Table 7.2:	Flat Plate Integral Thicknesses Calculated from LDV Measurements	7-9
Table 7.3:	FPG Integral Thicknesses Calculated From LDV Measurements	7-27
Table 8.1:	Flow Field Parameters	8-2
Table 8.2:	Boundary Layer Structure Parameters	8-2
Table 8.3:	Proposed Settings for Angular Bias/Record Length Study	8-4
Table B.1:	Error Summary	B-15
Table C.1:	Compliance With Criteria of Ref. [31]	C-1
Table C.2:	Confidence Intervals	C-3
Table C.3:	Flat Plate 16-Sample Raw Data	C-5
Table C.4:	Flat Plate 16-Sample Coincident Data	C-9
Table C.5:	FPG 16-Sample Raw Data	C-13
Table C.6:	FPG 16-Sample Coincident Data	C-17
Table C.7:	Flat Plate 8-Sample Raw Data	C-21
Table C.8:	Flat Plate 8-Sample Coincident Data	C-23
Table C.9:	FPG 16-Sample Coincident Data ($x = 70.98$ cm)	C-25
Table C.10:	FPG 16-Sample Coincident Data ($x = 70.44$ cm)	C-26

List of Symbols

Symbol	Description
a	Speed of Sound
A', B'	Constants in Crocco's integral and van Driest's modified wall shear stress relation
BW	Bandwidth
C_f	Skin friction coefficient
C_{fv}	Frequency-velocity calibration factor
d_p	Seed particle parameter
e	Specific internal energy in Eq. (2.4), otherwise general strain rate
f	Frequency
\mathbf{f}_b	Vector of body forces
Fl	Flatness
h	Enthalpy
M	Mach Number
n	Number of samples associated with statistical analysis
N	Record length; number of samples associated with statistical analysis
p	Pressure
Pr	Prandtl Number
\mathbf{q}	Heat flux vector
Q	Total heat energy in Eq. (2.1), otherwise magnitude of total velocity, $\sqrt{u^2 + v^2}$
r	Recovery factor, $\approx \sqrt[3]{Pr}$
R	Radius of curvature
R_u	Specific gas constant, $\hat{R}/\hat{M} = 287 \text{ kJ}/(\text{kg} \cdot \text{K})$ for air

R_{uv}	Velocity correlation coefficient
Re_x	Reynolds number based on distance from leading edge of flat plate
Re_δ	Reynolds number based on boundary layer thickness
Re_θ	Reynolds number based on integral momentum thickness
Sk	Skewness
t	Time
T	Temperature; Period of periodic function
u, v, w	Velocity components in cartesian coordinates
u^*	Van Driest friction velocity, $\sqrt{\tau_w/\rho_w}$
V	Velocity vector
x, y, z	Cartesian coordinates (body-intrinsic when no subscript present)
y^+	Van Driest scaling coordinate (yu^*/ν)
α	Confidence interval parameter
β	Clauser's equilibrium parameter, $(\delta^*/\tau_w)(dp_e/dx)$
χ	Argument of error function for intermittency function curve fit
δ	Boundary layer thickness
δ^*	Boundary layer displacement thickness
δ_i^*	"Incompressible," or kinematic, boundary layer displacement thickness
Δ	Absolute error in a given variable
ε	Percent error in a given variable
ϕ	General angle
γ	Ratio of specific heats, =1.4 for air at STP
γ_u	Intermittency function
φ	General angle; constant in error function curve fit of intermittency function

κ	Constant in empirical curve-fit for van Driest's wall shear stress relationship
λ	Wavelength of laser light
μ	Fluid viscosity
μ_x	Actual mean value of a variable whose mean is computed from a set of data as \bar{x}
ν	Kinematic viscosity
Π	Coles wake parameter
θ	Laser intersection angle; boundary layer momentum thickness
θ_i	"Incompressible," or kinematic, boundary layer momentum thickness
ρ	Density
σ	RMS value of a set of statistical data
τ	Total shear stress
ω	Vorticity, $\partial v/\partial x - \partial u/\partial y$; constant in empirical curve-fit for van Driest's wall shear stress relationship
ξ	Percent value used to determine confidence interval
ζ	Constant in error function curve fit of intermittency function

Subscripts

0	Stagnation condition
∞	Condition in wind tunnel settling chamber
aw	Adiabatic wall
b	Bragg cell
D	Doppler
e	Boundary layer edge
eff	Effective

S	Sample rate
T	Traverse coordinate system
ts	Test section coordinate system
w	Wall value
wt	Wind tunnel coordinate system

Superscripts

$\overline{()}$	Time-averaged quantity
$\tilde{()}$	Favré-averaged quantity
$()'$	Reynolds fluctuating component
$()''$	Favré fluctuating component
T	Turbulent quantity

List of Abbreviations

Abbreviation	Meaning
AFIT	Air Force Institute of Technology
APG	Adverse Pressure Gradient
BSA	Burst Spectrum Analyzer
CFD	Computational Fluid Dynamics
CP	Conventional Probe
FANS	Favré-Averaged Navier-Stokes Equations
FFT	Fast Fourier Transform
FPG	Favorable Pressure Gradient
HW	Hot-wire
LDV	Laser Doppler Velocimetry
LHS	Left-Hand Side (of an equation)
PM	Photomultiplier
RANS	Reynolds-Averaged Navier-Stokes Equations
RHS	Right-Hand Side (of an equation)
RMS	Root-Mean-Square
SNR	Signal-to-Noise Ratio
SRA	Strong Reynolds Analogy
TKE	Turbulent Kinetic Energy
ZPG	Zero Pressure Gradient (flat plate)

Abstract

This study used advanced laser Doppler velocimetry techniques to measure the turbulence intensities and Reynolds shear stresses in Mach 2.8 turbulent flat plate and Mach 2.9 favorable pressure gradient (FPG) boundary layers. The FPG was generated using a convex curved wall and had a strength of $\beta \cong 1.3$, where β is Clauser's equilibrium parameter. The maximum magnitude of the "extra" strain rates normalized by the main strain rates was 0.1, which meant the FPG was considered to be a strong pressure gradient. The flat plate results indicated that the LDV procedures used in this experiment prevented angular biasing of the velocity measurements reported in the literature. Analysis of the LDV system settings also showed that this biasing, which has been attributed in the past to the angular alignment of the lasers, may have actually been caused, at least in part, by the choice of record interval used during data collection. Measurements in the FPG test section demonstrated that the stabilizing effect of the FPG reduced the turbulence intensities below the location $y/\delta \leq 0.5$ but left them unchanged above that location. Near the wall, the u -turbulence intensity was found to be reduced to 70% of the flat plate value. In addition, the FPG reduced the magnitude of the incompressible Reynolds shear stresses ($-\overline{\rho u'v'}$) by approximately 75%. Due to the reduction in the turbulent shear stress, the wall shear stress was found to be reduced by 37%. Comparison of the LDV data to hot-wire data collected in the same facilities showed that the assumption of $p' \approx 0$, used in the reduction of the hot-wire data, was valid in the flat plate region but not the FPG region. The increase in the magnitude of p' was likely due to the streamline curvature associated with the generation of the FPG and the resulting pressure difference across the boundary layer.

EXPERIMENTAL INVESTIGATION OF A
SUPERSONIC TURBULENT BOUNDARY LAYER
INCLUDING
FAVORABLE PRESSURE GRADIENT EFFECTS

1. Introduction

1.1 Motivation

In the fields of aerospace engineering and fluid mechanics, conceptual design projects are relying more and more on computational fluid dynamics (CFD) simulations to provide required data and test results as the cost of wind tunnel and laboratory testing continues to increase. In order to ensure the validity of these designs and the data acquired from the numerical simulations, the computer codes need to accurately reflect the physics of the problems they are attempting to solve.

In problems where turbulence is involved, today's computers do not have sufficient speed or memory to resolve the length and time scales associated with turbulence. For instance, a Mach 2.9 flow with a freestream Reynolds number of $Re_\delta \approx 1.6 \times 10^6$ and a boundary layer thickness of $\delta \approx 0.009$ m has a Kolmogoroff turbulent length scale of approximately 2×10^{-7} m. [6] In a control volume 6.35 cm x 6.35 cm x 80 cm (the size of the test section in this experiment) there would have to be approximately 4×10^{17} grid points in order to accurately calculate a solution to the problem. This would require approximately 4×10^{28} calculations to obtain a numerical solution of the Navier-Stokes equations [5]; assuming an optimistic rate of one computation per

nanosecond, the computations would take 1.2×10^{12} years to complete! Trying to compute the solution for flow over an object of engineering interest, such as an airplane, would take even longer. This being the case, engineers and scientists must rely on an approximate, time-averaged form of the governing equations in order to generate solutions to problems of interest. Due to the non-linear nature of the Navier-Stokes equations, the time-averaging process introduces cross-correlation fluctuation terms into the governing equations (see Chapter 2). This leads to the problem of *turbulent closure*. In short, there are more unknowns than equations, and the system cannot be solved. Turbulence modeling attempts to relate these extra variables to other flow quantities in order to close the system.

1.2 Current Turbulence Models

Turbulence model development has taken the same path as most engineering problems: solutions for simplified cases were investigated first and then, with time, solutions for more complicated problems were developed. The first turbulence models were developed for low-speed, incompressible flow over a flat plate; these turbulence models were found to work reasonably well for mild pressure gradient flows, and thus their use for calculating the effects of pressure gradient was generally accepted. The next step in the evolution of turbulence modeling was their extension to compressible flows.

Compressible (and especially supersonic) flows have different physical characteristics than incompressible flows, but incompressible turbulence models are used in compressible calculations on an ad-hoc basis. The incompressible models provide fairly accurate results when computing flat plate flows, since most of the differences between compressible and incompressible flows can be accounted for by differences in density and temperature which occur across the boundary layer [32, 33]. However, in supersonic flows pressure gradient effects can cause large changes in the

turbulence quantities. In this case, the ad-hoc extension of subsonic models to supersonic flow is not valid, and new turbulence models need to be developed.

Turbulence models take on many forms, but the one thing all turbulence models have in common is that they presently need to be validated against empirical data gathered from experimentation. As a result, it becomes necessary to have a broad database of experimental results for generating and validating turbulence models. A broad database of turbulence information is also needed in order to determine what physical processes control the turbulence; hopefully, knowledge of how the turbulence changes in different physical environments will allow the extension of computer models to new situations without requiring expensive testing to validate the results.

1.3 Status of Current Turbulence Database

Although there have been many experiments performed in the past to measure quantities in compressible flows, the available turbulence database is still fairly scarce. Many of the past experiments have focused on determining flow characteristics over a flat plate, and many of the experiments attempting to measure turbulence quantities have been found to be flawed. According to Spina et al. [33],

The reason for the scarcity of measurements and their generally poor quality is simple: the measurement of turbulence quantities in supersonic boundary layers is exceedingly difficult, with the level of difficulty increasing with flow complexity and Mach number.

In addition to the problems that exist with data acquisition in supersonic flows, the physical characteristics of supersonic flows provide several means for generating a favorable pressure gradient (FPG). The FPG can be generated by imposing an expansion shock wave onto a flat plate

boundary layer (see Lewis et al. [25]), expanding the flow suddenly around a corner, or expanding the flow slowly over a gradual curve. The effect of the FPG on the turbulence will vary depending on the method with which the FPG is generated. [32] Spina et al. [33] noted that

The behavior of supersonic boundary layers subject to convex curvature has not been studied extensively...No data have been taken on smooth convex corners in supersonic flow leaving the expansion-corner studies...as the only flows that provide insight into the effects of convex streamline curvature...However, [these] studies actually provide more insight into the effect of a rapid application of bulk dilatation than the effect of streamline curvature.

In a review of the literature, only one study was found which attempted to analyze the effects of a FPG generated by a convex curved wall. However, this study (see Ref. [19]) was of limited use because the FPG was immediately preceded by an adverse pressure gradient (APG) region. The APG caused the turbulence quantities to be disturbed from their flat plate values, limiting the effectiveness of the data. [32]

1.4 Overview of Current Experiment

The current experiment was intended to expand the available turbulence database by providing much-needed data regarding the effects of streamline curvature and FPG effects. The data were collected using advanced laser Doppler velocimetry techniques to measure the flow velocities and turbulent quantities over a flat plate and a convex curved surface (see Figure 1.1 for a sketch of the convex surface). In a supersonic flow, the convex curved surface resulted in the generation of a FPG. Comparison of the flat plate data and the FPG data allowed the effects of the FPG to be examined. In addition, comparison of the LDV data with hot-wire data collected by Miller [26] in the same facilities allowed for examination of the assumptions used in the hot-wire data reduction. This examination was possible due to the advantages offered by the LDV system.

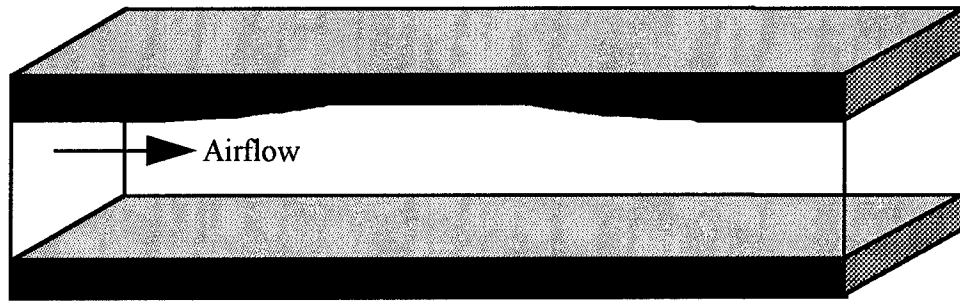


Figure 1.1: Sketch of FPG Test Section

1.5 Advantages of LDV

LDV has been in common use as a flow measurement device since the early 1970's. It offers the advantage of a "non-intrusive" means of measuring flow velocities and turbulence quantities. The use of LDV systems to perform data acquisition is considered non-intrusive because no flow-obstructive measurement device needs to be placed inside the test section; however (as will be discussed in Chapter 3), the flow needs to be seeded with particles which reflect the laser light, and careless seeding can cause the flow to be disturbed from its original state.

Aside from providing a non-intrusive method of measurement, LDV has the advantage of measuring the velocities and velocity fluctuations directly. The hot-wire measurements collected by Miller and other researchers actually measure density-weighted velocities; in order to extract the pure velocities from the collected data, several assumptions must be made. Comparison between hot-wire and LDV data has proven these assumptions valid for the flat plate case, but the lack of turbulence data in FPG regions has not allowed the assumptions made in hot-wire data reduction to be validated for this case. One of the goals of the current experiment was to compare

hot-wire data to LDV data in order to verify or reject the assumptions made in the case of a favorable pressure gradient.

1.6 Objectives

The primary objective of this research was to obtain turbulence measurements and gain insight into the important physical mechanisms in a turbulent boundary layer subjected to a favorable pressure gradient. In addition, the LDV data was to be compared to hot-wire data taken in the same experimental configuration to determine if the assumptions used in reducing the hot-wire data were valid. Finally, this study was intended to increase the amount of reliable turbulence information available. In order to make the presented results useful to other researchers, the criteria established by Settles and Dodson [31] was used to provide a minimum standard by which the results were presented:

1. *Baseline Applicability*: All candidate studies for use must be experiments involving turbulent flows in either supersonic or hypersonic Mach number range (i.e., $M \approx 3.0$ or higher).
2. *Simplicity*: Experimental geometries must be sufficiently simple that they may be modeled by CFD methods "without enormous difficulty."
3. *Specific Applicability*: All candidate studies passing this criterion must be capable of providing some useful test of turbulence modeling.
4. *Well-defined experimental boundary conditions*: All incoming conditions (especially the state of the incoming boundary layer) must be carefully documented. For studies claiming "two-dimensional" flow, data indicating the extent of the spanwise flow variations should be provided.
5. *Well-defined experimental error bounds*: The experimenter must provide an analysis of the accuracy and repeatability of the data, or error bars on the data themselves. Further, error bounds on the data must be substantiated in a quantifiable manner.
6. *Adequate documentation of data*: Data must be documented and tabulated in a machine-readable form.

7. *Adequate spatial resolution of data:* Experiments must present data of sufficiently high resolution, compared with the scaled flow in question, such that the key features of the flow are clearly resolved.

In addition to the criteria established by Settles and Dodson, an attempt was made to provide adequate data for converting reported values. That is, other researchers may wish to scale the data in a different manner than chosen within this report; an effort was made to provide the data required to convert the reported values into any common non-dimensional form.

1.7 Synopsis and Methodology of Current Research

In order to determine what measurements were required in the development of a turbulence model, it was first necessary to examine the governing equations of fluid motion; this examination is carried out in Chapter 2. The analysis of the governing equations showed the necessity of measuring the velocity cross-correlation term $\overline{u'v'}$. The cross-correlation term could be measured directly using an LDV system; in order to gain an understanding of the LDV system, the basic principles behind LDV were studied and are presented briefly in Chapter 3. The actual LDV system, along with all other equipment used in the research, is described in Chapter 4. Chapter 5 details how this equipment was put to use in order to obtain velocity measurements in the flat plate and FPG flowfields. Chapter 6 describes how these measurements were manipulated to calculate other variables of interest, while Chapter 7 presents and analyzes the results from the measurements and manipulations. Finally, Chapter 8 summarizes the findings, draws conclusions from the analysis of the data, and presents recommendations for future research.

2. Development of Governing Equations

When studying turbulent compressible flows, it is necessary to provide a detailed development of the governing equations for two reasons. First, the development provides insight into which terms in the governing equations contain the turbulent characteristics of the flow, as well as showing how turbulent compressible flows differ from incompressible ones. Second (and probably most important), the development shows how and why certain variables are defined differently for compressible and incompressible flows. These definitions are important for comparing data collected by different researchers, as the definitions used throughout the literature are not always consistent.

2.1 Compressible Navier-Stokes Equations

The governing equations for fluid flows are the Navier-Stokes equations. They are given in compressible form [1] as

$$\begin{aligned} \frac{D\rho}{Dt} + \rho \nabla \cdot \mathbf{V} &= 0 \\ \rho \frac{D\mathbf{V}}{Dt} &= \nabla \cdot \overline{\overline{\boldsymbol{\pi}}} + \rho \mathbf{f}_b \\ \rho \frac{Dh}{Dt} &= \frac{Dp}{Dt} + \frac{\partial Q}{\partial t} - \nabla \cdot \mathbf{q} + \Phi \end{aligned} \quad (2.1)$$

where the vector \mathbf{f}_b denotes body forces acting on the fluid, $D/Dt \equiv \partial/\partial t + \mathbf{V} \cdot \nabla$, and

$$\begin{aligned} \overline{\overline{\boldsymbol{\pi}}} &= -p\delta_{ij} + \tau_{ij} \\ \tau_{ij} &= \mu \left[\left(\frac{\partial u_i}{\partial x_j} + \frac{\partial u_j}{\partial x_i} \right) - \frac{2}{3} \delta_{ij} \frac{\partial u_k}{\partial x_k} \right] \\ \Phi &= \tau_{ij} \frac{\partial u_i}{\partial x_j} = \mu \left[2 \left(\frac{\partial u}{\partial x} \right)^2 + 2 \left(\frac{\partial v}{\partial y} \right)^2 + 2 \left(\frac{\partial w}{\partial z} \right)^2 + \left(\frac{\partial v}{\partial x} + \frac{\partial u}{\partial y} \right)^2 + \right. \\ &\quad \left. \left(\frac{\partial w}{\partial y} + \frac{\partial v}{\partial z} \right)^2 + \left(\frac{\partial u}{\partial z} + \frac{\partial w}{\partial x} \right)^2 \right] + \lambda \left(\frac{\partial u}{\partial x} + \frac{\partial v}{\partial y} + \frac{\partial w}{\partial z} \right)^2 \end{aligned} \quad (2.2)$$

2.2 Time Averaging of the Governing Equations

When turbulence is present in fluid flows, variables in the governing equations fluctuate very rapidly, leading to minute time scales associated with the flow. As the time scale associated with a flow decreases, the amount of computational work required to calculate a solution to the governing equations increases. Therefore, instead of trying to capture the minute time scales using the unsteady form of the governing equations, the equations are simplified using some sort of time-averaging (Reynolds or Favré averaging) process. In this way, only the time dependence of the mean flow needs to be modeled with the time-dependent terms of the Navier-Stokes equations, and the associated time scales can be dramatically increased. This increase in the length of the time scales allows the computation time to be decreased to a reasonable level.

In any of the various types of time averaging, an instantaneous variable g is assumed to consist of a time averaged part, \bar{g} , and a fluctuation from the mean, g' :

$$g(x, y, z, t) = \bar{g}(x, y, z, t) + g'(x, y, z, t) \quad (2.3)$$

It should be noted that, in the above equation, \bar{g} is a time average but is still allowed to vary with time. This allows the averaging process to capture possible time-dependence of the mean flow. However, it requires that the period over which quantities are averaged, T_1 , is long compared to the turbulent time scale but short compared to the overall time scale, T_2 . [37] See Figure 2.1 for a graphical representation of this concept.

As mentioned above, there are traditionally two types of time-averaging performed on the Navier-Stokes equations: Reynolds averaging and Favré averaging. The set of equations resulting from Reynolds averaging is referred to as the Reynolds-Averaged Navier-Stokes Equations (RANS); similarly, use of Favré averaging leads to the Favré-Averaged Navier-Stokes Equations, or FANS. Although a description of Reynolds averaging would be sufficient for explaining the

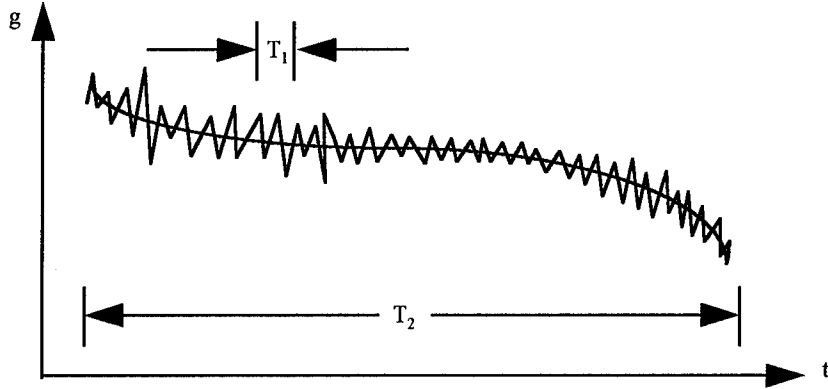


Figure 2.1: Time Scales for Averaging of Turbulent Variables (after Ref. [37])

measurements made by LDV systems, a description of the Favré averaging process is also presented in order to compare the LDV data with hot-wire and CFD results.

2.2.1 Reynolds Averaging. Reynolds averaging consists of replacing all turbulent variables in the Navier-Stokes equations with a time-average plus fluctuation term, and then taking the time average of the whole equation. Assuming steady mean flow and no body forces, the RANS equations become [1, 6]

$$\begin{aligned} \frac{\partial \bar{\rho}}{\partial t} + \frac{\partial (\bar{\rho} \bar{u}_j + \bar{\rho}' u'_j)}{\partial x_j} &= 0 & (2.4) \\ \frac{\partial (\bar{\rho} \bar{u}_i + \bar{\rho}' u'_i)}{\partial t} + \frac{\partial (\bar{\rho} \bar{u}_i \bar{u}_j)}{\partial x_j} &= -\frac{\partial \bar{p}}{\partial x_i} + \frac{\partial (\bar{\tau}_{ij} + \tau_{ij}^T)}{\partial x_j} \\ \frac{\partial (\bar{\rho} \bar{e}_0 + \bar{\rho}' h'_0)}{\partial t} + \frac{\partial (\bar{\rho} \bar{h}_0 \bar{u}_j)}{\partial x_j} &= \frac{\partial (\bar{u}_i \bar{\tau}_{ij} + \bar{u}'_i \tau'_{ij} - \bar{q}_j - q_j^T)}{\partial x_j} \end{aligned}$$

where

$$\begin{aligned}
\bar{\tau}_{ij} &= \mu \left[\left(\frac{\partial \bar{u}_i}{\partial x_j} + \frac{\partial \bar{u}_j}{\partial x_i} \right) - \frac{2}{3} \delta_{ij} \frac{\partial \bar{u}_k}{\partial x_k} \right] \\
\tau'_{ij} &= \mu \left[\left(\frac{\partial u'_i}{\partial x_j} + \frac{\partial u'_j}{\partial x_i} \right) - \frac{2}{3} \delta_{ij} \frac{\partial u'_k}{\partial x_k} \right] \\
\tau_{ij}^T &= -\overline{\rho u'_i u'_j} - \bar{u}_i \overline{\rho' u'_j} - \bar{u}_j \overline{\rho' u'_i} - \overline{\rho' u'_i u'_j} \\
\bar{q}_i &= -k \frac{\partial \bar{T}}{\partial x_i} \\
q_i^T &= \overline{\rho h'_0 u'_i} + \bar{h}_0 \overline{\rho' u'_i} + \bar{u}_i \overline{\rho' h'_0} - \overline{\rho' h'_0 u'_i}
\end{aligned} \tag{2.5}$$

The quantities e_0 and h_0 are the stagnation conditions.

2.2.2 *Favré Averaging.* Favré averaging is similar to Reynolds averaging, except that the mass-dependent terms in the governing equations are replaced by a mass-weighted time average, $\tilde{\phi}$, plus a fluctuation, ϕ'' :

$$\phi = \tilde{\phi} + \phi'' \tag{2.6}$$

where

$$\tilde{\phi} \equiv \frac{\overline{\rho \phi}}{\bar{\rho}} \tag{2.7}$$

With this definition, the FANS equations are given as [1]

$$\begin{aligned}
\frac{\partial \bar{\rho}}{\partial t} + \frac{\partial (\bar{\rho} \bar{u}_j)}{\partial x_j} &= 0 \\
\frac{\partial (\bar{\rho} \bar{u}_i)}{\partial t} + \frac{\partial (\bar{\rho} \bar{u}_i \bar{u}_j)}{\partial x_j} &= -\frac{\partial \bar{p}}{\partial x_i} + \frac{\partial (\bar{\tau}_{ij} + \tau_{ij}^T)}{\partial x_j} \\
\frac{\partial (\bar{\rho} \bar{e}_0)}{\partial t} + \frac{\partial (\bar{\rho} \bar{h}_0 \bar{u}_j)}{\partial x_j} &= \frac{\partial (\bar{u}_i \bar{\tau}_{ij} + \bar{u}_i'' \tau_{ij}^T - \bar{q}_j - q_j^T)}{\partial x_j}
\end{aligned} \tag{2.8}$$

In the Favré'-averaged equations, the definitions of $\bar{\tau}_{ij}$, τ_{ij}^T and q_j^T are somewhat different:

$$\bar{\tau}_{ij} = \mu \left[\left(\frac{\partial \tilde{u}_i}{\partial x_j} + \frac{\partial \tilde{u}_j}{\partial x_i} \right) - \frac{2}{3} \delta_{ij} \frac{\partial \tilde{u}_k}{\partial x_k} \right] + \mu \left[\left(\frac{\partial \bar{u}_i''}{\partial x_j} + \frac{\partial \bar{u}_j''}{\partial x_i} \right) - \frac{2}{3} \delta_{ij} \frac{\partial \bar{u}_k''}{\partial x_k} \right] \quad (2.9)$$

$$\tau_{ij}^T = -\overline{\rho u_i' u_j'}$$

$$q_i^T = \overline{\rho u_i'' h_0''}$$

2.3 Comments on the RANS, FANS, and Variable Definitions

The term τ_{ij}^T as given in the RANS is known as the Reynolds shear stress; the differences which arise in this term due to the effects of compressibility, as well as the differences between the definitions of τ_{ij}^T in the RANS and FANS result in inconsistent nomenclature throughout the literature. For instance, the term $-\overline{\rho u'v'}$ is the only term appearing in the Reynolds-averaged form of τ_{ij}^T when the flow is incompressible. As a result, many researchers refer to this term alone as the Reynolds shear stress, neglecting the other three terms in the definition of τ_{ij}^T . In order to avoid confusion within this report, the term $-\overline{\rho u'v'}$ will be referred to as the *incompressible* Reynolds shear stress.

Another source of confusion is the use of τ_{ij}^T to represent the turbulent shear stress terms in the FANS; many researchers consider this term as the Reynolds shear, even though it is not equivalent to either the incompressible Reynolds shear or the entire Reynolds shear stress. The differences between τ_{ij}^T in the RANS and FANS can be derived by examining the differences between the definitions used in the time-averaging process. In both cases, the instantaneous velocity is replaced by a mean plus a fluctuating term:

$$u = \bar{u} + u'; \quad u = \tilde{u} + u'' \quad (2.10)$$

Setting the two equations equal to each other and solving for u' leads to

$$u' = \tilde{u} - \bar{u} + u'' \quad (2.11)$$

Now, taking the time-average of the Favre' expansion (the second expression in Eq. (2.10)),

$$\bar{u} = \tilde{u} + \bar{u}'' \Rightarrow \tilde{u} - \bar{u} = -\bar{u}'' \quad (2.12)$$

Insertion of Eq. (2.12) into Eq. (2.11) results in the expression

$$u' = u'' - \bar{u}'' \quad (2.13)$$

A similar relation can be developed for the v -component of velocity; multiplying the two expressions together and taking the time-average leads to

$$\overline{u'v'} = \overline{u''v''} - \overline{u''v''} - \overline{v''u''} + \overline{u''v''} = \overline{u''v''} - \overline{u''v''} \quad (2.14)$$

Note that the time-average of a Favre' fluctuation term, $\bar{\phi}''$, is not equal to zero. In fact, this time average is related to the Reynolds-averaged variables by the relation

$$\begin{aligned} \bar{\phi}'' &= \bar{\phi} - \tilde{\phi} = \bar{\phi} - \frac{\bar{\rho}\bar{\phi}}{\bar{\rho}} = \bar{\phi} - \frac{(\bar{\rho} + \rho')(\bar{\phi} + \phi')}{\bar{\rho}} = \\ &\bar{\phi} - \bar{\phi} - \frac{\bar{\rho}'\bar{\phi}}{\bar{\rho}} - \frac{\bar{\rho}\phi'}{\bar{\rho}} - \frac{\rho'\phi'}{\bar{\rho}} \Rightarrow \\ &\bar{\phi}'' = -\frac{\bar{\rho}'\bar{\phi}}{\bar{\rho}} \end{aligned} \quad (2.15)$$

Multiplying Eq. (2.14) by the mean density, the incompressible Reynolds stress is related to the Favre'-averaged stress by

$$\overline{\bar{\rho}u'v'} = \overline{\bar{\rho}u''v''} - \overline{\bar{\rho}u''v''} \quad (2.16)$$

The term $\overline{\bar{\rho}u''v''}$ is the term usually reported as the Reynolds stress by researchers who prefer to use the Favre'-averaged equations. However, this term differs from the incompressible Reynolds stress by the amount

$$\overline{\bar{\rho}u''v''} = \bar{\rho} \frac{\overline{\rho'u'}}{\bar{\rho}} \frac{\overline{\rho'v'}}{\bar{\rho}} \quad (2.17)$$

Since this term is a fourth-order fluctuation, it is usually considered negligible so that

$$\overline{\bar{\rho}u'v'} \cong \overline{\bar{\rho}u''v''} \quad (2.18)$$

2.4 Hot-Wire and CFD Results vs. LDV Measurements

When comparing hot-wire and CFD measurements to data collected by LDV, it is necessary to understand the differences between the measurements, the assumptions used to reduce the data, and the possible sources of inconsistency between the results.

2.4.1 Hot-Wire. Hot-wire techniques measure the change in voltage required to keep a wire at constant temperature; this change in voltage is sensitive to the heat transfer from the wire, which is, in turn, sensitive to a mass-weighted velocity. Since the heat transfer to the wire is related to the flow Reynolds number, the hot-wire process is sensitive to the mass flux across the wire, ρV . [8] In order to separate the density from the velocity components, the assumption that $p' = 0$ must be made. [7] This assumption is somewhat controversial, and comparison between hot-wire results and LDV data should hopefully prove or disprove its validity.

2.4.2 CFD. CFD attempts to model τ_{xy}^T ; in order to reduce the number of unknowns in the model, most CFD codes use Favré'-averaging. Comparison of τ_{ij}^T in equations (2.5) and (2.9) shows the use of Favré'-averaging reduces the number of unknowns in τ_{xy}^T from four to one. However, LDV measures the product $\overline{u'v'}$ in the incompressible *Reynolds* shear, not the Favré'-averaged shear. As shown in section 2.3, the difference between the Reynolds-averaged results obtained by LDV and the Favré'-averaged results from CFD is usually considered negligible; however, in cases where the fluctuating velocity is large, discrepancies between the two results may arise.

2.5 Comments on Coordinate System Labeling

Throughout this report, four different coordinate systems will be used. In order to preempt any confusion, the four coordinate systems, the labeling scheme for each, and the differences between them are presented here.

2.5.1 Wind Tunnel Coordinate System. The wind tunnel coordinate system, denoted by (x_{wt}, y_{wt}, z_{wt}) , is a Cartesian system with the tunnel nozzle at $x_{wt} = 0$. The y -coordinate is pointed in the vertical direction and the z -coordinate is directed accordingly (see Figure 2.2).

2.5.2 Test Section Coordinate System. The test section coordinate system is labeled (x_{ts}, y_{ts}, z_{ts}) and is used in the computation of the wall coordinates. The origin of the test section system is placed at $x_{wt} = 0.60$ m; the system orientation is shown in Figure 2.2.

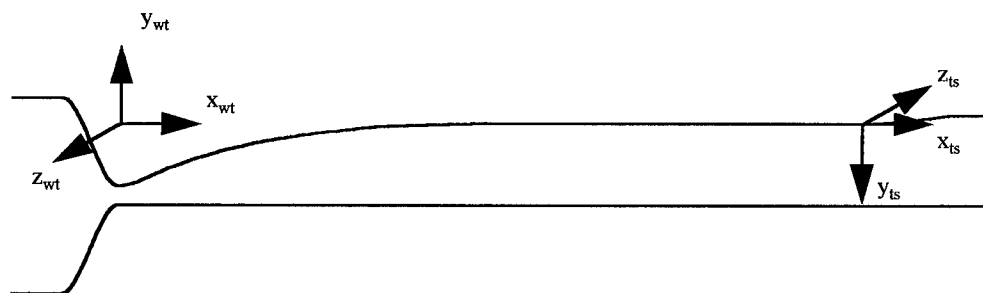


Figure 2.2: Wind Tunnel and Test Section Coordinate Systems

2.5.3 Traverse Coordinate System. The traverse coordinate system (x_T, y_T, z_T) dictates the coordinates used to control motion of the traverse. Its origin is placed on the wall of the test section with the orientation shown in Figure 2.3.

2.5.4 *Body-Intrinsic Coordinate System.* The final coordinate system is the body-intrinsic system, labeled (x,y,z) . The body-intrinsic system and the traverse system have the same origin but different orientations; its orientation is also shown in Figure 2.3.

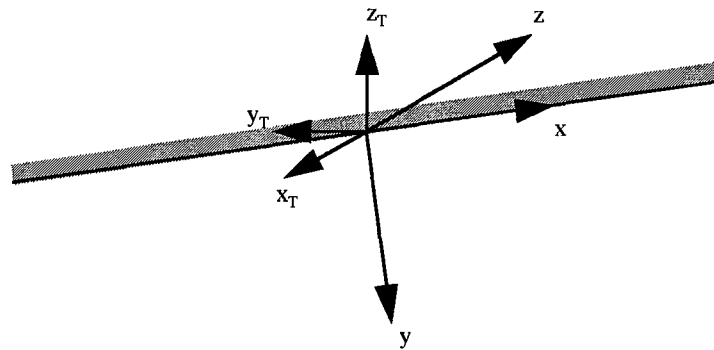


Figure 2.3: Traverse and Body-Intrinsic Coordinate Systems

Finally, it should be noted that the definitions given in section 2.2 are for a Cartesian coordinate system. However, it can be shown that, for two-dimensional flows where $\delta \ll R$ (R is the radius of curvature of the wall), the definitions given in section 2.2 are still valid in a body-intrinsic coordinate system. [4]

3. Principles of Laser Doppler Velocimetry

Laser Doppler velocimetry (LDV) provides a “non-intrusive” means of measuring flow velocities and turbulence levels. There are many factors which influence the measurements taken when using an LDV system; in order to understand the potential bias errors, it is necessary to provide a description of how the LDV system works.

3.1 Laser Interference in the Measurement Control Volume

When two laser beams of like wavelength intersect, the wave-like properties of the light interact to create an interference pattern. If the intersection occurs at the waist of the two beams, the interference pattern is a set of fringes which are nearly parallel [11]. The spacing between the fringes is a function of the laser beam intersection angle, θ , and the wavelength of the laser beams, λ , and is given as [10, 20]

$$x_f = \frac{\lambda/2}{\sin(\theta/2)} \quad (3.1)$$

When a particle passes through the area of intersection, it will scatter light from the fringes, creating an alternating “on-off” signal as it travels through the light and dark portions of the fringe pattern. The set of on-off signals associated with a single particle is referred to as a Doppler burst. A typical Doppler Burst is shown in Figure 3.1. As the particle crosses a fringe, the intensity of scattered light increases, resulting in a peak in the Doppler burst; as it passes through the dark space between the fringes, a valley is created in the Doppler burst pattern.

The intensity distribution across a laser beam is not uniform, resulting in the large intensity near the center of the Doppler burst. The non-uniform intensity distribution also confines the actual measurement volume to the space where the scattered light would be strong enough to be detected; this results in the control volume and fringe bands being restricted to an ellipsoid in the

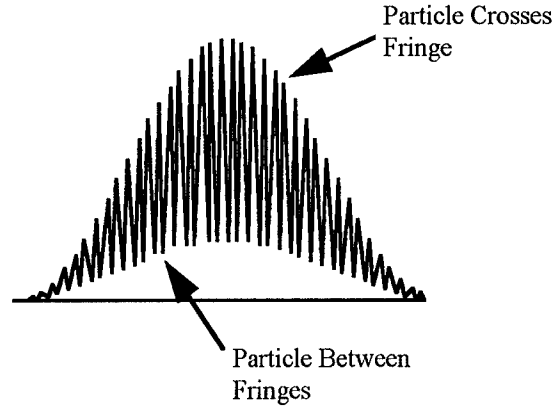


Figure 3.1: Typical Doppler Burst

center of the intersection region and fringe disks within the ellipsoid, respectively (see Figure 3.2).

[11]

The Doppler burst signals are collected by photomultipliers (also known as PM tubes) and processed by a Burst Spectrum Analyzer (BSA). The BSA processes the received Doppler burst patterns in order to determine the velocities of the particles traveling through the control volume.

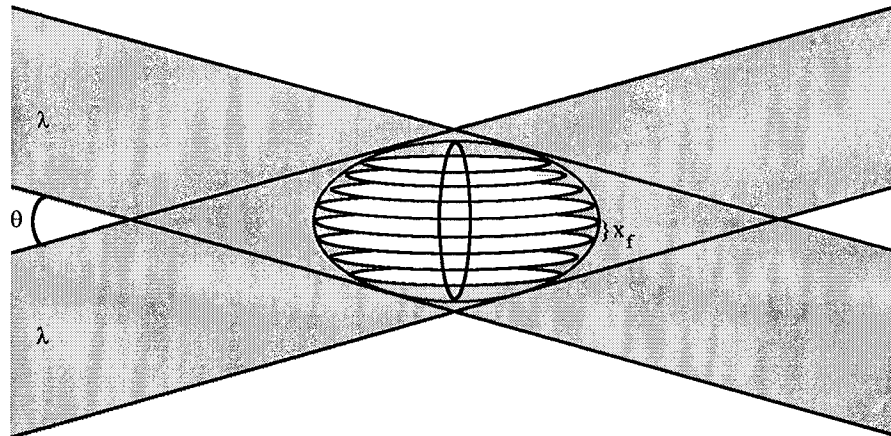


Figure 3.2: Fringe Disks and Measurement Volume

3.2 Velocity Calculation

The time taken to travel between two successive fringes corresponds to the time between two successive peaks in the Doppler burst and is labeled T_D (see Figure 3.3); the time T_D has a corresponding frequency, f_D . The relationship between T_D , f_D and the velocity is [10]

$$u = \frac{x_f}{T_D} = f_D x_f = f_D \frac{\lambda/2}{\sin(\theta/2)} \quad (3.2)$$

The ratio $[\lambda/2]/[\sin(\theta/2)]$ is termed the *calibration factor* and is denoted by the symbol C_{ν} .

The calibration factor is dependent on the optical setup alone and is known before any measurements are made; therefore, in order to calculate the velocity it is only necessary to determine the Doppler frequency, f_D .

The Doppler frequency is determined using N samples (referred to as the record length) to model the Doppler burst. The first sample is taken when the intensity of the Doppler signal is larger than a certain threshold (25 mV in Figure 3.3). Additional samples are then taken every T_s

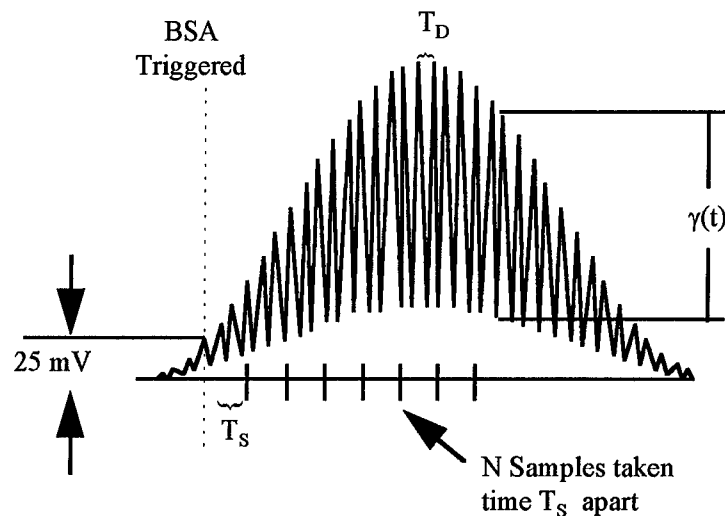


Figure 3.3: Doppler and Sampling Times

seconds. If the Doppler burst signal passes a second threshold (50 mV) the count of N samples is restarted. That is, the samples already collected are deleted and the sample counter is reset to one. The sample count can be reset at two more intensity levels, 100 and 150 mV. This procedure ensures the part of the Doppler burst with the highest intensity is used for the frequency calculation. [10] If the particle passes through each fringe at a given time interval, T_D , the Doppler burst will be a periodic signal with period T_D . Fourier theory shows that the frequency of a periodic function can be determined by sampling the function at a fixed rate, T_S . Thus, the Doppler frequency can be calculated using the N samples and a Fast-Fourier Transform (FFT). The accuracy of the FFT (and thus the velocity calculation) increases as N is increased. [10]

The sampling time, T_S , is limited by the bandwidth over which the BSA is trying to detect frequencies. The sampling frequency, $f_s = 1/T_S$, must be greater than the bandwidth and is usually set proportional to the bandwidth, $f_s = n(BW)$, where n is some number greater than one and BW is the bandwidth. It should be noted that n is not an adjustable variable; it is set internally within the BSA. The limitation on T_S means that, as the record length is increased, the total sampling time (also known as the *record interval*) is increased. In high-speed flows where a particle only takes a few microseconds to traverse the measurement volume, the accuracy of the FFT becomes limited by the record length, as the total sampling time must be less than the time taken to traverse the control volume.

3.3 Particle Validation

The velocity calculation assumes the particles are traveling normal to the plane of the fringes at a constant velocity; i.e., the Doppler burst is required to be a periodic function in order for the FFT to accurately calculate the velocity. Therefore, it is desirable to neglect particles

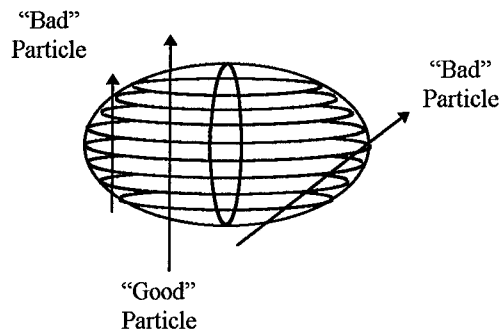


Figure 3.4: "Good" vs. "Bad" Particles

which do not enter the control volume at an angle normal to the fringe disks or which may be accelerating through the control volume. It is also desirable to filter out particles which may only cross the control volume near the edges (see Figure 3.4), as well as bursts received from two particles crossing the control volume at the same time. In order to filter out these effects, different types of particle and signal validation are employed by the BSAs.

3.3.1 Fringe Count. In order to filter out the particles that traverse near the edges of the control volume and those which are traveling almost parallel to the plane of the fringe disks, a minimum number of fringe crossings is required for the particle to be considered valid. This restricts valid particles to those traveling through the center portion of the control volume and nearly normal to the fringe plane.

3.3.2 Acceleration Detection. The velocity of each particle is calculated assuming the particle is not accelerating through the control volume. This assumption is justified by filtering out accelerating particles; this filtering is accomplished by comparing the time taken to cross a certain number of fringes. For instance, the time taken to cross three fringes is compared to the time taken to cross five fringes; if they are the same, the particle is non-accelerating and is accepted as valid.

3.3.3 *Local Maxima Check.* When the BSA is performing the time sampling, it has no way of knowing if the scattered light is coming off one or more particles. For instance, if two particles are traversing the control volume nearly simultaneously, they will produce the burst pattern shown in Figure 3.5. In order to minimize the chances of the BSA tracking two particles at once, the BSA compares the intensity pattern of light gathered at each sample. More specifically, it compares the two largest local maxima to the global maximum; the global maximum must be at least four times the local maxima in order for the burst to be accepted as valid (see Figure 3.6). A burst pattern like the one shown in Figure 3.5 would produce a signal violating the local maximum criteria, causing the BSA to reject the burst.

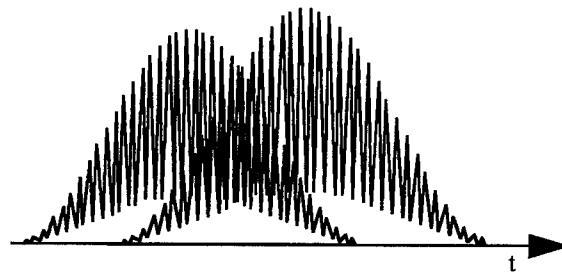


Figure 3.5: Burst Pattern From Two Nearly-Coincident Bursts

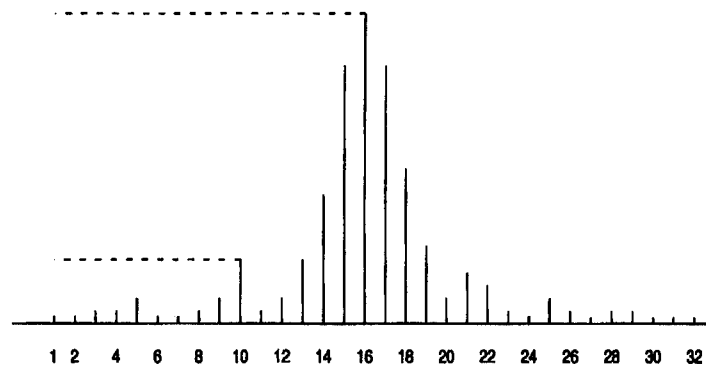


Figure 3.6: Local Maxima Validation (from Ref. [10])

3.3.4 *Envelope, Pedestal, and Quality Factor.* The envelope and pedestal are properties of the Doppler burst received by the BSA. The pedestal is generated by running the burst signal through a baseline clamp and a lowpass filter. The envelope is generated by running the burst signal through a bandpass filter, a rectifier, and finally a lowpass filter (see Figure 3.7). The quality factor is the ratio between the envelope and the pedestal; it sets a limit on the amplitude of the received signal, below which the burst is rejected. Adjustment of the envelope, pedestal, and quality factor allows for filtering of random noise, such as laser light which is scattered by defects

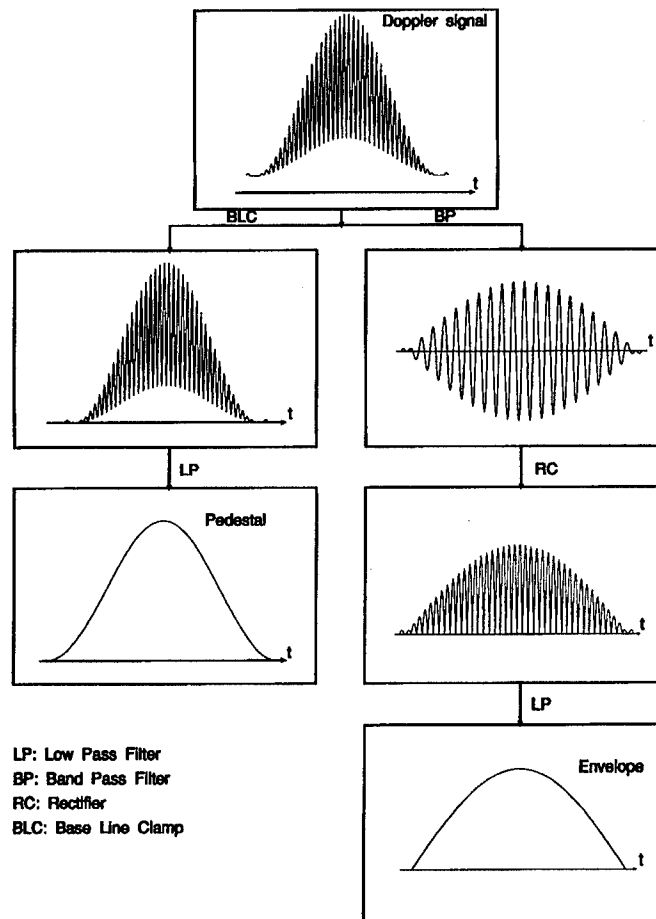


Figure 3.7: Envelope and Pedestal Generation (from Ref [10])

in the wind tunnel windows. Proper adjustment assures only bursts with high signal-to-noise ratios (SNRs) are used for velocity calculations.

3.4 *Directional Ambiguity and Frequency Shift*

When a particle traveling through the control volume produces a burst signal, the BSA cannot tell whether the particle is moving “up” or “down” (referenced to the orientation in Figure 3.2) through the control volume; the Doppler frequency depends only on the spacing between the fringes and not on the particle’s direction of motion. This inability to distinguish the direction of motion is referred to as *directional ambiguity*.

The problem of directional ambiguity is solved by passing one of the two laser beams through a Bragg cell, which introduces a frequency shift of magnitude f_b into the beam. This frequency shift causes the fringes to sweep across the control volume at a constant velocity, $v_f = x_f f_b$ [20]. The motion of the fringes causes a frequency shift in the burst signal that is dependent on the direction of the particle’s motion, overcoming the problem of directional ambiguity.

3.5 *Particle Correlation and Coincidence Window*

When using a two-component (four-laser beam) LDV system to simultaneously measure particle velocities in two dimensions, the velocity in one dimension is measured by one frequency of light, while a different frequency of laser light is used for the other direction. A particle will then produce two Doppler bursts, one corresponding to each frequency of light. As a result, two BSAs are needed to process the burst signals, one for each frequency. The signals at the two frequencies are independent of one another, so it becomes necessary to find a way of correlating the two. That is, a burst on one BSA needs to be paired with the burst on the other BSA which was produced by

the same particle. This correlation is accomplished using a *coincidence window*. The coincidence window is a time interval set by the user of the LDV system to determine if two bursts are produced by the same particle.

As a particle enters the control volume, one of the two BSAs will detect the particle first. Because different frequencies of laser light are used for each velocity component, the intensity of scattered light from one of the beams will generally be higher than that from the other beam. The BSA detecting the higher-intensity beam is used as a “master” BSA: when it detects a particle, it signals the other BSA to begin looking for the same particle. When (and if) the second BSA finds the particle, it records its own arrival time. The coincidence window is the maximum allowable time between the arrival time on one BSA and the arrival time on the second BSA. The coincidence window needs to be set large enough that the two bursts produced by the same particle are correlated, but yet small enough that the burst recorded on one BSA is not correlated with more than one burst on the other BSA. The size of the coincidence window is also limited by the time taken by a particle to cross the control volume: if the coincidence window is too large, there exists the possibility of correlating a particle inside the control volume with one outside the control volume. This artificial correlation of particle velocities can result in skewed measurements of the product $\overline{u'v'}$.

3.6 Angular Bias of Turbulence Measurements

Measurements of $\overline{u'v'}$ (as well as the turbulence intensities) made with the LDV system can be skewed by a phenomenon known as *angular bias*. Angular bias is the result of operating the LDV system with the fringe plane aligned at a substantial angle relative to the mean flow (normally 45°). [15] Traditionally, this angular orientation was required to resolve the problem of

equipment limitations when measuring high-speed flows. When the lasers are aligned in this manner, the velocity measured by the BSAs is $u \cos(45)$, which is considerably lower than measuring u directly, resulting in easier and more accurate detection by the BSAs.

The effect of angular bias comes into play in highly turbulent flows. If the magnitude of the v -component of velocity is the same order of magnitude as u and the control volume is oriented at an angle to the mean flow, there is the possibility that the particles may run parallel to the fringes (see Figure 3.8). In this case, the particles do not cross enough fringes to be validated and the particle's signal is discarded. Discarding these particles results in erroneous measurements of the turbulence intensities as well as the correlation $\overline{u'v'}$. In general, angular biasing will cause a decrease in the measured values of the turbulence intensities and the magnitude of $\overline{u'v'}$ [15].

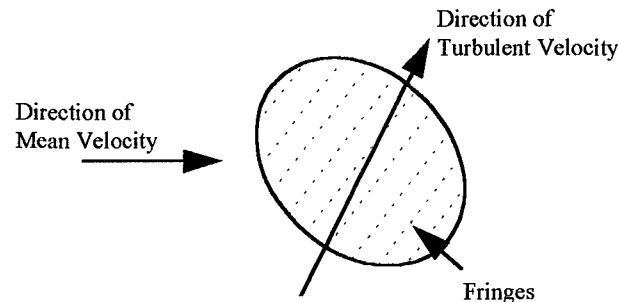


Figure 3.8: Turbulence Effect on Particle Direction

The effect on the product $\overline{u'v'}$ is most evident in early LDV experiments where the u and v velocities were not measured simultaneously (*cf.* Ref. [21]), but were measured separately with a single-component system, first measuring u and then v . The two results were correlated in a manner similar to that which is used to determine $\overline{u'v'}$ from slanted-wire hot-wire measurements.

Later LDV measurements partially corrected this problem using Bragg cells and frequency shifting (*cf.* Ref. [30]). Instead of the particle crossing the fringes, the fringes swept across the

path of the particle, resulting in enough crossings for the particle to be validated. However, in high-speed flows, if the fringe velocity is not fast enough the particle may still cross the control volume without crossing enough fringes to be validated.

Although the fringe velocity could be increased by increasing the frequency shift supplied by the Bragg cell, the speed with which the fringes can sweep across the control volume is limited by the sensitivity of the receiving optics and the processing capabilities of the BSAs. According to Elena [15], "to retain a high precision of measurements with the presently available counters, a frequency of 45 MHz must not be exceeded."

Finally, the most recent experiments have used two-component LDV systems, where the fringes from the second set of lasers are perpendicular to the fringes from the first set (*cf.* Ref. [16]). Thus, a particle running parallel to one set of fringes and not validated by that BSA should be detected and validated by the other BSA. However, if the lasers are still placed at a 45° angle to the mean flow, the light scattered from the low-intensity laser beam may not be powerful enough for its BSA to detect, and the influence on $\overline{u'v'}$ would once again be lost.

The effect of angular bias can be resolved by aligning the fringe disks so the fringes from the highest-intensity laser beams run normal to the mean flow. Thus, even in highly-turbulent flows, the fastest particles will cross the fringes generated by the high-intensity laser at an angle no less than 45°. Any particle running nearly parallel to the high-powered beams should be moving slow enough for the lower-intensity beams to detect.

3.7 Intensity Pattern of Scattered Light

In order to minimize the number of bursts rejected because the intensity of scattered light is too low, it is necessary to place the receiving optics where the intensity is the highest. Figure 3.9

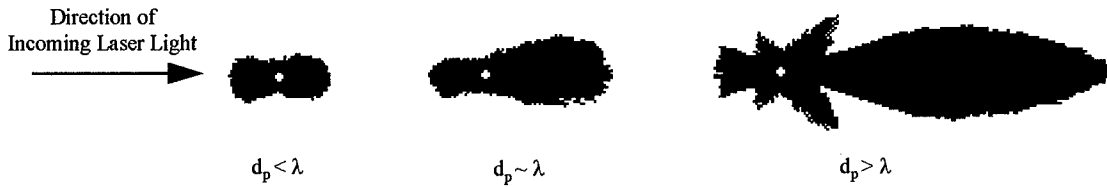


Figure 3.9: Intensity of Scattered Light [Dantec, Inc.]

shows the theoretical scattering diagram for the intensity of light scattered from a spherical particle. Note that the intensity distribution depends on the wavelength of light as well as the size of the particle (d_p in Figure 3.9 represents the particle diameter).

It is clear from Figure 3.9 that the intensity distribution is generally the highest on the “front” side of the particle. Durst et al. [14] presented the scattered light intensity on a radial log scale; this graphic is reproduced in Figure 3.10. Note that the intensity distribution is plotted on a logarithmic scale, and as such the intensity on the front side of the particle can be orders of magnitude higher than that on the back side. Therefore, in high-speed flows where the scattered light has relatively low intensities in all directions, the receiving optics are placed on the far side of the measuring volume from the transmitting optics, an alignment referred to as *forward scattering* mode.

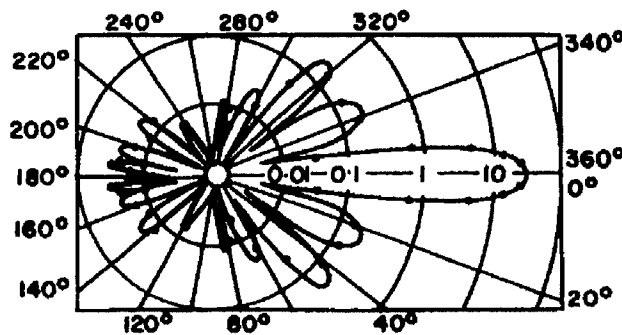


Figure 3.10: Magnitude of Intensity of Scattered Light [14]

While use of forward scattering mode enables the collection of more scattered light, it also increases the level of difficulty associated with data collection. The receiving optics are contained in a separate apparatus from the transmitting optics and must be precisely aligned with the control volume (when using backscatter mode with the current LDV system, the transmitting and receiving optics are contained in the same probe and pre-aligned to be focused on the same location: the process becomes a matter of "point-and-shoot"). When the transmitting optics are re-positioned, the receiving optics need to be realigned as well.

3.8 Seeding the Flow: Intrusive Aspects of LDV and the Problem of Velocity Slip

To this point, it has been assumed that the flow contains particles which will scatter the light from the laser beam; however, it is generally necessary to introduce these particles into the flow, a process known as *seeding*. Even when there are naturally-occurring particles in the flow, it is better to filter the natural particles and introduce particles of known size and material properties [15]. The necessity of introducing these particles means that LDV is not really non-intrusive, as is often suggested. In order to reduce the effects of seeding, several precautions must be taken. The most important aspects are efficient injector design, proper particle sizing and particle material considerations.

3.8.1 Injector Design. Ideally, an injector would not have to be placed inside the flow; if possible, an opening should be placed in the wall of the wind tunnel, through which seed particles are added to the flow. Careful attention needs to be placed on the sizing of the hole, as the hole diameter can affect the flow characteristics [15]. If the design of the wind tunnel does not permit injection from an opening in the wall, some type of injector needs to be placed in the flowfield.

Any injector which is placed in the flowfield will have a wake associated with its presence. Therefore, it is desirable to place the injector far upstream from the test section and, if possible, in a region where the flow velocities are low (to minimize the wake produced). If the injector were placed in a region of supersonic flow, its presence would induce a shock wave. Thus, in a supersonic wind tunnel, it is necessary to place the injector before the throat, when the flow is still subsonic. In all cases the injector should be streamlined to reduce the wake produced.

No matter what kind of injector is used, it is necessary to inject the particles at a speed equal to the local mean flow velocity in order to minimize pressure-difference effects [15]. It is also necessary to use the lowest seeding density possible in order to minimize the effects of the particles on the flow being studied.

3.8.2 Particle Sizing. Careful attention must be paid to the size of the particles injected into the flow; particles must be small enough to ensure that they follow the smallest motions of the fluid. This becomes especially important in the study of high-speed turbulence and flows near shock waves. Particles which do not follow the flow are said to experience *velocity slip*.

3.8.3 Particle Material Considerations. Particles should also be chosen according to material properties. When studying flows through shock waves it is desirable to choose particles with a fast response time; other times it may be advantageous to choose particles which will not cling to and cloud up test section windows. In other experiments, such as low-density flows, the density of seed particles may be high enough to actually change the material properties of the flow. Therefore, it is necessary to choose particles which will have the least effect on the flow properties and still follow the flow as closely as possible.

4. Equipment Description

4.1 Wind Tunnel Facilities

Data were collected in the AFIT Mach 3.0 wind tunnel. The tunnel is a combination draw-down/blow-down facility; see Figure 4.1 for a diagram of the facilities. A Leslie brand dome regulator was used to provide manual control of the stagnation pressure; the upstream Pitot pressure was read using a Endevco brand, 0-0.69 MPa pressure transducer and was set at a constant value of $2.13 \times 10^5 \pm 690$ Pa. The total temperature was monitored with an Omega Engineering type K thermocouple placed just upstream of the wind tunnel nozzle. The total temperature was constant during a single run to approximately ± 0.1 K.

4.1.1 High-Pressure Air Supply. The high pressure was supplied by two Atlas Compco compressors which could provide a combined continuous mass flow rate of approximately 0.45 kg/s at 0.69 MPa. The high pressure system supplied air to other facilities in AFIT besides the Mach 3.0 system, resulting in slight variations in the available pressure. The pressure was monitored during each traverse across the boundary layer to ensure it remained constant.

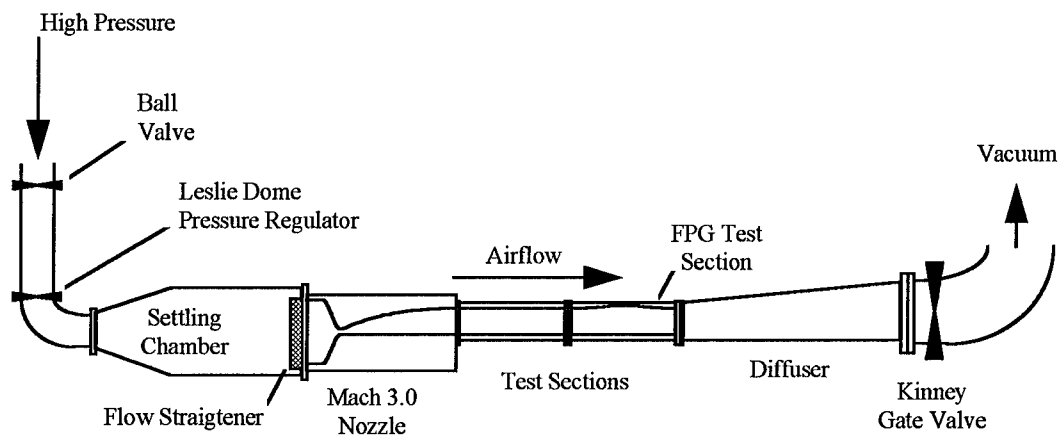


Figure 4.1: Schematic of Wind Tunnel Facilities

The high-pressure air was dried using two Pioneer Air Systems, Inc. model R500A refrigeration-type dryers. It was then passed through a centrifugal moisture and particle separator, and filtered through a layer of filament-reinforced industrial paper filters. The filters were expected to remove any naturally-occurring particles in the flow.

4.1.2 Vacuum System. The vacuum was created using three Stokes Penwalt model 212-11 MicroVac pumps. Each pump was powered by a 7.6 metric hp Reliance motor. The vacuum tank capacity of the system was approximately 16 cubic meters. The vacuum pumps were able to reduce the pressure in the tanks to 10 mm of Hg in approximately six minutes.

4.1.3 Wind Tunnel Operation. Flow through the tunnel was initiated by opening the Kinney Corp. GP-8 gate valve in order to expose the tunnel to the vacuum. The high pressure was then released by opening the El-O-Matic ED10 ball valve, starting the airflow through the tunnel. Once airflow was initiated, the tunnel took approximately eight seconds to reach steady state, followed by a 25-second steady-state period in which it was possible to collect data.

4.1.4 Test Section. The test section had a cross-sectional area 6.35 cm x 6.35 cm. The floor and wall sections were constructed of 1.905 cm aluminum alloy and were modular to allow for interchange of various models. The test section was actually comprised of two sub-sections (see Figure 4.1); each sub-section was 33.02 cm in length. All seams in the test section walls were fitted with rubber gaskets which sealed the wall sections when the vacuum system was engaged. The sections were also fitted with adjustable flanges which allowed each section to be shifted relative to the adjacent section in order to minimize shocks and expansions that might have formed off the seams. The FPG model was integrated into the ceiling of the second test section as shown in Figure 4.1; the specifics of the design are discussed below.

4.1.4.1 Model Design. The FPG model consists of a curved ceiling for the test

section; the equation for the curve is given in test section coordinates by [26]

$$y_{ts} = \begin{cases} 0 & 0 \leq x_{ts} \leq 4.32 \\ a_0 + a_1 x_{ts} + a_2 x_{ts}^2 + a_3 x_{ts}^3 & 4.32 \leq x_{ts} \leq 12.7 \\ -0.65 & 12.7 \leq x_{ts} \leq 16.51 \end{cases} \quad (4.1)$$

where the units are in cm and the coefficients are given in Table 4.1. It should be noted that the coordinates for this curve were also reported in Ref. [27], but the coordinates in Ref. [27] were incorrect. The accuracy of the wall position equation is ± 0.0008 cm. Figure 4.2 shows a scale drawing of the test section ceiling.

Table 4.1: Test Section Curve Coefficients

a_0	a_1	a_2	$a_3 \times 1000$
-0.2078	0.0897	-0.0095	-0.0360



Figure 4.2: Scale Schematic of Test Section Ceiling

With the equation for the curve known in test section coordinates, the relationship between the body-intrinsic coordinate x and the test section coordinate x_{ts} was given by

$$x = 64.32 + \int_{4.32}^{x_{ts}} \sqrt{1 + (dy_{ts}/dx_{ts})^2} dx_{ts} \quad (4.2)$$

A flat plate model was also used in order to collect data in the same location as the FPG; the flat plate and favorable pressure gradient data were collected at the location $x_{ts} = 11.5$ cm ($x_{wt} = 71.5$ cm). Flat plate data were also collected at $x_{wt} = 44$ cm, in the center of the upstream sub-section, in order to compare with the data collected by Miller. [26]

4.1.4.2 *Window Placement.* Use of the LDV system required the tunnel test section walls to be fitted with optical-grade glass windows. The windows chosen were made of 1.27 cm thick optical grade glass. Each window was circular, with a diameter of 7.62 cm. The windows were placed in the test section wall as shown in Figure 4.3. Note that the test section floor/ceiling had a length of 33.02 cm, while the wall was only 29.21 cm long. The difference was due to the fact that the adjustable flanges at the tunnel seams were designed slightly differently for the floor and ceiling sections than for the wall sections.

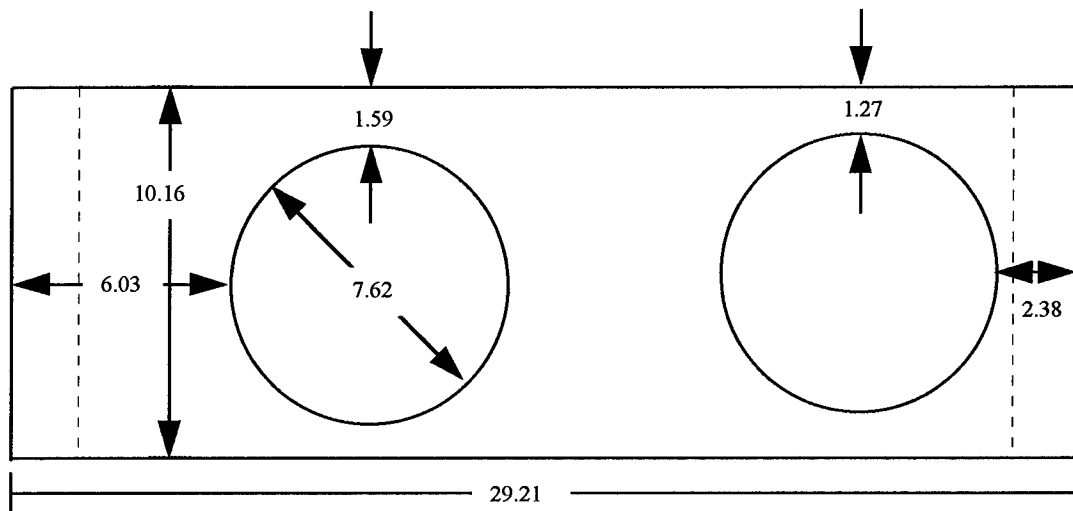


Figure 4.3: Optical Window Placement Schematic (Dimensions in cm)

Note that the left window in Figure 4.3 was slightly off-center in the vertical direction. The displacement was incorporated to allow measurements over a larger portion of the test section; more importantly, it allowed the window to expose the section of the FPG model where it curved back “into” the test section wall. Figure 4.4 shows the total possible area covered by the test section windows and the location of the test section.

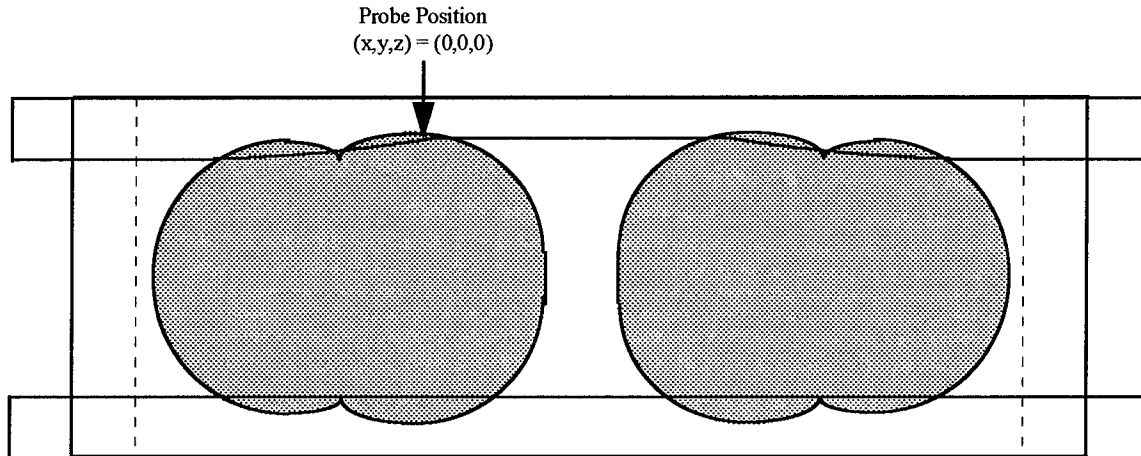


Figure 4.4: Optical Window Test Section Coverage

4.2 LDV System

The laser Doppler velocimetry system was manufactured by Dantec, Inc. Many parts of the system were interchangeable, so the details and specifications of the equipment used in this study are presented below.

4.2.1 Laser Optics. The laser optic system consisted of the laser itself, a transmitter which sent the laser beam to the transmitting optics, the transmitting optics, the receiving optics, and the photomultiplier (PM) tubes. Each component is described in detail below.

The laser was an Ion Laser Technology, Model 5500A-00 Argon-ion laser with a maximum (rated) output capability of 300 mW. Due to the deterioration of efficiency which occurs with age, the laser was found to have a maximum output power of approximately 275 mW. The laser was supplied with power using an Ion Laser Technology Model 5405A power supply. The power supply operated at 210V and 20A, requiring a 220 VAC power source. The laser was designed to operate in the TEM_{00} mode, where the laser beam is centered around the optical axis with the maximum power in the center. The $1/e^2$ beam diameter of the laser was 0.82 mm.

The transmitter was a Fiber Flow 60X41 transmitter. A Bragg cell in the transmitter split the laser into three wavelengths of light: 514.5 nm, 488.0 nm, and 476.5 nm. These frequencies corresponded to light beams which appeared green, blue, and violet, respectively. The Bragg cell also split each wavelength into two separate beams and supplied one of the two with a 40 MHz frequency shift. As described in Chapter 3, the frequency shift caused a motion of the fringes across the control volume. Note that the frequency shift supplied by the Bragg cell is less than the maximum limit (45 MHz) given in Ref. [15].

The transmitter was equipped with six DANTEC 60X24 fiber manipulators which were used to attach the fiber-optic cables to the transmitter. The manipulators allowed the ends of the fiber optic cables to be precisely adjusted in order to ensure the laser beam was centered on the cable, providing maximum transmitting efficiency. The laser beams were then passed through the fiber optic cables to the transmitting and receiving optics. The laser and transmitter are shown in Figure 4.5.

The transmitting optics were contained in a DANTEC 60X61 optic probe, while the receiving optics were in a model 60X60 optic probe (shown in Figure 4.6). Each probe contained an optic transducer, a distributor unit, and transmitting *and* receiving fibers. The transmitting probe was a two-component probe which projected the 514.5 and 488 nm laser beams, while the receiving probe was single-component and projected the 476.5 nm beam. Each probe had two transmitting fibers for each component; therefore, the transmitting optics were projecting four laser beams while the receiving optics were projecting two. Each probe was attached to the traverse mounting bench using DANTEC probe supports. The transmitting optics were placed on a 60X3611 support which allowed for angular adjustments in the $x_T - y_T$ plane, while the receiving optics were mounted on a 60X3631 probe support which used micrometers to allow precise adjustment in all three dimensions.

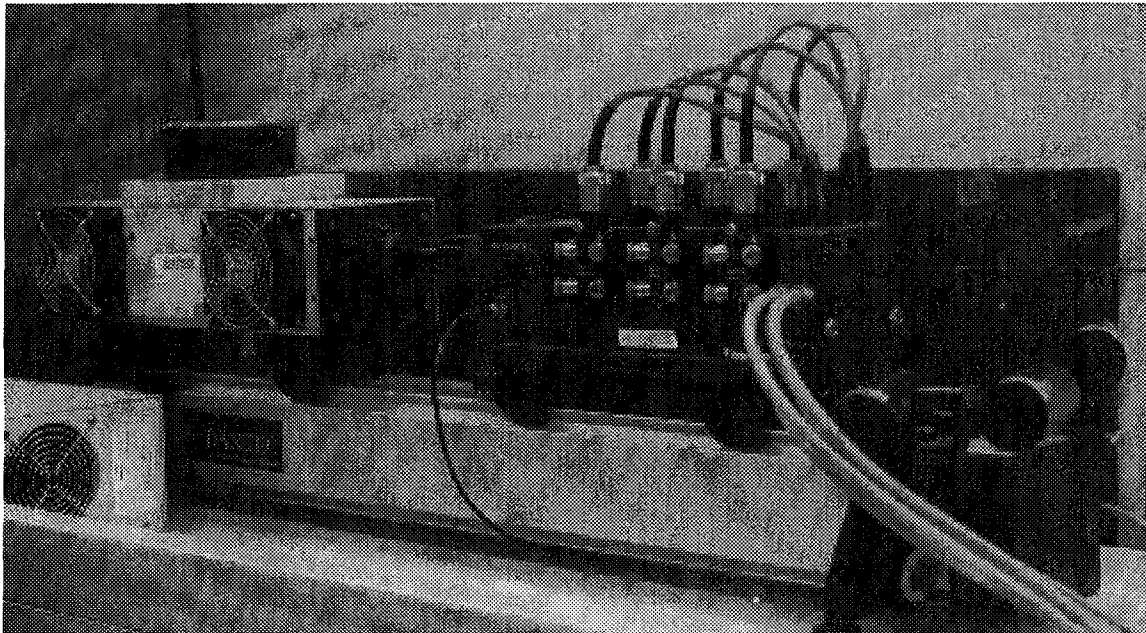


Figure 4.5: Laser and Transmitter

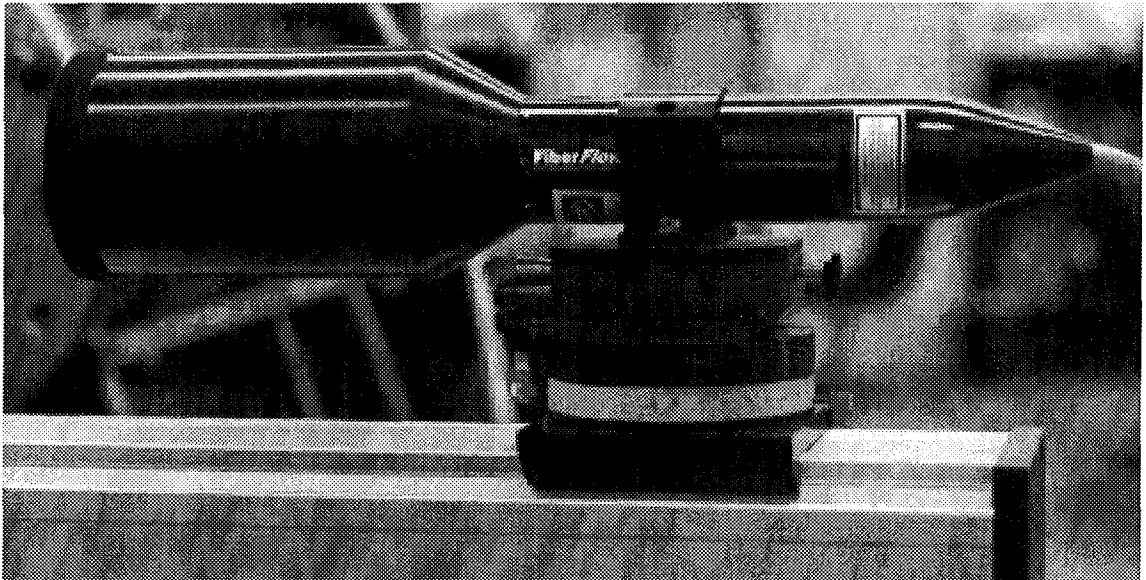


Figure 4.6: Optic Probe (Receiving Optics)

On the front of the transmitting probe was a 600 mm focal-length lens; the laser beams were separated by 38 mm on the front face of the lens (see Figure 4.7). The diameter of the lasers beams, the focal length of the lens on the transmitting optics and the beam separation on the face of the transmitting probe interacted to produce a measurement volume 9.0 mm in length (along the z-axis) and 0.276 mm in diameter. The receiving optics were fitted with a 55X12 beam expander as well as the 600 mm focal length lens. The beam expander was used to increase the amount of reflected light gathered by the optics.

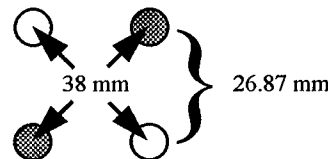


Figure 4.7: Beam Separation on Face of Optic Probe

The light collected by the receiving optics was sent through fiber optic cables to a DANTEC 55X35 color separator. The color separator split the received light into 514.5 and 488.0 nm wavelengths and transferred each wavelength to a DANTEC 55X35 photomultiplier (PM) tube. The PM tube converted the received light into an electrical signal associated with the frequency of the light. This electrical signal was then sent to the BSA for processing.

4.2.2 Data Acquisition Equipment. The Doppler bursts detected by the receiving optics were processed by one Dantec 57N20 BSA Enhanced (u -component of velocity) and one Dantec 57N35 BSA Enhanced Model S (v -component of velocity). The 57N20 BSA was used as the master BSA for coincidence filtering calculations; the interior clock had a frequency of 1 MHz.

The software used in the data collection was the Dantec Burstware[®] 2.0 package; the software was run on a Gateway 2000 486DX/33 personal computer.

4.2.3 *Traverse.* A Dantec 3D Traverse System was used to control the position of the measurement volume. The traverse was powered by three Cleveland Machine Controls stepper motors which were regulated by Dynapar encoders, model M20100003331. The encoders converted 1000 pulses into one revolution of the load screw, resulting in a 2 mm displacement of the traverse. The entire system was rated at an accuracy of $\pm 80 \mu\text{m}$ over a 600 mm range (0.13 $\mu\text{m}/\text{mm}$) and could support a maximum load of 445 N. The DANTEC traverse mounting bench was replaced by a 1.83 m long DANTEC laser mounting bench for reasons which will be described in Chapter 5.

4.2.4 *Seeding Apparatus.* The seeding apparatus consisted of a TSI, Inc. six-jet atomizer attached to an injector which was placed inside the settling chamber of the wind tunnel. The connection from the atomizer to the injector was accomplished using Tygon-brand plastic tubing (type R-3603, 1.27 cm inner diameter).

4.2.4.1 *Atomizer.* The atomizer was manufactured by TSI, Inc. and is shown in Figure 4.8. It was a variable-flow atomizer, allowing for particle-density control through two options. The first was to use a pressure control valve to regulate the pressure difference through the atomizer. The second method for particle density control was manual control over the number of jets in use.

4.2.4.2 *Seeding Material.* Due to cost and availability concerns, the seeding material chosen for use in this experiment was Bertoli brand extra light olive oil. The atomizer manual [34] gave the mean particle size for olive oil particles as $d_p \approx 0.6 \mu\text{m}$.

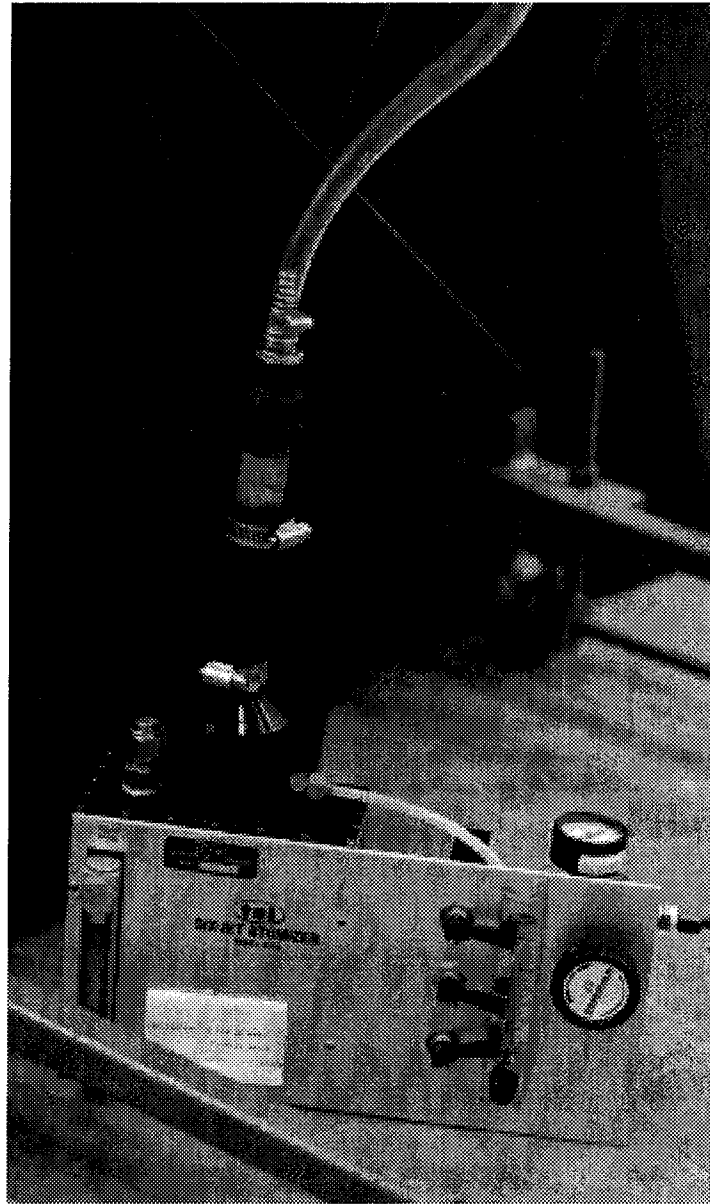


Figure 4.8: Six-Jet Atomizer

4.2.4.3 *Injector Design.* The injector was designed from copper tubing with an inner diameter of 1.27 cm. In order to minimize the effect of the injector on the flow, the copper tubing was streamlined by flattening it in a vise. Openings were cut into the injector such that particles would only be injected into the flow over the upper half of the wind tunnel. The injector was placed in the settling chamber, about 3 cm upstream of the flow straightener. A schematic of the injector and its attachment to the atomizer is shown in Figure 4.9.

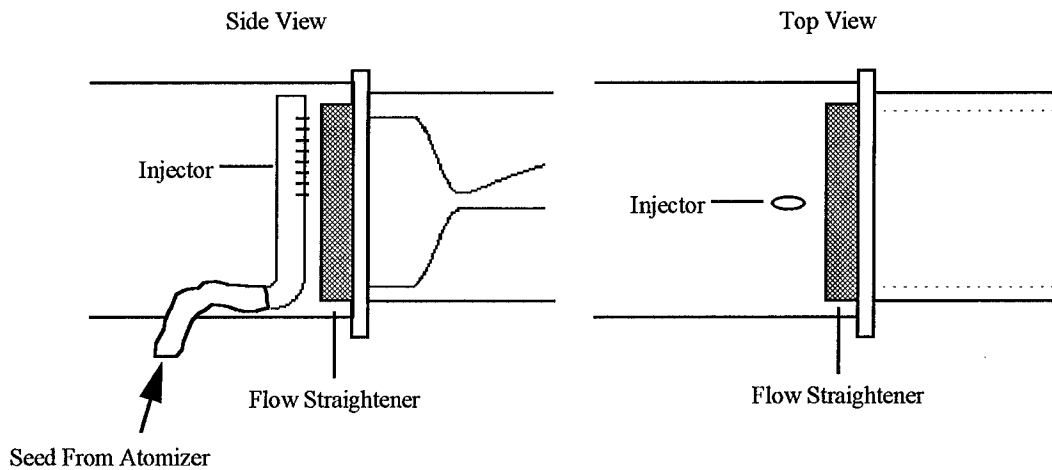


Figure 4.9: Injector Design and Location in Wind Tunnel

4.3 *Flow Visualization Equipment*

The shadowgraphs and schlierens were taken using a Xenon Corp. 437B Nanopulser which fed power to a De Leone Corp. N-787B broad-spectrum spark generator. The light from the spark was focused using one or two 14.4 cm diameter focal mirrors, each with a focal distance of 152.4 cm. In the case of the schlieren photographs (see Chapter 5 for details of the arrangement), the light beam was also passed through a 11.2 cm diameter focusing lens. The photographs were taken with a Polaroid 545i camera using Polaroid type 57 high-speed, ISO 3000/36° film.

5. Experimental Procedures

5.1 Wind Tunnel Operation

Airflow was initiated in the wind tunnel as described in Section 4.3.1. During the eight-second span when the wind tunnel was approaching steady-state operation, two jets on the atomizer were opened to begin injection of seed into the flow. Once the steady-state point was reached, data were collected for 12 seconds, collecting as many bursts as possible. Operation of the wind tunnel was stopped by closing the high-pressure supply and then shutting the gate valve to seal off the vacuum tanks.

5.2 LDV System Preparation

Due to the relatively low intensity of the laser beams, the high flow velocities and the associated low SNR, the LDV system was operated in forward-scatter mode. The two-component probe was used as the transmitter, while the single-component probe functioned as the receiver. In order to simplify data collection, it was desired to have both the transmitting and receiving optics attached to the traverse system; otherwise, whenever the transmitting optics were moved to a new location, the receiving optics would need to be realigned. In order to overcome this problem, both the transmitting and receiving optics needed to be placed on the traverse mounting bench, but the focal distance of the optics was too long to allow this to happen. The problem was solved by interchanging the mounting bench on the Dantec traverse system with the laser mounting bench; the laser mounting bench was long enough to allow both the transmitting and receiving probes to be placed on the traverse and moved simultaneously. Interchanging the two benches forced realignment of the laser transmitter with the laser, ensuring the laser system was operating at peak efficiency.

After the optic probes were attached to the traverse system, the traverse needed to be aligned with the wind tunnel and the optics with the test section wall; in addition, the receiving optics had to be aligned with the control volume and the BSA settings had to be optimized.

5.2.1 Traverse Alignment, Laser Orientation and Origin Placement

In order to prepare for data collection, the traverse had to be aligned with the test section. Once the traverse was aligned, the optics needed to be aligned with the test section wall in order to collect data in a body-intrinsic coordinate system.

5.2.1.1 *Traverse Alignment.* To simplify conversion between the traverse coordinate system and the test section coordinates, the traverse bench was aligned perpendicular to the wind tunnel (see Figure 5.2). The alignment was accomplished by pointing the lasers parallel to the traverse bench (the DANTEC probe supports were marked at 1° intervals, allowing the lasers to be accurately aligned with the traverse bench) and rotating the entire traverse assembly until the lasers were reflected off the windows back onto themselves. Once the traverse was aligned normal to the tunnel, the lasers were rotated 3.5° off the axis of the traverse bench (i.e., 3.5° off the z -axis, see θ in Figure 5.1). This was necessary to ensure that the extremely sensitive PM tubes in the receiving optics were not exposed to direct laser light from the transmitting optics. While this alignment caused a slight bias to the collected data, it was small enough to be neglected (see Appendix B).

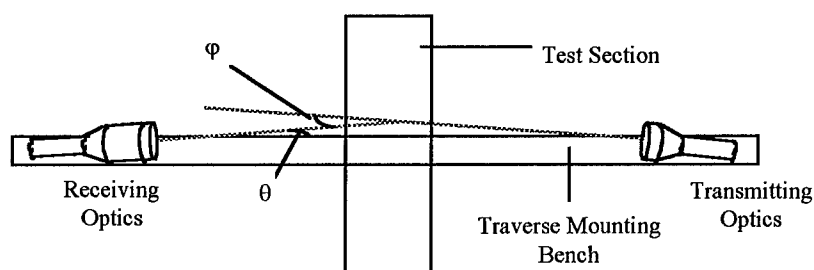


Figure 5.1: Traverse and Laser Alignment Relative to the Wind Tunnel

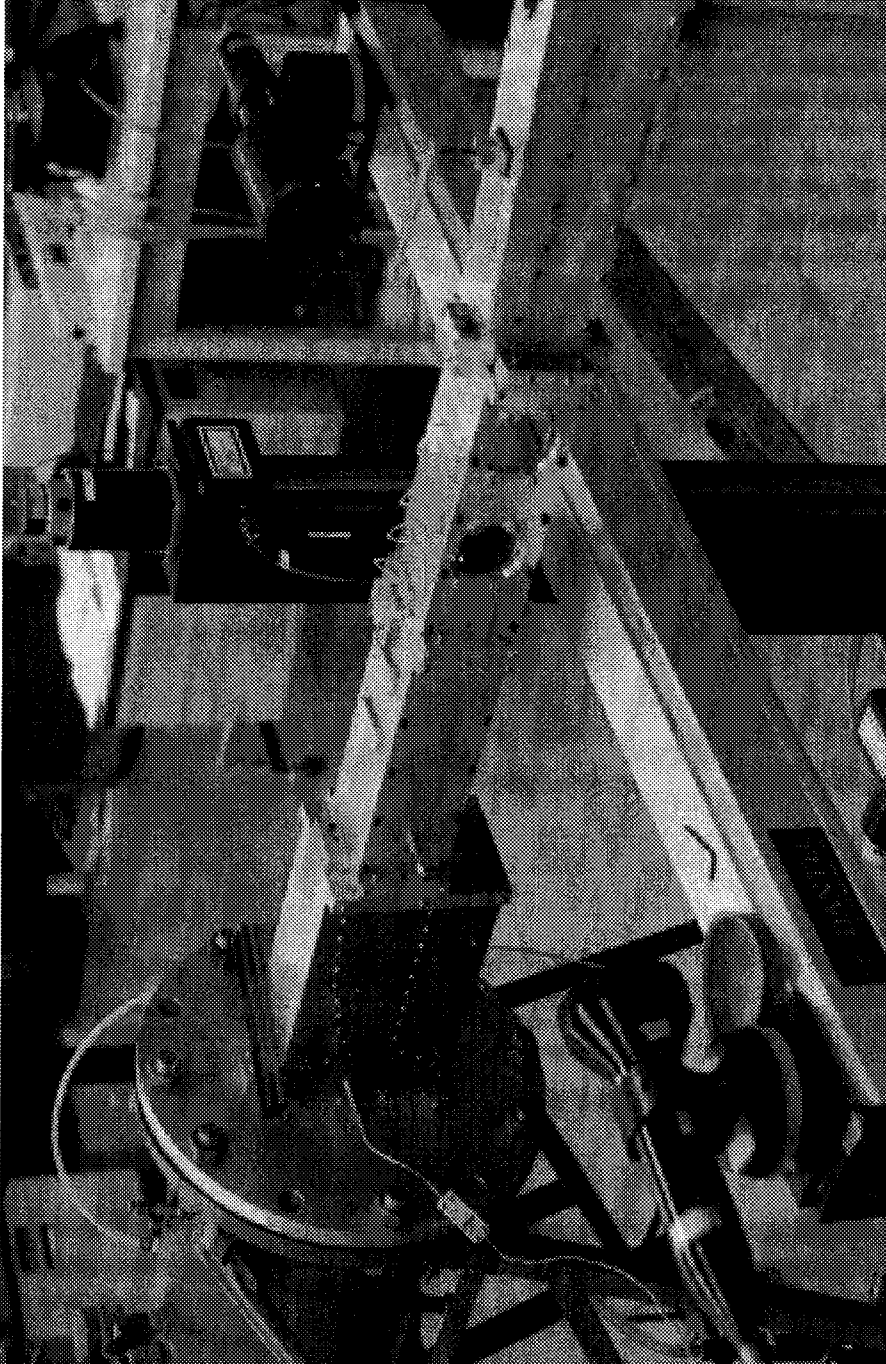


Figure 5.2: Traverse Aligned with Wind Tunnel

An attempt was made to align the traverse in a way which would keep the transmitted lasers normal to the tunnel wall, eliminating the bias described above. Due to the fact that the transmitted lasers could not be pointed directly at the receiving optics, this would force the traverse bench to be placed so that it was no longer perpendicular to the test section. Orienting the traverse in this manner would complicate calculation of traverse coordinates in the (x_T, y_T, z_T) space, but the measurement biasing would be eliminated. However, use of this orientation was not possible, because it would have forced the vertical support of the traverse to be placed directly below the wind tunnel (which was not physically possible). The traverse support could have been placed to the side of the wind tunnel by adjusting the traverse mounting bench off-center from the vertical support, but this option was also not physically feasible. Recall that the mounting bench on the traverse was originally the laser mounting bench and was larger (and heavier) than the normal traverse mounting bench; placing the larger bench off-center would cause a torque on the traverse system which would result in failure. The alignment which was chosen for use in data collection (where the traverse bench was normal to the tunnel) also forced the bench to be placed slightly off-axis, but not far enough to cause a large torque on the system.

Finally, note that the angle ϕ in Figure 5.1 is given by $\phi = 2\theta = 7^\circ$. For particles with a size on the order of the wavelength of laser light (600 nm in this study), the intensity pattern of scattered light is given by the center pattern in Figure 3.9. The receiving optics were 7° off-axis; thus, the relative intensity seen by the receiving optics was almost maximum, as shown in Figure 5.3.



Figure 5.3: Scattered Light Intensity Received by Optics

5.2.1.2 *Origin Placement and Streamwise Angular Alignment.* Once the traverse was aligned normal to the wind tunnel, the origin of the data-collection coordinate system needed to be set. The x_{wt} -location was placed in the correct location (all tests were conducted at $x_{wt} = 71.5$ cm, except for one flat plate test at $x_{wt} = 44$ cm) downstream of the nozzle by aligning the lasers with a mark on the outside of the test section ceiling. When the lasers were aligned in this direction, the traverse was moved in the $-z_T$ direction (recall that z_T is positive into the wall of the tunnel) until the lasers were near the wall of the test section.

The streamwise laser-angle alignment and placement of the origin in the z_T direction was a simultaneous process. Using a pair of argon-ion laser protective goggles, the reflection of the laser beams on the tunnel wall appeared as a set of small dots which were located at the center of the laser beam, where the intensity was maximum. The optics were rotated and the traverse was moved in the z_T direction until the two green laser beams (the 514.5 nm, highest-intensity beams) were bisected by the tunnel wall; this location was set as $(x,y,z) = (0,0,0)$. Note that, with the lasers aligned in this manner, the u -component of velocity ran parallel to the wall while the v -component was normal to the wall, with positive v pointing away from the wall. Aligning the lasers in this orientation was expected to reduce, if not eliminate, the effects of angular bias reported by other researchers. [13]

5.2.2 *Alignment of Receiving Optics.* After the transmitting optics were aligned with the test section wall, the receiving optics needed to be aligned with the control volume. Using the lasers projected from the receiving optics, the control volumes of the transmitting and receiving optics could be quickly aligned with a fair degree of accuracy. The alignment was then fine-tuned by lowering the lasers into the freestream, injecting a small amount of seed into the wind tunnel (while the wind tunnel was not in operation) and using the "on-line display" feature of the software.

The on-line display allowed for constant update of the validity and data acquisition rates; as the receiving optics were adjusted, the validity and data rates would change. The micrometer adjusters on the receiving probe allowed the receiving optics to be adjusted very accurately in order to maximize the data acquisition and validity rates. Using this technique, the maximum data acquisition rate seen during the alignment process was on the order of 4 kHz; the maximum validity rate during the alignment process was found to be approximately 92-94% simultaneously on each BSA (the BSA attached to the high-intensity lasers was able to achieve a higher validity rate than this, but only at the expense of the second component).

5.2.3 Software Settings. The final step before actual data collection was to adjust the settings on the BSAs to maximize the number of bursts collected while ensuring only the valid bursts were processed. The proper setting for most of the variables depended on the characteristics of the flow field: high vs. low speed, the amount of turbulence in the flow, if there were shocks present, etc. In order to determine the effects each setting had on the collected data and to decide on proper settings for the wind-tunnel experiment, preliminary tests were conducted using a high-speed nozzle attached to the atomizer; the results from these tests helped establish the settings used in the wind-tunnel tests.

During data collection in the wind tunnel, most of the variables were kept constant throughout the testing, but a few were altered from one data point to the next. The fixed and adjustable settings are presented and discussed below. It should be noted that BSA 1 was collecting the data from the 514.5 nm (green) laser beams, while BSA 2 collected the data from the 488 nm (blue) laser beams.

5.2.3.1 Fixed Settings. The fixed settings were quantities such as the envelope, pedestal, and quality factor which were kept constant throughout all tests. The constant settings

used in the data collection are presented in Tables 5.1 to 5.3. It should also be noted that the data collection mode under the “Valid” menu was set to “Valid Data.”

Table 5.1: “Quick” Menu Constant Software Settings

Category	BSA 1 Setting	BSA 2 Setting
Bandwidth (m/s)	325.12	246.7
Shifter Mode	Norm	Norm
Signal Gain (dB)	42	42
High Voltage (V)	1304	1504
Max. Anode Current (mA)	1.6	1.6
Pedestal Attenuation (dB)	6	6
Duty Cycle (%)	100	100
Dead Time	0	0

Table 5.2: “Soft” Menu Constant Software Settings

Category	BSA 1 Setting	BSA 2 Setting
Timer Clock	Master	Slave
Coincidence Mode	Master	Slave
Arrival Time Base	Internal	Internal
Burst Detection	Both	Both
Oversize Rejection	1	1
Buffer Mode	FIFO	FIFO
Max. Anode Current (mA)	1.6	1.6
Quality Factor (%)	50	50
Collection Mode	Burst	Burst

Table 5.3: “BSA Program” Menu Constant Software Settings

Category	BSA 1 Setting	BSA 2 Setting
Timeout	12	12
Number of Bursts	150000	150000
Velocity	Yes	Yes
Transit Time	Yes	Yes
Arrival Time	Yes	Yes

5.2.3.2 *Adjustable Settings.* Settings which were adjusted during data collection were the center frequency on BSA 1, the record length, and the size of the FIFO buffer. The center frequency on BSA 1 needed to be adjusted as the control volume was moved across the boundary layer and the measured velocities increased. The center frequency was set as close as possible to the average velocity at the given point.

As mentioned in Chapter 4, the control volume was 0.276 mm long in the streamwise direction; a particle traveling normal to the control volume (as was required by the validation processes described in Chapter 3) at 650 m/s (the highest velocity measured in the current experiment when considering fluctuations from the mean) would take 0.42 μ s to cross from one side to the other. Thus, the record interval had to be less than 0.42 μ s. Due to the finite sampling rates used by the BSAs, the limit on the record interval placed a limit on the record length, restricting it to 8 or 16 samples. Only a few comparison test runs were taken with the record length set at 8 samples; unless otherwise noted, it should be assumed that the record length was set to 16 samples.

The size of the FIFO buffer determined how many bursts were to be collected before the burst data were stored. For instance, if the FIFO buffer was set at 4000, the BSAs would collect 4000 bursts and then send them to memory; 4000 more bursts would be collected and then sent to memory, etc. A difficulty with the FIFO buffer size was that the last group of bursts collected did not get sent to the memory. For instance, if the BSA recorded 5234 bursts and the FIFO buffer was set to 4000, the last 1234 bursts would be lost. This became problematic in the FPG testing, when the streamlines diverged, resulting in a lower seeding density and fewer recorded bursts near the wall. In order to send as many bursts as possible to the memory, the FIFO buffer needed to be reduced, resulting in loss of a smaller number of burst records. However, if the FIFO buffer was

set too small, the BSA spent too much time transferring data to memory, resulting in fewer total bursts collected.

5.3 Data Collection Techniques

After the optics were aligned and the software was prepared, the LDV system was ready to begin data acquisition. The data were collected along a traverse path normal to the wall; the closest distance to the wall at which data collection was possible was limited by the optics. Aside from taking data at the same locations as the data taken by Miller [26], data were also collected at several locations in the flow in order to measure the flow strain rates.

5.3.1 Traverse Path Across the Boundary Layer. The traverse path ran normal to the wall at the location $x_{wt} = 0.715$ m. At this location, the equation for the wall position provides an equation for the normal line, given (in traverse coordinates) as

$$z_T = 7.0169y_T \quad (5.1)$$

The error associated with the traverse position was found to increase linearly with each data point taken across the boundary layer (see Appendix B). In addition, the total temperature rose slightly as the compressors heated from constant use. Therefore, in order to minimize the error and maintain conditions as constant as possible, each traverse across the boundary layer was limited to collection of data at approximately 15 points. Successive traverses across the boundary layer collected data at different values of y/δ in order to create a more robust velocity profile.

5.3.2 Wall Proximity Limitations. The closest position to the wall at which data could be collected was limited by the configuration of the optics, as shown in Figure 5.4. Note that Figure 5.4 gives the theoretical minimum distance from the wall as 0.71 mm, based on an infinitely thin laser beam and ideal conditions. In reality, the minimum distance was found to be approximately

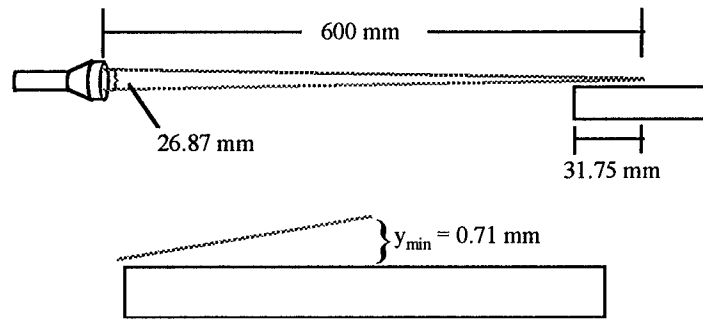


Figure 5.4: Wall-Proximity Limitation for Two-Component Measurements

1.13 mm due to laser beams of finite thickness and reflections off the wall. Because the 514.5 nm beams were oriented parallel to the wall, it was possible to obtain measurements of the u -velocity component down to a distance of $y \approx 0.07$ mm from the wall.

5.3.3 Finite-Difference Grid. Strain rates across the boundary layer were computed by collecting data at several locations in order to build a finite-difference grid. The finite-difference approximations used were central differences in the lateral direction and backward differences in the streamwise direction. A backward difference was chosen because of the termination of the wall curvature and the resulting compression shock slightly upstream of the measurement position. The finite difference grid used is shown in Figure 5.5.

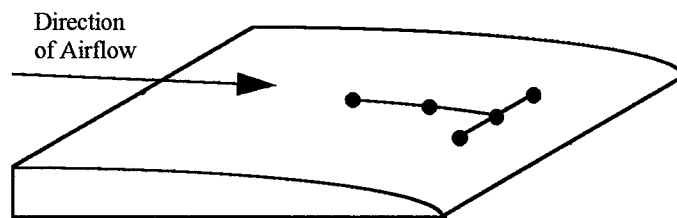


Figure 5.5: Finite-Difference Grid

The data were collected at the points $x_{wt} = 71.5$ cm, $x_{wt} = 70.96$ cm and $x_{wt} = 69.43$ cm. Converting these into the body-intrinsic coordinate system led to $x = 71.52$ cm, $x = 70.98$ cm, and $x = 70.44$ cm, respectively.

5.3.4 Atomizer Pressure. A pressure-control valve on the atomizer and one on the air supply to the atomizer allowed for fine-tuning of the atomizer pressure. In order to reduce the seeding effects, the pressure was kept as low as possible to reduce the amount of seed in the boundary layer but still allow sufficient data collection. The lowest acceptable pressure was found to be about 3.035×10^5 N/m². The effects of seeding density on the flow were investigated experimentally by collecting data with the pressure set at different levels; the results from these tests are presented in Appendix A.

5.4 Coincidence Filtering

Coincidence filtering of the data was performed by the BSAs, based on a value for the coincidence window which was set by the user. According to Ref. [11], best results would be obtained when the coincidence window was set at least twice as large as the record interval. Recalling from Section 5.2.3.2 that the fastest particles crossed the control volume in approximately 0.4 μ s, compliance with this advice restricted the record length to 8 samples. However, when the record length was set to 16 samples, the record interval was 0.333 μ s, slightly lower than the minimum traverse time. Following the recommendations of Ref. [11] would have presented possible biasing problems, as the coincidence window would have been set to 0.666 μ s. This setting would provide a high probability that a particle inside the control volume would be correlated with one already outside the control volume. To eliminate this possibility, when the record length was set to 16 samples the coincidence window was set equal to the record interval,

0.333 μ s. Thus, the coincidence window was always set to 0.333 μ s, independent of the choice for record length. The effects of coincidence filtering on the collected data were examined in detail; the results of this investigation are presented in Appendix A.

5.5 *Flow Visualization*

Flow visualization was accomplished using ten-nanosecond shadowgraph and schlieren photography. The schlieren was sensitive to the gradients in the density, while the shadowgraph was sensitive to the second-derivative of the density. The Kolmogoroff turbulent length scale for this flow was given in Chapter 1 as 2×10^{-7} m. In the highly-turbulent regions of the boundary layer the flow was moving at approximately 500 m/s; this gave the turbulent time scale as approximately 0.4 ns. Therefore, the ten-nanosecond spark generator was not expected to capture the smallest eddies in the flow. However, it had the shortest spark duration of any available source and proved adequate for capturing density gradients across the boundary layer.

5.5.1 Shadowgraph Alignment. The shadowgraph optic alignment is shown in Figure 5.6. The light source was placed slightly off the z-axis and at the focal point of the parabolic mirror. With proper alignment, this produced a 14.4 cm collimated light beam that traversed the test section along the z-axis. Proper alignment was achieved using a sighting laser: the laser was placed at the same height as the test section, and the laser beam was reflected off the focal mirror and projected back upon itself. The mirror was then turned horizontally until the light projected from the source was focused on the tunnel. The camera was placed on the opposite side of the test section from the light source, as close to the test section as possible.

5.5.2 Schlieren Alignment. The schlieren optical setup was similar to the shadowgraph setup as far as alignment of the light source and first focal mirror; however, as shown in Figure

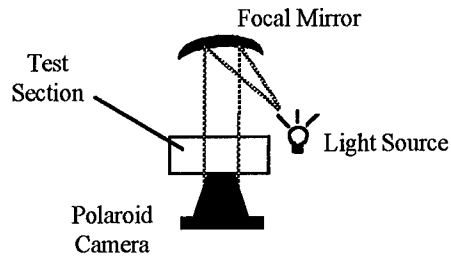


Figure 5.6: Shadowgraph Alignment

5.7, the schlieren setup was more complex. Once passing through the test section, the light was reflected off a second focal mirror in the direction of a knife edge which was placed at the focal point of the second mirror. The light was then reflected off a flat mirror, through a focusing lens, and to the camera.

In order to produce quality schlieren photographs, there were three variables that needed to be fine-tuned: the knife edge needed to be placed at the focal point of the mirror, the amount of light blocked by the knife edge needed to be precisely adjusted, and the camera had to be placed at

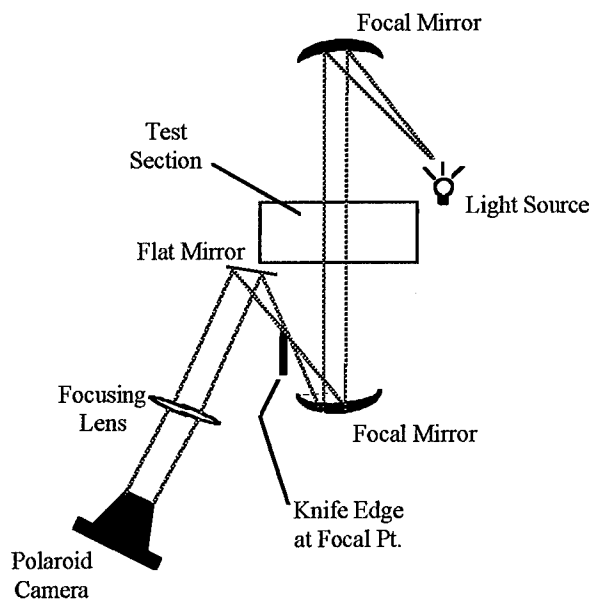


Figure 5.7: Schlieren Alignment

the correct location to ensure the schlieren was in focus.

Placing the knife edge at the focal point of the mirror was relatively simple; the spark generator was placed on "continuous" mode and the position of the knife edge was adjusted until the image of the spark on the knife edge came into focus. The camera was focused using a transparency with lettering on it which was placed on either side of the test section. The position of the camera was adjusted until the lettering on the transparency became clear, and its position was marked. The camera was focused once with the transparency in front of the test section and once behind; the position of the camera was marked at each location, and the final position was set half way between the two in order to place the focal point in the center of the test section. Slight adjustments were made during the course of taking pictures in order to fine-tune the focus.

The amount of light blocked by the knife edge was the hardest variable to adjust. Blocking too much light would (obviously) cause the schlieren to be too dark; conversely, if not enough light was blocked, the effect of the knife edge would be lost and the resulting photograph would look like a shadowgraph. The best schlieren photographs seemed to be the ones where 1/3 to 1/2 of the light was blocked. The process of taking schlierens involved trial-and error, attempting to align the lighting and the focus at the same time.

Schlieren photographs were taken with the knife edge in two separate orientations. One orientation had the knife edge horizontal in order to capture the $\partial \bar{\rho} / \partial y$ density gradients. The second orientation had the knife edge vertical to capture the streamwise density gradients.

6. Data Reduction Procedures

6.1 Velocity Calculation

The velocity was calculated using a FFT to compute the Doppler frequency as given in Chapter 3; the Doppler frequency was then converted into a velocity using the frequency-velocity calibration factor, $C_{f,v}$. For the optical setup in the current experiment, the calibration factors for the u and v components of velocity were

$$C_{f,v,u} = 8.128 \frac{m/s}{MHz}, \quad C_{f,v,v} = 7.709 \frac{m/s}{MHz} \quad (6.1)$$

Once the instantaneous velocities had been measured, the mean and fluctuating velocities (\bar{u} , \bar{v} , u' , v') were computed, allowing calculation of the total velocity, Q . However, since the flow was turbulent, the mean total velocity had to be separated from the fluctuating total velocity. This was accomplished by taking the Reynolds average of the total velocity:

$$\begin{aligned} Q^2 = u^2 + v^2 &\Rightarrow (\bar{Q} + Q')^2 = (\bar{u} + u')^2 + (\bar{v} + v')^2 \\ \bar{Q}^2 \left(1 + \frac{Q'}{\bar{Q}}\right)^2 &= \bar{u}^2 \left(1 + \frac{u'}{\bar{u}}\right)^2 + \bar{v}^2 + 2\bar{v}v' + \overline{(v')^2} \end{aligned} \quad (6.2)$$

Assuming that u'/u was small, the binomial expansion could be applied to the first term; taking the Reynolds average of the equation then led to

$$\bar{Q} = \sqrt{\bar{u}^2 + \bar{v}^2 + \overline{(v')^2}} \quad (6.3)$$

Subtracting this result from Eq. (6.2), the fluctuating velocity was given by

$$Q' = \frac{\bar{u}u'}{\bar{Q}} + \frac{\bar{v}v'}{\bar{Q}} \quad (6.4)$$

The data output by the BSAs did not include calculations of the instantaneous value of Q' ; the only information output were the root-mean square (RMS) values of the velocity

components. Therefore, the fluctuating total velocity had to be presented as an RMS value also.

Taking the square of Eq. (6.4) and noting that $\bar{u}/\bar{Q} \cong 1$ and $\bar{v}/\bar{Q} \ll 1$,

$$\overline{(Q')^2} \approx \overline{(u')^2} \quad (6.5)$$

6.2 Separation of Mean and Turbulent Mach Numbers

As in the calculation of the mean and fluctuating velocities, computation of the Mach number was complicated by the turbulent characteristics of the flow. In general, the Mach number-temperature relation is given as

$$M = \frac{Q}{a} = \frac{Q}{\sqrt{\gamma R_u T}} \quad (6.6)$$

For turbulent flow, the equation was expanded to give

$$\bar{M} + M' = \frac{\bar{Q} + Q'}{\bar{a} + a'} = \frac{\bar{Q}}{\bar{a}} \frac{1 + Q'/\bar{Q}}{1 + a'/\bar{a}} \quad (6.7)$$

Assuming Q'/\bar{Q} and $a'/\bar{a} \ll 1$, the binomial expansion was used to show

$$\bar{M} + M' = \frac{\bar{Q}}{\bar{a}} \left(1 + \frac{Q'}{\bar{Q}}\right) \left(1 - \frac{a'}{\bar{a}}\right) = \frac{\bar{Q}}{\bar{a}} \left(1 + \frac{Q'}{\bar{Q}} - \frac{a'}{\bar{a}} - \frac{a'Q'}{\bar{a}\bar{Q}}\right) \quad (6.8)$$

Taking the Reynolds average of Eq. (6.8) and noting that $\overline{a'Q'}/\bar{a}\bar{Q} \ll 1$ led to

$$\bar{M} = \frac{\bar{Q}}{\bar{a}} \left(1 - \frac{\overline{a'Q'}}{\bar{a}\bar{Q}}\right) \cong \frac{\bar{Q}}{\bar{a}} = \frac{\bar{Q}}{\sqrt{\gamma R_u \bar{T}}} \quad (6.9)$$

Subtracting this result from Eq. (6.9) gave an expression for the turbulent Mach number:

$$M' = \frac{\bar{Q}}{\bar{a}} \left(\frac{Q'}{\bar{Q}} - \frac{a'}{\bar{a}}\right) \quad (6.10)$$

Therefore, in order to calculate the fluctuating Mach number, it became necessary to calculate a'/\bar{a} . Manipulation of the speed of sound relation led to

$$\bar{a} + a' = \sqrt{\gamma R_u (\bar{T} + T')} = \sqrt{\gamma R_u \bar{T}} \left[1 + \frac{T'}{\bar{T}} \right]^{1/2} = \bar{a} \left[1 + \frac{1}{2} \frac{T'}{\bar{T}} - \dots \right] \quad (6.11)$$

where the last simplification was made possible by assuming T'/\bar{T} was small and using the binomial expansion. Subtracting \bar{a} from both sides,

$$\frac{a'}{\bar{a}} = \frac{1}{2} \frac{T'}{\bar{T}} + O \left[\left(\frac{T'}{\bar{T}} \right)^2 \right] \quad (6.12)$$

Where the symbol O represents “terms of the order of magnitude [of the bracketed terms].”

Using the assumption of small fluctuating Mach number and the Strong Reynolds Analogy (SRA), Morkovin [28] derived an expression for the value of T'/\bar{T} :

$$\frac{T'}{\bar{T}} = -(\gamma - 1) \bar{M}^2 \left(\frac{Q'}{\bar{Q}} \right) \quad (6.13)$$

The SRA assumes that the ratio of the fluctuating total temperature to the total temperature, T'_0/\bar{T}_0 , is zero. This assumption was verified by Miller, who found this ratio to be less than 0.02 for the flat plate case. [26]

For Mach 2.8 flow over a flat plate, values of $Q'/\bar{Q} \leq 0.1$ could be expected. [16, 22, 26] In the FPG case, the stabilizing effect of the FPG was expected to further reduce the fluctuations. Therefore, Eq. (6.13) could be used to provide an estimate for the largest values of T'/\bar{T} :

$$\left| \frac{T'}{\bar{T}} \right| \leq (1.4 - 1)(2.8)^2 (0.1) = 0.31 \quad (6.14)$$

Inserting Eq. (6.12) into Eq. (6.10) and retaining only first-order terms, the expression for the fluctuating Mach number became

$$M' = \bar{M} \frac{Q'}{\bar{Q}} \left[1 + \frac{1}{2} (\gamma - 1) \bar{M}^2 \right] \quad (6.15)$$

Thus, the RMS value of the fluctuating Mach number was

$$\overline{(M')^2} = \bar{M} \frac{\overline{(Q')^2}}{\bar{Q}} \left[1 + \frac{1}{2}(\gamma - 1)\bar{M}^2 \right] \quad (6.16)$$

6.3 Mach Number Calculation

The local Mach number was calculated using the measured velocity and total temperature in conjunction with the assumptions of adiabatic flow and a thermally and calorically perfect gas. The adiabatic energy equation was derived for turbulent flow by expanding the adiabatic relationship between temperature, stagnation temperature and Mach number:

$$\begin{aligned} \frac{T_0}{T} &= 1 + \frac{\gamma - 1}{2} M^2 \Rightarrow & (6.17) \\ \bar{T} + T' &= \frac{\bar{T}_0 + T'_0}{1 + \frac{\gamma - 1}{2} (\bar{M} + M')^2} \Rightarrow \\ \bar{T} \left[1 + \frac{T'}{\bar{T}} \right] &= \frac{\bar{T}_0}{1 + \frac{\gamma - 1}{2} (\bar{M} + M')^2} \end{aligned}$$

Where T'_0 was neglected based on the SRA. Again using the binomial expansion and retaining only the first-order terms, Eq. (6.17) could be written as

$$\frac{\bar{T}_0}{\bar{T}} \left[1 - \left(\frac{T'}{\bar{T}} \right) + \dots \right] = 1 + \frac{\gamma - 1}{2} \left[\bar{M}^2 + 2\bar{M}M' + (M')^2 \right] \quad (6.18)$$

Taking the time average of both sides, the turbulent adiabatic energy equation was found to be

$$\frac{\bar{T}_0}{\bar{T}} = 1 + \frac{\gamma - 1}{2} \bar{M}^2 + \frac{\gamma - 1}{2} \overline{(M')^2} \approx 1 + \frac{\gamma - 1}{2} \bar{M}^2 \quad (6.19)$$

The above equation was inserted into Eq. (6.9); the resulting equation was manipulated to yield

$$\bar{M} = \left[\frac{2\bar{Q}^2}{2\gamma R_u \bar{T}_0 - \bar{Q}^2 (\gamma - 1)} \right]^{1/2} \quad (6.20)$$

It should be noted that the Mach number was calculated assuming constant total temperature (adiabatic flow) throughout the boundary layer. This assumption was verified for the flat plate case by measurements made by Kistler. [22] He reported values of

$$\frac{T_{0,\infty} - T_0}{T_{0,\infty} - T_{aw}} \leq 0.6 \quad (6.21)$$

where T_{aw} is the adiabatic wall temperature. The adiabatic wall temperature is calculated using the *adiabatic recovery factor*, $r \approx \sqrt[3]{Pr}$, and the relationship

$$r = \frac{T_{aw} - T_e}{T_{0,\infty} - T_e} \quad (6.22)$$

where T_e is the temperature at the edge of the boundary layer. Manipulating Eq. (6.21),

$$\frac{1 - (T_0/T_{0,\infty})}{1 - (T_{aw}/T_{0,\infty})} \leq 0.6 \quad (6.23)$$

while Eq. (6.22) becomes

$$\frac{T_{aw}}{T_{0,\infty}} = \frac{1 + r[(\gamma - 1)/2]M_e^2}{1 + [(\gamma - 1)/2]M_e^2} \quad (6.24)$$

For $Pr = 0.71$, $r = 0.892$; with $M_e = 2.9$, $T_{aw}/T_{0,\infty} = 0.932$ and

$$\frac{T_0}{T_{0,\infty}} \geq 0.96 \approx \text{const} \quad (6.25)$$

and the Mach number profile can be calculated. The result given in Eq. (6.25) also agrees with results presented by van Driest. [35] In addition, Miller et al. [27] found that $T_0/T_{0,\infty}$ was essentially constant across the flat plate boundary layer in the facilities used for the present experiment.

6.4 Density and Temperature Calculation

Calculation of the density and temperature profiles were complicated by the fact that the only measurements taken in the test section were the wall temperature and pressure. The density and temperature in the boundary layer were *estimated* based on certain assumptions; if the validity of these assumptions broke down, the reported values of the temperature and density (and thus the incompressible Reynolds shear) would be inaccurate. Thus, in order to minimize the error associated with the calculations, different assumptions and methods of calculation were used for the flat plate and FPG cases.

6.4.1 *Flat Plate.* In the flat plate region, the density was calculated assuming the pressure normal to the surface was constant; with this assumption, the modified Crocco-Busemann approximation yields [35, 6]

$$\frac{\rho_w}{\bar{\rho}} = \frac{\bar{T}}{T_w} = 1 + B' \left(\frac{\bar{u}}{u_e} \right) - (A')^2 \left(\frac{\bar{u}}{u_e} \right)^2 \quad (6.26)$$

where ρ_w and T_w are the density and temperature at the wall and A' and B' are given by

$$(A')^2 = \frac{[(\gamma - 1)/2] r M_e^2}{T_w/T_e} \quad (6.27)$$
$$B' = \frac{1 + [(\gamma - 1)/2] r M_e^2}{T_w/T_e} - 1$$

The density at the wall, ρ_w , was calculated using the measured wall temperature and pressure and the perfect gas relation:

$$\rho_w = \frac{P_w}{R_u T_w} \quad (6.28)$$

6.4.2 *FPG Region.* The assumption of constant pressure across the boundary layer was not necessarily valid in the FPG test section and needed to be evaluated. In the presence of a

curved body, the streamlines will experience curvature, causing a pressure gradient normal to the streamlines. The magnitude of this gradient was given by Spina et al as [33]

$$\frac{\partial p}{\partial n} \approx \frac{-\rho u^2}{R} = -\frac{\gamma M^2 p}{R} \quad (6.29)$$

and the pressure difference between the wall and the outer edge of the boundary layer could be estimated as

$$\Delta p \approx -\gamma M_e^2 p_e \left(\frac{\delta}{R} \right) \quad (6.30)$$

If the ratio δ/R was made small enough (usually by a large radius of curvature and therefore a small streamwise pressure gradient, approaching the flat plate case) the pressure difference could be made negligible. For the present test configuration, the radius of curvature at the test location was 48.08 cm and $\delta \approx 1.28$ cm; with $M_e = 2.9$,

$$\frac{\Delta p}{p_e} \approx -\gamma M_e^2 \left(\frac{\delta}{R} \right) = -0.31 \quad (6.31)$$

Equation (6.31) shows that the assumption of constant pressure across the boundary layer was not valid in the FPG test section. In order to avoid large errors in density calculations caused by making this assumption, an alternate method for calculating the temperature and density was used.

The alternate method assumed that the pressure distribution between the wall and the freestream was linear. A numerical investigation of the flowfield in the current experimental configuration (*cf.* Ref. [17]) found that the pressure variation across the boundary layer was nearly linear, justifying this assumption. In order to perform the linear interpolation, the wall and edge pressures were required. The wall pressure had been measured; the edge pressure was calculated using the assumption that there were no shocks present in the freestream, leading to a constant total pressure along the edge of the boundary layer and

$$p_e = p_0 \left[1 + \frac{\gamma - 1}{2} M_e^2 \right]^{-\frac{\gamma}{\gamma - 1}} \quad (6.32)$$

The pressure at any point in the boundary layer could then be estimated using linear interpolation. The temperature across the boundary layer was found assuming constant total temperature and using Eq. (6.19); with the temperature and pressure known, the density was calculated using the perfect gas relation.

It is important to mention here that this analysis was not expected to provide an exact measure of the density, temperature and pressure across the boundary layer. The sole purpose was to obtain an estimation of the density across the boundary layer in order to present the direct measurements of $\overline{u'v'}$ in a manner which allowed comparison to data in the literature; the form most commonly used was $-\overline{\rho u'v'}/\tau_w$, necessitating the estimation of the density.

6.5 Boundary Layer, Displacement and Momentum Thickness Calculations

Two boundary layer thicknesses were calculated: one thickness based on the velocity (δ_u) and one on the Mach number (δ_M). It was necessary to calculate both thicknesses for two reasons. First, in order to accurately compare the present results with the Mach number measurements of Miller et al. [27] which were based on conventional Pitot and cone-static pressure profiles, δ_M needed to be calculated. The second reason for calculating both thicknesses was that the Mach-number boundary layer thickness gave an estimation of the temperature boundary layer thickness, the thickness which was measured from the flow visualization results.

The boundary layer thicknesses were calculated by choosing the largest velocity or Mach number from a given traverse as the edge value, non-dimensionalizing the profile by the edge value, and searching outward from the wall until a value of u/u_e or $M/M_e \geq 0.995$ was attained. The

value of δ was then calculated by linear interpolation between the data points just above and below the boundary layer edge.

Integral analysis of the boundary layer equations leads to the definition of the displacement and momentum thickness. [4] The displacement and momentum thicknesses are given by

$$\begin{aligned}\delta^* &\equiv \int_0^{\infty} \left(1 - \frac{\bar{\rho}\bar{u}}{\rho_e u_e}\right) dy \\ \Theta &\equiv \int_0^{\infty} \frac{\bar{\rho}\bar{u}}{\rho_e u_e} \left(1 - \frac{\bar{u}}{u_e}\right) dy\end{aligned}\tag{6.33}$$

respectively. The integration was carried out numerically using the measured data and a trapezoidal integration scheme. In order to filter out the uncertainty associated with the density calculations, “incompressible” (or kinematic) displacement and momentum thicknesses were also calculated:

$$\begin{aligned}\delta_i^* &\equiv \int_0^{\infty} \left(1 - \frac{\bar{u}}{u_e}\right) dy \\ \Theta_i &\equiv \int_0^{\infty} \frac{\bar{u}}{u_e} \left(1 - \frac{\bar{u}}{u_e}\right) dy\end{aligned}\tag{6.34}$$

Note that the kinematic thicknesses were based solely on measured data, reducing the possibility of error incurred from inaccurate assumptions. Also note the asymptotic nature of the integrals reduced the error associated with random fluctuations which may have affected the choice of δ_u and δ_M ; as a result, these parameters were less subject to random errors.

6.6 Turbulence Statistics

Calculation of statistical variables associated with the turbulent flow was important for two reasons. The first was that some of the statistical variables appeared directly in the time-averaged forms of the Navier-Stokes equations. The second was that measurement of the turbulent statistics helped to describe various features of the turbulent flowfield.

As expected, the main component around which all the turbulent statistics were developed is the fluctuation from the mean, $x' = x - \bar{x}$. The variable x was used here to denote the fact that the statistical calculations were performed for both the u and v components of velocity. Since x' was centered about the mean, its average value was zero by definition. Thus, in order to get an estimate of the average size of the fluctuation from the mean, the RMS value of x' was employed. The RMS value (also known as the standard deviation) of x' is defined as

$$x_{RMS} = \sigma_x \equiv \sqrt{\sum (x')^2 / (n - 1)} \quad (6.35)$$

where the summation is carried out over the n samples collected. It should be noted that, to be statistically correct, the denominator of the summation should be $n - 1$ as shown above. However, the Burstware[®] software performed these calculations based on a denominator of n . Because of the large number of samples collected ($n \geq 2000$ for all data points), the difference between the two was negligible ($err \leq 0.05\%$). The skewness (Sk_x) and flatness (Fl_x) were also calculated by the Burstware[®] as

$$Sk_x \equiv \frac{\sum (x')^3}{\sigma_x^3 n}, \quad Fl_x \equiv \frac{\sum (x')^4}{\sigma_x^4 n} \quad (6.36)$$

Once again, these were not the statistically unbiased definitions, but the large number of samples collected negated the error caused by the above formulations.

The skewness function is important to LDV measurements in helping to determine whether or not the results were biased by seeding problems. The flatness can be used to calculate the intermittency function, γ_u . The intermittency function is the ratio between the flatness of the Gaussian curve (3.0) and the flatness of the measurements (i.e., $\gamma_u \equiv 3.0/Fl_u$) and provides a measure of the fraction of time that the flow is turbulent at a given location.

The distribution of the intermittency function was compared with the Gaussian integral curve given by

$$\gamma_u = 0.5(1 - \text{erf}\chi) \quad (6.37)$$

where

$$\chi = \left(\sqrt{2} \frac{\zeta}{\delta_u} \right)^{-1} \left[\frac{y}{\delta_u} - \varphi \right] \quad (6.38)$$

and

$$\text{erf}\chi = \frac{2}{\sqrt{\pi}} \int_0^\chi e^{-t^2} dt \quad (6.39)$$

The constants ζ and φ were adjusted until the Gaussian curve matched the measured distribution; “such a curve shows that the instantaneous position of the edge of the boundary layer has a random character with a mean position at $y/\delta_u = [\varphi]$.” [Klebanoff] The constant ζ represented the standard deviation of the boundary layer edge from φ .

The next statistical variable to be calculated was arguably the most important. The velocity correlation $\overline{u'v'}$ appeared directly in the RANS and, along with the density, comprised the incompressible Reynolds shear stress. The correlation was calculated using the formula

$$\overline{u'v'} = \sum (u'v')/n \quad (6.40)$$

Note that, while the average values of u' and v' were zero, the average of the product $u'v'$ may not be zero.

The final statistical value calculated was the velocity correlation coefficient, R_{uv} , given by

$$R_{uv} = \frac{\overline{u'v'}}{\sigma_u \sigma_v} \quad (6.41)$$

R_{uv} was used to provide insight into the nature of the turbulence. For instance, if the turbulence was isotropic (no preferred direction of turbulent structures), R_{uv} should have had a

magnitude of 1.0. [6] The Cauchy-Schwartz inequality indicated that $|R_{uv}| \leq 1.0$. [3] Finally, low-speed flat plate data indicated that $|R_{uv}| \cong 0.4 - 0.5$. [6]

6.7 Wall Shear Stress

The wall shear stress was calculated using the bisection method to iteratively solve the skin-friction relationship developed by van Driest [35]:

$$\frac{0.242}{A' \sqrt{C_f (T_w/T_e)}} \left[\sin^{-1} \left(\frac{2(A')^2 - B'}{\sqrt{4(A')^2 + (B')^2}} \right) + \sin^{-1} \left(\frac{B'}{\sqrt{4(A')^2 + (B')^2}} \right) \right] \quad (6.42)$$

$$= \kappa + \log(\text{Re}_x C_f) - \omega \log(T_w/T_e)$$

where $\kappa = 0.41$ and $\omega = 0.68$. It should be noted that this relation is for turbulent flow over a flat plate; its usefulness in computing the wall shear in the FPG test section will be determined later. It is also important to point out that Re_x represents the Reynolds number based on the distance from the leading edge of a flat plate immersed in a uniform flowfield. In order to estimate a value for Re_x , the wind tunnel was modeled as a flat plate in uniform flow where the throat of the wind tunnel was taken as the leading edge of the flat plate. The inaccuracy of this assumption and its effect on the reported data will also be discussed later.

6.8 Van Driest Velocity Profile

In order to compare the velocity profiles in compressible flows, van Driest [35] proposed transformation of the velocity profile into an effective velocity given by

$$u_{eff} = \int_0^{\bar{u}} \sqrt{\frac{\bar{\rho}}{\rho_w}} d\bar{u} \quad (6.43)$$

The values of $\bar{\rho}/\rho_w$ were calculated using the Crocco-Busemann relation given in Eq. (6.26); using this relation in Eq. (6.43) allows the effective velocity to be calculated analytically. Performing the integration leads to

$$u_{eff} = \frac{u_e}{A'} \left[\sin^{-1} \left(\frac{2(A')^2(\bar{u}/u_e) - B'}{\sqrt{4(A')^2 + (B')^2}} \right) + \sin^{-1} \left(\frac{B'}{\sqrt{4(A')^2 + (B')^2}} \right) \right] \quad (6.44)$$

Van Driest also suggested non-dimensionalizing the effective velocity by the wall-friction velocity, u^* , where

$$u^* \equiv \sqrt{\frac{\tau_w}{\rho_w}} \quad (6.45)$$

The non-dimensional velocity u_{eff}/u^* was plotted versus a scaled y -coordinate,

$$y^+ \equiv \frac{y u^* \rho_w}{\mu_w} \quad (6.46)$$

where μ_w is the fluid viscosity measured at wall temperature. This analysis allowed the empirical relationship between y^+ and u/u^* which has been developed for low-speed, incompressible flat plate flow, to be extended to high-speed, compressible flat plate flow. [36] Thus,

$$\frac{u_{eff}}{u^*} = \frac{1}{\kappa} \ln y^+ + C + \frac{2\Pi}{\kappa} \sin^2 \left(\frac{\pi y}{2\delta} \right) \quad (6.47)$$

where $\kappa = 0.41$ and $C = 5.0$. Π is the Coles wake parameter, given by White [36] as

$$\Pi \approx 0.8[\beta + 0.5]^{3/4} \quad (6.48)$$

The variable β in Eq. (6.48) is Clauser's equilibrium parameter, defined as

$$\beta \equiv \frac{\delta^*}{\tau_w} \frac{dp_e}{dx} \quad (6.49)$$

It should be noted that Eq. (6.47) is valid in the "logarithmic" region ($80 \leq y^+ \leq 500$) as well as the outer portion of the boundary layer. However, for flow very near the wall ($y^+ \leq 10$) the flow

is moving slow enough that it is laminar. This region is referred to as the *laminar sublayer*; in the laminar sublayer, the velocity correlation is given as $u/u^* = y^+$. [6] For the current experiment, the laminar sublayer was only (approximately) 5 μm thick; due to the wall-proximity limitations on the LDV system, data collection was not possible in the laminar sublayer.

6.9 Turbulent Kinetic Energy

The turbulent kinetic energy (TKE) provides a measure of the energy contained in the turbulent motion of the flow. The TKE is defined as

$$TKE \equiv \frac{(u')^2 + (v')^2 + (w')^2}{2} \quad (6.50)$$

For a two-dimensional flow, even though $\bar{w} = 0$, the fluctuation in the lateral direction, w' , will not necessarily be zero. The current experimental setup did not permit measurements of w' ; in order to calculate the TKE, an assumption was made to estimate its size. It was assumed that the fluctuation w' is of the same order as v' , and the estimated TKE was calculated as

$$TKE \equiv \frac{(u')^2 + (v')^2 + (v')^2}{2} \approx \frac{(u')^2}{2} + (v')^2 \quad (6.51)$$

6.10 Strain Rate Calculation

As mentioned in Chapter 5, data were collected at the points in a finite-difference grid. Using the notation shown in Figure 6.1, the central-derivatives in the y - and z -directions at the point (i, j) were estimated as [1]

$$\begin{aligned} \left. \frac{d\bar{u}}{dy} \right|_{i,j,k} &= \frac{\bar{u}_{i,j+1,k} - \bar{u}_{i,j-1,k}}{y_{i,j+1,k} - y_{i,j-1,k}} \\ \left. \frac{d\bar{u}}{dz} \right|_{i,j,k} &= \frac{\bar{u}_{i,j,k+1} - \bar{u}_{i,j,k-1}}{z_{i,j,k+1} - z_{i,j,k-1}} \end{aligned} \quad (6.52)$$

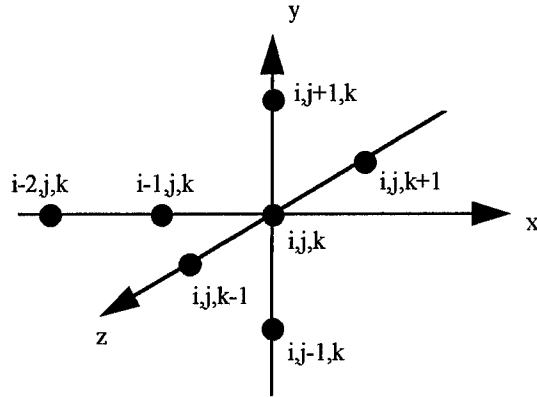


Figure 6.1: Finite-Difference Grid Notation

The backward-difference approximation was complicated by the fact that the data were not taken at evenly-spaced locations. Using a Taylor's series, the velocity at locations $x_{i=-1}$, $x_{i=-2}$ was given as

$$\begin{aligned}\bar{u}(x_{-1}) &= \bar{u}(x_0) + \left. \frac{d\bar{u}}{dx} \right|_{x_0} (x_{-1} - x_0) + \left. \frac{d^2\bar{u}}{dx^2} \right|_{x_0} \frac{(x_{-1} - x_0)^2}{2} + \dots \\ \bar{u}(x_{-2}) &= \bar{u}(x_0) + \left. \frac{d\bar{u}}{dx} \right|_{x_0} (x_{-2} - x_0) + \left. \frac{d^2\bar{u}}{dx^2} \right|_{x_0} \frac{(x_{-2} - x_0)^2}{2} + \dots\end{aligned}\quad (6.53)$$

where the subscripts were understood to represent the value of i . Multiplying the top equation by $-(x_{-2} - x_0)^2$, the lower equation by $(x_{-1} - x_0)^2$, adding, and solving for the derivative at x_0 ,

$$\left. \frac{d\bar{u}}{dx} \right|_{x_0} \cong \frac{dx_1^2 \bar{u}(x_{-2}) - dx_2^2 \bar{u}(x_{-1}) + [dx_2^2 - dx_1^2] \bar{u}(x_0)}{[dx_2 dx_1^2 - dx_1 dx_2^2]}\quad (6.54)$$

where $dx_1 \equiv x_{-1} - x_0$ and $dx_2 \equiv x_{-2} - x_0$.

6.11 Streamwise Pressure Gradient

The streamwise pressure gradient, dp_e/dx , was needed in the calculation of Clauser's equilibrium parameter given in Eq. (6.49). The pressure gradient was calculated assuming the streamwise rate of change of pressure was constant across the boundary layer, i.e.,

$$\frac{dp_e}{dx} \approx \frac{dp_w}{dx} \quad (6.55)$$

With this assumption, the measured values of wall pressure were inserted into Eq. (6.54) in place of \bar{u} , resulting in a value for dp_e/dx .

7. Results and Discussion

Recall that the underlying goal of the present study was to use advanced laser Doppler velocimeter techniques to investigate the turbulent structures in a supersonic boundary layer and the effect of a pressure gradient on those structures. In order to present and analyze the measured LDV data in a concise and methodical manner, it is first necessary to discuss some of the supporting data, such as measurements of the wind tunnel operating conditions and the flow visualization results. Sections 7.1 and 7.2 discuss these supporting measurements; the remaining sections of this chapter present and analyze the flat plate and FPG region results. Since the present LDV system had never been operated in the facilities used for this experiment, several tests were performed to determine the susceptibility of the measurements to such variables as the record length, seeding density, and coincidence window. The results from these tests are presented in Appendix A. A detailed error analysis for all the measured and computed variables is presented in Appendix B. Finally, to be useful as a basis for the development of turbulence models, the criteria of Settles and Dodson [31] (see Chapter 1) needed to be met. Any elements of the criteria which had not been previously addressed (data repeatability, flow two-dimensionality, and tabulated data) are presented in Appendix C.

7.1 Pressure and Temperature Measurements

Measurements of the stagnation pressure showed that the wind tunnel was operated at a stagnation pressure of $2.13 \times 10^5 \pm 1.38 \times 10^3$ Pa. The average stagnation temperature was approximately 298 K with a ± 0.1 K variation during each run. The mean value was found to increase slightly as testing progressed due to constant operation of the compressors. The mean temperature never rose above 303 K. Because of this variation in temperature, the stagnation temperature and pressure were recorded for each data point and the data was reduced accordingly.

The results from the wall pressure measurements in the FPG region are summarized in Table 7.1. Note from Eq. (4.2) that the location $x = 63.22$ cm was still in the flat plate region, upstream of the wall curvature. The pressure change from this station to the location $x = 71.52$ cm was negligible in the flat plate case, allowing the pressure measurement at $x = 63.22$ cm to be used for the flat plate wall pressure as well. Using the data from Table 7.1 and Eq. (6.54), the streamwise derivative of the wall pressure, dp_w/dx , was estimated. Assuming the rate of change of the edge pressure was equal to the rate of change of wall pressure (this assumption was qualitatively verified by comparison to CFD results presented in Ref. [17] and shown in Figure 7.1), the pressure gradient in the FPG region was

$$\frac{dp_e}{dx} \approx \frac{dp_w}{dx} = -2 \times 10^4 \frac{\text{Pa}}{\text{m}} \quad (7.1)$$

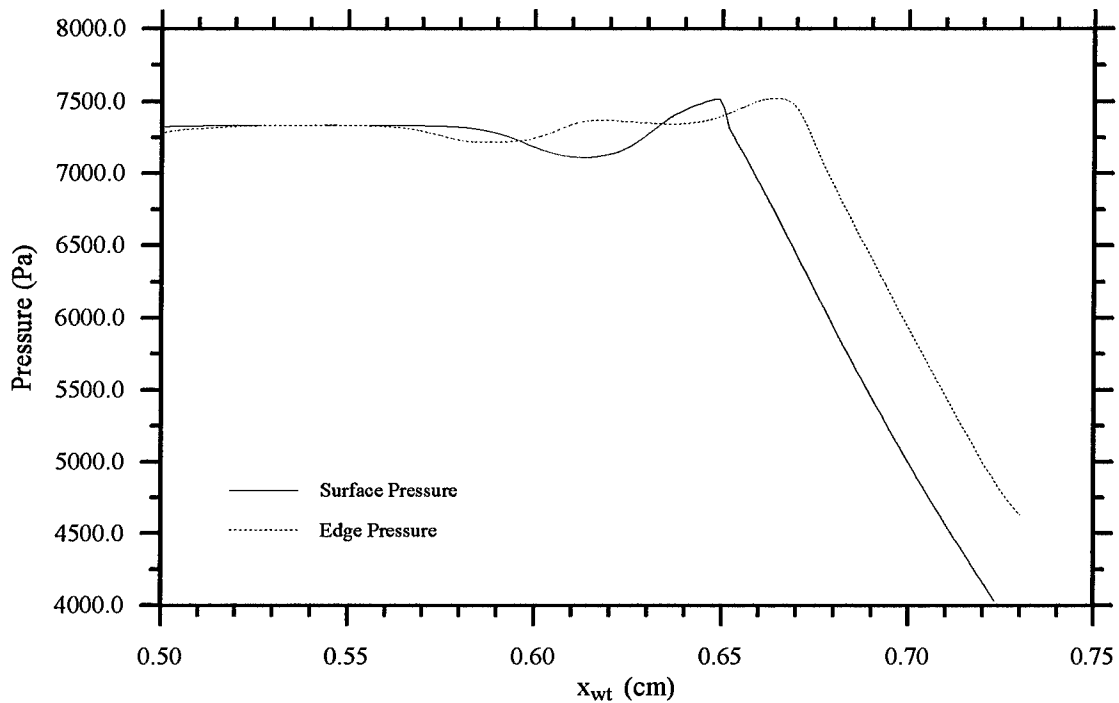


Figure 7.1: Pressure Distribution Along Wall and Boundary Layer Edge [17]

Table 7.1: Wall Pressure Measurements In the FPG Test Section

x (cm)	63.22	68.92	71.52
P_w (Pa)	8690	6000	5310

Wall temperature measurements were restricted to the flat plate and produced a result of $T_w = 295$ K. For Mach 2.8 flow over a flat plate, the ratio of adiabatic wall temperature to total temperature was given in Chapter 6 as $T_{aw}/T_{0,\infty} = 0.93$. With $T_{0,\infty} \approx 298$ K, $T_{aw} \approx 278$ K (a 6% difference from the measured value of T_w). Therefore, if necessary, the assumption of an adiabatic wall may be justified.

7.2 Flow Visualization

The FPG shadowgraph and schlieren results are presented in Figures 7.2 to 7.4. Figure 7.2 shows the shadowgraph, Figure 7.3 displays the schlieren which emphasizes the $\partial/\partial y$ gradient of density, and Figure 7.4 presents the schlieren which captures the $\partial/\partial x$ gradient of density. In all cases, the airflow was moving from left to right. Examination of Figures 7.2 to 7.4 showed that the seam just upstream of the test section generated two weak shocks which propagated downstream. Since these waves were very weak, their effects on the flow were deemed negligible. The strong shock near the wall on the right side of the photographs was due to the fact that the wall curvature terminated at $x_{ts} = 12.7$ cm.

Although the smallest eddies appeared smeared, as expected (see Section 5.5), Figure 7.3 was still able to capture the $\partial\bar{\rho}/\partial y$ gradients in the flowfield, clearly showing the edge of the boundary layer. Since the schlieren provided density gradient information, the boundary layer evident in the schlieren (and shadowgraph) photographs was δ_T , the thermal boundary layer thickness. The boundary layer thickness estimated from the photographs was $\delta_T \approx 12.0$ mm.

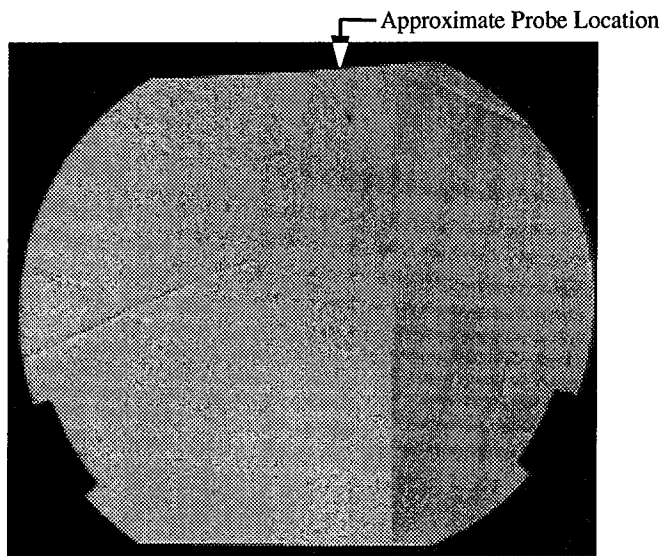


Figure 7.2: Shadowgraph of FPG Region

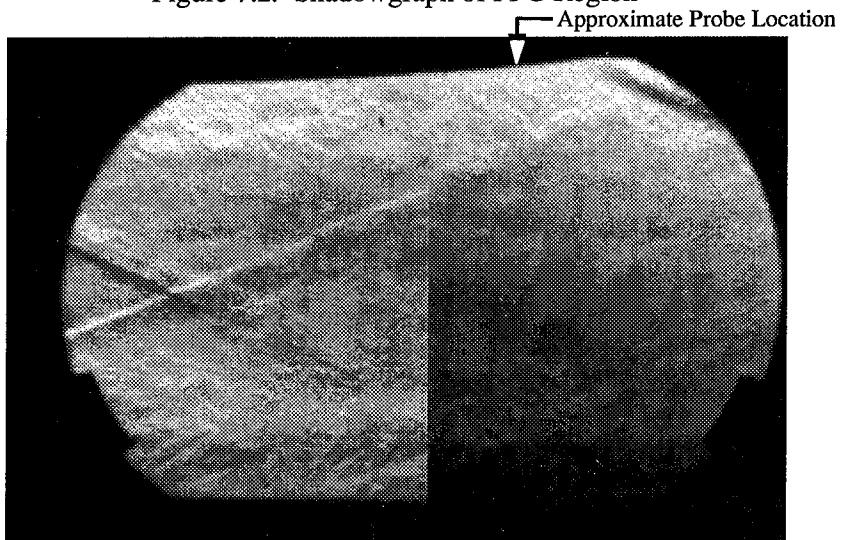


Figure 7.3: Schlieren (Horizontal Knife Edge) in FPG Region

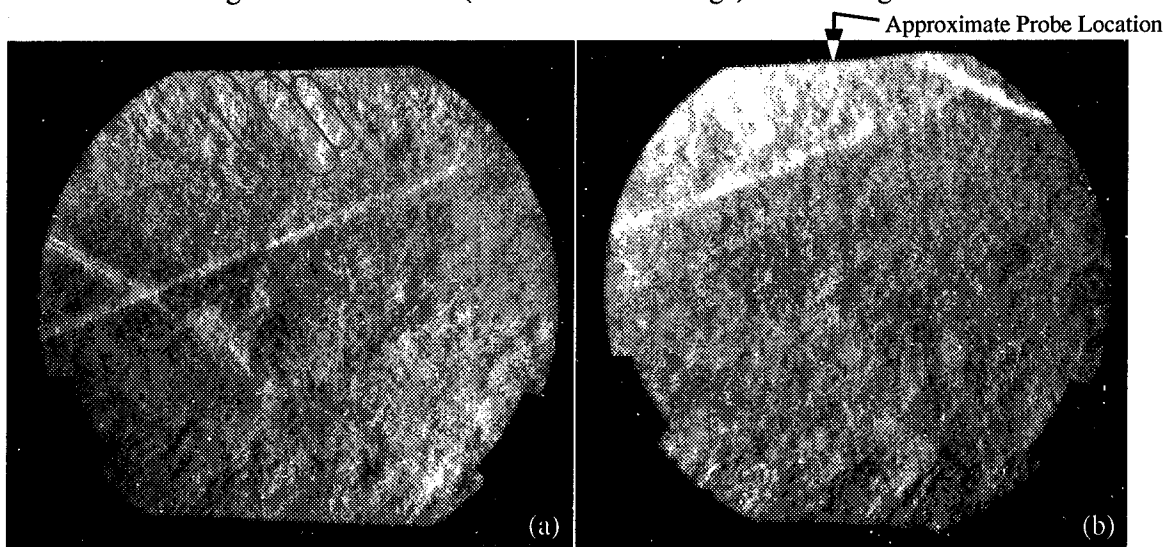


Figure 7.4: Schlieren (Vertical Knife Edge) in FPG Region

Due to the slight unsteadiness in the 10 ns light source, the background shading varied from photograph to photograph. Therefore, the schlierens in Figure 7.4 were presented separately in order to refrain from inadvertently introducing artificial gradients into a composite photograph. The changes in the shading in Figure 7.4a showed that, as the flow sped up through the expansion area, the density changed. Examination of the adiabatic relationships given in Eqs. (6.19) and (6.32) showed that, as the Mach number increased, the density decreased. Therefore, the darkest sections of the photograph corresponded to the highest density regions in that photograph. With this knowledge, Figure 7.4b showed that the density began to increase once again after the flow reached the end of the curved wall. Detailed inspection of Figure 7.4a also revealed the presence of organized structures within the boundary layer region. The angle these structures made with the test section wall appeared to be approximately 40-60°.

7.3 Flat Plate Results

Investigation of the flat plate (zero-pressure gradient, or ZPG) results was important for two reasons: first, the flat plate data were used as a basis for comparison against which the effects of the FPG were assessed. Second, the flat plate data allowed the present measurement techniques to be evaluated against accepted experimental data and correlations from the literature.

7.3.1 Mean Flow Characteristics. Mean flow characteristics which were compared to data in the literature included the velocity, Mach number, and density profiles. In addition, the boundary layer thicknesses ($\delta, \delta^*, \delta_i^*, \theta, \theta_i$) were compared to accepted empirical correlations in order to assess the accuracy of the measurements.

7.3.1.1 Velocity Profiles and Boundary Layer Thickness. In order to determine the boundary layer thickness, the mean velocity was scaled by the edge velocity ($u_e \approx 599$ m/s at x

= 71.5 cm) and plotted versus distance from the wall (see Figure 7.5). Scaling the velocity by the edge value was necessary because the wind tunnel conditions changed slightly between traverses across the boundary layer, leading to a slight fluctuation in the freestream velocity. The value of delta was taken as the distance from the wall at which $u/u_e = 0.995$. From Figure 7.5, the boundary layer thickness over the flat plate was found to be approximately 9.0 mm. The mean velocity profile over the flat plate was plotted versus y/δ in Figure 7.6 and compared to Pitot and cone-static pressure probe data presented in Ref. [26]. It should be noted that, in Figure 7.6 and all subsequent presentations of hot-wire and conventional probe (CP) results, the y/δ_M coordinate associated with hot-wire and conventional probe measurements has been multiplied by the ratio δ_M/δ_u calculated from the present LDV data in order to present an accurate comparison. For the flat plate case $\delta_M/\delta_u = 1.11$ while in the FPG region $\delta_M/\delta_u = 1.09$. As can be seen in Figure 7.6, the agreement of the present results to those in Ref. [26] was excellent.

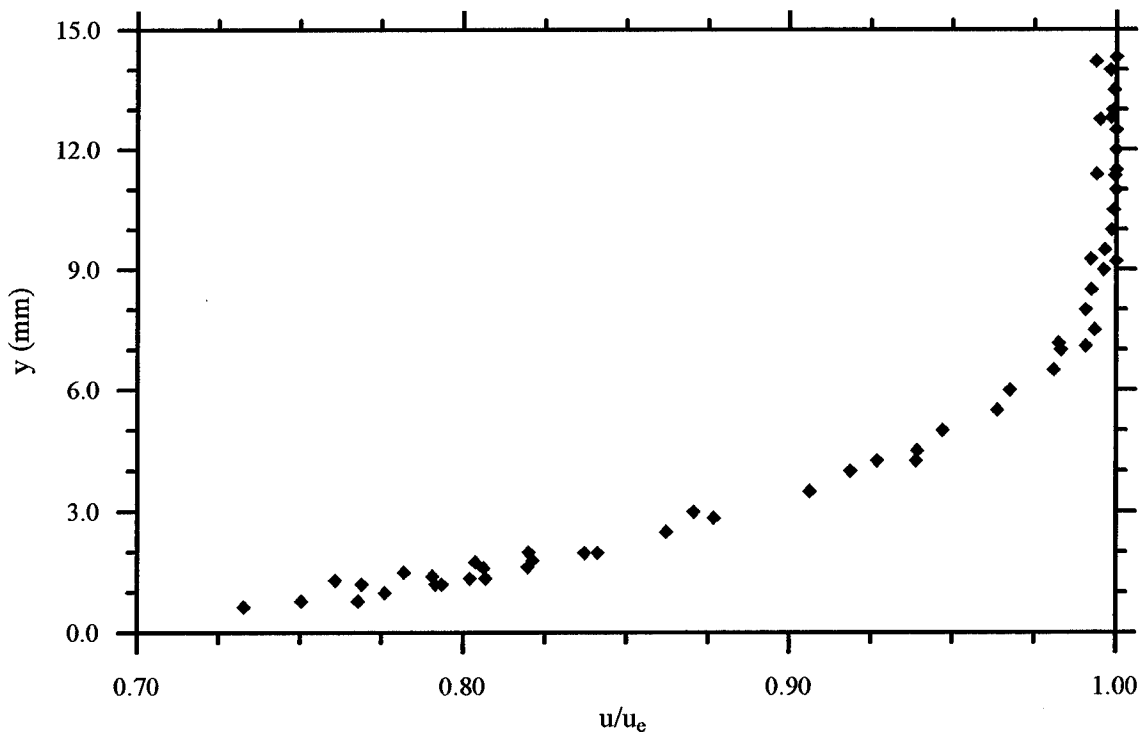


Figure 7.5: Flat Plate Velocity Profile versus Distance From the Wall

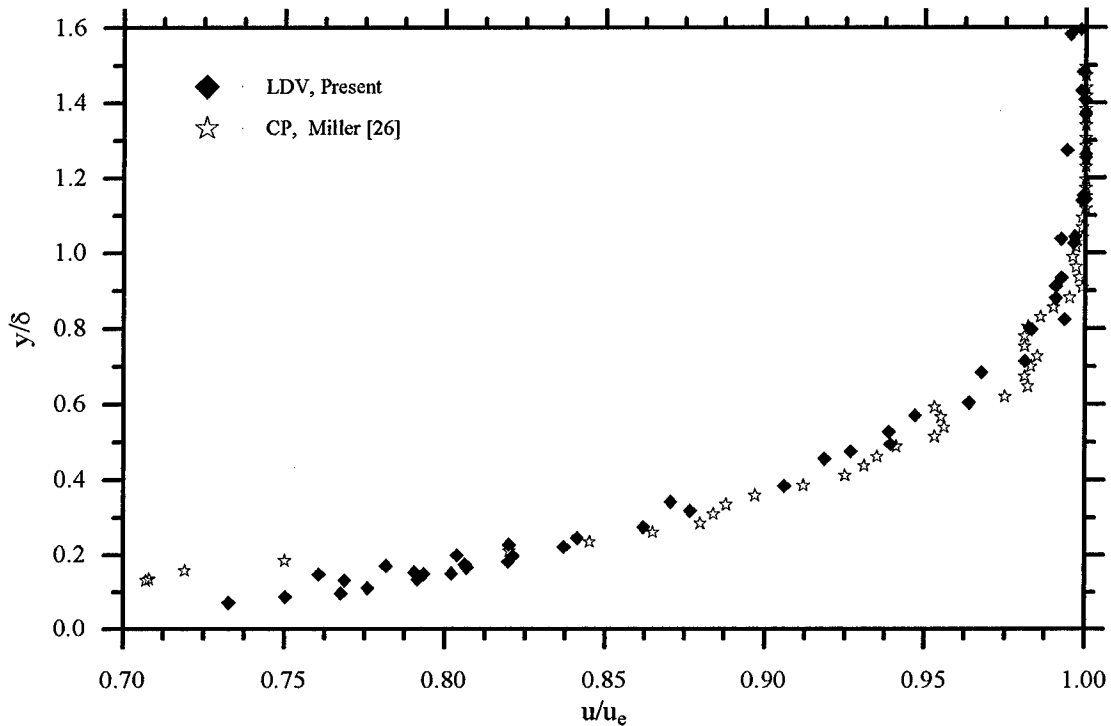


Figure 7.6: Flat Plate Mean Velocity Profile

7.3.1.2 *Mach Number.* The flat plate Mach number profile was calculated as discussed in Section 6.3 and is presented in Figure 7.7. The data presented in Ref. [26] was taken at the location $x = 44$ cm, where $M_e \approx 2.9$, as opposed to $M_e \approx 2.8$ measured downstream at $x = 71.5$ cm (the reduced freestream Mach number at $x = 71.5$ cm was due to the continued boundary-layer growth within the wind tunnel). Since the Mach number was dependent on the location in the wind tunnel, LDV data needed to be collected at $x = 44$ cm in order to compare the present LDV data to the conventional data. The $x = 44$ cm location was in the center of the first wind tunnel test section, hence in a position not covered by the optical windows (see Figure 4.4). In order to collect data at this location, the tunnel walls were replaced with optical-grade Plexiglas. The Plexiglas allowed the lasers to make measurements of the mean velocity, but the quality of the Plexiglas was not good enough to provide for accurate measurements of the higher-order velocity correlations. The results from the Mach number calculations at $x = 44$ cm showed excellent agreement with the

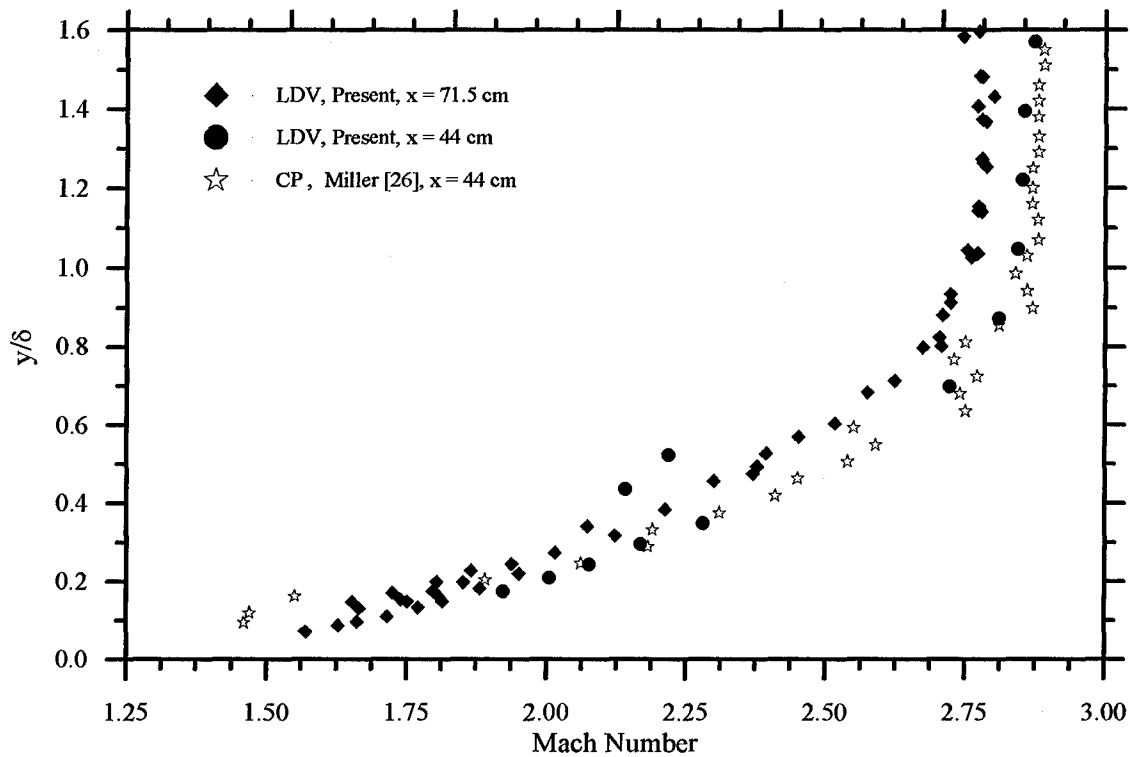


Figure 7.7: Flat Plate Mach Number Profile

conventional data, proving the assumptions used to extract the Mach number from the LDV data were valid.

7.3.1.3 Density. For flow over a flat plate, the density profile was calculated using the modified Crocco-Busemann relation; results from these calculations are presented in Figure 7.8. The assumptions used to extract the density from the LDV data were the most questionable and affected calculation of other variables such as the wall shear stress. Therefore, in order to validate the density calculations, the density profile was compared to results from the literature. Specifically, the computed density was compared to conventional probe measurements taken by Dotter [13] in the facilities used for the current experiment and CFD calculations given in Ref. [17]. The agreement was once again excellent; the discrepancy from the CFD results near the freestream is probably due to the freestream turbulence in the wind tunnel.

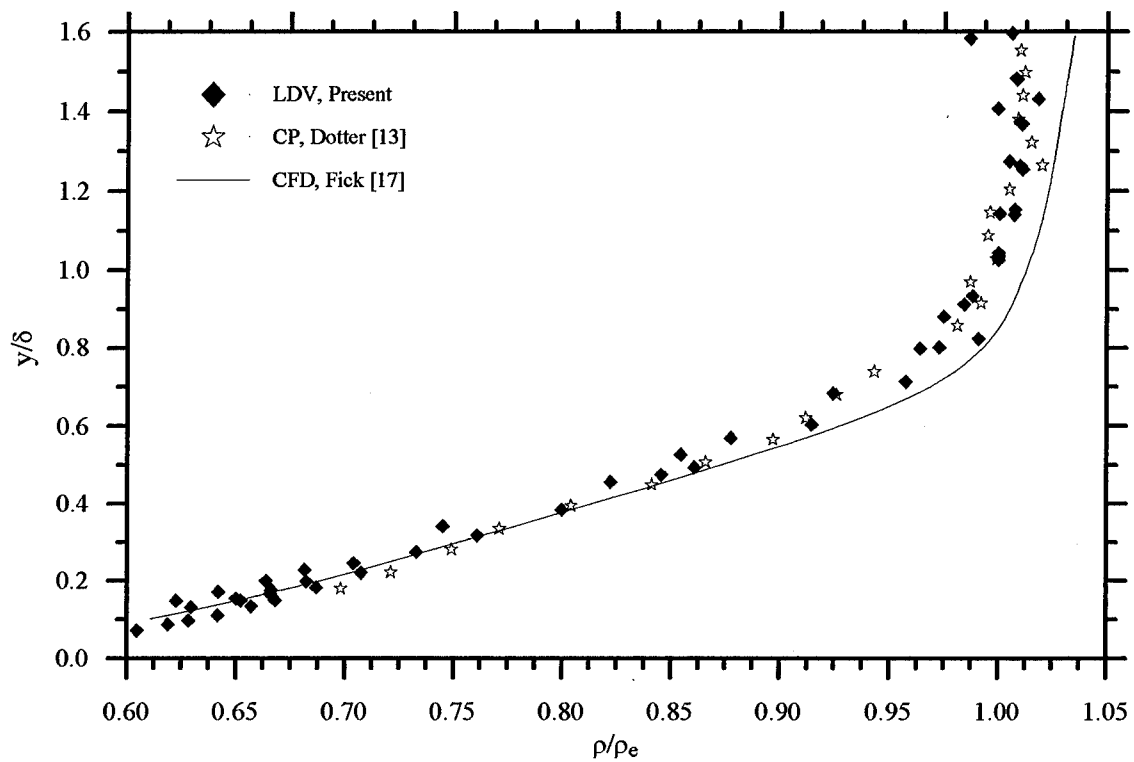


Figure 7.8: Flat Plate Non-Dimensional Density Profile

7.3.1.4 *Integral Momentum Thicknesses.* The momentum integral thicknesses were calculated at each traverse position across the boundary layer. The results from these calculations are presented in Table 7.2.

Table 7.2: Flat Plate Integral Thicknesses Calculated From LDV Measurements

x (cm)	δ^* (mm)	θ (mm)	δ_i^* (mm)	θ_i (mm)
71.5	1.31	1.27	0.50	0.61
67	1.50	1.09	0.46	0.59

To determine the accuracy of the measured integral thicknesses, the results from Table 7.2 were compared with data from the literature. The value of θ was validated by comparison with hot-wire results from Ref. [22] and LDV results from Ref. [16]; the hot-wire results presented in

Ref. [22] indicated that, for Mach 2.8 flat plate flow, $\theta \approx 1.5$ mm, while the LDV results from Ref. [16] measured $\theta = 0.84$ mm. Obviously, the exact value of θ depends on the experimental facility; the value measured in the current experiment falls between the values presented in the literature and was accepted as accurate.

7.3.2 Turbulence Intensities. Turbulence intensities were calculated for both the u and v components of velocity and are presented in Figures 7.9 and 7.10, respectively. In Figure 7.9, note the close agreement to the LDV data of Ref. [16]; the LDV data of Ref. [30] did not compare quite as well, but it was reasonable. In contrast, the hot-wire data of Refs. [26] and [22] followed each other fairly well, but showed a significant reduction in the value of the turbulence intensity near the wall when compared to the LDV data. In order to extract the turbulence intensities from the hot-wire data, the assumption of negligible static pressure fluctuations (i.e., $p' \cong 0$) was made.

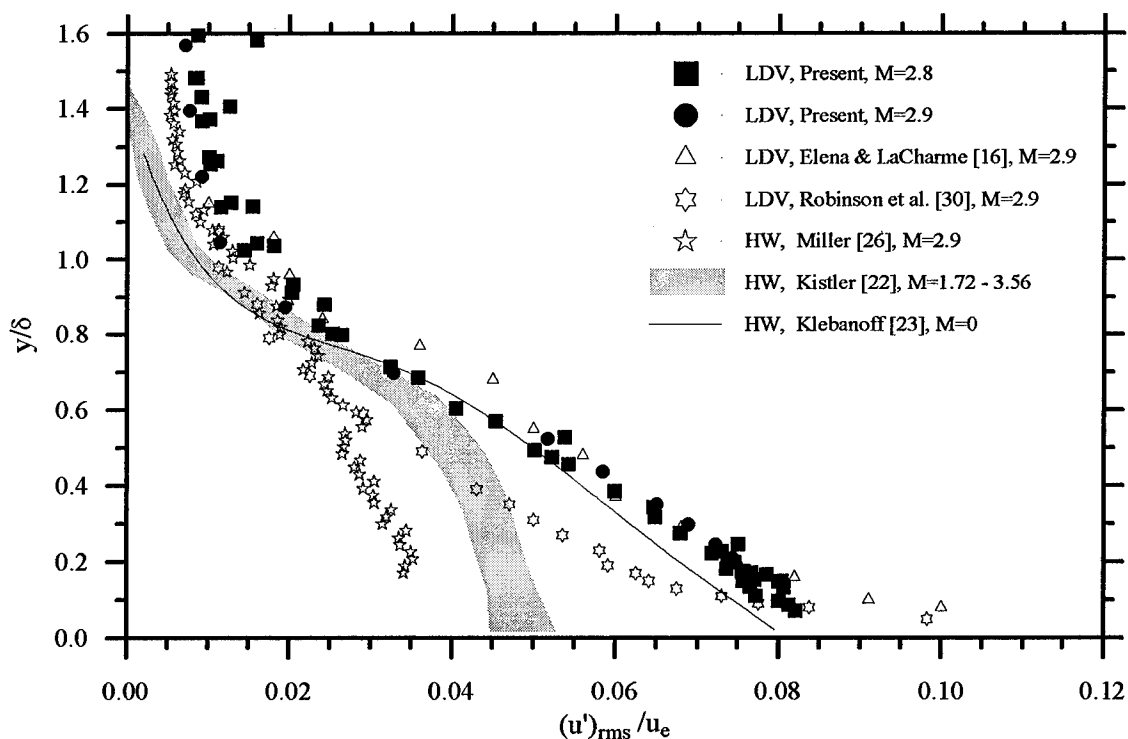


Figure 7.9: Flat Plate u -Turbulence Intensity Profile

The differences between the hot-wire and LDV data may signal possible errors in this assumption. Finally, the LDV data appeared to follow the hot-wire data of Ref. [23] closely. The data from Ref. [23] was hot-wire data taken in low-speed, incompressible flow, where the $p' \cong 0$ assumption was not necessary. These results tended to reinforce Morkovin's hypothesis that the turbulent structures (at least to first order) are relatively unaffected by compressibility. [28]

Figure 7.10 shows a plot of the v -turbulence intensity profile. Note the excellent agreement in all the data except for the data from Ref. [26]. In fact, the large perturbation of the Ref. [26] data from the other flat plate data prompted examination of the results from Ref. [26]. If both the turbulence intensities were plotted on the same axes, the v -component data from Ref. [26] fell nearly on top of the LDV u -component data and vice-versa (see Figure 7.11), prompting one to believe that the author of Ref. [26] may have inadvertently switched the data from the hot-wires.

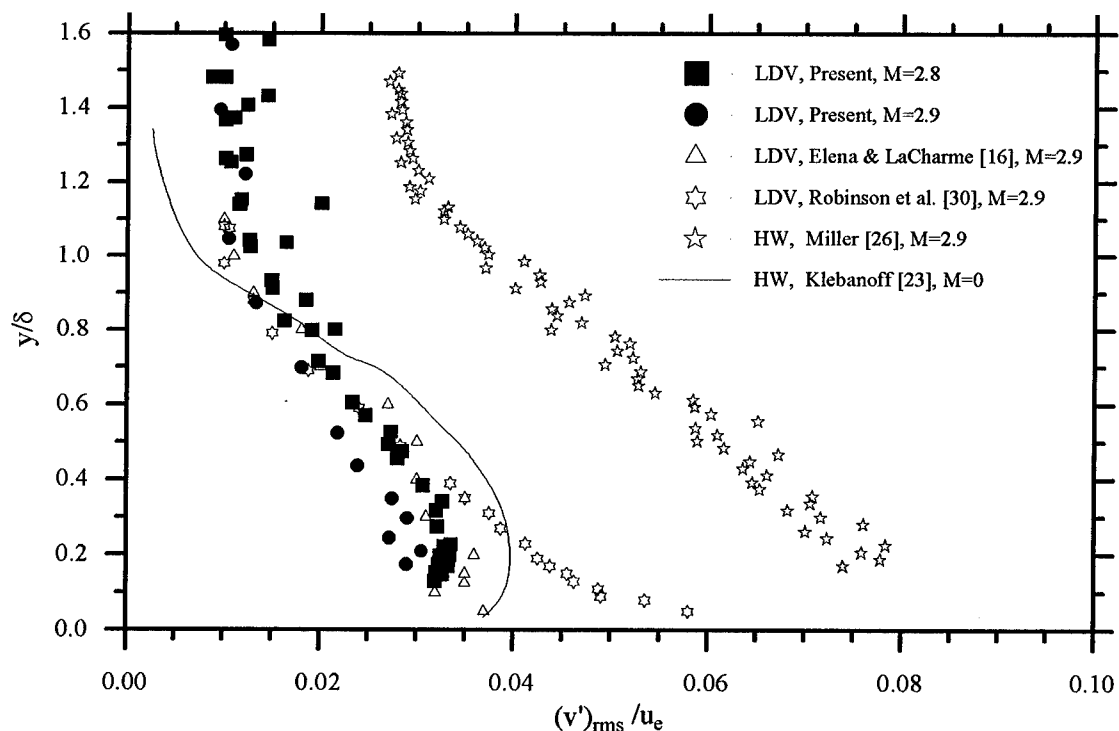


Figure 7.10: Flat Plate v -Turbulence Intensity Profile

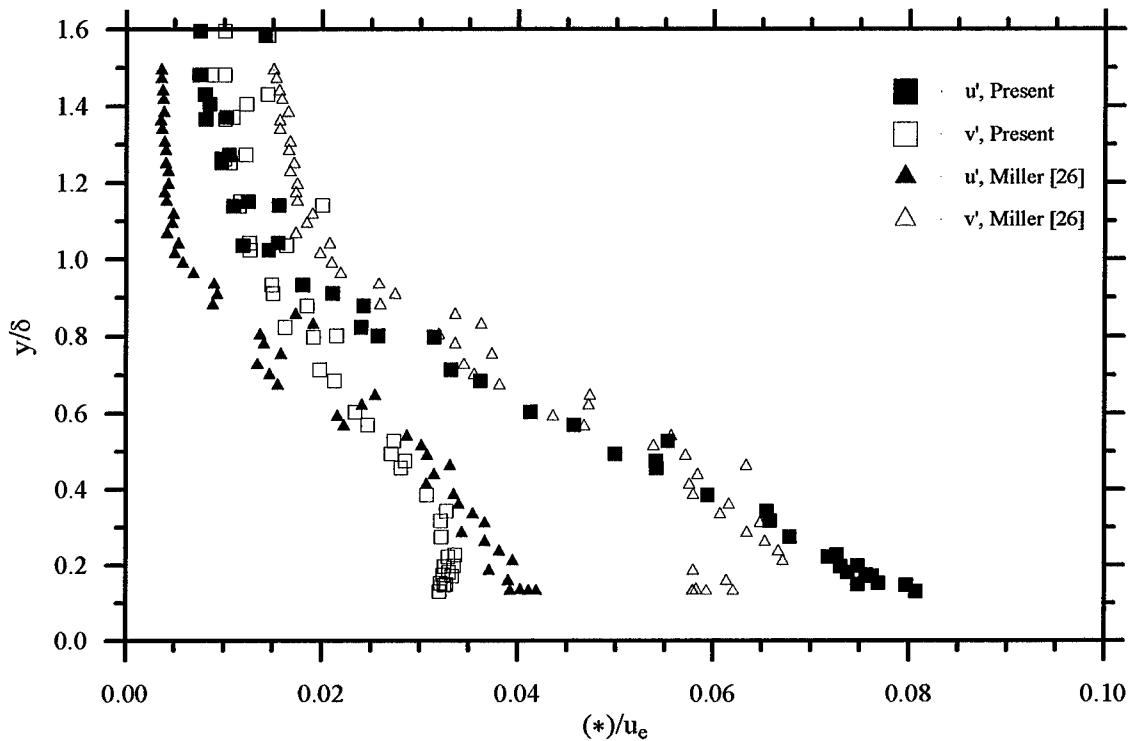


Figure 7.11: Turbulence Intensity Data from Reference [26] vs. Present LDV Measurements

In any event, with the exception of the data presented in Ref. [26], the present results agreed well with accepted data from the literature and were taken as valid.

7.3.3 Fluctuating Mach Number. The fluctuating Mach number profile is given in Figure 7.12. Note that, in all regions of the boundary layer, the fluctuating Mach number was much less than 1.0. This is important because if the fluctuating Mach number approaches unity, local “shocklets” can form in the flow. [33] In addition, Morkovin’s hypothesis can also be stated as “the dynamics of a compressible boundary layer will follow the incompressible pattern closely, as long as the fluctuating Mach number, M' , remains small.” [33] Since $M' \ll 1$ for the current flowfield, Morkovin’s hypothesis should hold for the flat plate case.

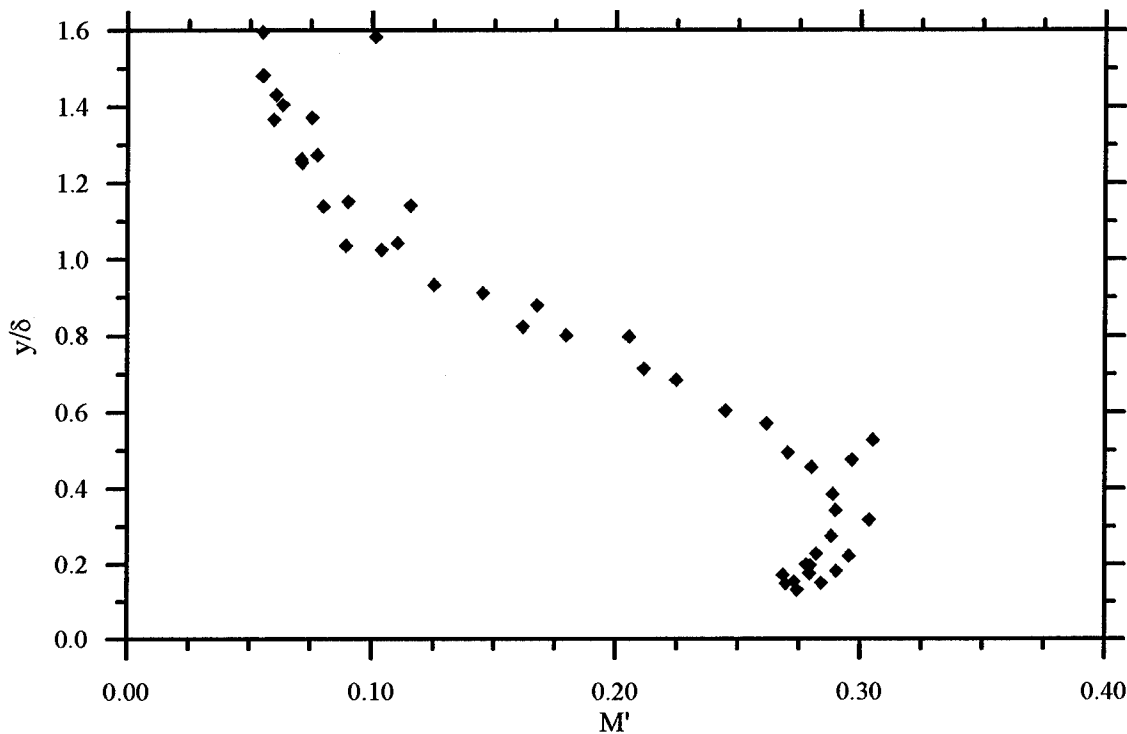


Figure 7.12: Fluctuating Mach Number over Flat Plate

7.3.4 *Wall Shear Stress.* Before continuing examination of the velocity measurements, it was necessary to calculate the wall shear stress in order to determine the scaling parameters used in the presentation of the incompressible Reynolds stress and in van Driest's velocity profiles. The wall shear stress was calculated using the relationship developed by van Driest given in Eq. (6.42) and was found to have an average value of 67.0 Pa. Recall that van Driest's correlation was developed for uniform flow over a flat plate and that its use required the tunnel to be modeled as a flat plate in Mach 2.8 flow whose leading edge was at the same location as the throat of the wind tunnel. In reality, the wind tunnel had a finite boundary layer thickness at the throat, and as the flow passed through the nozzle it was exposed to a substantial favorable pressure gradient. In addition, from $x = 27$ cm to the test location ($x = 71.52$ cm) the tunnel walls were flat, but due to boundary layer growth the freestream was under the influence of a slight adverse pressure gradient.

Therefore, the assumptions used in the derivation of van Driest's relation were not completely valid for the current experimental configuration.

7.3.5 "Incompressible" Reynolds Stresses. Recall that the incompressible Reynolds stress was defined as $-\overline{\rho u'v'}$. In order to present this term in a non-dimensional fashion, two methods of scaling were employed. The first method was the most common, non-dimensionalizing by the wall shear stress. Figure 7.13 presents the LDV data in this manner compared to the data from the literature. Note that the incompressible Reynolds shear stresses measured in this study did not exhibit a tendency to roll off near the wall. The roll-off experienced by other researchers has been attributed, at least in part, to angular biasing. [15] Aligning the lasers so the fringe pattern ran perpendicular to the mean direction of flow seemed to have eliminated this bias.

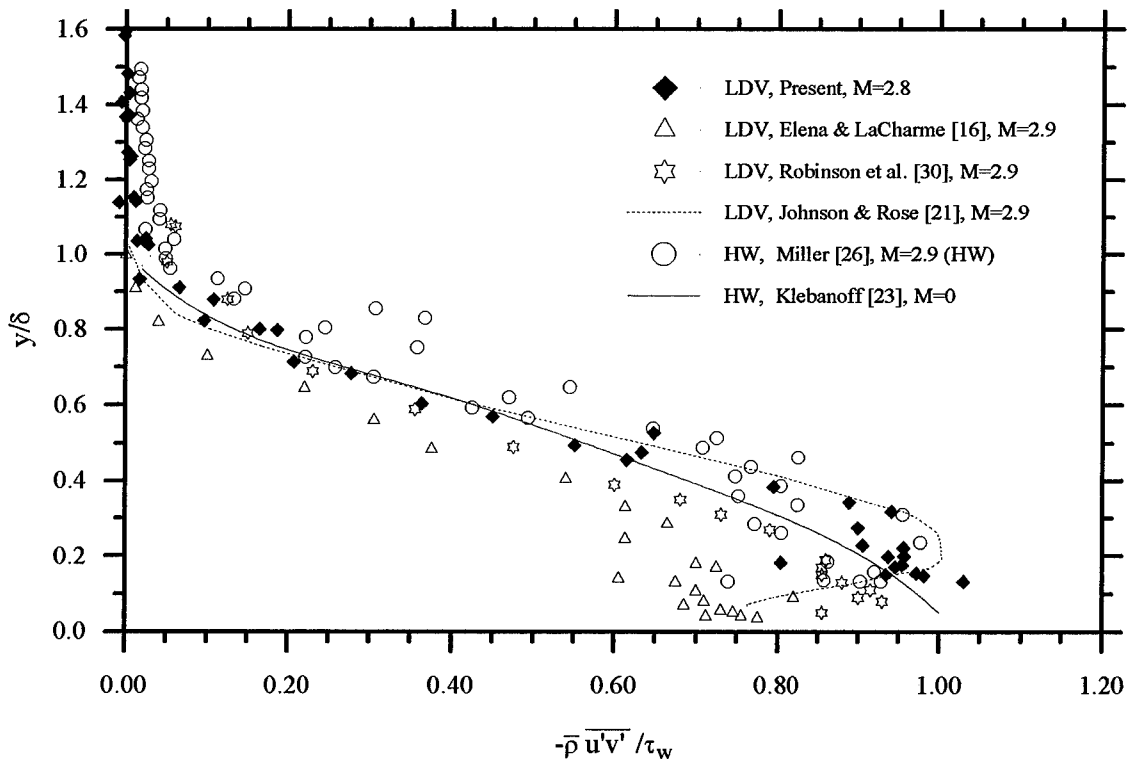


Figure 7.13: Incompressible Reynolds Shear Stress Scaled by Wall Shear Stress

Note that in Figure 7.13 the incompressible Reynolds shear stress measured in the current experiment tended to overshoot the wall shear stress. The overshoot could have been the result of one of two errors. The most likely error was that the wall shear stress was underestimated. A larger value of the wall shear stress would shift the LDV data to the left, causing the overshoot to be decreased or eliminated. The second possible explanation for the overshoot was that the flat plate data was actually taken in a slightly adverse pressure gradient (APG) as mentioned above. Studies in APG flows (such as that performed in Ref. [18]) have shown that an APG causes the turbulent shear stress profile in a plot of $-\overline{\rho u'v'}/\tau_w$ to overshoot the wall shear stress value before curling back towards unity.

It can be shown that the boundary layer shear stress should tend toward the value of the wall shear stress by integrating the boundary layer momentum equation from the wall to a point in the boundary layer a distance y from the wall (where y is still within the boundary layer). The integration leads to the relation [6]

$$\mu \frac{\partial \bar{u}}{\partial y} + \tau_{xy}^T = \tau_w + \frac{dp_e}{dx} y \quad (7.2)$$

For a flat plate, $dp_e/dx \approx 0$, so

$$\mu \frac{\partial \bar{u}}{\partial y} + \tau_{xy}^T = \tau_w \quad (7.3)$$

In the logarithmic region $\mu(\partial \bar{u}/\partial y) \ll \tau_{xy}^T$, so $\tau_{xy}^T \cong \tau_w$. Recall from Chapter 2 that $\tau_{xy}^T = -\overline{\rho u'v'} - \bar{u}\overline{\rho'v'} - \bar{v}\overline{\rho'u'} - \overline{\rho'u'v'}$. Neglecting the last three terms, $\tau_w \cong -\overline{\rho u'v'}$, and the profile in Figure 7.13 was expected to tend towards unity. Note that if the last three terms in τ_{xy}^T were not negligible, the wall shear stress would be underestimated.

The fact that the profile in Figure 7.13 was expected to tend towards unity was used to estimate a value for the “actual” wall shear stress by extrapolating the curve. The value of wall

shear stress found using this process was 70 Pa, a 4.3% difference from the value calculated using van Driest's relationship. The measured values for the incompressible Reynolds shear stress are presented in Figure 7.14 scaled by this new value of the wall shear stress. Note that, when scaled in this manner, the measured data fell almost exactly on top of Klebanoff's curve for incompressible flow, lending support to Morkovin's hypothesis.

The second method of non-dimensionalization was to scale the correlation $-\overline{u'v'}$ by the square of the local velocity, \overline{u}^2 . This scaling was used for three reasons. First, this scaling eliminated any linear biasing which may have influenced the velocity measurements (see Appendix B). Second, this scaling enabled easier comparison with CFD results. Note that $-\overline{u'v'}/\overline{u}^2$ is equivalent to the incompressible Reynolds shear stress divided by $\overline{\rho u}^2$; CFD turbulence models

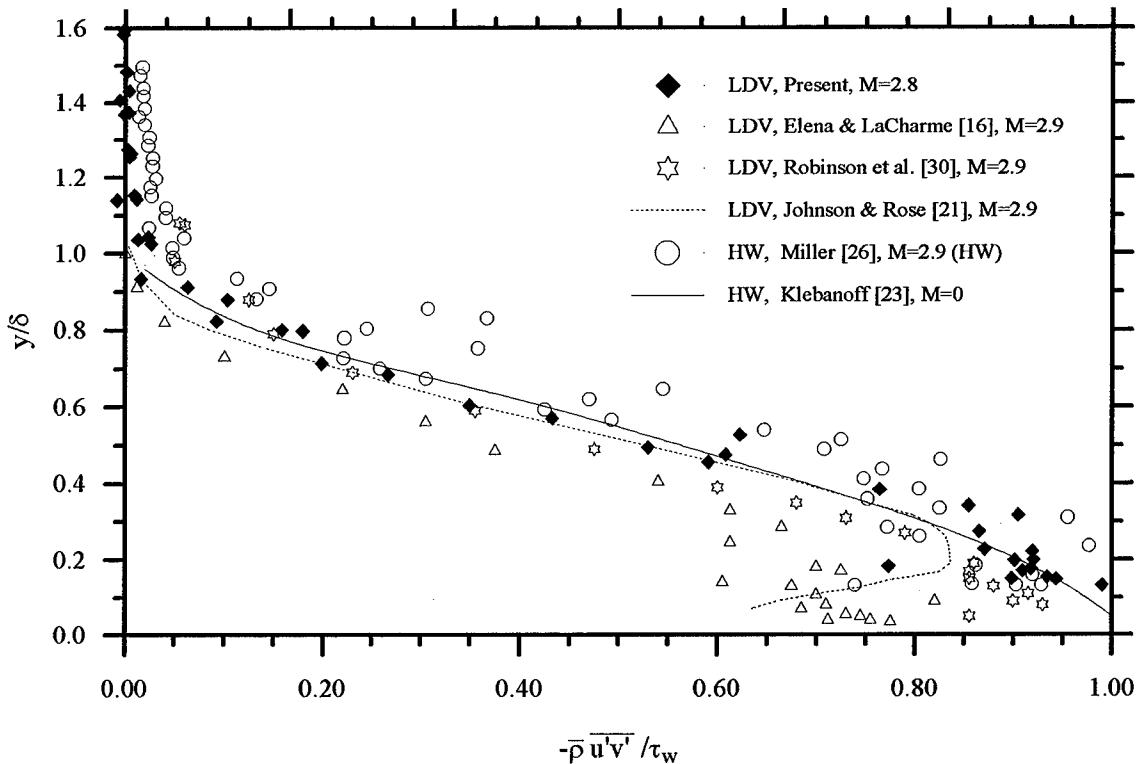


Figure 7.14: Incompressible Reynolds Shear Scaled by Extrapolated Wall Shear Stress

cannot resolve the term $\overline{u'v'}$, only $\tau_{xy}^T \approx -\overline{\rho u'v'}$. Therefore, use of this scaling allowed for simple comparison to CFD results. Finally, and most importantly, scaling by \overline{u}^2 allowed the presentation of a meaningful turbulent shear stress profile that only contained information from direct measurements. Thus, scaling the incompressible Reynolds shear stress by the local velocity eliminated the possibility of incurring errors associated with inaccurate calculation of other scaling parameters. LDV measurements of the incompressible Reynolds shear stress scaled using local quantities are presented in Figure 7.15. Note the excellent agreement with the hot-wire data from Ref. [26]. This agreement showed that the assumption of $p' = 0$ used to reduce the hot-wire data was valid for flat plate flow.

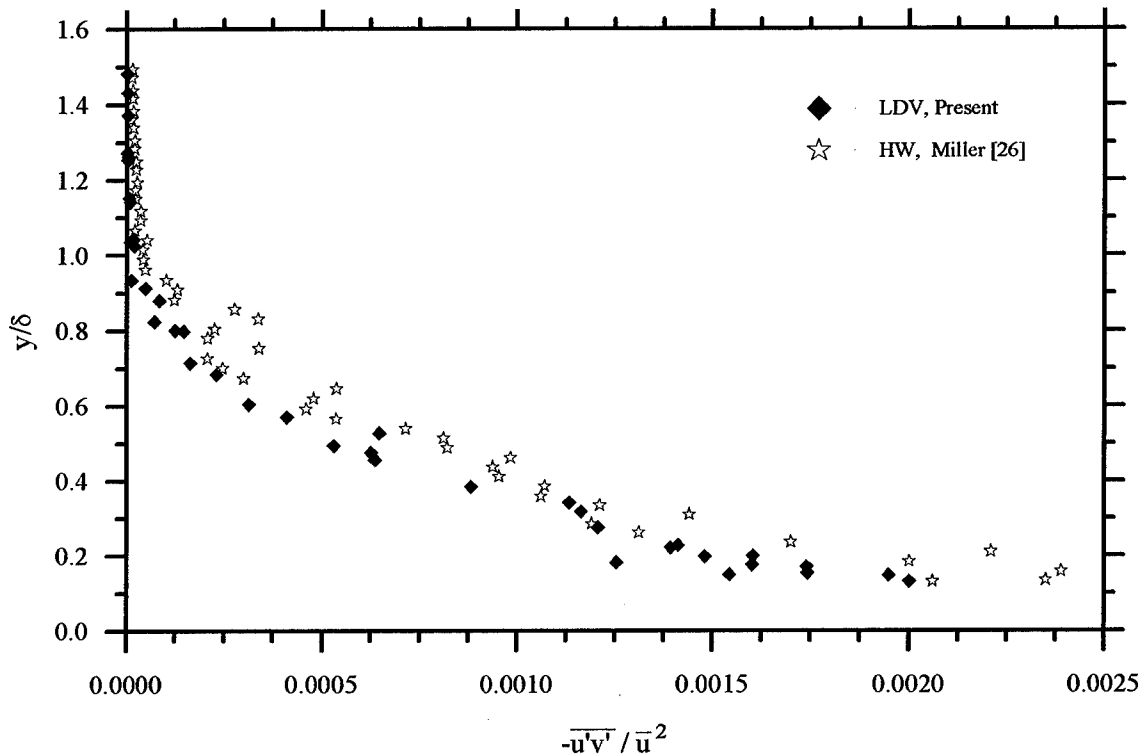


Figure 7.15: Incompressible Reynolds Shear Stress Scaled by Local Quantities

7.3.6 *Van Driest Velocity Profile.* The mean velocity was plotted using the scaling laws given by van Driest [35] as presented in Section 6.8. This velocity profile is plotted in Figure 7.16, along with the flat plate correlation given in Eq. (6.47). For a flat plate, Clauser's equilibrium parameter β was equal to 0, leading to a value of $\Pi = 0.476$ for the Coles wake parameter.

The solid line in Figure 7.16 represents a semi-empirical curve which has been proven throughout the literature to be accurate, so the slight disagreement of the present data to the curve seemed a bit disheartening. However, it should be pointed out that the data points in Figure 7.16 were generated using the estimated wall shear stress of 70 Pa; as discussed in Section 7.3.5, this value was probably underestimated. Increasing the wall shear stress tended to shift the points closer to the semi-empirical curve (a value of $\tau_w \cong 75$ Pa collapsed the data the best), pointing out

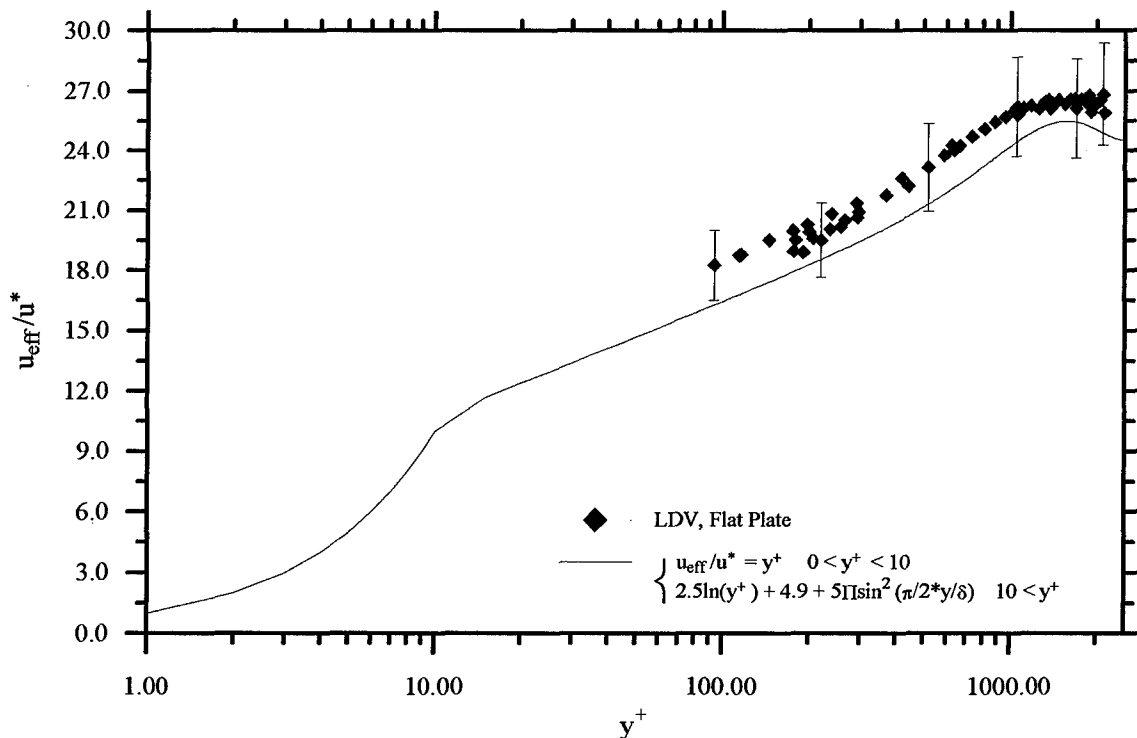


Figure 7.16: Flat Plate Van Driest Velocity Profile

once again that the wall shear stress was probably underestimated. It should be mentioned here that a value of $\tau_w \cong 75$ Pa is just inside the documented accuracy of van Driest's skin friction relation ($\pm 10\%$, cf. Ref. [9]) when compared to the estimated value of $\tau_w = 70$ Pa. However, to accurately present the measured incompressible Reynolds shear stresses, it is highly recommended that direct measurements of the wall shear stress be obtained experimentally.

7.3.7 Turbulence Statistics

7.3.7.1 *Skewness, Flatness, and Intermittency.* The values of skewness, flatness, and intermittency were important when comparing the LDV measurements to data in the literature since they helped determine if the present measurements were being biased by the seeding process. For example, non-uniform seeding in the current experiment would cause the measured velocity profiles to be skewed differently than they were in other experiments.

The probability of biasing is also increased in compressible flows due to temperature and density gradients in the boundary layer. A warmer, less-dense "clump" of fluid may be able to hold more seed particles than a clump of cold, dense fluid (it would have more "free space" between the fluid molecules for the seed particles to occupy). The LDV system would then register more bursts for the warmer clump of fluid than the cold clump. This would skew the measurements towards the velocity of the warmer, less-dense clump of fluid when, in reality, they should be skewed towards the velocity of the cold, dense clump of fluid.

In order to determine if the measurements were being biased, plots of the skewness and flatness were compared to data in the literature. Unfortunately, most of the data available for the skewness and flatness in compressible flows was data collected in other LDV experiments. Thus, if the skewness and flatness data in the literature were subject to biasing, comparing the present data to that which had the same possibility of being biased would be problematic. Obviously, there

exists a need for skewness and flatness data collected by means which are not subject to the possible density biasing discussed here. However, for lack of other data with which to compare, the LDV skewness and flatness data in the literature has been taken as valid. The skewness data collected in the present study is shown in Figure 7.17 compared to data from Ref. [16]. The data from the present study agrees well with that from Ref. [16], indicating that the methods used in this study were as valid as those used by past researchers.

The flatness data is presented in Figure 7.18 and compared to data from Ref. [16]. The correlation was once again very good, especially considering the scatter in the data. The flatness did not provide much insight into the physics of the flowfield, but examination of the intermittency function (which is calculated using the flatness) did provide useful information.

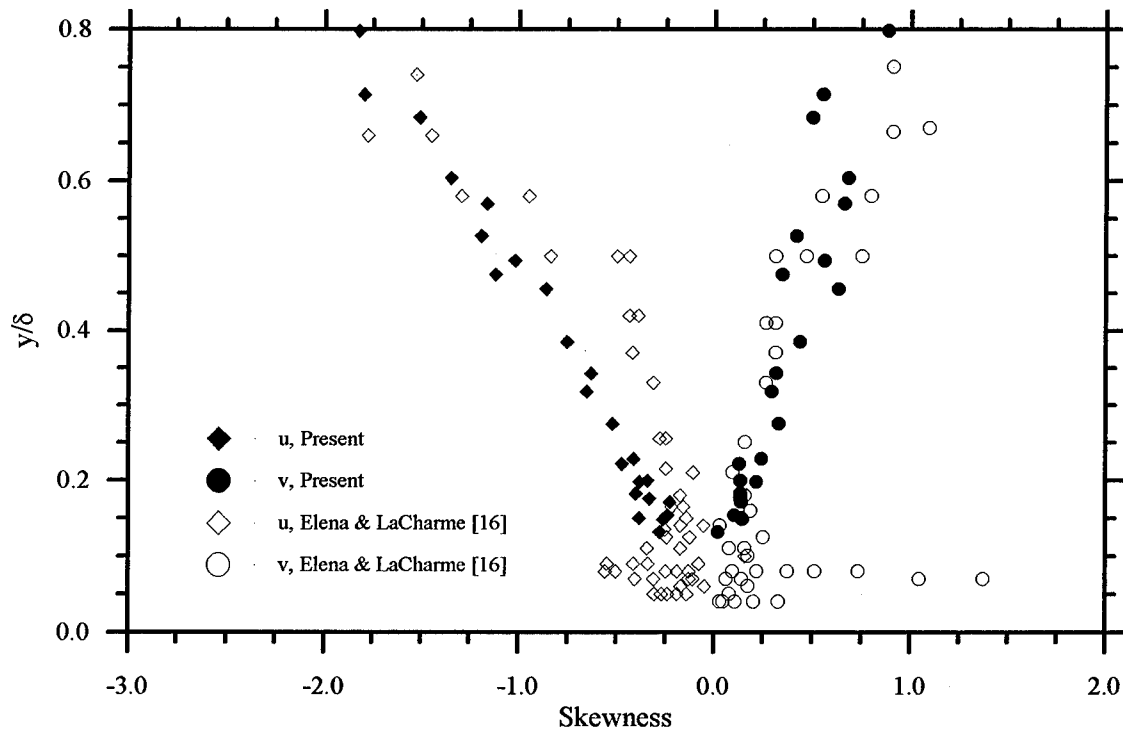


Figure 7.17: Skewness of Velocity Components in Flat Plate Flow

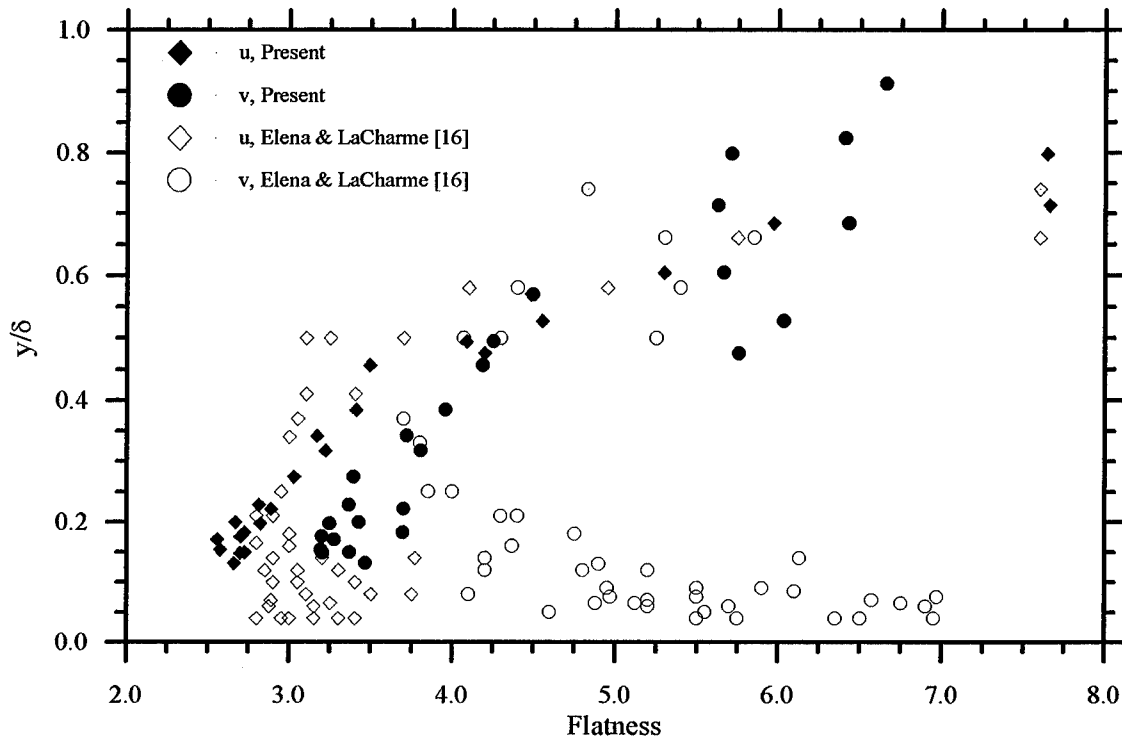


Figure 7.18: Flatness of Velocity Components in Flat Plate Flow

The profile of the intermittency function is shown in Figure 7.19. Even though the flatness curve in Figure 7.18 agreed well with the data from Ref. [16], there was a noticeable difference in the intermittency profile. The curve fit to the data from Ref. [16] had $\zeta = 0.114\delta$ and $\varphi = 0.64$, whereas in the present experiment they were $\zeta = 0.22\delta$ and $\varphi = 0.68$. This showed that the boundary-layer edge was essentially at the same location as in Ref. [16], but the standard deviation from the mean position was almost twice as large. The increase in the standard deviation was probably due to the 1% freestream turbulence level measured in the current experiment, compared with a freestream turbulence level of about 0.5% measured in Ref. [16].

7.3.7.2 Correlation Coefficient. The profile of the correlation coefficient R_{uv} is presented in Figure 7.20. Near the wall $-R_{uv} \approx 0.42$; recall from Chapter 6 that experimental data indicated $-R_{uv} = 0.4 - 0.5$ for low-speed, incompressible flow. [6] Thus, the compressibility

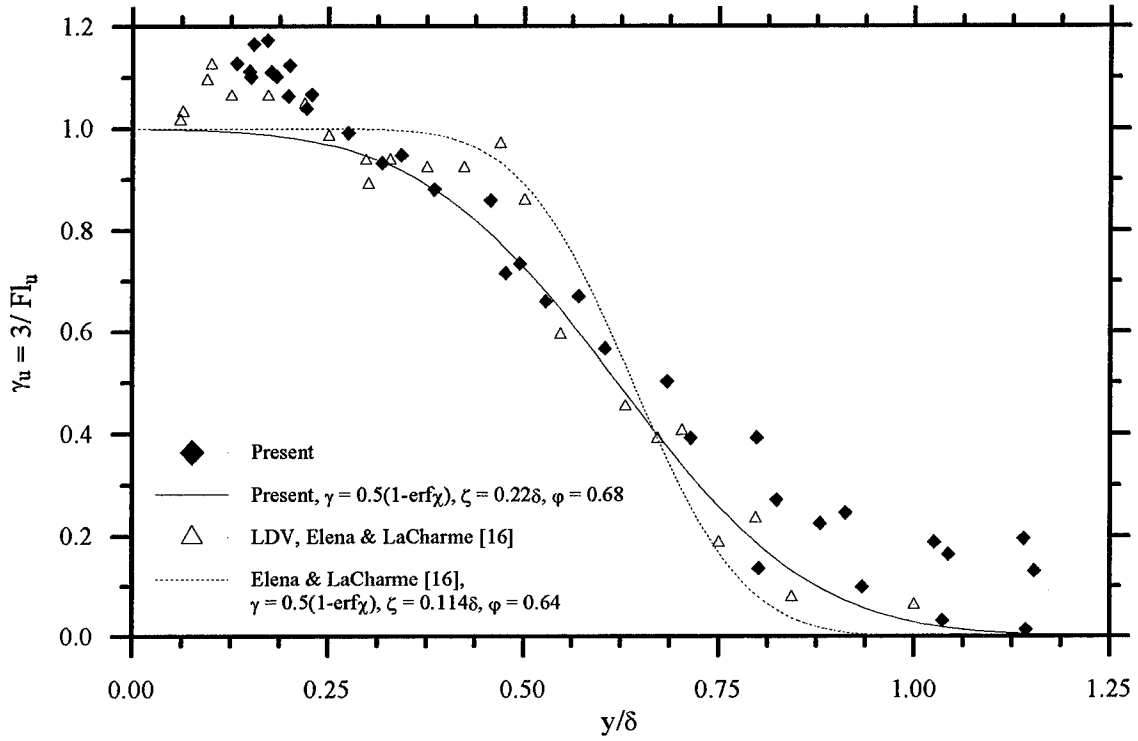


Figure 7.19: Flat Plate Intermittency Function Profile

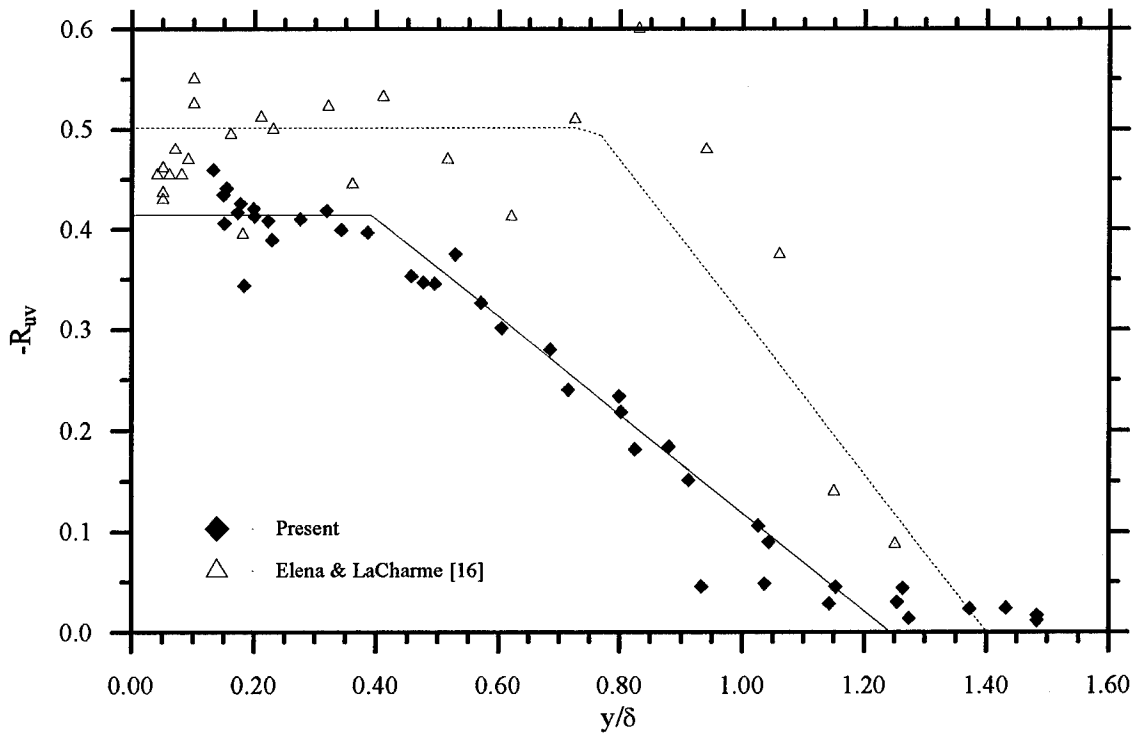


Figure 7.20: Flat Plate Correlation Coefficient

effects associated with high-speed flow did not appear to have a large influence on the correlation coefficient. In addition, the present results showed a reduction in the correlation coefficient throughout the boundary layer when compared to the data of Ref. [16], possibly due to the higher freestream turbulence level in the present facilities.

7.3.7.3 Turbulent Kinetic Energy. Results from the TKE calculations are presented in Figure 7.21 along with CFD results from Ref. [17]. The CFD calculations showed a nearly-linear profile through the boundary layer, while the measurements tended to decrease near the wall. This roll-off was due to the estimation of $w' \approx v'$ (see Section 6.9): in the literature, w' has been shown to be about $1.5 v'$ near the wall, while it is approximately equal to v' in the freestream. [6] This under-estimation of w' near the wall led to the inaccuracy in the computed TKE in this region. Also note that the CFD results consistently underestimated the measured TKE. Once again, this was probably due to the non-zero freestream turbulence level in the wind tunnel.

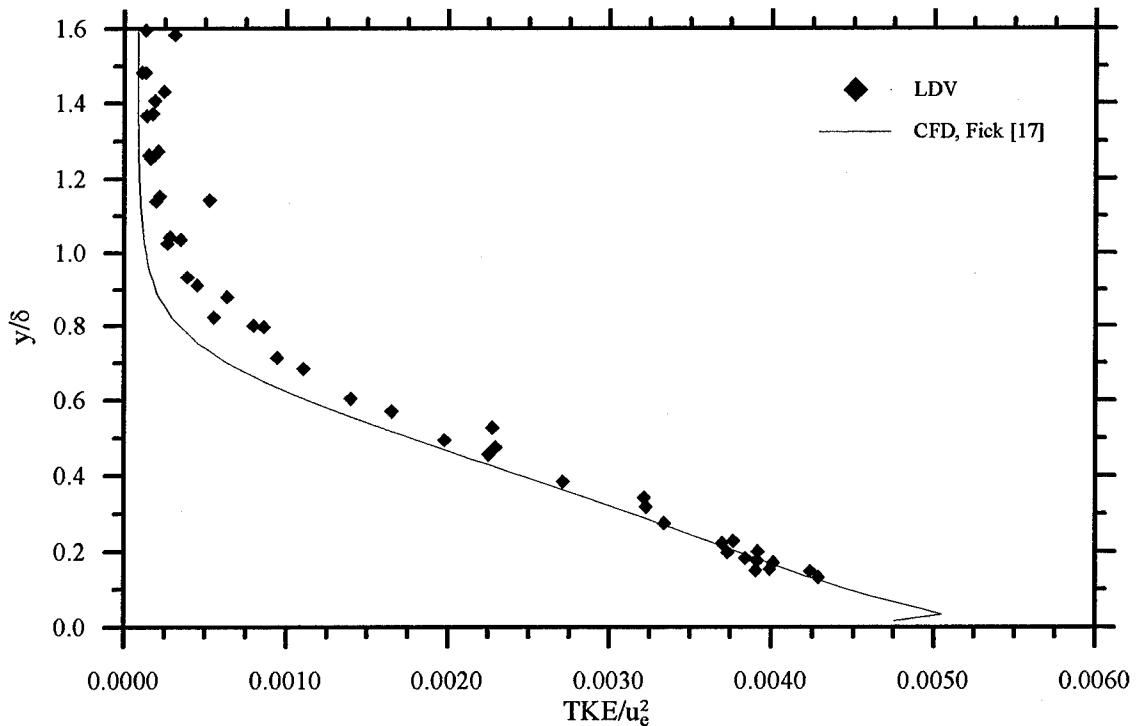


Figure 7.21: Flat Plate TKE Profile

7.4 FPG Results

With the testing procedures validated against existing data and producing viable results, the data from the FPG testing were compared to the flat plate data. The FPG results and their implications are discussed below.

7.4.1 Mean Flow Characteristics

7.4.1.1 Velocity. In the FPG test section, u_e was found to be approximately 607 m/s. Scaling the measured velocities by this value, the non-dimensional velocity profile was used to calculate a value for δ_u . Following the same procedure as that used for the flat plate, $\delta_u = 11.9$ mm; the resulting non-dimensional profile is shown in Figure 7.22. The FPG did not

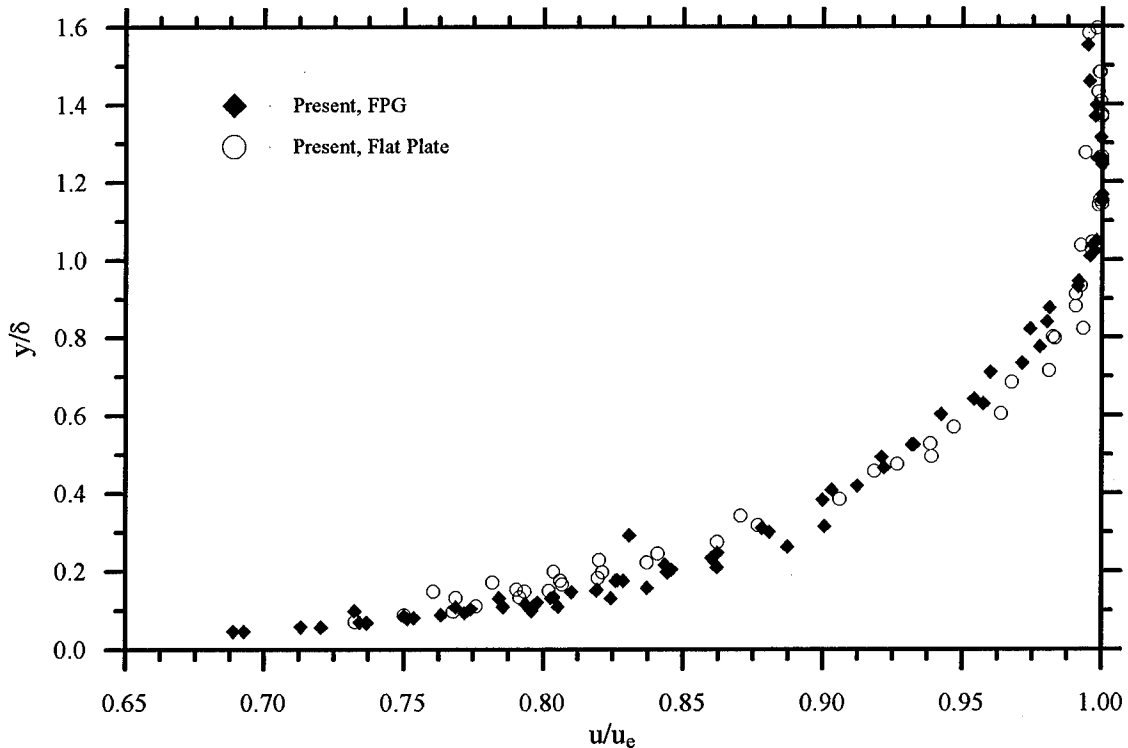


Figure 7.22: FPG Velocity Profile in Non-Dimensional Coordinates

have a large effect on the non-dimensional velocity profile; in the outer region of the boundary layer the velocity defect was increased while in the near-wall region it decreased, but in either case the change was very slight.

7.4.1.2 Mach Number and Density. The Mach number profile is presented in Figure 7.23, while the density profile is presented in Figure 7.24. The Mach number profile shows good agreement with the measurements presented in Ref. [26], especially when considering the large errors associated with the value of δ (see Appendix B). Recall that the density profile in the FPG region was calculated in a different manner than for the flat plate (see Section 6.4.2); in order to determine the validity of the calculations, the density profile was compared to CFD results from Ref. [17]. Once again, the profile matched extremely well and the assumptions used to calculate the density (the assumptions of constant total temperature and a linear pressure distribution through the boundary layer) were justified.

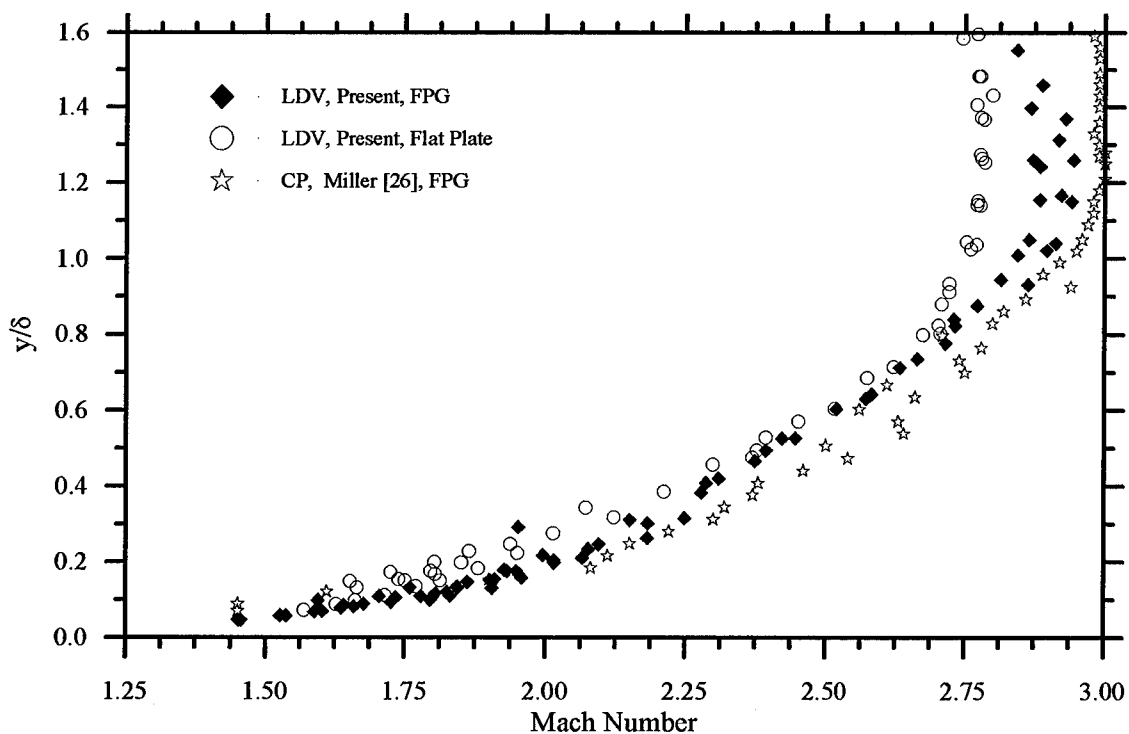


Figure 7.23: FPG Mach Number Profile

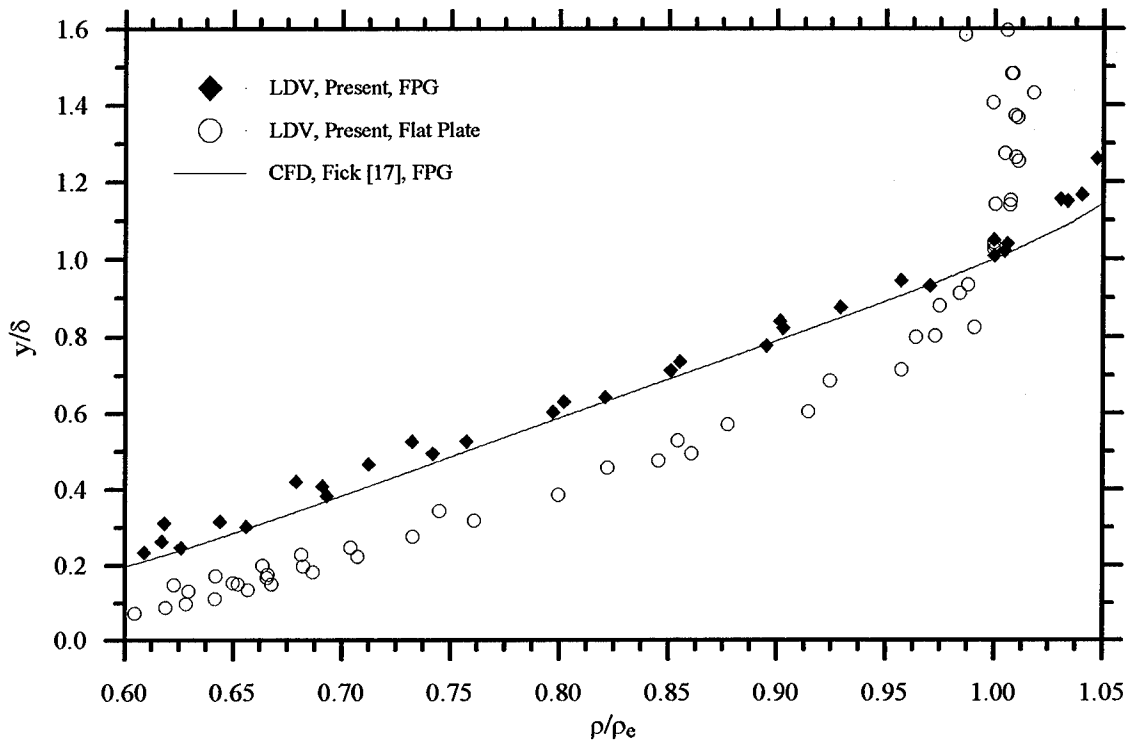


Figure 7.24: FPG Non-Dimensional Density Profile

7.4.1.3 Integral Momentum Thicknesses. The integral momentum thickness results for the FPG region are presented in Table 7.3. Note that, when comparing these results to the flat plate values given in Table 7.2, the thicknesses tended to increase dramatically. This at first seemed counter-intuitive, as a stabilizing FPG should be expected to decrease the thicknesses. It appeared that this may have been the case between $x = 70.44$ and $x = 70.98$ cm, where the thicknesses decreased slightly. In this region, the wall was only slightly curved, and the stabilizing effect of the FPG was strong enough to overcome the effect of the wall curvature. However, at the location $x = 70.5$ cm the wall curvature outweighed the effects of the FPG, leading to an increase in the integral momentum thicknesses.

Table 7.3: FPG Integral Thicknesses Calculated From LDV Measurements

x (cm)	δ^* (mm)	θ (mm)	δ_i^* (mm)	θ_i (mm)
70.44	2.80	1.11	0.41	0.67
70.98	2.76	1.09	0.41	0.66
71.52	3.95	1.43	0.56	0.89

7.4.2 *Turbulence Intensities.* The u - and v -component turbulence intensities are presented in Figure 7.25 and compared to the flat plate values. Note that, in both cases, the FPG drastically reduced the turbulence intensities in the lower half of the boundary layer but had relatively no effect above $y/\delta \approx 0.5$.

7.4.3 *Fluctuating Mach Number.* The fluctuating Mach number results for the FPG test section are presented in Figure 7.26. Near the wall, the FPG tended to decrease the value of the

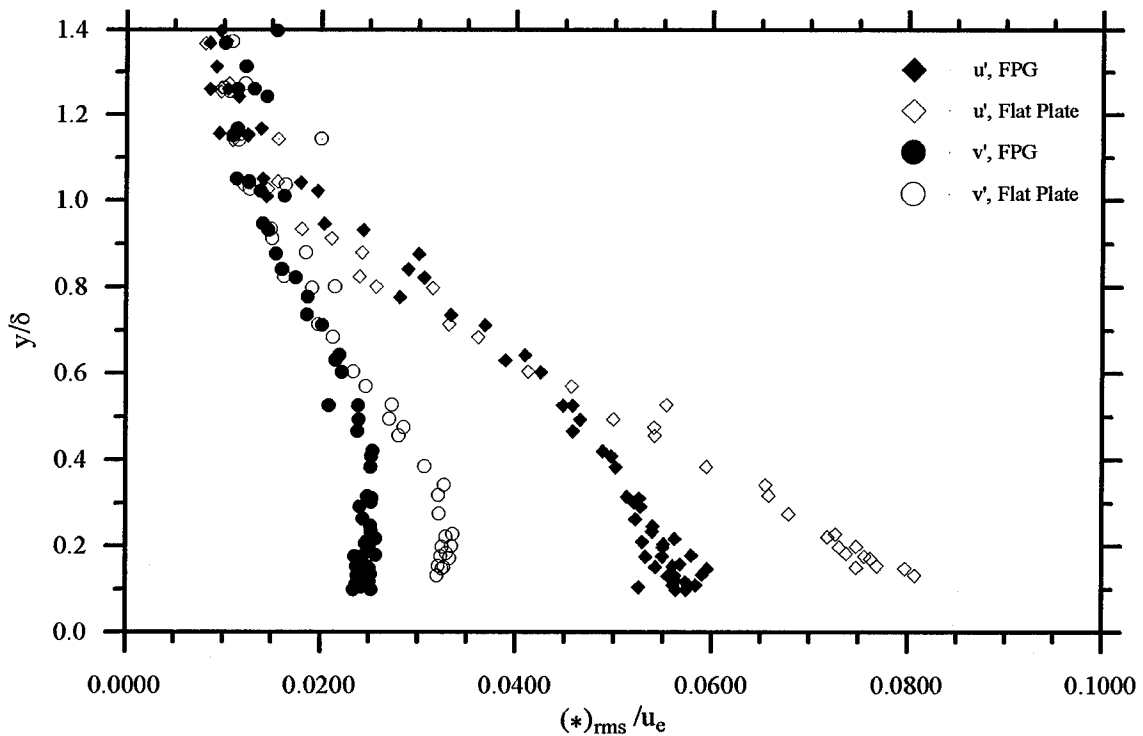


Figure 7.25: FPG vs. ZPG Turbulence Intensity Comparison

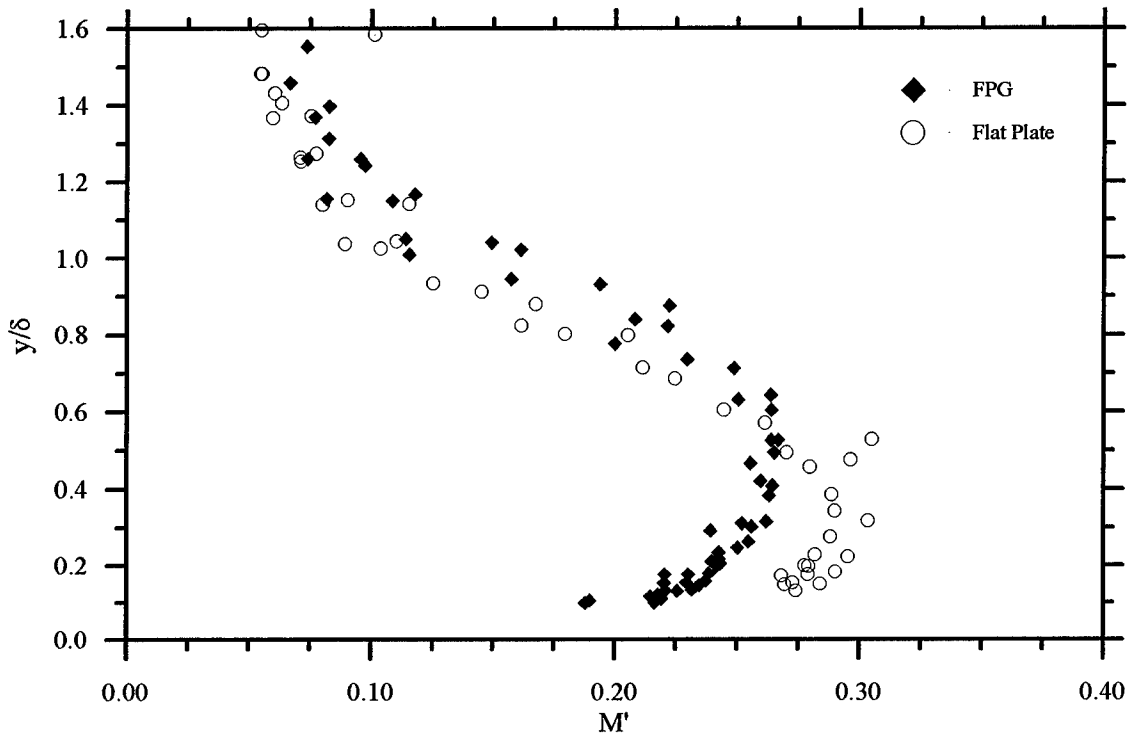


Figure 7.26: FPG Fluctuating Mach Number

fluctuating Mach number when compared to the flat plate results. This not only provided evidence of the stabilizing effect of the FPG, but it also indicated that there were no local shocklets present in the FPG boundary layer.

7.4.4 Wall Shear Stress. The wall shear stress in the FPG region was calculated using the relationship given by Eq. (7.2). From Eq. (7.1), $dp_e/dx = -2 \times 10^4$ Pa/m, so that

$$\tau_w \cong -\overline{\rho u'v'} \Big|_y + 2 \times 10^4 y \quad (7.4)$$

Using the value of $-\overline{\rho u'v'}$ calculated at the innermost point, the wall shear stress in the FPG region was found to be $\tau_w = 44$ Pa ($C_f = 1.15 \times 10^{-3}$). When compared to the flat plate value of approximately 70 Pa, the FPG was seen to reduce the wall shear by approximately 40%.

7.4.5 "Incompressible" Reynolds Stresses. The incompressible Reynolds stresses measured in the FPG region are compared to the flat plate results in Figure 7.27. Note that the FPG caused a significant reduction in the ratio of the turbulent shear stress to the wall shear stress when compared to the flat plate curve. Noting that the magnitude of the wall shear stress was reduced by the FPG, the reduction in the absolute magnitude of $-\overline{\rho u'v'}$ was higher than that implied by the curves in Figure 7.27.

A better feel for the effect of the FPG on the absolute magnitude of $-\overline{\rho u'v'}$ was achieved by scaling the incompressible Reynolds stress by the local density and velocity; this scaling was used in the data presented in Figure 7.28. When scaled by local parameters, the FPG was seen to reduce $-\overline{\rho u'v'}$ by approximately 75% near the wall (as opposed to the 60% reduction seen when

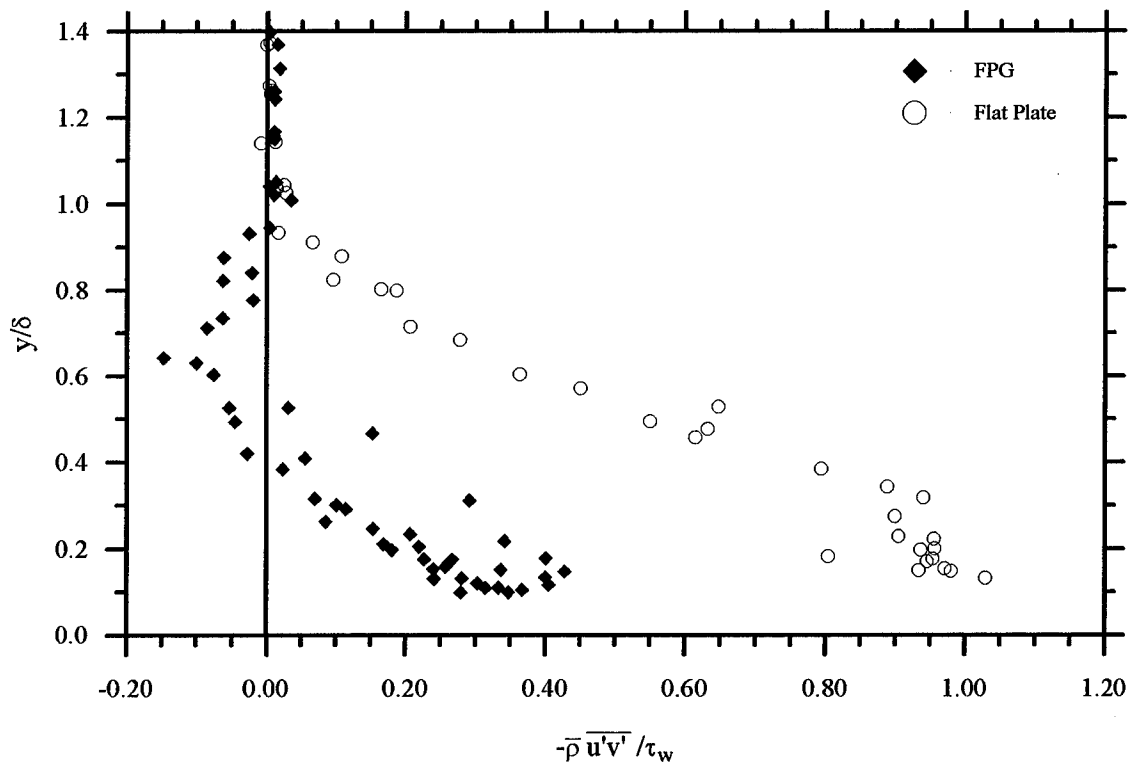


Figure 7.27: FPG Incompressible Reynolds Stresses Scaled by Wall Shear Stress

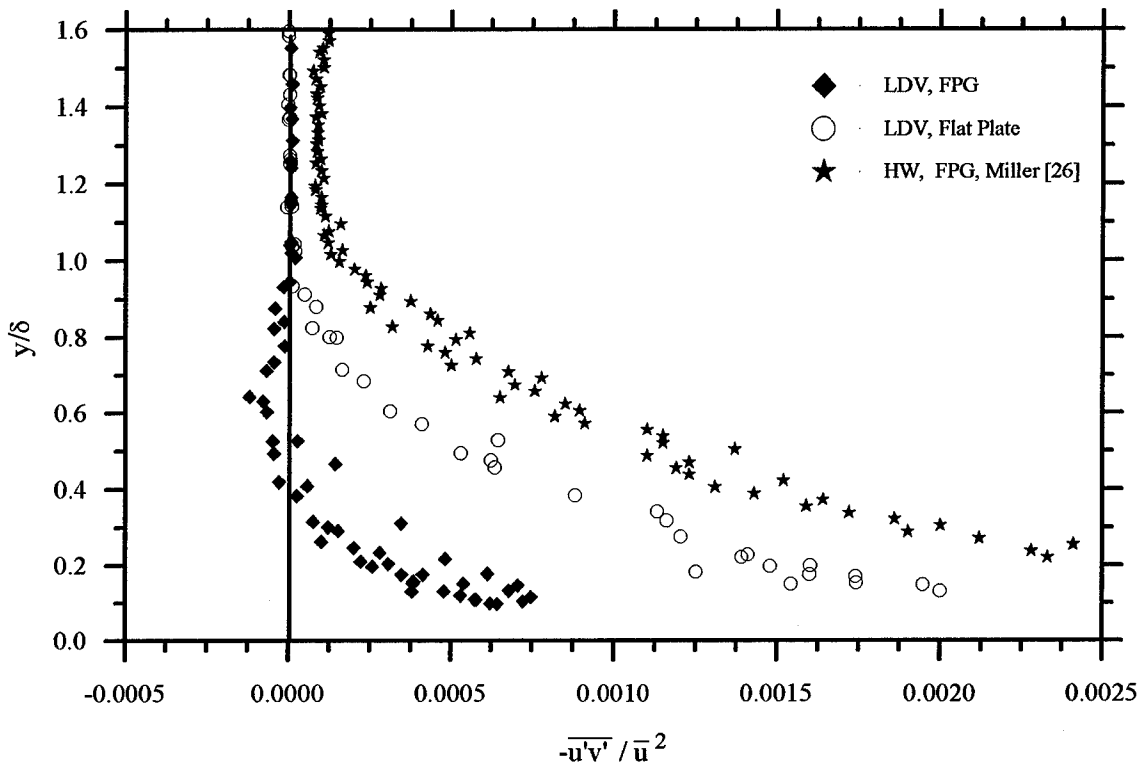


Figure 7.28: FPG vs. ZPG Incompressible Reynolds Shear Stress Scaled by Local Quantities

scaled by τ_w). This was the expected result based on the reduced wall shear stress and heat flux values reported by Spina et al. for FPG flows. [33] Note that, above $y/\delta \approx 0.5$, the velocity fluctuations were found to be practically uncorrelated (i.e., $\overline{u'v'} \approx 0$). The stabilizing effect of the FPG was more than likely responsible for this effect.

The hot-wire data from Ref. [26] was also presented in Figure 7.28 for comparison. The hot-wire data followed the same trends as the LDV data, but the magnitudes of the hot-wire data were substantially larger. Recall that the agreement between the flat plate hot-wire and LDV data (see Figure 7.15) was excellent. The large difference in the FPG region was more than likely the result of inaccurate assumptions in the reduction of the hot-wire data. That is, the hot wire data reduction assumed $p' = 0$; the results in Figure 7.28 indicated that this assumption was probably

invalid in the FPG region. In order for the assumption of $p' = 0$ to become invalid in the FPG region, the FPG would have to cause the pressure fluctuations to *increase*. In contrast, to this point the FPG has been seen to stabilize and *reduce* all other fluctuating quantities. If the size of the pressure fluctuations was magnified by the FPG, the increase was probably due to the streamline curvature and the associated pressure change across the boundary layer rather than the streamwise pressure gradient. That is, the non-zero value of dp/dy across the FPG boundary layer may have provided a mechanism for generating p' . Using a Prandtl mixing-length model, $p' \approx l_p(dp/dy)$, where l_p is a mixing length associated with the pressure fluctuations. Thus, over the flat plate $dp/dy \approx 0$, leading to $p' \approx 0$; in the FPG region $dp/dy \neq 0$, so $p' \neq 0$.

Finally, Figures (7.27) and (7.28) showed that the profile of the FPG incompressible Reynolds shear stress actually became negative around $y/\delta \approx 0.65$. This negative value could prove problematic when trying to develop a turbulence model for use in CFD codes. Due to the fact that CFD turbulence modeling has focused on flat plate and adverse pressure gradient flows, current CFD models (such as the model used in Ref. [17]) do not admit the possibility of $\tau_{xy}^T < 0$.

7.4.6 Van Driest Velocity Profile. The van Driest velocity profile for the FPG region is presented in Figure 7.29. The FPG was found to slightly increase the effective velocity when compared to the calculated flat plate value; however, recall that the flat plate value was fairly inaccurate due to the error in the computed wall shear stress. When comparing the FPG data to the flat plate empirical curve fit, the FPG was seen to have a substantial effect on the effective velocity profile. It should be noted that in the FPG region, $\beta = -1.3$, leading to an undefined value for the Coles wake parameter, Π . Therefore, it was not possible to calculate a correlation to use for comparison with the FPG profile.

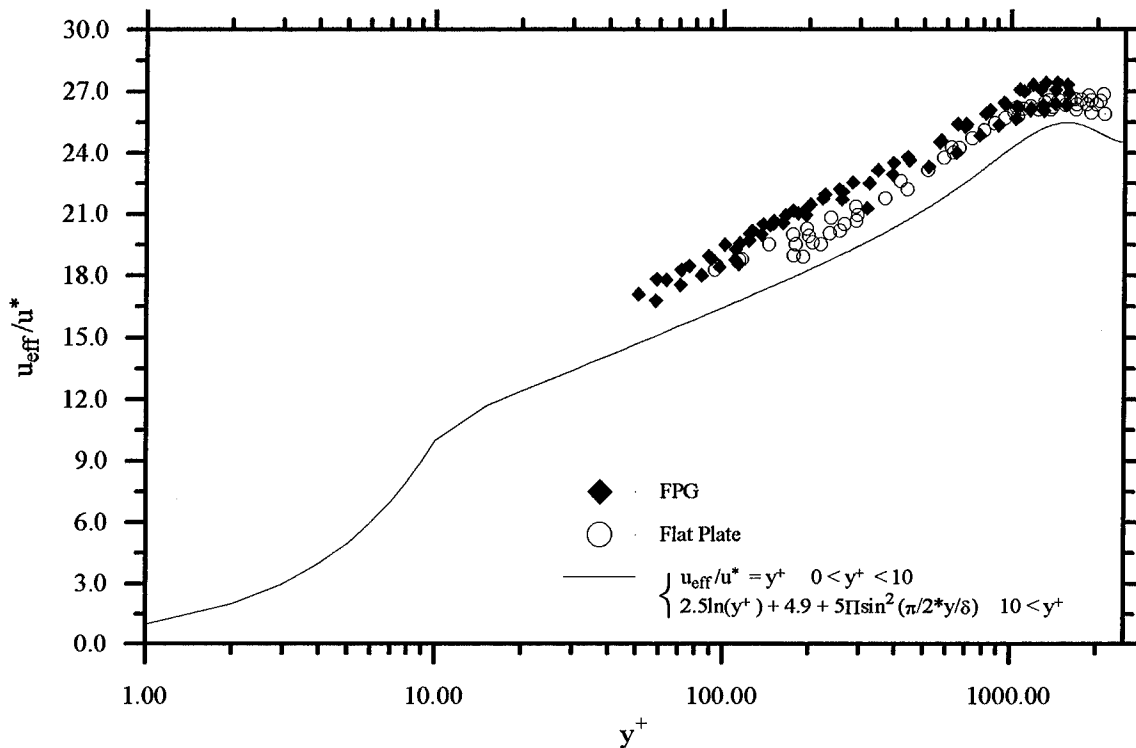


Figure 7.29: FPG van Driest Velocity Profile

7.4.7 Turbulence Statistics

7.4.7.1 *Skewness, Flatness, and Intermittency.* Comparison of the flat plate and FPG skewness (see Figure 7.30) showed that the FPG reduced the magnitude of both the u and v components of skewness. In the flat plate case, the high negative value of Sk_u and high positive value of Sk_v , showed that more particles were crossing through the control volume from the side nearest the wall (“below” the control volume). The FPG reduced the skewness, indicating a more even balance in the number of particles entering the control volume from above and below.

As in the flat plate case, examination of the flatness in the FPG region did not provide a great deal of insight into the effects of the FPG on the flow, but the measurements are compared to the flat plate values in Figures 7.31 and 7.32 for completeness. In contrast to the flatness, the intermittency function provided some insight into the stabilizing effects of the FPG. The

intermittency profile for the FPG region is compared to the flat plate intermittency in Figure 7.33. The error function curve fit showed that, for the FPG region, $\varphi = 0.8$ and $\zeta = 0.17\delta$. Recall that the flat plate curve fit resulted in $\varphi = 0.68$ and $\zeta = 0.22\delta$. Since φ represented the random location of the boundary layer edge, the FPG was seen to push this location outward towards δ . The FPG also slightly reduced the standard deviation around φ , but not by a significant amount. Recall from the turbulence intensity results in Figure 7.25 that the turbulence was not affected much above $y/\delta \approx 0.5$; since the random position of the boundary layer edge was outside this value, the standard deviation represented by ζ should not have changed significantly. Comparison of the magnitudes of the flat plate and FPG intermittency profiles also showed that, although the FPG decreased the magnitudes of the velocity fluctuations, it caused the flow to be turbulent for a higher percentage of time: i.e., the FPG was distributing the energy from a few particles with large velocity fluctuations over many particles, each with a smaller fluctuating velocity.

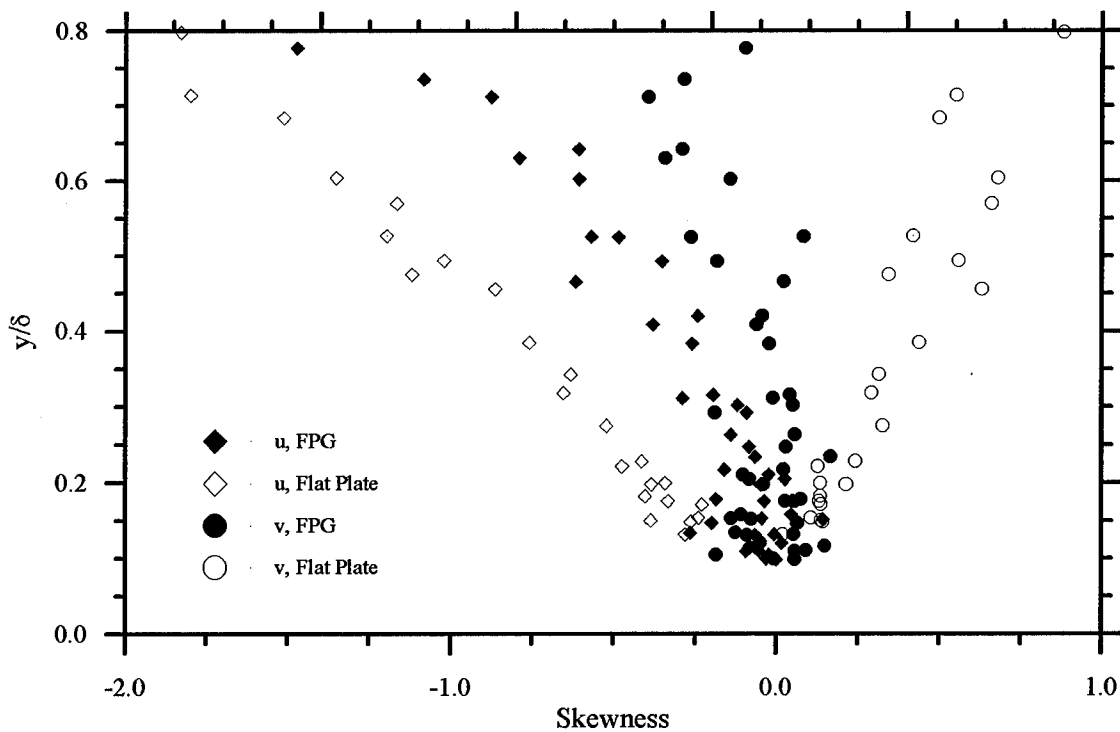


Figure 7.30: FPG vs. ZPG Skewness Comparison

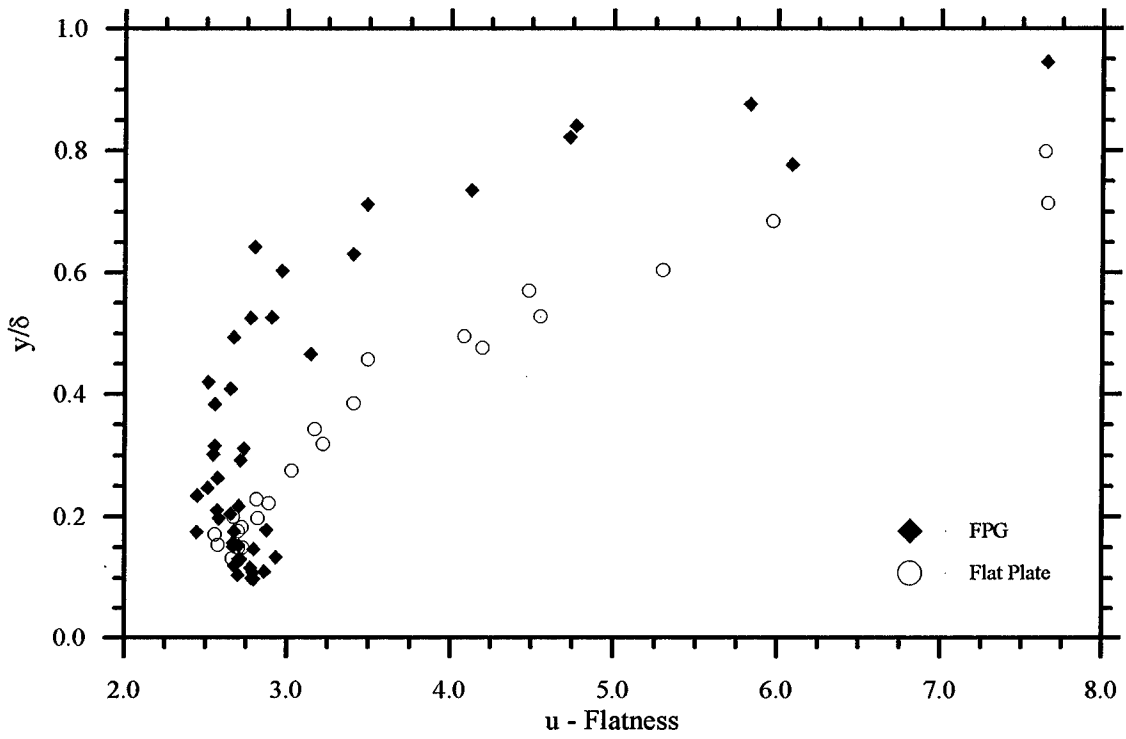


Figure 7.31: u -Component Flatness Comparison

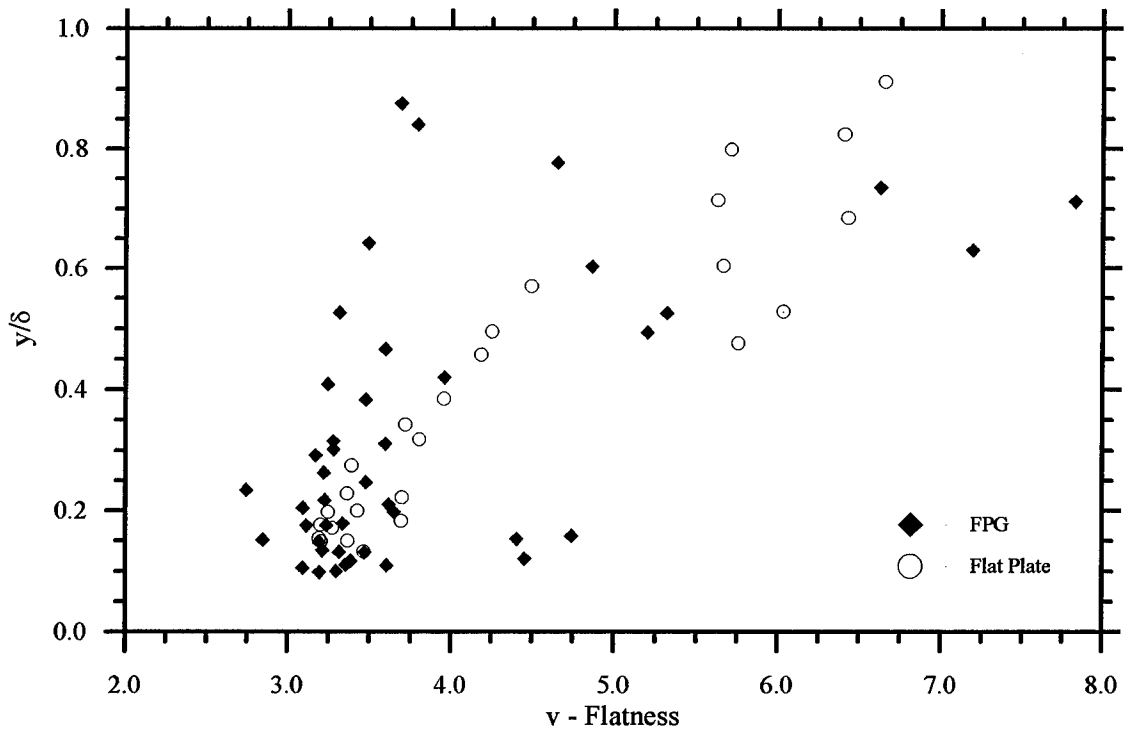


Figure 7.32: v -Component Flatness Comparison

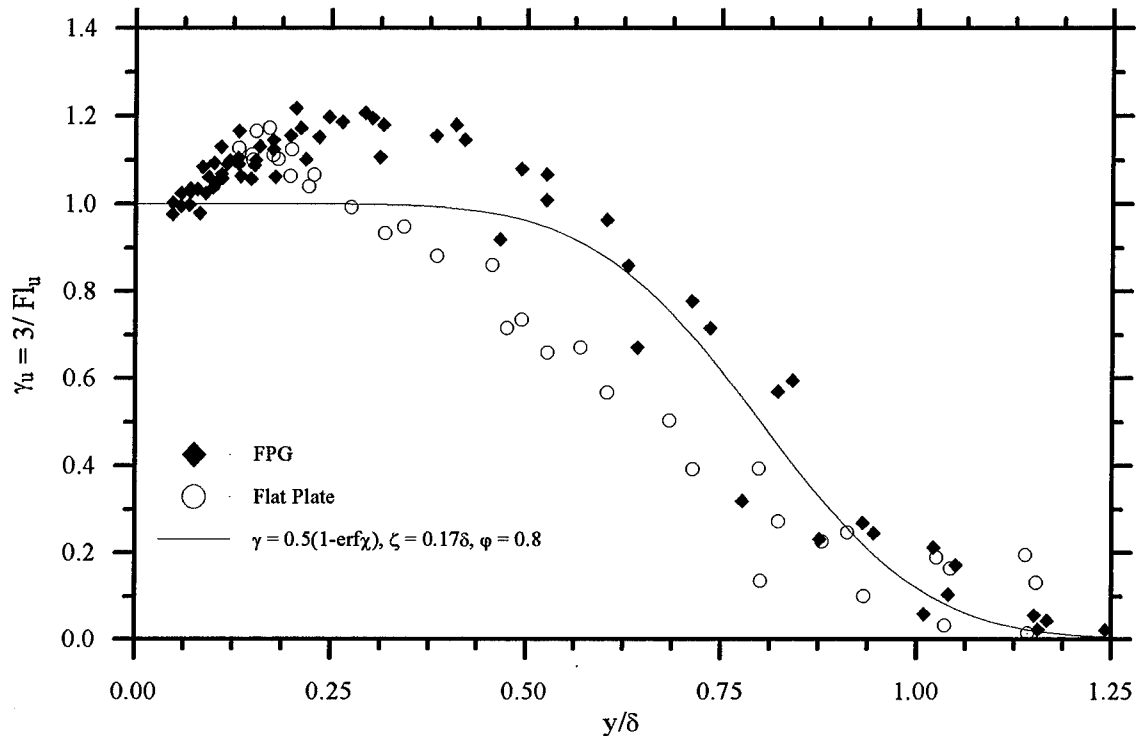


Figure 7.33: Intermittency Function Comparison

7.4.7.2 *Correlation Coefficient.* The calculated correlation coefficient profile for the FPG region is compared to the flat plate profile in Figure 7.34. Recall that above $y/\delta \approx 0.5$ the FPG caused a reduction in the velocity correlation $\overline{u'v'}$ while leaving the turbulence intensities relatively unaffected. These effects were reflected in the fact that the correlation coefficient was approximately zero above $y/\delta \approx 0.5$. Below $y/\delta \approx 0.5$, the flow velocity decreased due to the presence of the wall, causing the correlation coefficient to tend toward the low-speed value associated with flat plate flow ($-R_{uv} = 0.4 - 0.5$).

7.4.7.3 *Turbulent Kinetic Energy.* The FPG TKE profile is shown in Figure 7.35; however, due to the estimation of $w' \cong v'$, the accuracy of this profile was very questionable, especially near the wall. Note the excellent comparison to the CFD results; the discrepancy near the wall was probably due to an underestimation of w' in this region.

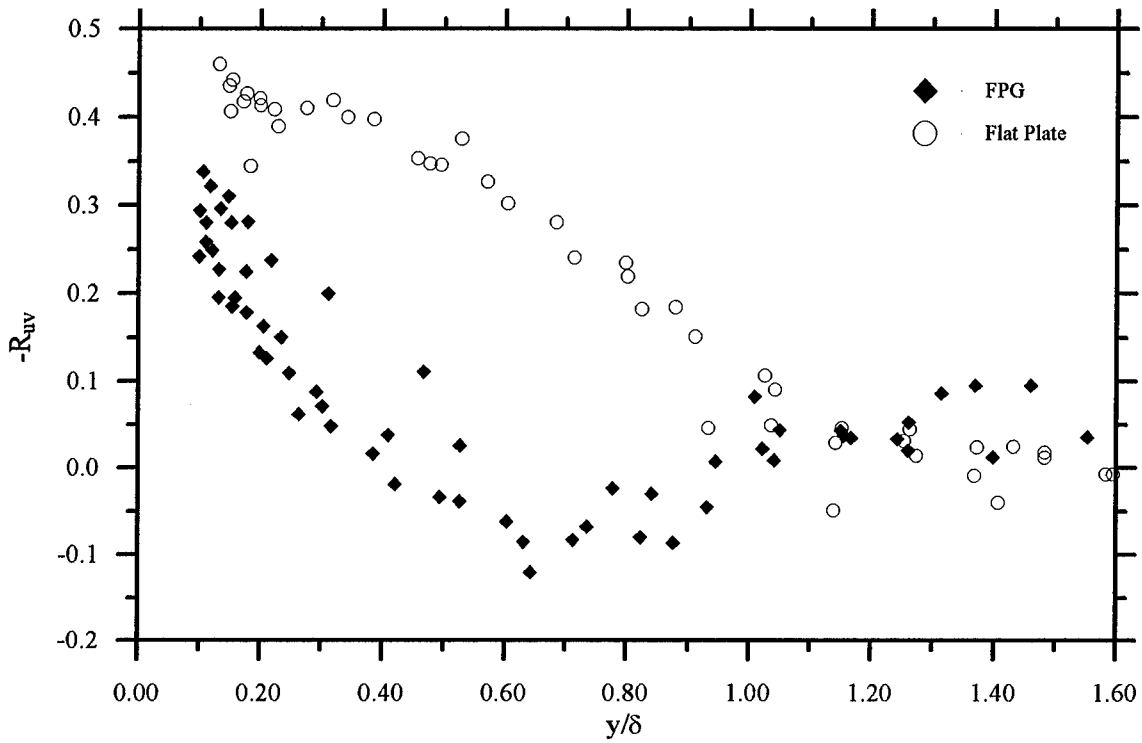


Figure 7.34: FPG and ZPG Correlation Coefficient Comparison

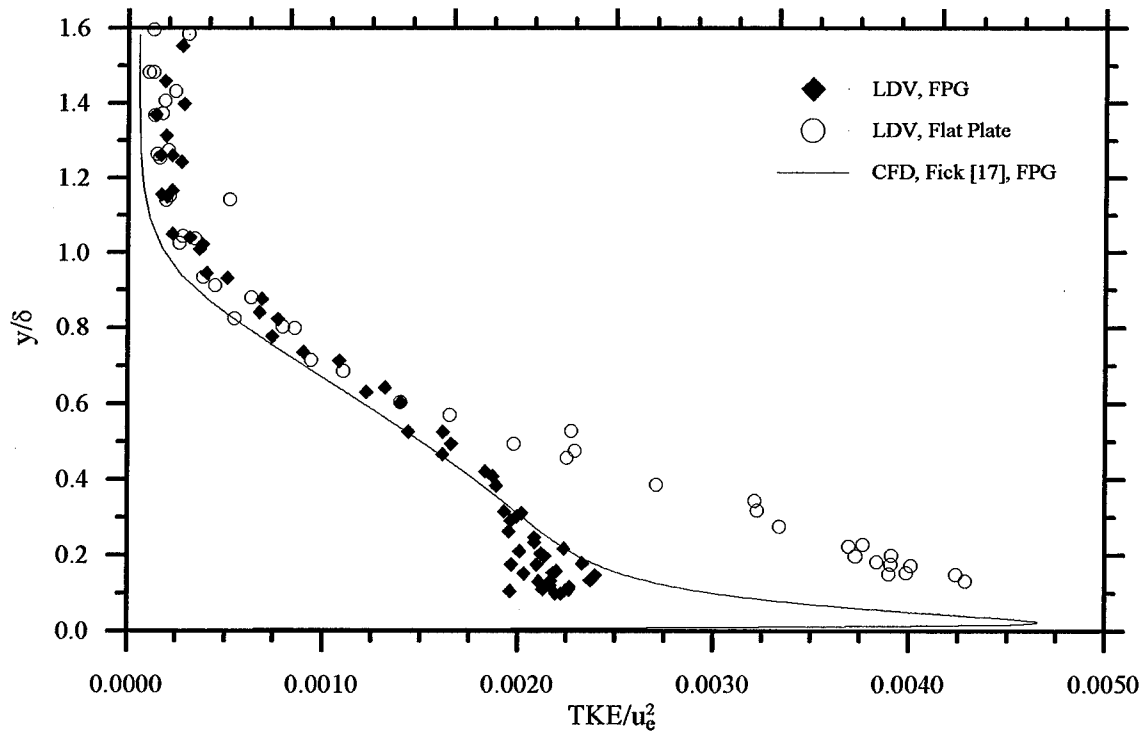


Figure 7.35: FPG TKE Profile

7.5 Strain Rate Profiles

Strain rate profiles were calculated across the boundary layer for both the flat plate and the FPG; the flat plate strain rates calculated were $\partial\bar{u}/\partial x$, $\partial\bar{u}/\partial y$, $\partial\bar{v}/\partial x$ and $\partial\bar{v}/\partial y$. The strain rates calculated in the FPG region also included $\partial\bar{u}/\partial z$ and $\partial\bar{v}/\partial z$. The results from these calculations are presented in Figures 7.36 to 7.41. It should be noted that the strain rates were calculated using finite-difference methods, and as a result the error in the calculations was relatively large (see Appendix B).

Upon examination of Figures 7.36 to 7.39, it was apparent that the FPG did not have a large effect on the strain rates in the direction normal to the wall. The comparison of the flat plate and FPG values of $\partial\bar{u}/\partial x$ showed that the FPG did not affect the strains except in the very near-wall region, where they went negative. The FPG was seen to shift $\partial\bar{v}/\partial x$ from the flat-plate value of zero to a finite negative value; this value was essentially constant across the boundary layer. The values of $\partial\bar{u}/\partial z$ and $\partial\bar{v}/\partial z$ were also measured for the FPG test section; the values of these strain rates were found to be at least an order of magnitude below any other measured strain rate and were considered negligible.

Finally, Smith and Smits [32] pointed out that Clauser's equilibrium parameter is not always sufficient for characterizing the strength of a pressure gradient in supersonic flows. For instance, a pressure gradient generated by a curved wall will affect the strain rates differently than the same pressure gradient generated over a flat plate. As a result, they suggested classifying a distortion as weak if the ratio of each extra strain rate, e , to the main strain rate, $(\partial\bar{u}/\partial y)$, was approximately 0.01. A distortion where $e/(\partial\bar{u}/\partial y) \approx 0.1$ was considered strong. The maximum value of $e/(\partial\bar{u}/\partial y)$ present in this study was for the $\partial\bar{v}/\partial y$ strain rate; its magnitude was approximately 0.1 and the distortion created by the FPG was classified as strong.

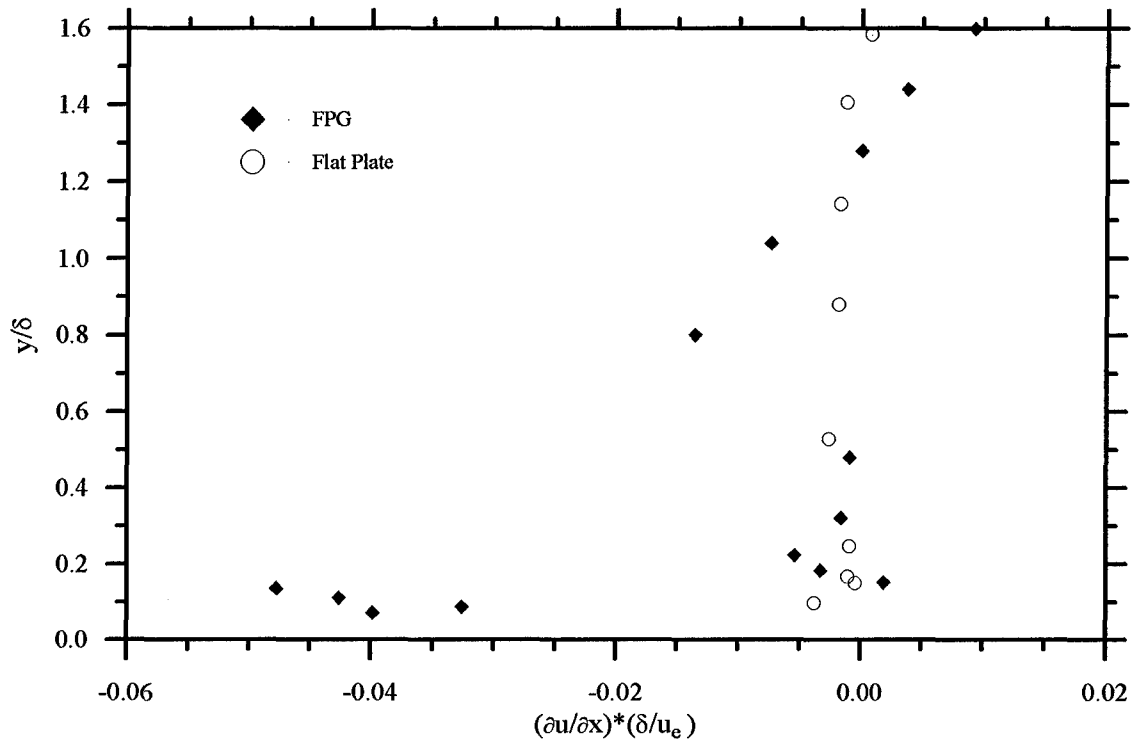


Figure 7.36: $\partial \bar{u} / \partial x$ Strain Rates Over Flat Plate and in FPG Test Section

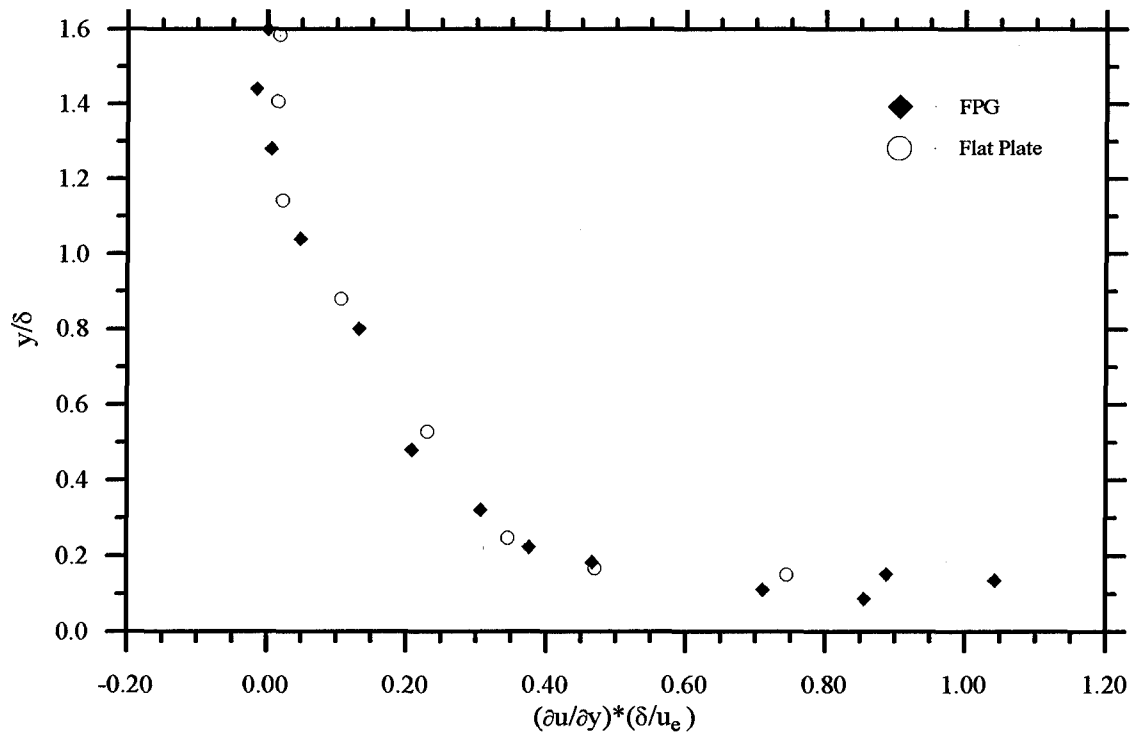


Figure 7.37: $\partial \bar{u} / \partial y$ Strain Rates Over Flat Plate and in FPG Test Section

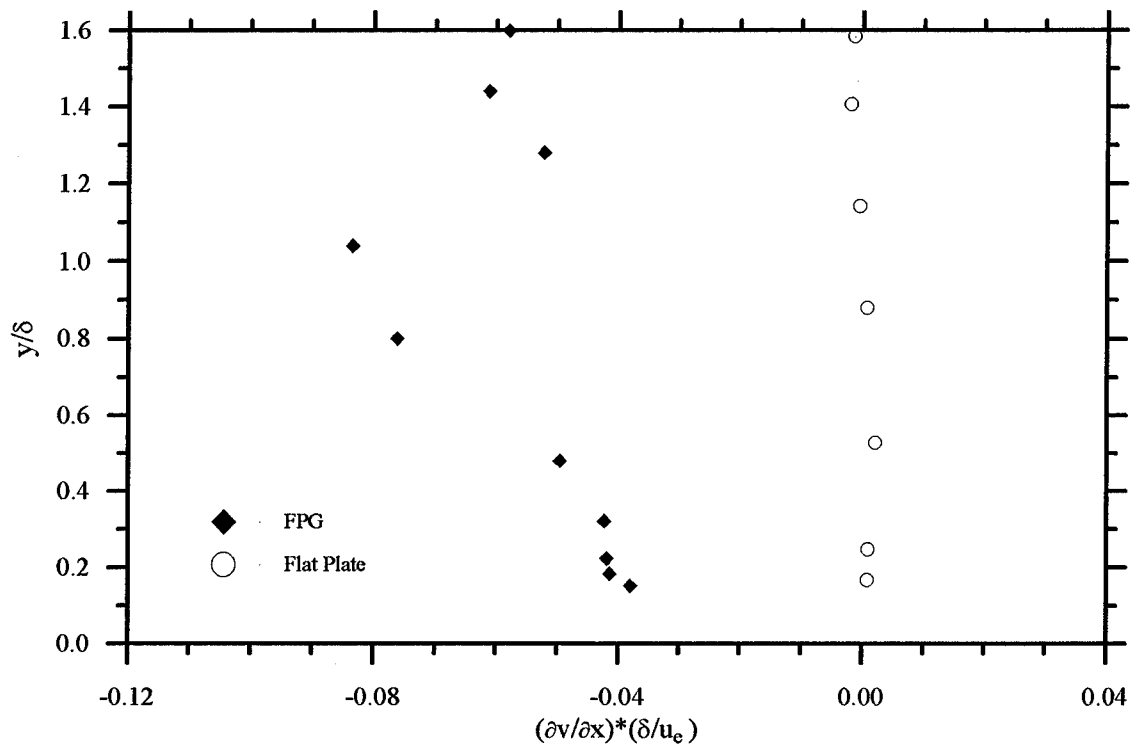


Figure 7.38: $\partial \bar{v} / \partial x$ Strain Rates Over Flat Plate and in FPG Test Section

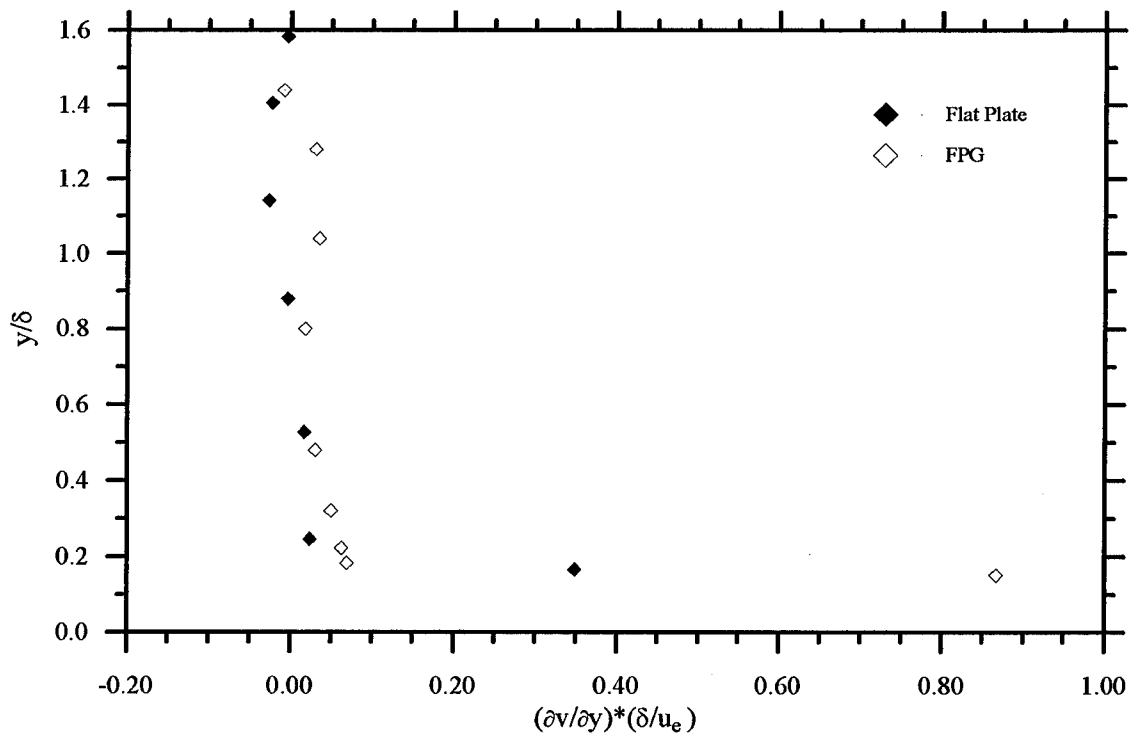


Figure 7.39: $\partial \bar{v} / \partial y$ Strain Rates Over Flat Plate and in FPG Test Section

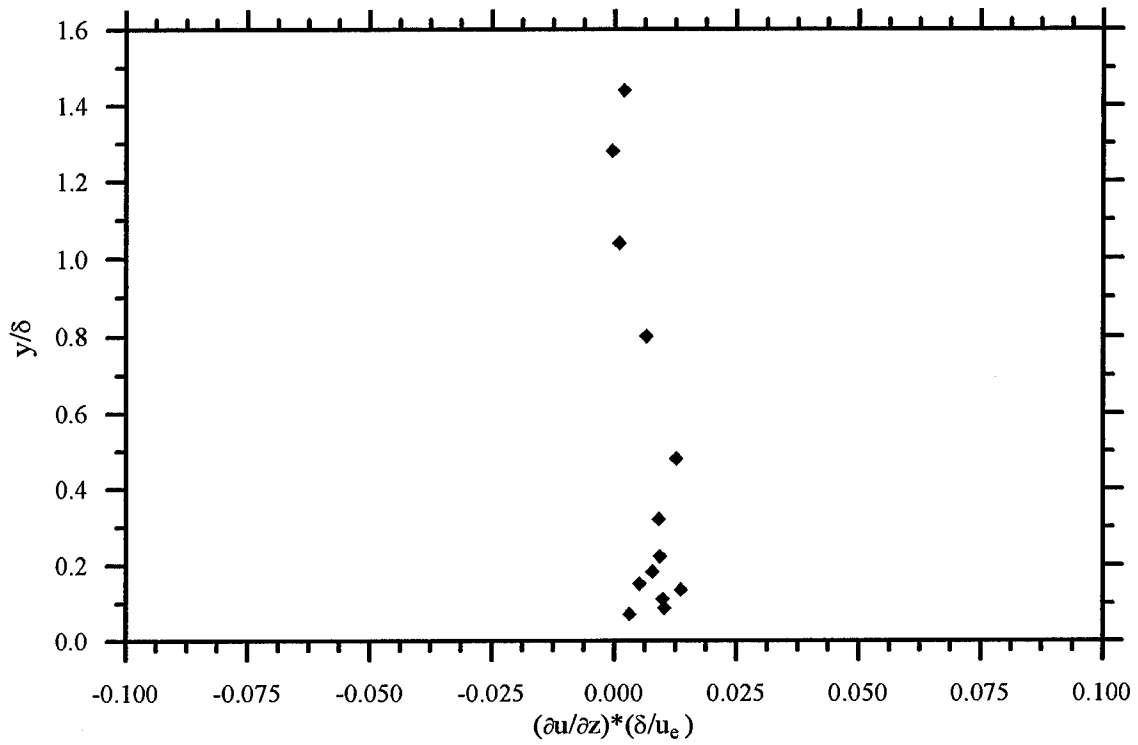


Figure 7.40: $\partial \bar{u} / \partial z$ Strain Rates in FPG Test Section

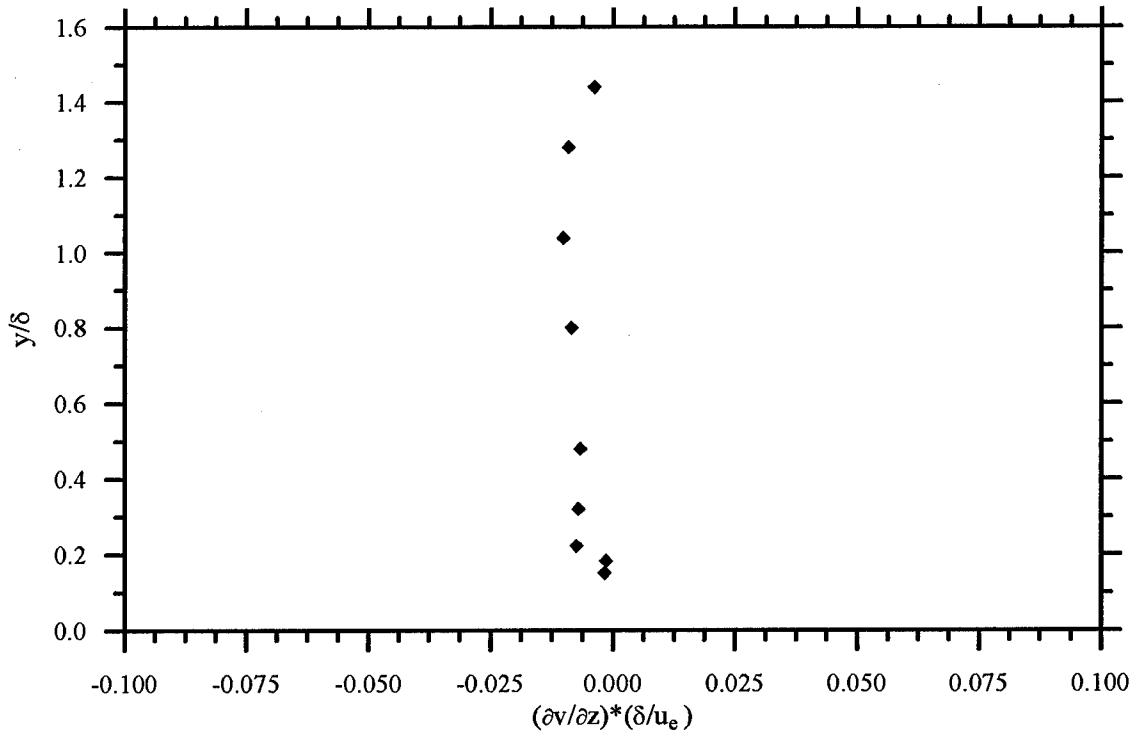


Figure 7.41: $\partial \bar{v} / \partial z$ Strain Rates in FPG Test Section

7.6 Progression of Turbulent Quantities in FPG Test Section

The data collected for use in generating the strain rates allowed a comparison of the turbulent quantities as they developed through the FPG test section. The progression of the u turbulence intensity and the incompressible Reynolds shear stresses are shown in Figures 7.42 and 7.43, respectively. In both cases the intermediate data fell in between the flat plate and FPG test section data, as was expected.

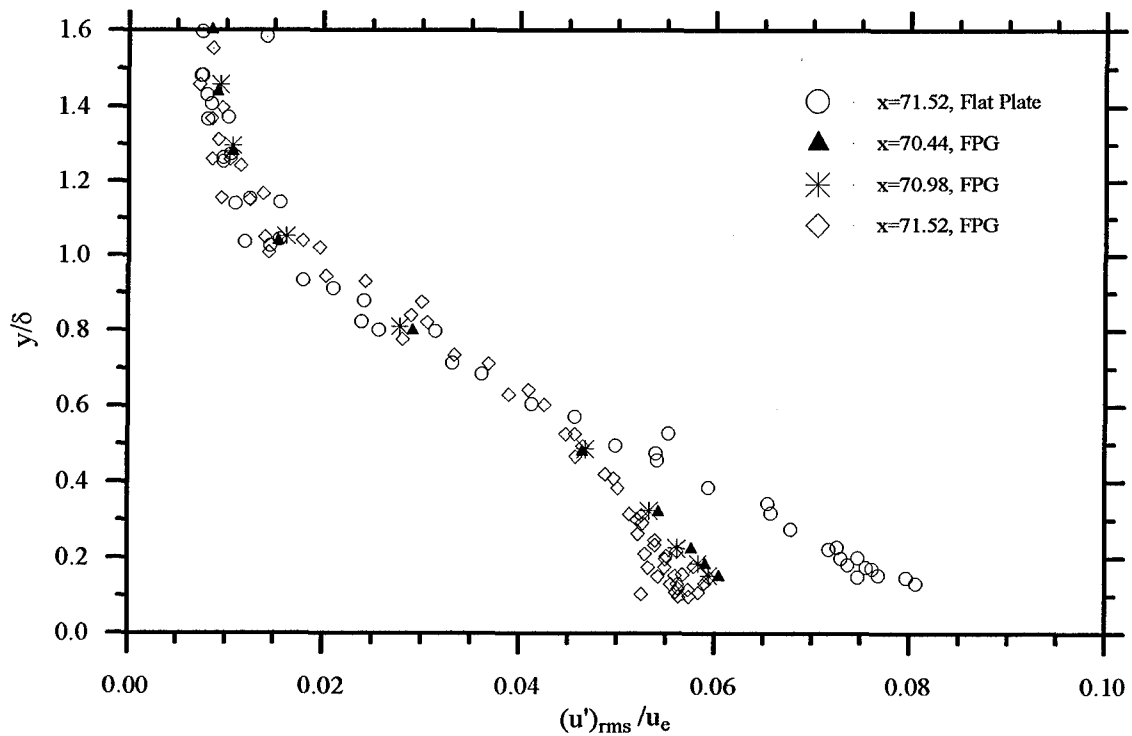


Figure 7.42: Progression of u Turbulence Intensity Through Boundary Layer

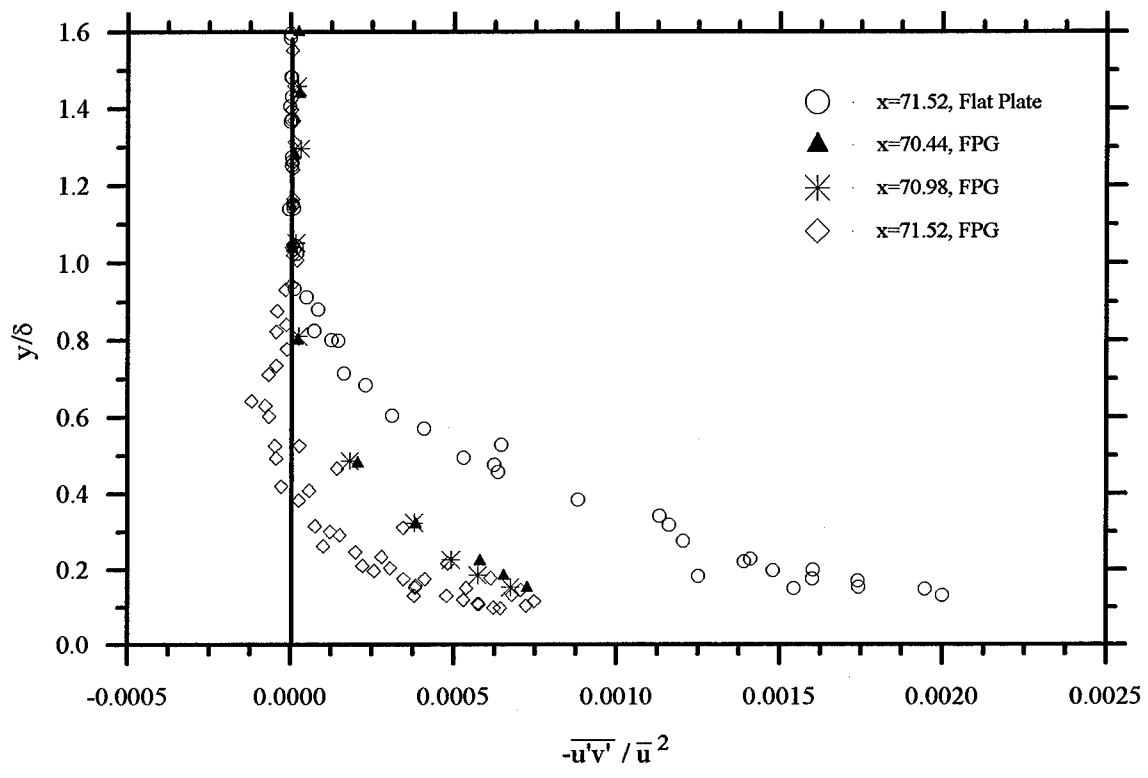


Figure 7.43: Progression of Incompressible Reynolds Shear Stress Through FPG Test Section

8. Summary, Conclusions, and Recommendations

8.1 Summary and Conclusions

The main goal of the present study was to increase the database of available turbulence information for compressible flows. Specifically, the effects of a favorable pressure gradient generated by a convex curved wall were studied in detail. The data in the FPG region showed that the FPG had a stabilizing effect on the turbulent quantities. The magnitudes of the turbulence intensities were reduced (when compared to the corresponding flat plate data) below the value $y/\delta \approx 0.5$; above this value, the turbulence intensities were unaffected by the FPG. The magnitude of the incompressible Reynolds shear stress was also reduced by the FPG; in the near-wall region the magnitude was approximately 25-30% of the flat plate value.

The FPG was also seen to affect the accuracy with which the hot-wire data could be reduced. That is, discrepancies between the hot-wire data and the LDV data in the FPG region indicated that the assumption of $p' = 0$ used in the reduction of the hot-wire measurements was not valid in the FPG test section.

In addition to studying the effects of the FPG on the turbulence, the current experiment used methods which took steps to improve on the LDV measurements of flat plate data presented in the literature. Specifically, the fringe disks in the laser Doppler measurement volume were aligned perpendicular to the mean flow direction in order to prevent the problems associated with angular bias. Comparison and analysis of raw and coincident data (see Appendix A) showed that this "angular" bias may also have been due to the choice of record interval. In any event, the procedures used in the current experiment eliminated the near-wall roll-off of the turbulent shear stresses observed by other researchers.

Finally, in order for this study to be useful as a source of turbulence information, there were a number of variables which needed to be reported for classifying the flow and allowing simple manipulation of the results. The variables which were determined as being necessary to accomplish this purpose are presented in Tables 8.1 and 8.2.

Table 8.1: Flow Field Parameters

Variable	Flat Plate	FPG
$T_{0,\infty}$ (K)	298	298
$p_{0,\infty}$ (Pa)	2.13×10^5	2.13×10^5
T_w (K)	295	295
u_e (m/s)	602	607
M_e	2.79	2.91
T_e (K)	116	110
p_e (Pa)	7870	6530
ρ_e (kg/m ³)	0.0237	0.207

Variable	Flat Plate	FPG
ρ_w (kg/m ³)	0.102	0.0626
dp_w/dx (Pa/m)	0	-2×10^4
C_f	1.63×10^{-3}	1.15×10^{-3}
τ_w (Pa)	70.0	44.0
Re_θ	8880	9160
Re_{δ_u}	1.75×10^5	1.97×10^5
Re_x	1.26×10^5	1.17×10^5

Table 8.2: Boundary-Layer Structure Parameters

Variable	Flat Plate	FPG
δ_u (mm)	9.85	11.9
δ_M (mm)	10.8	13.1
δ_i^* (mm)	0.499	0.556
β	0	-1.34
ζ/δ	0.17	0.22

Variable	Flat Plate	FPG
δ^* (mm)	1.31	3.95
θ (mm)	1.27	1.43
θ_i (mm)	0.615	0.887
$e/(d\bar{u}/dy) _{\max}$	0	0.1

8.2 Recommendations

The data gathered in the current experiment has been proven useful as a basis against which CFD turbulence-models can be evaluated (*cf.* Ref [17]); however, there are several aspects

of the experiment which could be improved in order to make the data even more valuable in the future.

The first recommendation is to obtain accurate measurements of the wall shear stress over the flat plate and in the FPG region. The wall shear stress is the determining factor in the heat transfer to the surface and the magnitude of the friction drag. The current LDV setup was limited to measurements a finite distance from the wall, making it hard, if not impossible, to determine a value for the wall shear stress. For instance, the most accurate estimation of τ_w seemed to come from the relationship given in Eq. (7.2); however, if the terms $-\overline{u\rho'v'}$, $-\overline{v\rho'u'}$, or $-\overline{\rho'u'v'}$ are not negligible, even this estimation is not very accurate. For instance, recall from Section 7.3.6 that Eq. (7.2) gave the flat plate shear stress as approximately 70 Pa, while a value of 80 Pa was required to collapse the data onto the empirical van Driest curve. Obtaining accurate measurements of the wall shear stress would not only aid in the analysis of the data in this report, but it would be useful for future research conducted in the present facilities as well.

The second recommendation is to collect 8- and 16-sample data with a more powerful laser (one capable of producing an adequate SNR in the freestream) in order to determine if the coincidence-filtering bias was really due to the angular alignment of the lasers or if it could be attributed to the size of the record interval (see Appendix A). In order to accomplish this comparison, the study should include (but would not be limited to) measurements of turbulence quantities using the settings shown in Table 8.3.

The third recommendation is to collect skewness measurements via some means which are not subject to the possible density biasing that may occur in compressible flow LDV measurements. Comparison of the skewness profiles would help confirm or deny the validity of the LDV results presented in this report and throughout the literature.

Table 8.3: Proposed Settings for Angular Bias/Record Length Study

Laser Alignment Angle	Record Length (BSA 1)	Record Length (BSA 2)	Coincidence Window Size
0°	8 Samples	8 Samples	Twice Record Interval
0°	16 Samples	16 Samples	Equal to Record Interval
0°	8 Samples	16 Samples	Twice Record Interval
0°	16 Samples	32 Samples	Equal to Record Interval
45°	8 Samples	8 Samples	Twice Record Interval
45°	16 Samples	8 Samples	Equal to Record Interval

Fourth, it is recommended that hot-wire and LDV measurements be taken over a flat plate with an imposed FPG pressure gradient with roughly the same strength as the one generated in this study. Comparison of the hot-wire and LDV data would show whether or not the assumption $p' = 0$ is valid for the flat plate, imposed pressure gradient case. If the assumption were found to hold, it would be obvious that the discrepancies between the hot-wire and LDV data collected in the current experiment were the result of the streamline curvature and not the FPG. That is, it would show that the pressure difference across the boundary layer in the FPG test section caused an increase in the magnitude of p' , even though the FPG tended to stabilize all other fluctuating quantities.

Finally, although there is no known method for doing so at this time, measurements of the fluctuating pressure p' should be achieved in order to determine the limits on the validity of the hot-wire data reduction.

A. Factors Affecting LDV Results

While collecting LDV data, several parameters (record length, seeding density, coincidence window, etc.) were found to affect the flow and were varied in order to determine their effect on the measured values of the velocity. In addition, past researchers have noted a discrepancy between the coincidence-filtered data and the raw data; if this discrepancy was present in the current experiment, the differences would have to be noted in the reported results. That is, the presented data in Chapter 7 would require a label to denote whether it was raw or coincidence-filtered. Therefore, the factors which would affect the LDV measurements (and thus the presented results) are examined below.

A.1 Variation of Testing Parameters

As mentioned above, several testing parameters were varied initially to determine their effects on the measured velocities. The three most important parameters were the record length, seeding density, and the size of the coincidence window.

A.1.1 Record Length. Recall that the record length was confined to a setting of either 8 or 16 samples. When the record length was set to 8 samples, the LDV system was unable to resolve the relatively low freestream turbulence (see Figure A.1). In addition, when the record length was set to 8 samples the second-order correlation $\overline{u'v'}$ showed enormous scatter near the wall (Figure A.2). In contrast, the 16-sample results were well-behaved in both cases. To avoid the inaccuracies present in the 8-sample measurements, the record length was set to 16 samples for the remainder of the tests. With the record length set at 16 samples, the coincidence window setting was restricted to 0.333 μ s, the length of the record interval.

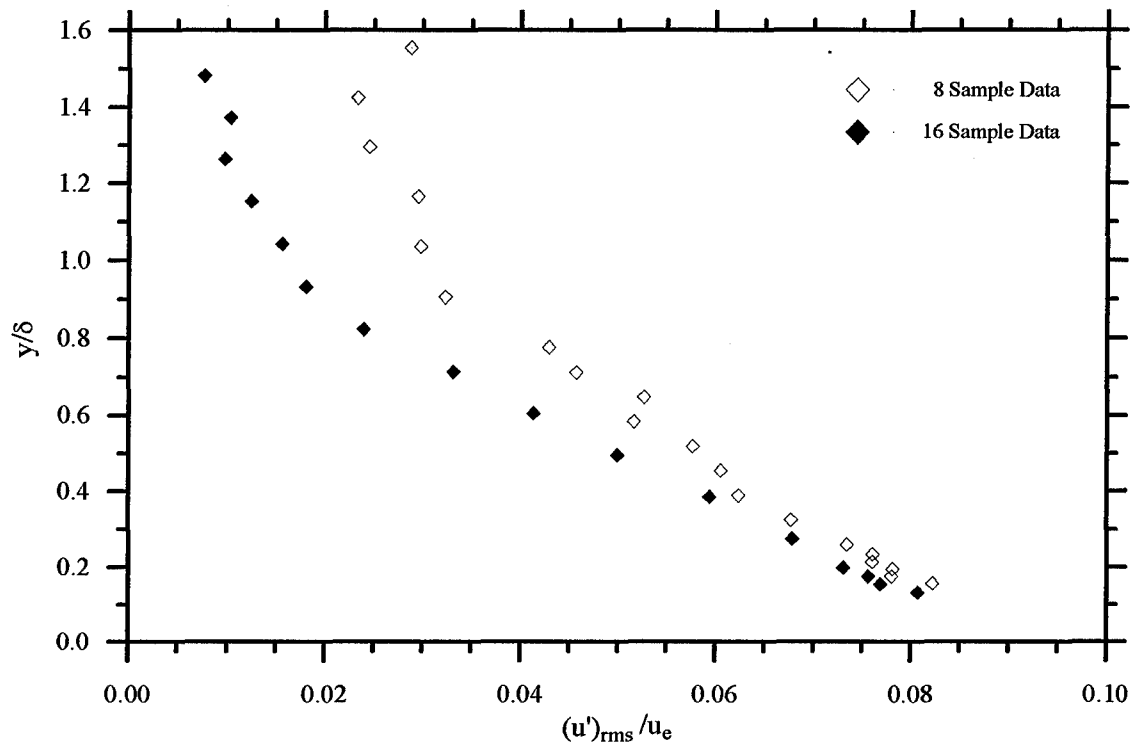


Figure A.1: 8-Sample vs. 16-Sample Turbulence Intensity Data Over a Flat Plate

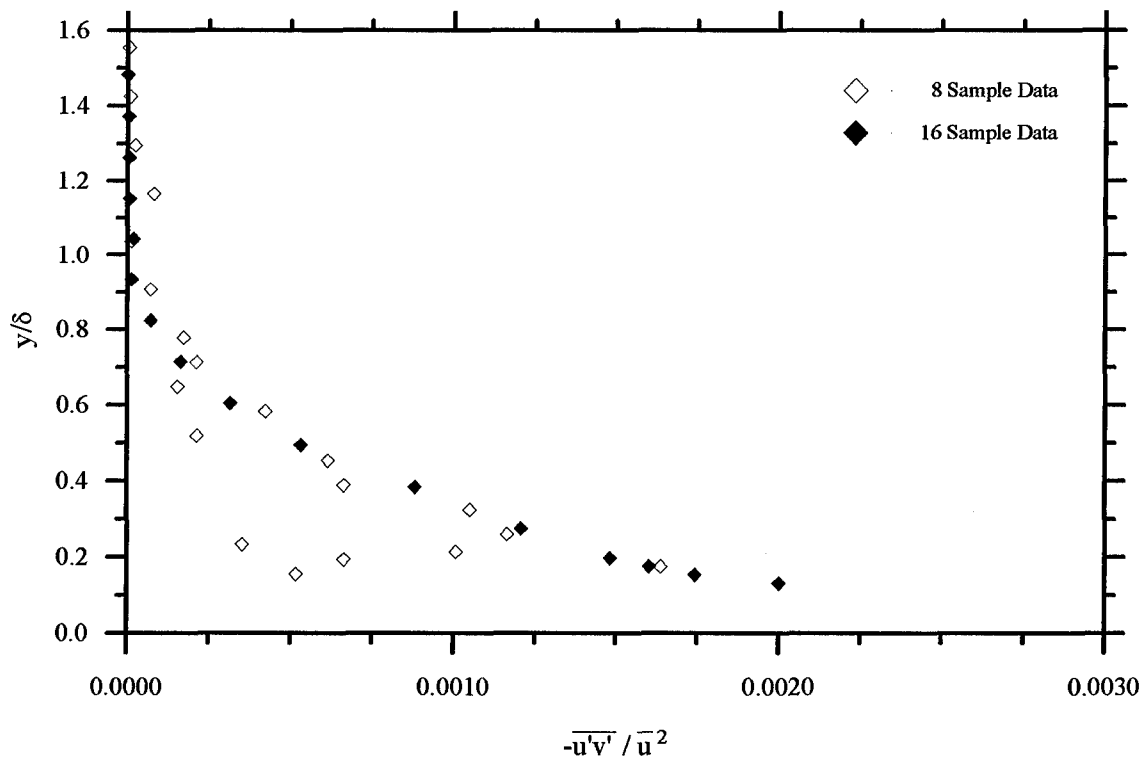


Figure A.2: 8-Sample vs. 16-Sample Second-Order Correlation Over a Flat Plate

A.1.2 Seeding Density. In accordance with the advice of Elena [15], the seeding density was set as low as possible to minimize the effects of the seed on the flow. The seeding was controlled via a pressure regulator on the atomizer; the optimum (i.e., normal) setting was found to be approximately 3×10^5 Pa with two atomizer jets opened. Lower seeding pressures ($\sim 2.6 \times 10^5$ Pa with two jets opened) were found to be acceptable in the flat plate case, but in the FPG section the seeding density decreased as the streamlines expanded. This decrease in the seed density (particularly near the wall) complicated the measurements by reducing the number of bursts collected to an unacceptable level. In order to collect a sufficient number of bursts, several tests were run at each data point near the wall and the turbulence statistics were calculated by combining the burst data from the individual tests. To avoid these complications, a seeding density suitable for use in both the flat plate and FPG test cases was chosen. Figure A.3 shows the effects of the normal and low seeding on the measurements in the FPG test section. The change in the correlation $\overline{u'v'}$ between the two cases was negligible. Since $\overline{u'v'}$ was a second-order term, it should have been the most sensitive to any changes in the flow structure; $\overline{u'v'}$ was relatively unaffected by the change in the seeding density, indicating that use of the higher setting did not bias the results.

A.1.3 Coincidence Window. In order to determine the effect the size of the coincidence window had on the coincidence-filtered data, several of the data points in the interior of the boundary layer were reprocessed with the coincidence window set to $0.033 \mu\text{s}$ and $3.33 \mu\text{s}$, providing an order-of-magnitude difference on each side of the chosen value for the coincidence window. With the record length set to 16, there was absolutely no effect on the number of coincident particles when the window was varied over this large span. Therefore, the chosen coincidence window was proven to be acceptable.

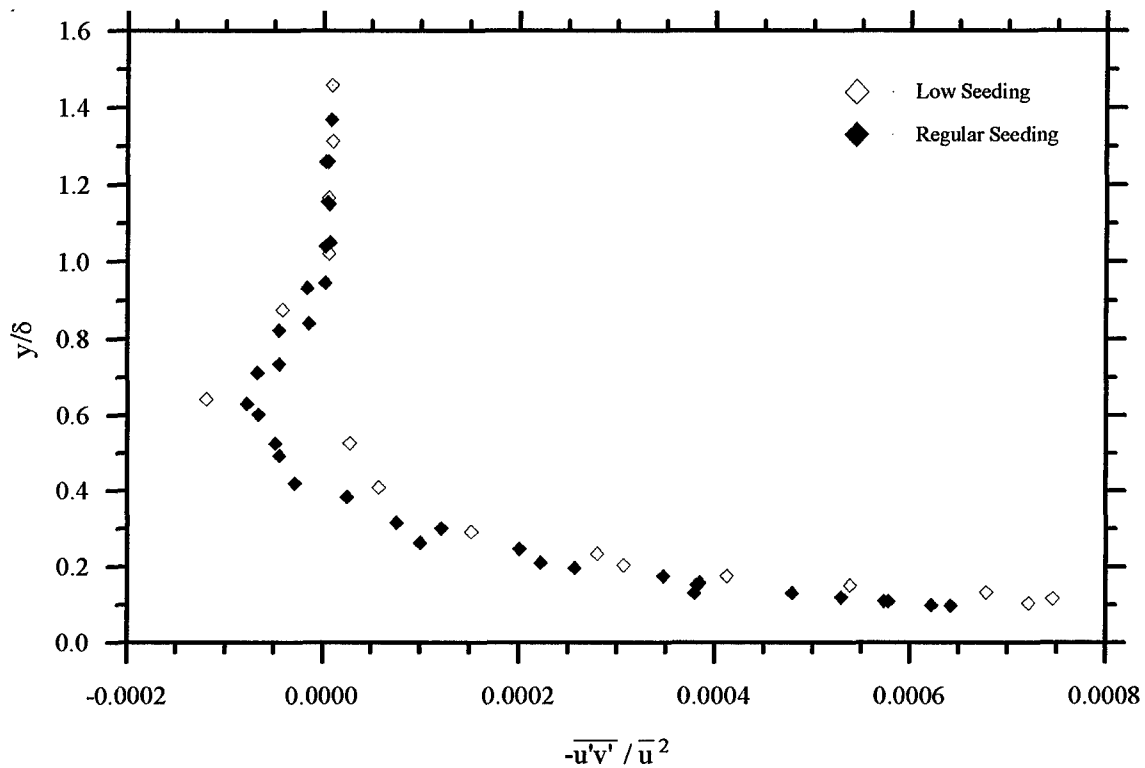


Figure A.3: Effects of Seeding Density on Second-Order Correlation in FPG Test Section

A.2 Raw vs. Coincident Data

Throughout the literature, researchers have reported decreases in the turbulence intensities and the second-order correlation when comparing coincidence-filtered data to the raw measurements. This result has been attributed, at least in part, to angular biasing. [15] A decrease in the turbulent quantities would show that the coincident data were not a uniform sample of the overall data, but were biased toward the less-turbulent particles. Figures A.4 and A.5 show the comparisons between the raw and coincident data. The agreement was excellent, showing that the coincident data were a representative sample of the overall data collected. The biasing which had been noted by previous researchers [16,19,30] was reduced or eliminated, most likely by keeping the fringe pattern perpendicular to the mean flow, thereby eliminating the problem of angular bias.

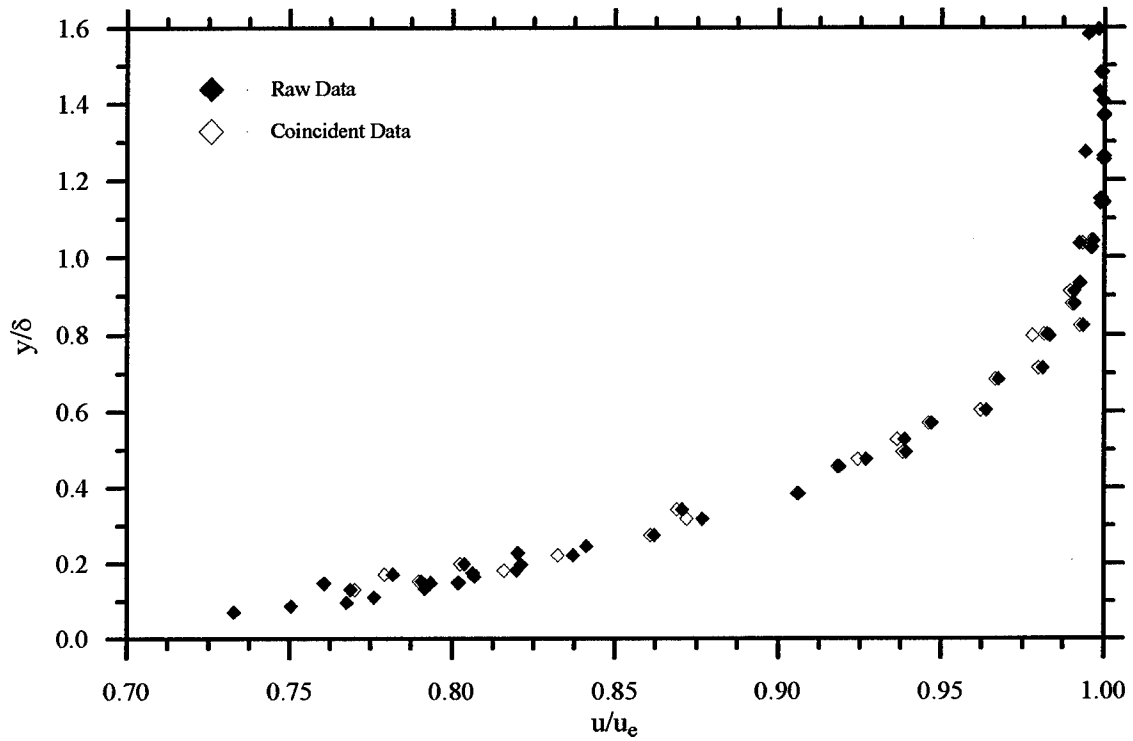


Figure A.4: Raw vs. Coincident Mean Velocity Profiles

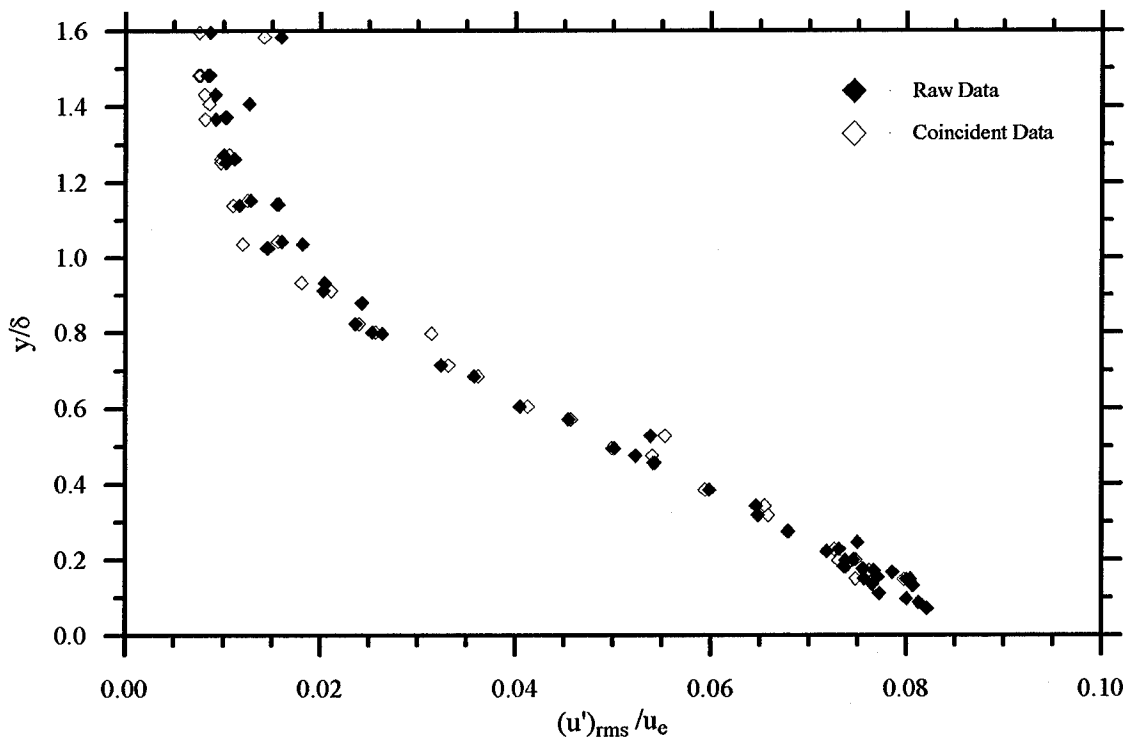


Figure A.5: Raw vs. Coincident Turbulence Intensity Profiles

The biasing towards slower particles which has been observed by other researchers could also have been attributed to the choice of record interval. In the past, the record interval has been set to approximately half the traverse time of the fastest particles (Figure A.6a). In the present experiment, with the record length set to 16 samples, the record interval was approximately equal to the traverse time of the fastest particles (Figure A.6b). The biasing caused by coincidence filtering has been observed to be highest near the wall, where the particle velocities are slower. Figures A.6c and A.6d present the burst pattern produced by particles traveling at half the speed of the fastest particles. Figure A.6c shows the case where the record interval was set to half the traverse time of the fastest particles. For the slow particle, the record interval was only 1/4 of the traverse time; there was a significant amount of time after the record interval where the burst

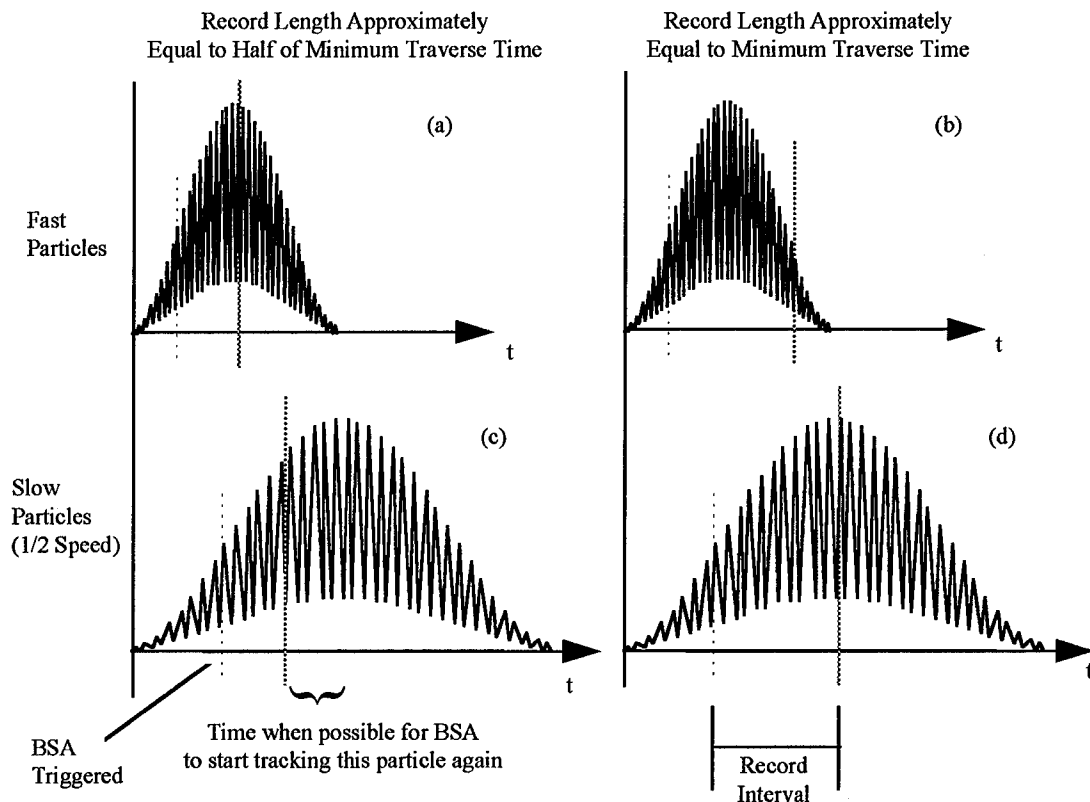


Figure A.6: Possible Biasing Due to Length of Record Interval

pattern was still increasing and the BSA could start tracking the same particle over again. The slower the particle, the higher the probability that the same particle would get counted twice. In contrast, Figure A.6d shows the case where the slow particle was tracked with the record interval set equal to the traverse time of the fastest particles (the procedure used in the current experiment). The record interval ended at approximately the same point as the peak of the burst pattern; since the burst intensity was decreasing after this point, the BSA would not begin to track the same particle again.

The time available for the BSA to start tracking the same particle over again was not only dependent on the length of the record interval, but also on the time between when the particle entered the control volume and the start of the record interval (see Figure A.6c). If this time was large, even the shortest record interval would extend past the peak of the Doppler burst, preventing the BSA from tracking the same particle more than once. The time spacing between when the particle entered the control volume and the start of the record interval was dependent on the BSA burst processing algorithm and the power of the laser beam.

Recall from Chapter 3 that the BSAs used in the current experiment would restart the record length count as the Doppler burst intensity increased past certain threshold values, ensuring the peak of the Doppler burst was used to calculate the Doppler frequency. If this method was not incorporated into the data acquisition process (as may have been the case in early LDV equipment), there would have been a higher probability that the record interval did not extend past the peak of the Doppler burst and that a single particle could have been tracked more than once. Even if the count-restarting method was used, its advantages could have been negated by using a laser which was too powerful: as the laser beam power increases, the intensity of the scattered light increases. A higher intensity of scattered light would enable easier detection of the particles traveling through the control volume; however, if the laser beam was too powerful, the scattered

light intensity may have exceeded the final BSA threshold at the first or second sampling time. This would have led to a short time between when the particle entered the control volume and the start of the record interval, increasing the possibility of tracking the same particle more than once. Advances in LDV technology allowed the current measurements to be taken with a 300 mW laser, as opposed to the more powerful lasers used in the past (the data from Ref. [16] was collected using a 9 W laser), helping to reduce the possibility of tracking the same particle more than once.

Note that, if the record interval was set such that there *was* a possibility of counting the slower particles more than once, the raw and coincident data near the wall would both be biased towards lower velocities than were actually present in the flow. As a result, one might believe that the coincident data would still follow the raw data closely, but this would not be the case. If the same particle was counted twice on each BSA, the coincidence filtering would produce not two, but *four* coincident bursts (see Figure A.7), further biasing the coincident data toward the particles with lower velocities. Note that, if the biasing were due to the angular alignment alone (as is implied in the literature), both the raw and coincident data would be biased, but on a one-to one ratio, not a four-to-one ratio. That is, the biasing would occur because the BSA fails to track a particle altogether, not because the effect of the particle is altered during the coincidence-filtering

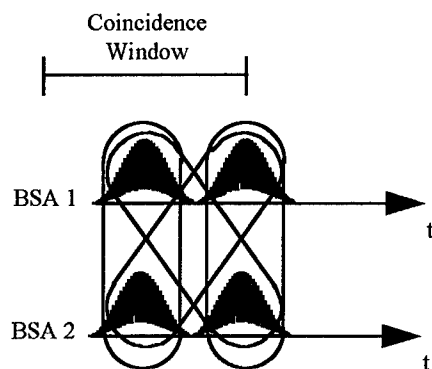


Figure A.7: Number of Coincident Bursts Produced by a Single Particle

process. If there were a problem with angular biasing, the turbulent quantities would exhibit a roll-off near the wall, but the roll-off would be present in both the raw and coincident data, resulting in a negligible difference between the two sets of data.

In order to determine if the biasing experienced by other researchers was a result of the record interval or the fringe alignment, the 8-sample data collected in the present experiment was analyzed. The coincident and raw turbulence intensity profiles were compared; if the biasing was present in the coincident data, it could be attributed to the record interval setting and not the fringe alignment, and vice-versa. Figure A.8 presents the comparison of 8-sample raw and coincident turbulence intensities. Near the wall, there was a slight decrease in the turbulence intensity due to the coincidence filtering; however, contrary to what was expected, the decrease became larger in the freestream. The decrease in the coincidence-filtered data near the outer edge of the boundary

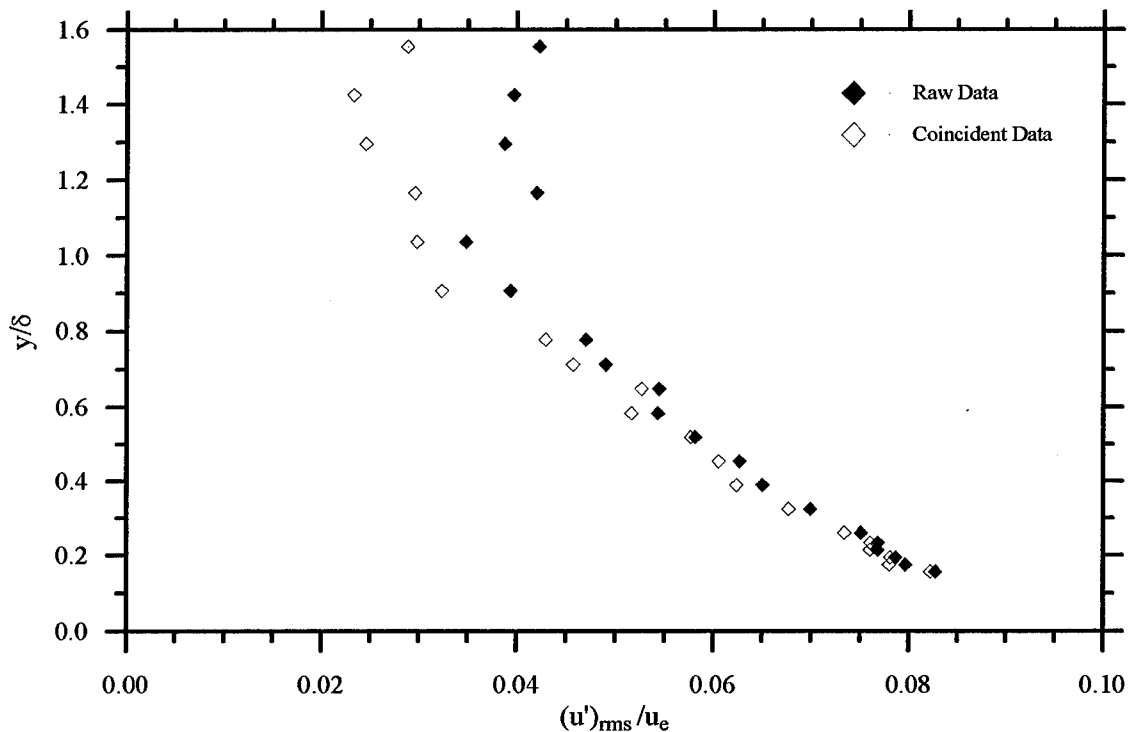


Figure A.8: 8-Sample Raw and Coincident Turbulence Intensities

layer was probably due to the angular alignment of the optics and the choice of record interval used for the v -component measurements.

Recall from Chapter 5 that the record length on BSA 2 was set the same as the record length on BSA 1. In the past, when the lasers were aligned $\pm 45^\circ$ to the flow, the two velocity components measured were of the same order of magnitude, so setting the two record lengths equal to one another was required. However, with the lasers oriented so the fringes were perpendicular to the two main velocity components, the lasers were measuring velocities of different magnitudes, so the record length should have been set accordingly for each BSA. Use of the record interval required by the u -component of velocity on both BSAs meant the v -component lasers (which were measuring a much lower velocity) had a high possibility of counting the same particle multiple times. In addition, near the wall the turbulence caused fluctuating velocities with magnitudes up to 120 m/s. In contrast, the freestream v -component was approximately 30-50 m/s with low fluctuations. Thus, *on the average*, the magnitude of the measured v -component of velocity was *lower* in the freestream. Therefore, the record interval on BSA 2 was set such that there was a high possibility of tracking the same particle more than once, and the probability increased towards the freestream. If there was a high correlation between particles with lower v velocities and lower magnitudes of u' (as seems reasonable), then the biasing present in Figure A.8 may have been due to the choice of record interval on BSA 2.

In any event, the biasing near the wall observed in Figure A.8 was larger than that observed in Figure A.5, indicating that the majority of the biasing observed in this and past experiments was probably caused by the choice of record interval and not by the angular alignment of the fringe disks in the LDV measurement volume. In order to determine absolutely if this was the case, it is recommended that a detailed study into the possibility of record length biasing be performed.

B. Error Analysis

In any experiment, there is a certain amount of error associated with the measurements. It is necessary to determine the magnitude of these errors in order to determine the validity of the experiment. If the actual measured quantities are used to compute other values, the error of the computed values needs to be determined as well.

In order to determine the error of a computed quantity, its dependence on the measured variables needs to be determined. For instance, if a function f depends on x_1 and x_2 , x_1 may have a greater effect on f than x_2 ; as a result, the error in x_1 would affect f more than the error in x_2 . This effect is quantified by differentiating f with respect to each of the dependent variables:

$$\Delta f = \left. \frac{\partial f}{\partial x_1} \right|_{f_0} \Delta x_1 + \left. \frac{\partial f}{\partial x_2} \right|_{f_0} \Delta x_2 \quad (\text{B.1})$$

where f_0 is the mean value of f around which the function is being linearized. It is often more convenient to express the error in f as a percent of the measured value f_0 ; in this case, the percent error to f is given as $\varepsilon_f \equiv \Delta f / f_0 \times 100\%$:

$$\varepsilon_f = \left. \frac{\partial f}{\partial x_1} \right|_{f_0} \frac{x_{1_0}}{f_0} \varepsilon_{x_1} + \left. \frac{\partial f}{\partial x_2} \right|_{f_0} \frac{x_{2_0}}{f_0} \varepsilon_{x_2} \quad (\text{B.2})$$

In order to simplify notation, note that the symbol Δf will be used to denote absolute error in the quantity f , while ε_f will be used to denote the percent error in f .

Equations (B.1) and (B.2) give the maximum possible error to f ; however, if the errors in x_1 and x_2 are independent, it may be reasonable to expect that they will not both be at their peak values at the same time. In this case, the error to f may be given by a Euclidean norm:

$$\varepsilon_f = \left[\left(\frac{\partial f}{\partial x_1} \bigg|_{f_0} \frac{x_{1_0}}{f_0} \varepsilon_{x_1} \right)^2 + \left(\frac{\partial f}{\partial x_2} \bigg|_{f_0} \frac{x_{2_0}}{f_0} \varepsilon_{x_2} \right)^2 \right]^{\frac{1}{2}} \quad (\text{B.3})$$

Unless stated otherwise, error calculations performed here will use the formulation given in Eq. (B.3).

In the following analysis, the first four sections examine the error associated with the actual measurements (velocity, stagnation pressure, and stagnation temperature); once these values have been determined, the error associated with calculated quantities is evaluated.

B.1 Traverse Location Error

Even though the traverse system was rated as being accurate to $\pm 0.13 \mu\text{m}/\text{mm}$ (see Chapter 4), the location error was greatly increased due to an apparent glitch in the LDV software. After the lasers had been aligned at the origin location, the traverse was moved to the first data acquisition location. The error in this location was $\approx 0.15 \mu\text{m}$. However, after the data were collected and processed, when the software returned to the traverse-control window the location of the traverse was not always read correctly. For example, if data were collected at the location $y = 0.63 \text{ mm}$, upon returning to the traverse-control window the software might have read the location as $y = 0.62 \text{ mm}$. If the error occurred (it did not occur every time), the expected location was decreased by 0.01 mm . Therefore, assuming the traverse across the boundary layer started at the wall, the location error increased as the distance from the wall increased. The data were collected along a line normal to the wall, so there were two non-zero traverse coordinates which had the possibility of being affected by this error; however, the truncation error was not observed to affect more than one of the two coordinates at a time. Thus, the location error associated with the I^{th} data collection point away from the wall, Δy_I , was

$$\Delta y_I = \Delta y_0 + 0.01(I - 1) \quad (\text{B.4})$$

where Δy_0 was the error associated with placement of the origin and units were in mm. The error associated with the origin placement and the error in the probe angle alignment are discussed in the next section.

B.2 Origin Placement and Probe Angle Alignment Error

The procedure used for aligning the lasers with the test section wall was described in Chapter 5. This procedure at first appeared to be very accurate, but as this section will point out, the angular uncertainty associated with the measurements turned out to be rather large.

The dots produced by the lasers on the wall of the tunnel were measured and found to have a diameter of 0.60 mm. The distance between the dots was measured as 1.98 mm. When setting the angle of the lasers, it was assumed that the dots were placed along the edge of the wall within 1/4 radius of the center. Figure B.1 shows a graphical representation of the maximum error possible under these assumptions.

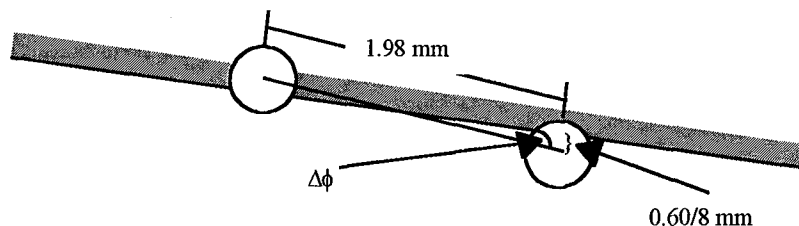


Figure B.1: Probe Angle Alignment Error

With this accuracy, the angular error, $\Delta\phi$, was given by

$$\Delta\phi = \tan^{-1}\left(\frac{0.60/8}{1.98/2}\right) = 4.289^\circ = 0.0749 \text{ rads.} \quad (\text{B.5})$$

Assuming the dots produced by the lasers could be aligned within 1/4 radius of the center also gave an estimate for the possible displacement of the origin:

$$\Delta y_0 = \frac{0.60}{8} \text{ mm} = 0.074 \text{ mm} \quad (\text{B.6})$$

B.3 Velocity Measurement Error

There were two main sources of error associated with the velocity measurements: biasing error and random error. Biasing error could occur from poor calibration of the optics and misalignment of the lasers in the z -direction. Random errors which might have influenced the velocity measurements included the processing performed by the BSA's, fluctuations in the wind tunnel conditions, traverse positioning, and laser angle alignment.

In the following analysis, the symbol u was used to represent any of the velocity-related terms (\bar{u} , u' , \bar{v} , v'); when there was a discrepancy between the formulations for the individual components it was noted accordingly.

B.3.1 Biasing Errors. The first type of possible biasing error resulted from imperfections in the optics: slight changes in the laser intersection angle due to possible defects in the optical glass, changes in the interference pattern due to the fact that the lasers were not going through the optical glass normal to the surface (the 3.5° offset relative to the z -coordinate direction caused each beam to be offset at a slightly different angle), etc. Imperfections such as these would cause a shift in the calibration factor, C_{fv} , used to convert the Doppler frequencies into velocities. However, if the measured velocities were scaled by other measured velocities (i.e., u/u_e , u'_{rms}/u , etc.), the error in the calibration factor would be scaled out. In the cases where the measured velocities were not scaled by other measured velocities ($-\overline{\rho u'v'}/\tau_w$, etc.) it was assumed that this bias was negligible compared to other sources of error.

The second source of biasing error was due to the fact that the lasers were aligned at a 3.5° angle to the mean flow. This alignment caused the lasers to consistently measure the u -velocity

component as being lower than the actual value. The actual value of u , u_a , was given by $u_a = u / \cos(3.5^\circ) = 1.002u$. Therefore, the biasing error due to the laser alignment was approximately 0.2% and was ignored when compared to the other sources of error.

B.3.2 Random Errors. As mentioned above, there were four main possibilities for sources of random error in the velocity measurements: error associated in the processing capabilities of the BSA's, error associated with random fluctuations in the wind tunnel conditions, traverse location errors, and errors from the streamwise angular alignment of the lasers.

B.3.2.1 Error from BSA Calculations. The error incurred from the BSA's calculation of the velocity was due to the limitations on the curve fit used to set up the FFT which was used to calculate the Doppler frequency, f_D . In general, the frequency resolution of the BSAs (i.e., the accuracy of the FFT) was given by [10]

$$\Delta f_D = \frac{n(BW)}{2^8 N} \quad (B.7)$$

For the current experiment, different bandwidth settings were used on each BSA as given in Table 5.1. For the bandwidth chosen on BSA 1, $n = 1.2$; for BSA 2 $n = 1.5$. With these values, the selected bandwidths, and a record length of 16, the errors in the u and v components of velocity were

$$\begin{aligned} \Delta u_{BSA} &= 0.095 \text{ m/s} \\ \Delta v_{BSA} &= 0.090 \text{ m/s} \end{aligned} \quad (B.8)$$

B.3.2.2 Repeatability. The random errors associated with the wind tunnel conditions were determined from the repeatability test results (see Appendix C). The twenty test runs gave these errors as $\varepsilon_{\bar{u}_{rep}} \approx 0.19\%$, $\varepsilon_{\bar{v}_{rep}} \approx 0.04\%$, $\varepsilon_{u'_{rep}} \approx 0.07\%$, $\varepsilon_{v'_{rep}} \approx 0.03\%$ and $\varepsilon_{\overline{u'v'_{rep}}} \approx 0.02\%$, where $\varepsilon_{\bar{v}_{rep}}$ and $\varepsilon_{v'_{rep}}$ were defined as $\varepsilon_{\bar{v}_{rep}} \equiv \Delta \bar{v}_{rep} / \bar{u}$ and $\varepsilon_{v'_{rep}} \equiv \Delta v'_{rep} / \bar{u}$.

B.3.2.3 Traverse Location Error. The error to the velocity measurements due to the traverse location error depended on the position of the control volume within the boundary layer. In regions where the velocity gradients were high, a small change in the traverse location caused a large change in the measured velocity. For two-dimensional boundary layer flow, the error in the velocity depended primarily on the velocity gradient normal to the wall:

$$\Delta \bar{u}_{i,I} = \left. \frac{\partial \bar{u}}{\partial y} \right|_I \Delta y_I, \quad \Delta u'_{i,I} = \left. \frac{\partial u'}{\partial y} \right|_I \Delta y_I \quad (\text{B.9})$$

where the subscript I once again denoted the I^{th} data collection point away from the wall. It should be noted that, as I increased, the traverse error increased while the velocity gradient decreased, helping to minimize the error.

B.3.2.4 Streamwise Angular Alignment Error. The final source of error in the velocity measurements was due to the angular alignment of the lasers. Assuming the lasers could be misaligned by the angle $\Delta\phi$, the relationship between the actual value of u , u_a , and the measured value of u is shown in Figure B.2 below.

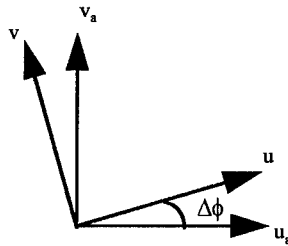


Figure B.2: Velocity Error Due to Angular Misalignment

Examination of Figure B.2 showed the relationship between the measured and actual velocity components was given by

$$\begin{aligned} u_a &= u \cos(\Delta\phi) - v \sin(\Delta\phi) \\ v_a &= u \sin(\Delta\phi) + v \cos(\Delta\phi) \end{aligned} \quad (\text{B.10})$$

Using Taylor expansions for the trigonometric terms, the associated errors were given as

$$\begin{aligned}\Delta u_\phi &= u_a - u = -u(\Delta\phi)^2 - v(\Delta\phi) \\ \Delta v_\phi &= v_a - v = u(\Delta\phi) - v(\Delta\phi)^2\end{aligned}\tag{B.11}$$

where $\Delta\phi$ was in radians. Normalizing these equations by u , the percent changes were found to be

$$\begin{aligned}\varepsilon_{u_\phi} &= \left| \Delta u_\phi / u \right| = (\Delta\phi)^2 + (v/u)(\Delta\phi) \\ \varepsilon_{v_\phi} &= \left| \Delta v_\phi / u \right| = (\Delta\phi) + (v/u)(\Delta\phi)^2 \approx \Delta\phi\end{aligned}\tag{B.12}$$

Note that the last term in ε_{v_ϕ} could be ignored because it was third-order ($v/u \ll 1.0$).

The total error in the velocity was then given by the Euclidian norm of the independent error terms:

$$\varepsilon_{u_i} = \sqrt{\varepsilon_{u_{BSA,i}}^2 + \varepsilon_{u_{rep}}^2 + \varepsilon_{u_{i,i}}^2 + \varepsilon_{u_{\phi,i}}^2}\tag{B.13}$$

The error in the velocity components was calculated at each point across the boundary layer and was found to be maximum near the wall due to the large velocity gradients. In order to simplify the remaining error calculations, the error in the velocity was taken to be constant across the boundary layer, equal to the maximum error possible. In this case,

$$\begin{aligned}\varepsilon_{\bar{u}} &= \frac{\Delta\bar{u}}{\bar{u}} = 8.8\%, & \varepsilon_{\bar{v}} &= \frac{\Delta\bar{v}}{\bar{u}} = 8.5\% \\ \varepsilon_{u'} &= \frac{\Delta u'}{\bar{u}} = 1.7\%, & \varepsilon_{v'} &= \frac{\Delta v'}{\bar{u}} = 7.9\%\end{aligned}\tag{B.14}$$

With the error in the measured velocities known, the error in the total velocity could be computed from Eq. (6.3) and was given by

$$\varepsilon_{\bar{Q}} = \frac{\bar{u}^2}{\bar{Q}^2} \left[(\varepsilon_{\bar{u}})^2 + \left(\frac{\bar{v}}{\bar{u}} \varepsilon_{\bar{v}} \right)^2 + \left(\frac{v'}{\bar{u}} \varepsilon_{v'} \right)^2 \right]^{\frac{1}{2}} \approx \varepsilon_{\bar{u}} = 8.8\%\tag{B.15}$$

The error in the second-order velocity correlation, $\overline{u'v'}$, was

$$\varepsilon_{u'v'} = \sqrt{(\varepsilon_u)^2 + (\varepsilon_v)^2} = 8.1\% \quad (\text{B.16})$$

Finally, note that the slope of the u -velocity profile went to zero at the freestream; this led to a reduction in the error associated with the edge velocity. The error was only dependent on the BSA's processing capabilities, the repeatability and the angular alignment:

$$\varepsilon_{u_e} = \sqrt{\varepsilon_{u_e,BSA}^2 + \varepsilon_{u_e,rep}^2 + \varepsilon_{u_e,\phi}^2} = 1.3\% \quad (\text{B.17})$$

Assuming the v -component of velocity was measured just as accurately in the freestream (v did not go to zero, but the slope was reduced and the error should have been less than that given by Eq. (B.15)), the error in the total velocity at the edge was

$$\varepsilon_{\bar{Q}_e} = 1.5\% \quad (\text{B.18})$$

B.4 Total Pressure and Temperature

Stagnation values of the pressure and temperature were also measured. The error in the stagnation pressure was estimated at 1380 Pa out of approximately 2.13×10^5 Pa, or

$$\varepsilon_{p_0} = \frac{\Delta p_{0,\infty}}{p_0} \approx \frac{1380}{2.13 \times 10^5} = 0.6\% \quad (\text{B.19})$$

There were two source of error in the total temperature: the error in the measurement of the total temperature and the assumption that the total temperature was constant across the boundary layer. Recall from Eq. (6.25) that the assumption of constant total temperature could lead to an error of up to 4%. The actual temperature measurement was estimated to have an accuracy of ± 0.2 K; with total temperatures of at least 292 K, this gave an error of $\varepsilon_{T_{0,\infty}} = 0.1\%$.

Combining these two sources of error gave the maximum error in the total temperature as

$$\varepsilon_{T_0} = \frac{\Delta T_0}{T_{0,\infty}} = 4.0\% \quad (\text{B.20})$$

B.5 Mach Number, Temperature, Pressure, and Density Error

The error in the Mach number was

$$\varepsilon_{\bar{M}_e} = \left[\left(\varepsilon_{\bar{Q}} \right)^2 + \left(\frac{1}{2} \varepsilon_{T_0} \right)^2 \right]^{\frac{1}{2}} = 9.0\% \quad (\text{B.21})$$

and the error in the edge Mach number, M_e , was

$$\varepsilon_{\bar{M}_e} = \left[\left(\varepsilon_{\bar{Q}_e} \right)^2 + \left(\frac{1}{2} \varepsilon_{T_{0,\infty}} \right)^2 \right]^{\frac{1}{2}} = 15\% \quad (\text{B.22})$$

Using the error in M_e , the error in the edge temperature and pressure were given by

$$\varepsilon_{T_e} = \left\{ \left(\varepsilon_{T_{0,\infty}} \right)^2 + \left[(\gamma - 1) \left[1 + \frac{\gamma - 1}{2} M_e^2 \right]^{-1} M_e^2 \varepsilon_{M_e} \right]^2 \right\}^{\frac{1}{2}} = 1.8\% \quad (\text{B.23})$$

$$\varepsilon_{p_e} = \left\{ \left(\varepsilon_{p_0} \right)^2 + \left[\gamma \left[1 + \frac{\gamma - 1}{2} M_e^2 \right]^{-1} M_e^2 \varepsilon_{M_e} \right]^2 \right\}^{\frac{1}{2}} = 6.4\% \quad (\text{B.24})$$

and the error in the edge density was

$$\varepsilon_{\rho_e} = \sqrt{\varepsilon_{p_e}^2 + \varepsilon_{T_e}^2} = 6.6\% \quad (\text{B.25})$$

The errors in the wall pressure and temperature were from direct measurements and were thus similar to the error in the stagnation measurements: $\varepsilon_{p_w} = 0.6\%$ and $\varepsilon_{T_w} = 0.1\%$. Using these results, the error in the wall density was found to be

$$\varepsilon_{\rho_w} = \sqrt{\varepsilon_{p_w}^2 + \varepsilon_{T_w}^2} = 0.6\% \quad (\text{B.26})$$

and the error in the wall viscosity (which was calculated using Sutherland's formula) was

$$\varepsilon_{\mu_w} = \frac{(3/2)(T_w + 110.4) - T_w}{(T_w + 110.4)} \varepsilon_{T_w} = 0.1\% \quad (\text{B.27})$$

If the density and temperature were calculated using the Crocco-Busemann integral relation, the error was dependent on the validity of the assumptions used in the derivation of the relationship. However, the relation has been found to be very accurate when the assumptions hold [6], and the error was assumed to be less than the error produced in the FPG temperature and density calculations. In order to simplify the analysis of any variables which follow, the errors in the temperature and density were taken as those incorporated from the assumption of a linear pressure distribution through the FPG boundary layer.

When the temperature and density were calculated assuming a linear pressure distribution through the boundary layer, the comparison of the computed density to CFD and experimental results in Figures 7.8 and 7.24 showed that the assumptions used in their calculation were fairly accurate, and the error in pressure across the boundary layer could be estimated as $\varepsilon_p \approx \varepsilon_{p_e} = 6.6\%$. The error in the temperature was then given by

$$\varepsilon_T = \left\{ \left(\varepsilon_{T_0} \right)^2 + \left[(\gamma - 1) \left[1 + \frac{\gamma - 1}{2} M^2 \right]^{-1} M^2 \varepsilon_M \right]^2 \right\}^{\frac{1}{2}} \leq 11.7\% \quad (\text{B.28})$$

and the error in density was

$$\varepsilon_\rho = \sqrt{\varepsilon_p^2 + \varepsilon_T^2} = 13.4\% \quad (\text{B.29})$$

B.6 Boundary Layer Thickness Error

The error in the boundary layer thickness was determined graphically. The process used to generate $\Delta\delta$ is shown in Figure B.3. The velocity or Mach number profile (scaled by the edge value) was plotted versus the location off the wall; error bars were included to give the possible values of the velocity or Mach number. The line drawn on the right side of the graph indicated the position of $0.995u_e$, the value used to determine the edge condition. The two horizontal lines gave

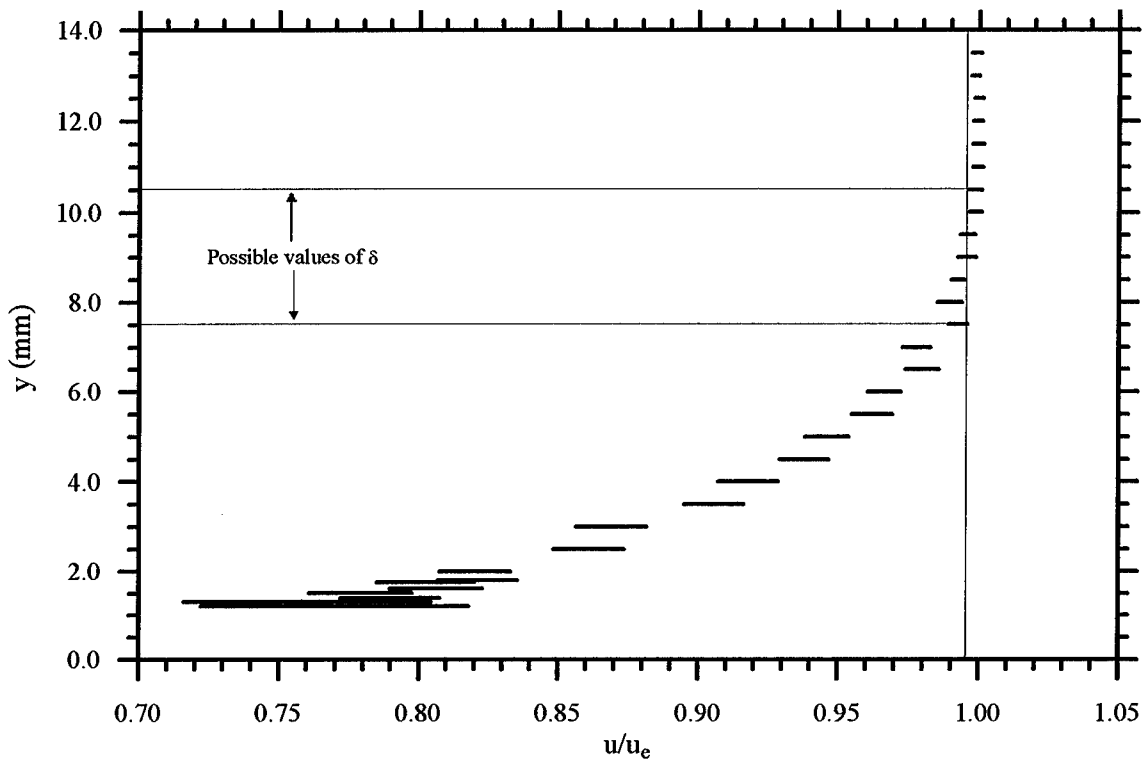


Figure B.3: Graphical Derivation of $\Delta\delta$

the position of the minimum and maximum value at which the non-dimensional velocity profile could reach 0.995; the value of δ fell somewhere between these two lines. It is obvious from Figure B.3 that the error in δ was relatively large; the percent errors were estimated as $\varepsilon_{\delta} = 28\%$ for both the velocity and Mach number boundary-layer thicknesses.

B.7 Wall Shear Stress Error

The error in the wall shear stress due to van Driest's relationship has been documented as $\varepsilon_{\tau_w} \approx 10\%$ [9]; however, this was the error when the assumptions used to generate the wall shear stress are assumed valid. The analysis in Chapter 7 showed that the wall shear stress was not predicted well by van Driest's relationship due to inaccuracies in the assumptions used to derive the relationship. As a result, the error in the wall shear stress was estimated by comparing the

computed value to the value which would shift the data points in Figure 7.16 on top of the empirical correlation. The calculated value was 70 Pa and the value needed to shift the data was approximately 75 Pa, an error of 7.1%.

B.8 Van Driest Velocity Error

The error in the van Driest velocities was due to the error in the effective velocity and the error in the scaling parameter u^* , which were found to be

$$\varepsilon_{u_{eff}} = \sqrt{(0.5\varepsilon_\rho)^2 + (0.5\varepsilon_{\rho_w})^2 + (2\varepsilon_u)^2} = 18.9\% \quad (\text{B.30})$$

$$\varepsilon_{u^*} = \sqrt{(0.5\varepsilon_{\tau_w})^2 + (0.5\varepsilon_{\rho_w})^2} = 3.5\% \quad (\text{B.31})$$

respectively. Thus, the error in the van Driest velocity was

$$\varepsilon_{u_{eff}/u^*} = \sqrt{(\varepsilon_{u_{eff}})^2 + (\varepsilon_{u^*})^2} = 19.2\% \quad (\text{B.32})$$

B.9 Turbulence Statistics Error

The error to the second-order velocity correlation $\overline{u'v'}$ was given by

$$\varepsilon_{\overline{u'v'}} = \sqrt{(\varepsilon_u)^2 + (\varepsilon_v)^2} = 8.1\% \quad (\text{B.33})$$

Using the variable x to denote either the u or v component of velocity, the error in the root-mean square was given by

$$\Delta\sigma_x = \frac{1}{2} \left[\frac{\sum(x')^2}{n} \right]^{-\frac{1}{2}} \left[2 \frac{\sum x' \Delta x'}{n} \right] \quad (\text{B.34})$$

which led to

$$\varepsilon_{\sigma_x} = \left[\frac{\sum(x')^2}{n} \right]^{-\frac{1}{2}} \left[\frac{\sum(x')^2}{n} \right] \varepsilon_{x'} = \varepsilon_{x'} \quad (\text{B.35})$$

With this formulation, the error in the RMS values of the u and v components of velocity were given by

$$\varepsilon_{\sigma_u} = \varepsilon_{u'} = 1.7\%, \quad \varepsilon_{\sigma_v} = 7.9\% \quad (\text{B.36})$$

Using a similar derivation, the error in the skewness and flatness were found to be

$$\begin{aligned} \varepsilon_{Sk_x} &= \sqrt{(3\varepsilon_{\sigma_x})^2 + (3\varepsilon_{x'})^2} = \sqrt{18}\varepsilon_{x'} \\ \varepsilon_{Fl_x} &= \sqrt{(4\varepsilon_{\sigma_x})^2 + (4\varepsilon_{x'})^2} = \sqrt{32}\varepsilon_{x'} \end{aligned} \quad (\text{B.37})$$

resulting in

$$\begin{aligned} \varepsilon_{Sk_u} &= 7.2\% & \varepsilon_{Sk_v} &= 33.5\% \\ \varepsilon_{Fl_u} &= 9.6\% & \varepsilon_{Fl_v} &= 44.7\% \end{aligned} \quad (\text{B.38})$$

The error in the intermittency function was the same as the error to the flatness,

$$\varepsilon_{\gamma_u} = \varepsilon_{Fl_u} = 9.6\% \quad (\text{B.39})$$

and the error in the correlation coefficient was given as

$$\varepsilon_{R_{uv}} = \sqrt{(\varepsilon_{\sigma_u})^2 + (\varepsilon_{\sigma_v})^2 + (\varepsilon_{u'v'})^2} = 11.4\% \quad (\text{B.40})$$

B.10 Strain Rate Error

The error in the strain rate was dependent on the method of calculation: for the second-order central differences, the error in the derivative of a general variable u with respect to y (or z) was

$$\varepsilon_{\partial u / \partial y} = \sqrt{(2\varepsilon_u)^2 + (2\varepsilon_y)^2} \quad (\text{B.41})$$

The percent error in the position was dependent on whether the y - or z -derivative was being examined. The error in the z position was essentially negligible, while the error in the y -direction increased across the boundary layer as given in Eq. (B.4). The maximum error in the y position

was at the outer edge of the boundary layer, where $y \approx 10$ mm, leading to $\varepsilon_y \approx 1\%$. Thus, the errors in the central-difference strain rates were

$$\begin{aligned}\varepsilon_{\partial u/\partial y} &= 17.7\% & \varepsilon_{\partial u/\partial z} &= 12.4\% \\ \varepsilon_{\partial v/\partial y} &= 17.1\% & \varepsilon_{\partial v/\partial z} &= 12.0\%\end{aligned}$$

The error in the x -direction derivatives were computed from Eq. (6.54) assuming the position error in the x direction was negligible. Thus,

$$\begin{aligned}\varepsilon_{\partial u/\partial x} &= \sqrt{3}\varepsilon_u = 15.2\% \\ \varepsilon_{\partial v/\partial x} &= \sqrt{3}\varepsilon_v = 14.7\%\end{aligned}$$

B.11 Error Summary

The errors calculated above are summarized below in Table B.1. For the sake of brevity, the error associated with each figure in Chapter 7 has not been presented; it should suffice to say that if one variable is scaled by another, the error in the resulting variable is the Euclidean norm (*cf.* Eq. (B.3)) of the constituent parts.

Table B.1: Error Summary

Variable	% Error
\bar{u}	8.8
\bar{v}	8.5
u'	1.7
v'	7.9
$\overline{u'v'}$	8.1
\bar{Q}	8.8
\bar{M}	9.0
\bar{p}_0	0.6
$\bar{T}_{0,\infty}$	0.1
\bar{T}_0	4.0
δ_u	28.0
δ_M	28.0
τ_w	7.1
M_e	1.5

Variable	% Error
u_e	1.3
Q_e	1.5
T_e	1.8
p_e	6.4
ρ_e	6.6
T_w	0.1
p_w	0.6
ρ_w	0.6
\bar{T}	11.7
\bar{p}	6.6
$\bar{\rho}$	13.5
u_{eff}	18.9
u^*	3.5
u_{eff}/u^*	19.2

Variable	% Error
σ_u	1.7
σ_v	7.9
Sk_u	7.2
Sk_v	33.5
Fl_u	9.6
Fl_v	44.7
γ_u	9.6
R_{uv}	11.4
$\partial\bar{u}/\partial x$	15.2
$\partial\bar{v}/\partial x$	14.7
$\partial\bar{u}/\partial y$	17.7
$\partial\bar{v}/\partial y$	17.1
$\partial\bar{u}/\partial z$	12.4
$\partial\bar{v}/\partial z$	12.0

C. Compliance With Criteria of Settles and Dodson

In order to ensure compliance with the criteria established by Settles and Dodson [31] which were presented in Chapter 1, a list of the criteria and how they were met is presented in Table C.1. If it was found that one or more of the criteria still needed to be met, they were addressed individually in the remaining sections of this chapter.

Table C.1: Compliance With Criteria of Ref. [31]

Criterion Number	Criterion Category	How/Where Criterion Met
1	Baseline Applicability	$M_e = 2.9 \approx 3.0$
2	Simplicity	Geometry able to be modeled by CFD (<i>cf.</i> Ref.[17])
3	Specific Applicability	Has been compared to CFD in order to validate code (<i>cf.</i> Ref. [17])
4	Well-Defined Experimental Boundary Conditions	Incoming conditions tabulated (Section 8.1) 2D Check: see Section C.2
5	Defined Error Bounds	Appendix B; Section C.1
6	Documentation of Data	Section C.3
7	Spatial Resolution of Data	Figures in Chapter 7 are large with as much resolution as possible.

C.1 Repeatability

The repeatability of the test results was determined using two separate methods. The first was to take twenty test runs at a given location to find the effect of wind tunnel fluctuations on the measurements. These tests provided confidence intervals for the mean flow variables, turbulence intensities, skewness, flatness and the second-order velocity correlation. A confidence interval is a measure of the probability that the error in the measured mean, \bar{x} , will be less than a certain value

when compared to the actual value, μ_x . That is, a 99% confidence interval of 1% means that there is a 99% probability that

$$\left| \frac{\bar{x} - \mu_x}{\bar{x}} \right| \leq 0.01$$

However, the value of μ_x was not known, so it was not possible to directly calculate the value of the confidence interval on the RHS of the above equation. In order to obtain a value for the confidence interval, it was necessary to use Student's t distribution and the relation [3]

$$\left| \frac{\mu_x - \bar{x}}{\bar{x}} \right| \leq \frac{st_{n,\alpha/2}}{\bar{x}\sqrt{N}} \quad (C.1)$$

where N was the number of data points used to calculate \bar{x} . If N was large enough, $s \cong \sigma_x$; Student's t distribution was a tabulated function based on $n = N - 1$ and α . α was a variable which described the accuracy of the confidence interval and was given by $\alpha = 1 - \xi/100\%$, where ξ was the percent accuracy of the confidence interval. Therefore, a 99% confidence interval meant $\alpha = 0.01$.

For the repeatability study in the present experiment, twenty test runs were performed but two were discarded due to the fact that the mean velocity was extremely low when compared to the other test runs, suggesting the data collection was initiated before the tunnel reached steady state or was not cut off until the vacuum was depleted and the flow velocity decreased. In any event, this same practice of manually evaluating the mean flow velocities was used in the actual data collection tests, so discarding these two tests should not have biased the confidence intervals associated with the presented results. After discarding the two flawed data sets, there were 18 samples used to calculate the 99% confidence intervals; from Ref. [3], $t_{n,\alpha/2} = t_{17,0.05} = 2.898$. Using this value in Eq. (C.1), the 99% confidence intervals for the velocity data and the turbulence statistics output by the Burstware[®] software were computed and are presented in Table C.2.

Table C.2: Confidence Intervals

\bar{u}	\bar{v}	u'_{rms}	v'_{rms}	$\overline{u'v'}$
0.15%	0.076%	1.53%	0.99%	13.59%

Sk_u	Sk_v	Fl_u	Fl_v
2.60%	14.10%	3.23%	8.00%

The second method of proving the repeatability was to take several traverses across the boundary layer at each test location. The test results for four separate traverses across the flat plate boundary layer are presented in Figure C.1; the most sensitive variable, $\overline{u'v'}$, showed excellent repeatability.

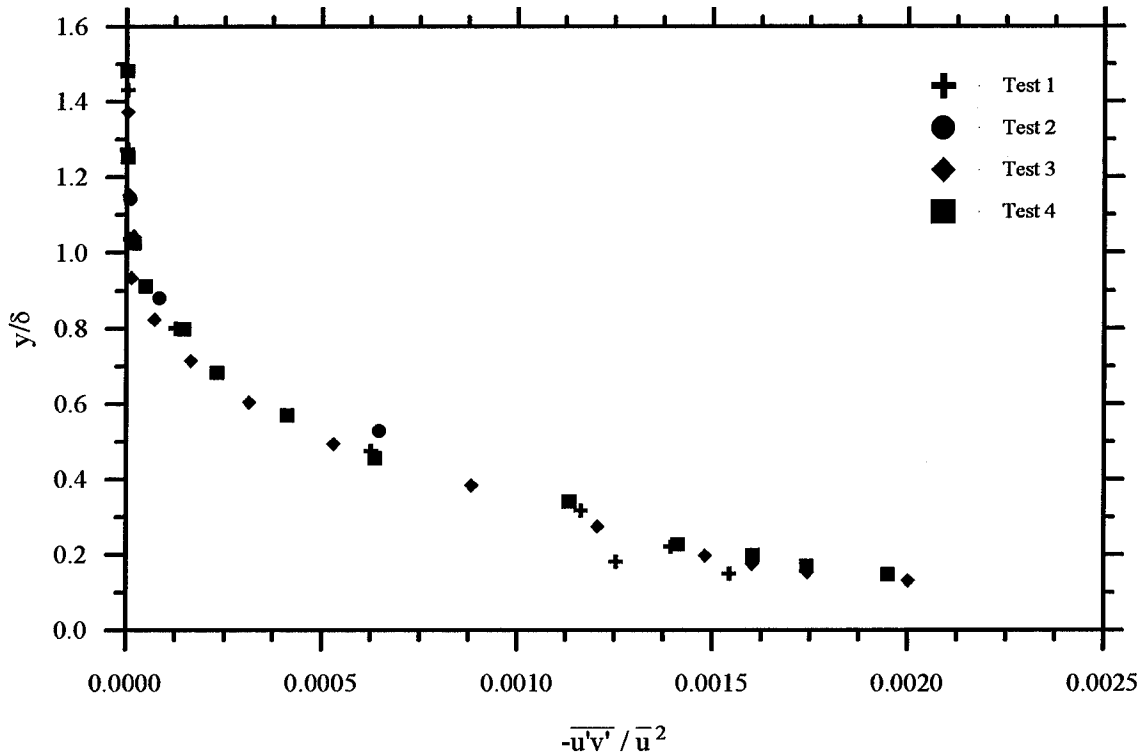


Figure C.1: Repeatability of Second-Order Correlation Over a Flat Plate

C.2 Two-Dimensionality Check

In accordance with the guidelines set up by Settles and Dodson, a two-dimensionality check was performed. The check was accomplished by comparing data taken when building the finite-difference grid. Three profiles were taken along the z -axis; the velocity profiles generated are compared in Figure C.2. Although the values at $z = -5$ mm were slightly lower than those at $z = 5$ mm, the difference was essentially negligible and the flow was assumed to be two-dimensional.

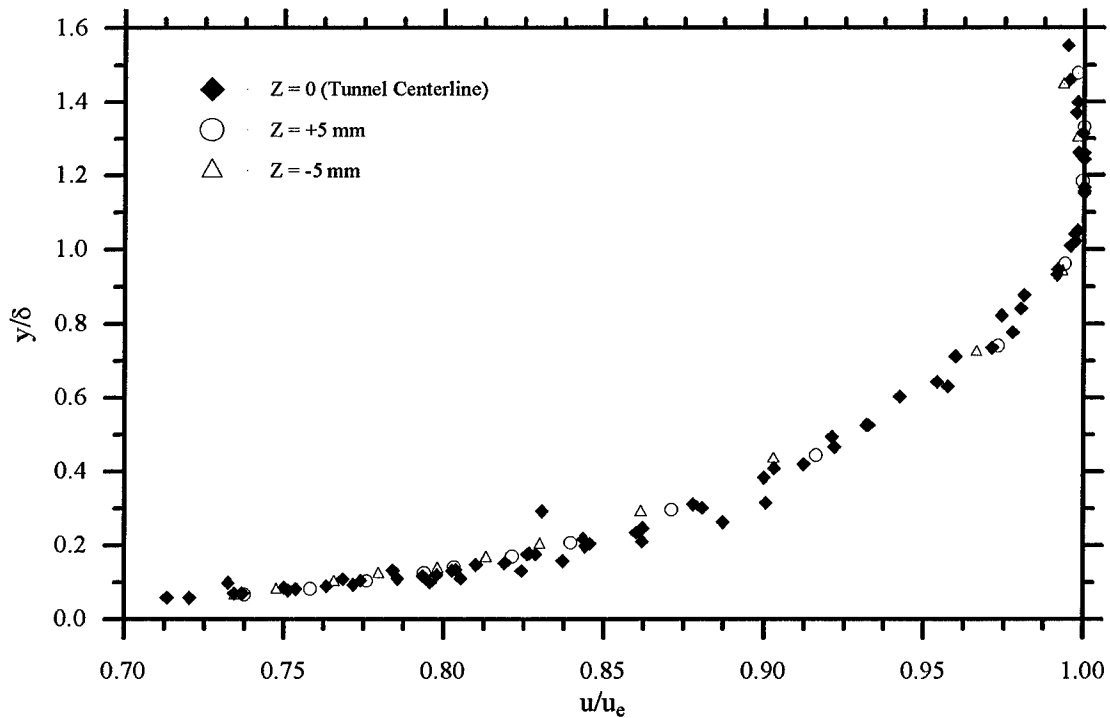


Figure C.2: Velocity Comparison for Two-Dimensionality Check

C.3 Tabulated Data

Tables C.3 to C.6 on the following pages contain point-by-point data collected by the LDV system and the data from the resulting calculations.

Table C.3: Flat Plate 16-Sample Raw Data

y (mm)	y/δ_u	y/δ_M	ρ (kg/m ³)	T (K)	M	M'	u (m/s)	u/u_e	u'/u	u'/u_e	Sk_u	Fl_u	γ_u	v (m/s)	v/u_e	v'/u	v'/u_e	Sk_v	Fl_v
0.64	0.07	0.06	0.15	196	1.57	0.26	444	0.73	1.12E-01	8.21E-02	-0.17	2.56	1.17	0.00	0.00E+00	0.00E+00	0.00E+00	0.00	0.00
0.78	0.09	0.08	0.16	191	1.63	0.27	455	0.75	1.08E-01	8.13E-02	-0.24	2.65	1.13	0.00	0.00E+00	0.00E+00	0.00E+00	0.00	0.00
0.78	0.10	0.09	0.16	188	1.66	0.27	463	0.77	1.04E-01	8.00E-02	-0.11	2.43	1.24	0.00	0.00E+00	0.00E+00	0.00E+00	0.00	0.00
0.99	0.11	0.10	0.16	184	1.71	0.27	471	0.78	9.95E-02	7.72E-02	-0.24	2.55	1.18	0.00	0.00E+00	0.00E+00	0.00E+00	0.00	0.00
1.20	0.13	0.12	0.16	185	1.66	0.27	460	0.77	1.05E-01	8.06E-02	-0.26	2.67	1.12	10.34	1.73E-02	4.21E-02	3.23E-02	0.03	3.67
1.20	0.13	0.12	0.17	180	1.77	0.28	480	0.79	9.67E-02	7.63E-02	-0.33	2.66	1.13	0.00	0.00E+00	0.00E+00	0.00E+00	0.00	0.00
1.20	0.15	0.14	0.17	181	1.75	0.29	479	0.79	1.01E-01	8.04E-02	-0.26	2.63	1.14	0.00	0.00E+00	0.00E+00	0.00E+00	0.00	0.00
1.30	0.15	0.13	0.16	188	1.65	0.27	457	0.76	1.05E-01	8.00E-02	-0.26	2.70	1.11	9.20	1.53E-02	4.37E-02	3.32E-02	0.08	3.58
1.34	0.15	0.14	0.17	177	1.81	0.29	486	0.80	9.43E-02	7.56E-02	-0.37	2.71	1.11	19.31	3.18E-02	4.16E-02	3.34E-02	0.07	3.81
1.34	0.17	0.15	0.17	178	1.80	0.29	487	0.81	9.73E-02	7.85E-02	-0.31	2.63	1.14	16.78	2.78E-02	4.40E-02	3.55E-02	-0.16	5.01
1.40	0.15	0.14	0.17	180	1.74	0.27	473	0.79	9.75E-02	7.70E-02	-0.27	2.58	1.16	10.34	1.73E-02	4.13E-02	3.26E-02	0.10	3.42
1.50	0.17	0.16	0.17	182	1.72	0.27	469	0.78	9.81E-02	7.67E-02	-0.23	2.54	1.18	9.63	1.60E-02	4.33E-02	3.38E-02	0.11	3.52
1.60	0.18	0.16	0.17	175	1.80	0.28	482	0.81	9.36E-02	7.55E-02	-0.34	2.73	1.10	10.42	1.74E-02	4.09E-02	3.29E-02	0.17	3.37
1.63	0.18	0.16	0.18	172	1.88	0.29	497	0.82	8.98E-02	7.36E-02	-0.44	2.85	1.05	19.49	3.21E-02	4.09E-02	3.55E-02	0.09	3.88
1.75	0.20	0.18	0.17	176	1.80	0.28	483	0.80	9.27E-02	7.45E-02	-0.35	2.71	1.11	8.98	1.49E-02	4.23E-02	3.42E-02	0.08	3.78
1.80	0.20	0.18	0.18	171	1.85	0.28	491	0.82	8.98E-02	7.37E-02	-0.39	2.81	1.07	10.21	1.71E-02	4.04E-02	3.32E-02	0.18	3.51
1.98	0.22	0.20	0.18	167	1.95	0.30	508	0.84	8.58E-02	7.19E-02	-0.50	2.95	1.02	20.42	3.37E-02	4.06E-02	3.39E-02	0.05	4.30
1.98	0.25	0.23	0.18	168	1.94	0.31	507	0.84	8.92E-02	7.50E-02	-0.44	2.78	1.08	17.66	2.93E-02	4.46E-02	3.75E-02	-0.45	6.58
2.00	0.23	0.21	0.18	172	1.87	0.28	492	0.82	8.91E-02	7.31E-02	-0.42	2.85	1.05	8.44	1.41E-02	4.15E-02	3.40E-02	0.19	3.67
2.50	0.27	0.25	0.19	159	2.01	0.29	516	0.86	7.88E-02	6.79E-02	-0.53	3.01	1.00	9.91	1.66E-02	3.80E-02	3.27E-02	0.27	3.80
2.84	0.32	0.29	0.19	155	2.12	0.30	532	0.88	7.39E-02	6.48E-02	-0.68	3.20	0.94	21.59	3.56E-02	3.77E-02	3.31E-02	0.02	5.38
3.00	0.34	0.31	0.19	157	2.07	0.29	523	0.87	7.42E-02	6.46E-02	-0.62	3.14	0.95	7.71	1.28E-02	3.76E-02	3.27E-02	0.23	4.25
3.50	0.38	0.35	0.21	146	2.21	0.29	542	0.91	6.60E-02	5.98E-02	-0.78	3.46	0.87	9.04	1.51E-02	3.38E-02	3.06E-02	0.38	4.46
4.00	0.46	0.41	0.21	142	2.30	0.28	552	0.92	5.91E-02	5.43E-02	-0.89	3.66	0.82	8.49	1.41E-02	3.13E-02	2.88E-02	0.43	4.73
4.25	0.48	0.43	0.22	140	2.37	0.29	562	0.93	5.64E-02	5.22E-02	-1.14	4.39	0.68	24.39	4.02E-02	3.21E-02	2.98E-02	-0.26	8.90
4.25	0.53	0.49	0.22	138	2.39	0.30	566	0.94	5.73E-02	5.38E-02	-1.21	4.66	0.64	18.47	3.06E-02	4.30E-02	4.03E-02	-1.09	8.23
4.50	0.49	0.44	0.22	136	2.38	0.27	562	0.94	5.34E-02	5.01E-02	-1.02	4.05	0.74	8.98	1.50E-02	2.93E-02	2.75E-02	0.46	4.87
5.00	0.57	0.52	0.23	133	2.45	0.26	569	0.95	4.79E-02	4.54E-02	-1.20	4.66	0.64	9.05	1.51E-02	2.63E-02	2.49E-02	0.45	5.97
5.50	0.60	0.54	0.24	128	2.52	0.24	577	0.96	4.19E-02	4.04E-02	-1.39	5.50	0.55	9.46	1.58E-02	2.44E-02	2.35E-02	0.54	6.24
6.00	0.68	0.62	0.24	126	2.57	0.22	581	0.97	3.69E-02	3.57E-02	-1.54	6.24	0.48	10.00	1.67E-02	2.21E-02	2.14E-02	0.36	7.71
6.50	0.71	0.64	0.25	122	2.62	0.21	587	0.98	3.30E-02	3.24E-02	-1.83	8.05	0.37	10.37	1.73E-02	2.03E-02	1.99E-02	0.34	7.08
7.00	0.80	0.72	0.25	121	2.67	0.18	590	0.98	2.68E-02	2.63E-02	-2.06	9.88	0.30	11.61	1.93E-02	1.84E-02	1.81E-02	0.01	11.23
7.09	0.88	0.81	0.25	121	2.71	0.17	598	0.99	2.44E-02	2.42E-02	-2.81	18.52	0.16	24.22	4.01E-02	2.65E-02	2.62E-02	-3.47	30.98

Table C.3: Flat Plate 16-Sample Raw Data (cont')

y (mm)	y/δ_u	y/δ_M	$-u'v'/u_e^2$	$-u'v'/u_e^2$	$-u'v'/u_e^2$	$-u'v'/\tau_w$	R_{uv}	TKE/u_e^2	Δu (m/s)	u_{eff}/u_e^*	y^+	ρ/ρ_e
0.64	0.07	0.06	0.00E+00	0.00E+00	0.00E+00	0.00	0.00	3.37E-03	46.61	18.25	93.69	0.60
0.78	0.09	0.08	0.00E+00	0.00E+00	0.00E+00	0.00	0.00	3.30E-03	9.81	18.76	114.18	0.62
0.78	0.10	0.09	0.00E+00	0.00E+00	0.00E+00	0.00	0.00	3.20E-03	33.10	18.78	116.33	0.63
0.99	0.11	0.10	0.00E+00	0.00E+00	0.00E+00	0.00	0.00	2.98E-03	9.23	19.51	144.93	0.64
1.20	0.13	0.12	0.00E+00	0.00E+00	0.00E+00	0.00	0.00	4.30E-03	29.34	18.96	176.66	0.63
1.20	0.13	0.12	0.00E+00	0.00E+00	0.00E+00	0.00	0.00	2.93E-03	8.42	19.97	175.68	0.66
1.20	0.15	0.14	0.00E+00	0.00E+00	0.00E+00	0.00	0.00	3.23E-03	7.25	19.52	178.97	0.65
1.30	0.15	0.13	0.00E+00	0.00E+00	0.00E+00	0.00	0.00	4.30E-03	27.38	18.89	190.33	0.62
1.34	0.15	0.14	0.00E+00	0.00E+00	0.00E+00	0.00	0.00	3.98E-03	9.73	20.28	196.17	0.67
1.34	0.17	0.15	0.00E+00	0.00E+00	0.00E+00	0.00	0.00	4.34E-03	8.47	19.91	199.85	0.67
1.40	0.15	0.14	0.00E+00	0.00E+00	0.00E+00	0.00	0.00	4.03E-03	9.14	19.59	206.09	0.65
1.50	0.17	0.16	0.00E+00	0.00E+00	0.00E+00	0.00	0.00	4.08E-03	9.18	19.50	219.62	0.64
1.60	0.18	0.16	0.00E+00	0.00E+00	0.00E+00	0.00	0.00	3.94E-03	8.81	20.05	235.53	0.67
1.63	0.18	0.16	0.00E+00	0.00E+00	0.00E+00	0.00	0.00	3.83E-03	9.41	20.82	238.63	0.69
1.75	0.20	0.18	0.00E+00	0.00E+00	0.00E+00	0.00	0.00	3.95E-03	8.72	20.15	256.22	0.66
1.80	0.20	0.18	0.00E+00	0.00E+00	0.00E+00	0.00	0.00	3.82E-03	8.42	20.50	264.98	0.68
1.98	0.22	0.20	0.00E+00	0.00E+00	0.00E+00	0.00	0.00	3.73E-03	9.28	21.35	289.86	0.71
1.98	0.25	0.23	0.00E+00	0.00E+00	0.00E+00	0.00	0.00	4.22E-03	8.08	20.92	295.30	0.70
2.00	0.23	0.21	0.00E+00	0.00E+00	0.00E+00	0.00	0.00	3.83E-03	7.77	20.64	292.82	0.68
2.50	0.27	0.25	0.00E+00	0.00E+00	0.00E+00	0.00	0.00	3.38E-03	8.13	21.75	368.02	0.73
2.84	0.32	0.29	0.00E+00	0.00E+00	0.00E+00	0.00	0.00	3.19E-03	9.17	22.60	415.77	0.76
3.00	0.34	0.31	0.00E+00	0.00E+00	0.00E+00	0.00	0.00	3.16E-03	7.98	22.20	439.24	0.75
3.50	0.38	0.35	0.00E+00	0.00E+00	0.00E+00	0.00	0.00	2.73E-03	7.71	23.15	515.23	0.80
4.00	0.46	0.41	0.00E+00	0.00E+00	0.00E+00	0.00	0.00	2.30E-03	7.73	23.76	585.64	0.82
4.25	0.48	0.43	0.00E+00	0.00E+00	0.00E+00	0.00	0.00	2.25E-03	8.44	24.25	622.18	0.85
4.25	0.53	0.49	0.00E+00	0.00E+00	0.00E+00	0.00	0.00	3.07E-03	7.76	24.01	633.84	0.85
4.50	0.49	0.44	0.00E+00	0.00E+00	0.00E+00	0.00	0.00	2.01E-03	7.31	24.24	662.44	0.86
5.00	0.57	0.52	0.00E+00	0.00E+00	0.00E+00	0.00	0.00	1.63E-03	7.02	24.71	732.05	0.88
5.50	0.60	0.54	0.00E+00	0.00E+00	0.00E+00	0.00	0.00	1.37E-03	6.95	25.08	809.66	0.91
6.00	0.68	0.62	0.00E+00	0.00E+00	0.00E+00	0.00	0.00	1.10E-03	6.79	25.43	878.46	0.92
6.50	0.71	0.64	0.00E+00	0.00E+00	0.00E+00	0.00	0.00	9.19E-04	6.66	25.69	956.87	0.96
7.00	0.80	0.72	0.00E+00	0.00E+00	0.00E+00	0.00	0.00	6.73E-04	6.48	25.99	1024.90	0.96
7.09	0.88	0.81	0.00E+00	0.00E+00	0.00E+00	0.00	0.00	9.80E-04	7.34	25.79	1057.41	0.97

Table C.3: Flat Plate 16-Sample Raw Data (cont)

y (mm)	y/δ_u	y/δ_M	ρ (kg/m ³)	T (K)	M	M'	u (m/s)	u/u_e	u'/u	u'/u_e	Sk_u	Fl_u	γ_u	v (m/s)	v/u_e	v'/u	v'/u_e	Sk_v	Fl_v
7.16	0.80	0.72	0.25	122	2.71	0.18	596	0.98	2.57E-02	2.33E-02	-3.28	26.42	0.11	26.66	4.40E-02	3.08E-02	3.03E-02	-3.30	25.36
7.50	0.82	0.74	0.26	118	2.70	0.16	595	0.99	2.37E-02	2.36E-02	-2.29	12.87	0.23	12.25	2.05E-02	1.75E-02	1.74E-02	-0.18	13.00
8.00	0.91	0.83	0.25	119	2.72	0.14	595	0.99	2.04E-02	2.02E-02	-2.32	13.37	0.22	13.75	2.29E-02	1.61E-02	1.59E-02	-0.49	17.77
8.50	0.93	0.84	0.26	118	2.72	0.14	594	0.99	2.05E-02	2.04E-02	-5.06	62.23	0.05	15.05	2.52E-02	1.56E-02	1.55E-02	-1.33	28.94
9.00	1.03	0.93	0.26	117	2.76	0.10	598	1.00	1.45E-02	1.44E-02	-2.46	21.66	0.14	15.80	2.63E-02	1.36E-02	1.35E-02	-1.33	31.52
9.21	1.14	1.05	0.26	118	2.77	0.12	603	1.00	1.54E-02	1.54E-02	-5.83	94.15	0.03	23.96	3.97E-02	2.73E-02	2.73E-02	-4.30	34.43
9.26	1.04	0.94	0.26	118	2.77	0.13	602	0.99	1.82E-02	1.81E-02	-8.12	127.06	0.02	22.94	3.78E-02	2.58E-02	2.56E-02	-4.03	34.14
9.50	1.04	0.94	0.26	117	2.75	0.11	596	1.00	1.60E-02	1.60E-02	-3.17	31.47	0.10	17.94	3.00E-02	1.35E-02	1.35E-02	-1.08	26.22
10.00	1.14	1.03	0.26	116	2.78	0.08	600	1.00	1.16E-02	1.15E-02	-2.26	27.54	0.11	17.59	2.93E-02	1.26E-02	1.26E-02	-1.64	34.78
10.50	1.15	1.04	0.26	116	2.77	0.09	598	1.00	1.28E-02	1.28E-02	-2.61	28.35	0.11	19.50	3.26E-02	1.25E-02	1.25E-02	-2.05	40.08
11.00	1.25	1.14	0.26	116	2.79	0.08	600	1.00	1.02E-02	1.02E-02	-3.14	70.14	0.04	19.07	3.18E-02	1.19E-02	1.19E-02	-2.53	48.86
11.34	1.41	1.30	0.26	118	2.77	0.09	603	1.00	1.26E-02	1.26E-02	-7.86	175.87	0.02	23.21	3.85E-02	2.19E-02	2.18E-02	-4.88	48.32
11.38	1.27	1.15	0.26	118	2.78	0.07	603	0.99	1.01E-02	1.00E-02	-5.33	117.97	0.03	18.11	2.99E-02	1.31E-02	1.30E-02	-4.14	70.74
11.50	1.26	1.14	0.26	116	2.79	0.08	598	1.00	1.11E-02	1.11E-02	-4.54	111.33	0.03	20.63	3.45E-02	1.14E-02	1.14E-02	-2.02	42.21
12.00	1.37	1.24	0.26	116	2.79	0.07	600	1.00	9.20E-03	9.20E-03	-4.68	156.11	0.02	19.41	3.23E-02	1.15E-02	1.15E-02	-3.26	59.68
12.50	1.37	1.23	0.26	116	2.78	0.07	598	1.00	1.01E-02	1.01E-02	-5.24	153.24	0.02	20.58	3.44E-02	1.08E-02	1.08E-02	-2.40	52.24
12.76	1.58	1.46	0.25	120	2.75	0.11	600	1.00	1.59E-02	1.59E-02	-9.79	177.74	0.02	20.37	3.38E-02	1.64E-02	1.63E-02	-4.04	59.55
14.00	1.60	1.45	0.26	116	2.77	0.06	599	1.00	8.62E-03	8.61E-03	-2.95	79.84	0.04	17.67	2.94E-02	1.14E-02	1.14E-02	-3.98	73.02
14.21	1.76	1.62	0.25	120	2.74	0.10	600	0.99	1.42E-02	1.41E-02	-9.39	193.82	0.02	18.31	3.03E-02	1.63E-02	1.62E-02	-4.26	62.30
14.31	1.60	1.45	0.26	116	2.81	0.08	607	1.00	9.93E-03	9.93E-03	-7.52	202.02	0.01	17.06	2.81E-02	1.46E-02	1.46E-02	-5.41	76.96

Table C.3: Flat Plate 16-Sample Raw Data (cont)

y (mm)	y/δ_u	y/δ_M	$-u^2/v^2$	$-u^2/v^2$	$-u^2/v^2$	$-u^2/v^2$	R_{uv}	TKE/u_e^2	Δu (m/s)	u_{eff}/u_e^*	y^+	ρ/ρ_e
7.16	0.80	0.72	0.00E+00	0.00E+00	0.00E+00	0.00E+00	0.00	1.24E-03	7.88	26.20	1048.21	0.97
7.50	0.82	0.74	0.00E+00	0.00E+00	0.00E+00	0.00E+00	0.00	5.81E-04	6.04	26.13	1104.12	0.99
8.00	0.91	0.83	0.00E+00	0.00E+00	0.00E+00	0.00E+00	0.00	4.58E-04	6.24	26.26	1171.27	0.98
8.50	0.93	0.84	0.00E+00	0.00E+00	0.00E+00	0.00E+00	0.00	4.46E-04	5.86	26.10	1251.31	0.99
9.00	1.03	0.93	0.00E+00	0.00E+00	0.00E+00	0.00E+00	0.00	2.87E-04	6.20	26.46	1317.64	1.00
9.21	1.14	1.05	0.00E+00	0.00E+00	0.00E+00	0.00E+00	0.00	8.65E-04	6.60	26.12	1373.56	1.00
9.26	1.04	0.94	0.00E+00	0.00E+00	0.00E+00	0.00E+00	0.00	8.19E-04	6.63	26.56	1356.18	1.00
9.50	1.04	0.94	0.00E+00	0.00E+00	0.00E+00	0.00E+00	0.00	3.09E-04	6.30	26.25	1398.50	1.00
10.00	1.14	1.03	0.00E+00	0.00E+00	0.00E+00	0.00E+00	0.00	2.26E-04	6.13	26.55	1464.12	1.01
10.50	1.15	1.04	0.00E+00	0.00E+00	0.00E+00	0.00E+00	0.00	2.38E-04	6.25	26.34	1545.68	1.01
11.00	1.25	1.14	0.00E+00	0.00E+00	0.00E+00	0.00E+00	0.00	1.93E-04	6.11	26.60	1610.49	1.01
11.34	1.41	1.30	0.00E+00	0.00E+00	0.00E+00	0.00E+00	0.00	5.57E-04	6.25	26.11	1691.24	1.00
11.38	1.27	1.15	0.00E+00	0.00E+00	0.00E+00	0.00E+00	0.00	2.19E-04	6.19	26.62	1666.60	1.00
11.50	1.26	1.14	0.00E+00	0.00E+00	0.00E+00	0.00E+00	0.00	1.90E-04	6.19	26.37	1692.87	1.01
12.00	1.37	1.24	0.00E+00	0.00E+00	0.00E+00	0.00E+00	0.00	1.74E-04	6.01	26.59	1756.96	1.01
12.50	1.37	1.23	0.00E+00	0.00E+00	0.00E+00	0.00E+00	0.00	1.68E-04	6.10	26.37	1840.16	1.01
12.76	1.58	1.46	0.00E+00	0.00E+00	0.00E+00	0.00E+00	0.00	3.92E-04	5.95	25.94	1903.03	0.99
14.00	1.60	1.45	0.00E+00	0.00E+00	0.00E+00	0.00E+00	0.00	1.66E-04	5.93	26.53	2049.70	1.01
14.21	1.76	1.62	0.00E+00	0.00E+00	0.00E+00	0.00E+00	0.00	3.63E-04	5.98	25.90	2118.60	0.98
14.31	1.60	1.45	0.00E+00	0.00E+00	0.00E+00	0.00E+00	0.00	2.61E-04	5.94	26.84	2094.98	1.02

Table C.4: Flat Plate 16-Sample Coincident Data

y (mm)	y/δ_u	y/δ_M	ρ (kg/m ³)	T (K)	M	M'	u (m/s)	u/u_e	u'/u	u'/u_e	Sk_u	Fl_u	γ_u	ν (m/s)	ν/u	ν/u_e	Sk_ν	Fl_ν	
1.34	0.15	0.14	0.17	177	1.81	0.28	486	0.80	9.33E-02	7.48E-02	-0.39	2.73	1.10	19.45	3.21E-02	4.08E-02	3.27E-02	0.14	3.37
1.40	0.15	0.14	0.17	180	1.74	0.27	473	0.79	9.73E-02	7.69E-02	-0.24	2.57	1.17	10.38	1.73E-02	4.06E-02	3.21E-02	0.11	3.19
1.50	0.17	0.16	0.17	183	1.72	0.27	468	0.78	9.78E-02	7.62E-02	-0.23	2.56	1.17	9.27	1.54E-02	4.27E-02	3.33E-02	0.14	3.27
1.60	0.18	0.16	0.17	175	1.80	0.28	482	0.81	9.38E-02	7.56E-02	-0.33	2.70	1.11	10.40	1.74E-02	4.01E-02	3.23E-02	0.13	3.20
1.63	0.18	0.16	0.17	173	1.87	0.29	495	0.82	9.04E-02	7.37E-02	-0.40	2.72	1.10	19.69	3.23E-02	4.03E-02	3.29E-02	0.14	3.69
1.75	0.20	0.18	0.17	176	1.80	0.28	482	0.80	9.32E-02	7.48E-02	-0.34	2.67	1.12	8.99	1.50E-02	4.17E-02	3.34E-02	0.14	3.42
1.80	0.20	0.18	0.18	171	1.85	0.28	491	0.82	8.90E-02	7.31E-02	-0.38	2.82	1.06	10.11	1.69E-02	3.96E-02	3.25E-02	0.21	3.25
1.98	0.22	0.20	0.18	168	1.93	0.30	505	0.83	8.63E-02	7.18E-02	-0.48	2.89	1.04	20.72	3.42E-02	3.95E-02	3.29E-02	0.13	3.70
2.00	0.23	0.21	0.18	172	1.87	0.28	492	0.82	8.86E-02	7.26E-02	-0.42	2.81	1.07	8.24	1.37E-02	4.09E-02	3.36E-02	0.24	3.36
2.50	0.27	0.25	0.19	160	2.01	0.29	515	0.86	7.88E-02	6.78E-02	-0.52	3.03	0.99	9.87	1.65E-02	3.73E-02	3.21E-02	0.33	3.39
2.84	0.32	0.29	0.19	157	2.10	0.30	529	0.87	7.55E-02	6.58E-02	-0.65	3.22	0.93	22.21	3.66E-02	3.68E-02	3.21E-02	0.29	3.80
3.00	0.34	0.31	0.19	157	2.07	0.29	522	0.87	7.53E-02	6.55E-02	-0.63	3.17	0.95	8.17	1.36E-02	3.76E-02	3.27E-02	0.32	3.72
3.50	0.38	0.35	0.21	146	2.21	0.29	542	0.91	6.56E-02	5.94E-02	-0.76	3.41	0.88	9.27	1.55E-02	3.38E-02	3.06E-02	0.44	3.95
4.00	0.46	0.41	0.21	142	2.30	0.28	551	0.92	5.89E-02	5.41E-02	-0.86	3.49	0.86	8.35	1.39E-02	3.05E-02	2.80E-02	0.63	4.18
4.25	0.48	0.43	0.22	141	2.36	0.30	561	0.92	5.85E-02	5.40E-02	-1.12	4.20	0.71	25.13	4.14E-02	3.08E-02	2.85E-02	0.35	5.76
4.25	0.53	0.49	0.22	139	2.38	0.31	565	0.94	5.91E-02	5.53E-02	-1.20	4.55	0.66	22.56	3.74E-02	2.91E-02	2.73E-02	0.42	6.03
4.50	0.49	0.44	0.22	136	2.37	0.27	561	0.94	5.32E-02	4.99E-02	-1.02	4.08	0.73	9.30	1.53E-02	2.88E-02	2.70E-02	0.56	4.25
5.00	0.57	0.52	0.23	133	2.45	0.26	568	0.95	4.82E-02	4.56E-02	-1.17	4.48	0.67	9.26	1.54E-02	2.60E-02	2.46E-02	0.66	4.49
5.50	0.60	0.54	0.24	128	2.51	0.24	576	0.96	4.28E-02	4.12E-02	-1.35	5.30	0.57	9.75	1.63E-02	2.42E-02	2.33E-02	0.68	5.66
6.00	0.68	0.62	0.24	127	2.57	0.22	580	0.97	3.74E-02	3.61E-02	-1.51	5.97	0.50	10.39	1.73E-02	2.20E-02	2.12E-02	0.50	6.43
6.50	0.71	0.64	0.25	122	2.61	0.21	586	0.98	3.38E-02	3.31E-02	-1.80	7.66	0.39	10.74	1.80E-02	2.02E-02	1.97E-02	0.55	5.63
7.00	0.80	0.72	0.25	123	2.64	0.21	587	0.98	3.21E-02	3.14E-02	-1.83	7.64	0.39	12.99	2.16E-02	1.95E-02	1.91E-02	0.88	5.71
7.09	0.88	0.81	0.25	121	2.70	0.17	597	0.99	2.44E-02	2.42E-02	-2.58	13.34	0.22	25.49	4.22E-02	1.86E-02	1.84E-02	-1.42	25.01
7.16	0.80	0.72	0.25	122	2.70	0.18	595	0.98	2.61E-02	2.56E-02	-3.09	22.08	0.14	27.86	4.59E-02	2.18E-02	2.14E-02	-2.35	27.44
7.50	0.82	0.74	0.26	118	2.70	0.16	594	0.99	2.41E-02	2.39E-02	-2.22	11.07	0.27	12.69	2.12E-02	1.63E-02	1.62E-02	0.58	6.41
8.00	0.91	0.83	0.25	119	2.71	0.15	594	0.99	2.13E-02	2.10E-02	-2.32	12.20	0.25	14.03	2.34E-02	1.51E-02	1.50E-02	0.50	6.65
8.50	0.93	0.84	0.26	118	2.72	0.13	594	0.99	1.81E-02	1.80E-02	-3.30	30.18	0.10	15.14	2.53E-02	1.50E-02	1.49E-02	-1.32	30.20
9.00	1.03	0.93	0.26	117	2.76	0.10	598	1.00	1.46E-02	1.45E-02	-2.38	15.93	0.19	16.13	2.69E-02	1.27E-02	1.26E-02	-0.20	16.19
9.21	1.14	1.05	0.26	118	2.77	0.12	604	1.00	1.56E-02	1.56E-02	-10.44	221.05	0.01	25.25	4.18E-02	2.00E-02	2.00E-02	-4.28	48.50
9.26	1.04	0.94	0.26	118	2.78	0.09	602	0.99	1.20E-02	1.19E-02	-5.01	92.96	0.03	24.16	3.98E-02	1.65E-02	1.64E-02	-4.04	57.74
9.50	1.04	0.94	0.26	117	2.75	0.11	596	1.00	1.56E-02	1.55E-02	-2.53	18.28	0.16	18.04	3.02E-02	1.26E-02	1.26E-02	0.15	10.13
10.00	1.14	1.03	0.26	116	2.78	0.08	600	1.00	1.10E-02	1.09E-02	-1.49	15.39	0.19	17.92	2.98E-02	1.16E-02	1.15E-02	-0.80	19.64
10.50	1.15	1.04	0.26	116	2.77	0.09	598	1.00	1.25E-02	1.25E-02	-2.43	22.91	0.13	19.62	3.28E-02	1.17E-02	1.17E-02	-1.10	27.59

Table C.4: Flat Plate 16-Sample Coincident Data (cont)

y (mm)	y/δ_u	y/δ_M	$-u^2/v^2/u^2$	$-u^2v^2/u_e^2$	$-\rho u^2v^2/\tau_w$	R_{uv}	TKE/u_e^2	ΔM (m/s)	u_{eff}/u^*	y^+	ρ/ρ_e
1.34	0.15	0.14	1.54E-03	7.27E-04	0.93	0.41	3.90E-03	39.82	20.72	191.92	0.90
1.40	0.15	0.14	1.74E-03	7.59E-04	0.97	0.44	3.99E-03	8.99	20.01	201.63	0.93
1.50	0.17	0.16	1.74E-03	7.39E-04	0.95	0.42	4.01E-03	9.02	19.86	214.86	0.91
1.60	0.18	0.16	1.60E-03	7.46E-04	0.95	0.43	3.91E-03	8.90	20.50	230.43	0.92
1.63	0.18	0.16	1.25E-03	6.26E-04	0.80	0.34	3.84E-03	8.91	21.16	233.46	0.77
1.75	0.20	0.18	1.60E-03	7.48E-04	0.96	0.41	3.91E-03	9.01	20.56	250.67	0.92
1.80	0.20	0.18	1.48E-03	7.32E-04	0.94	0.42	3.73E-03	8.33	20.95	259.24	0.90
1.98	0.22	0.20	1.39E-03	7.44E-04	0.96	0.41	3.70E-03	9.22	21.68	283.58	0.92
2.00	0.23	0.21	1.41E-03	7.08E-04	0.91	0.39	3.77E-03	7.75	21.10	286.48	0.87
2.50	0.27	0.25	1.21E-03	7.03E-04	0.90	0.41	3.34E-03	8.11	22.19	360.05	0.86
2.84	0.32	0.29	1.16E-03	7.33E-04	0.94	0.42	3.23E-03	9.27	22.95	406.76	0.90
3.00	0.34	0.31	1.13E-03	6.94E-04	0.89	0.40	3.21E-03	7.99	22.64	429.72	0.85
3.50	0.38	0.35	8.81E-04	6.21E-04	0.79	0.40	2.71E-03	7.73	23.65	504.07	0.76
4.00	0.46	0.41	6.35E-04	4.80E-04	0.61	0.35	2.25E-03	7.74	24.27	572.95	0.59
4.25	0.48	0.43	6.24E-04	4.92E-04	0.63	0.35	2.29E-03	8.57	24.69	608.70	0.61
4.25	0.53	0.49	6.45E-04	5.11E-04	0.65	0.38	2.27E-03	15.64	24.46	620.11	0.62
4.50	0.49	0.44	5.29E-04	4.30E-04	0.55	0.35	1.98E-03	7.28	24.74	648.09	0.53
5.00	0.57	0.52	4.10E-04	3.52E-04	0.45	0.33	1.65E-03	7.02	25.23	716.19	0.43
5.50	0.60	0.54	3.13E-04	2.84E-04	0.36	0.30	1.40E-03	6.96	25.58	792.12	0.35
6.00	0.68	0.62	2.30E-04	2.16E-04	0.28	0.28	1.10E-03	6.62	25.96	859.43	0.27
6.50	0.71	0.64	1.64E-04	1.61E-04	0.21	0.24	9.40E-04	6.71	26.21	936.14	0.20
7.00	0.80	0.72	1.47E-04	1.46E-04	0.19	0.23	8.58E-04	6.55	26.37	1002.70	0.18
7.09	0.88	0.81	8.36E-05	8.47E-05	0.11	0.18	6.31E-04	7.47	26.34	1034.50	0.10
7.16	0.80	0.72	1.24E-04	1.28E-04	0.16	0.22	7.95E-04	8.04	26.74	1025.50	0.16
7.50	0.82	0.74	7.15E-05	7.48E-05	0.10	0.18	5.50E-04	6.14	26.68	1080.20	0.09
8.00	0.91	0.83	4.86E-05	5.11E-05	0.07	0.15	4.46E-04	6.50	26.79	1145.90	0.06
8.50	0.93	0.84	1.24E-05	1.30E-05	0.02	0.05	3.84E-04	5.88	26.68	1224.20	0.02
9.00	1.03	0.93	1.96E-05	2.12E-05	0.03	0.11	2.65E-04	6.29	27.03	1289.10	0.03
9.21	1.14	1.05	8.92E-06	9.49E-06	0.01	0.03	5.21E-04	6.71	26.71	1343.80	0.01
9.26	1.04	0.94	9.62E-06	1.05E-05	0.01	0.05	3.42E-04	6.75	27.18	1326.80	0.01
9.50	1.04	0.94	1.77E-05	1.89E-05	0.02	0.09	2.80E-04	6.27	26.81	1368.20	0.02
10.00	1.14	1.03	-6.20E-06	-6.81E-06	-0.01	-0.05	1.93E-04	6.16	27.14	1432.40	-0.01
10.50	1.15	1.04	6.65E-06	7.17E-06	0.01	0.05	2.15E-04	6.27	26.90	1512.20	0.01

Table C.4: Flat Plate 16-Sample Coincident Data (cont)

y (mm)	y/δ_u	y/δ_M	ρ (kg/m ³)	T (K)	M	M'	u (m/s)	u/u_e	u/u	u'/u_e	Sk_u	Fl_u	γ_u	v (m/s)	v/u_e	v'/u	v'/u_e	Sk_v	Fl_v
11.00	1.25	1.14	0.26	116	2.78	0.07	600	1.00	9.69E-03	9.69E-03	-1.99	26.14	0.11	19.37	3.23E-02	1.07E-02	1.06E-02	-1.77	43.72
11.34	1.41	1.30	0.26	118	2.77	0.06	603	1.00	8.52E-03	8.52E-03	0.01	3.97	0.75	24.57	4.07E-02	1.23E-02	1.23E-02	-1.76	22.14
11.38	1.27	1.15	0.26	118	2.78	0.08	603	0.99	1.06E-02	1.05E-02	-7.05	136.67	0.02	18.34	3.02E-02	1.23E-02	1.22E-02	-2.81	35.81
11.50	1.26	1.14	0.26	116	2.78	0.07	598	1.00	9.71E-03	9.71E-03	-0.91	8.00	0.38	20.99	3.51E-02	1.01E-02	1.01E-02	0.23	5.51
12.00	1.37	1.24	0.26	116	2.78	0.06	600	1.00	8.08E-03	8.08E-03	-0.34	5.43	0.55	19.74	3.29E-02	1.01E-02	1.01E-02	-1.59	38.62
12.50	1.37	1.23	0.26	116	2.78	0.08	598	1.00	1.03E-02	1.03E-02	-4.08	77.24	0.04	20.53	3.43E-02	1.09E-02	1.09E-02	-3.63	71.03
12.76	1.38	1.46	0.25	120	2.74	0.10	600	1.00	1.42E-02	1.41E-02	-10.27	215.91	0.01	20.71	3.43E-02	1.45E-02	1.45E-02	-3.40	68.70
12.80	1.43	1.29	0.26	116	2.80	0.06	606	1.00	8.04E-03	8.03E-03	0.06	4.16	0.72	16.56	2.73E-02	1.44E-02	1.44E-02	-7.21	108.13
13.00	1.48	1.34	0.26	116	2.78	0.05	600	1.00	7.45E-03	7.44E-03	-0.75	15.11	0.20	19.39	3.23E-02	1.00E-02	1.00E-02	-2.79	64.82
13.50	1.48	1.33	0.26	116	2.77	0.06	598	1.00	7.59E-03	7.59E-03	-0.26	4.75	0.63	19.99	3.34E-02	8.72E-03	8.71E-03	-1.11	32.77
14.00	1.60	1.45	0.26	116	2.77	0.05	599	1.00	7.52E-03	7.51E-03	-0.78	16.51	0.18	18.08	3.01E-02	1.01E-02	1.00E-02	-3.06	61.66
14.21	1.76	1.62	0.25	120	2.74	0.07	600	0.99	9.70E-03	9.64E-03	-1.04	14.17	0.21	18.59	3.08E-02	1.18E-02	1.17E-02	-0.79	12.46
14.31	1.60	1.45	0.26	116	2.81	0.06	606	1.00	8.55E-03	8.55E-03	-1.96	24.80	0.12	17.66	2.91E-02	1.01E-02	1.01E-02	-0.77	9.54

Table C.4: Flat Plate 16-Sample Coincident Data (cont)

y (mm)	y/δ_u	y/δ_M	$-u'v'/u^2$	$-u'v'/u_e^2$	$-\rho u'v'/\tau_w$	R_{uv}	TKE/u_e^2	Δu (m/s)	u_{eff}/u^*	y^+	ρ/ρ_e
11.00	1.25	1.14	3.13E-06	3.45E-06	0.00	0.03	1.60E-04	6.11	27.17	1575.60	0.00
11.34	1.41	1.30	4.27E-06	4.53E-06	-0.01	-0.04	1.87E-04	6.35	26.69	1654.60	-0.01
11.38	1.27	1.15	1.82E-06	1.99E-06	0.00	0.01	2.07E-04	6.17	27.21	1630.50	0.00
11.50	1.26	1.14	4.31E-06	4.67E-06	0.01	0.04	1.49E-04	6.25	26.94	1656.20	0.01
12.00	1.37	1.24	-7.66E-07	-8.45E-07	0.00	-0.01	1.34E-04	6.04	27.17	1718.90	0.00
12.50	1.37	1.23	2.63E-06	2.86E-06	0.00	0.02	1.73E-04	6.09	26.95	1800.30	0.00
12.76	1.58	1.46	-1.63E-06	-1.69E-06	0.00	-0.01	3.09E-04	6.00	26.52	1861.80	0.00
12.80	1.43	1.29	2.81E-06	3.14E-06	0.00	0.02	2.42E-04	6.14	27.38	1833.10	0.00
13.00	1.48	1.34	1.28E-06	1.40E-06	0.00	0.02	1.28E-04	5.96	27.14	1862.10	0.00
13.50	1.48	1.33	7.71E-07	8.33E-07	0.00	0.01	1.05E-04	6.09	26.92	1944.30	0.00
14.00	1.60	1.45	-5.93E-07	-6.49E-07	0.00	-0.01	1.29E-04	5.96	27.11	2005.30	0.00
14.21	1.76	1.62	-5.02E-06	-5.20E-06	-0.01	-0.04	1.83E-04	6.01	26.50	2072.70	-0.01
14.31	1.60	1.45	-4.12E-06	-4.63E-06	-0.01	-0.05	1.40E-04	5.98	27.43	2049.60	-0.01

Table C.5: FPG 16-Sample Raw Data

y (mm)	y/δ_u	y/δ_M	ρ (kg/m ³)	T (K)	M	M'	u (m/s)	w/u_e	u'/u	u''/u_e	Sk_u	Fl_u	γ_u	v (m/s)	v/u_e	v'/u	v''/u_e	Sk_v	Fl_v
0.57	0.05	0.04	0.09	208	1.45	0.21	419	0.69	1.04E-01	7.13E-02	-0.12	3.07	0.98	0.00	0.00E+00	0.00E+00	0.00E+00	0.00	0.00
0.64	0.05	0.04	0.09	207	1.46	0.21	420	0.69	1.02E-01	7.10E-02	-0.21	2.99	1.00	0.00	0.00E+00	0.00E+00	0.00E+00	0.00	0.00
0.64	0.07	0.06	0.10	195	1.59	0.22	445	0.73	9.02E-02	6.62E-02	-0.04	2.90	1.03	0.00	0.00E+00	0.00E+00	0.00E+00	0.00	0.00
0.71	0.06	0.05	0.09	201	1.53	0.22	434	0.71	9.83E-02	7.01E-02	-0.27	2.93	1.02	0.00	0.00E+00	0.00E+00	0.00E+00	0.00	0.00
0.78	0.06	0.05	0.09	201	1.54	0.21	436	0.72	9.15E-02	6.59E-02	-0.17	3.01	1.00	0.00	0.00E+00	0.00E+00	0.00E+00	0.00	0.00
0.78	0.09	0.07	0.10	191	1.64	0.22	454	0.75	8.60E-02	6.45E-02	-0.03	2.77	1.08	0.00	0.00E+00	0.00E+00	0.00E+00	0.00	0.00
0.85	0.07	0.06	0.10	195	1.60	0.22	449	0.74	8.91E-02	6.57E-02	-0.29	2.92	1.03	0.00	0.00E+00	0.00E+00	0.00E+00	0.00	0.00
0.92	0.07	0.06	0.10	197	1.59	0.21	446	0.74	8.97E-02	6.61E-02	-0.13	3.01	1.00	0.00	0.00E+00	0.00E+00	0.00E+00	0.00	0.00
0.99	0.08	0.08	0.10	190	1.66	0.20	459	0.75	7.75E-02	5.84E-02	-0.13	3.06	0.98	0.00	0.00E+00	0.00E+00	0.00E+00	0.00	0.00
0.95	0.11	0.09	0.10	186	1.70	0.22	465	0.77	8.27E-02	6.36E-02	-0.02	2.66	1.13	0.00	0.00E+00	0.00E+00	0.00E+00	0.00	0.00
1.06	0.08	0.07	0.10	193	1.64	0.21	455	0.75	8.18E-02	6.14E-02	-0.09	2.90	1.03	0.00	0.00E+00	0.00E+00	0.00E+00	0.00	0.00
1.13	0.09	0.09	0.10	185	1.73	0.22	470	0.77	8.03E-02	6.19E-02	-0.04	2.83	1.06	0.00	0.00E+00	0.00E+00	0.00E+00	0.00	0.00
1.20	0.09	0.08	0.10	190	1.68	0.21	463	0.76	7.91E-02	6.04E-02	-0.05	2.93	1.02	0.00	0.00E+00	0.00E+00	0.00E+00	0.00	0.00
1.20	0.13	0.11	0.11	181	1.76	0.23	475	0.78	7.95E-02	6.23E-02	-0.03	2.57	1.17	0.00	0.00E+00	0.00E+00	0.00E+00	0.00	0.00
1.27	0.10	0.10	0.10	184	1.73	0.21	471	0.77	7.50E-02	5.81E-02	0.08	2.85	1.05	0.00	0.00E+00	0.00E+00	0.00E+00	0.00	0.00
1.27	0.10	0.09	0.10	195	1.59	0.19	446	0.73	7.65E-02	5.61E-02	0.01	2.89	1.04	0.00	0.00E+00	0.00E+00	0.00E+00	0.00	0.00
1.34	0.10	0.09	0.11	180	1.79	0.22	482	0.80	7.36E-02	5.85E-02	-0.03	2.74	1.09	0.00	0.00E+00	0.00E+00	0.00E+00	0.00	0.00
1.34	0.15	0.13	0.11	174	1.86	0.24	491	0.81	7.39E-02	5.99E-02	-0.18	2.84	1.06	0.00	0.00E+00	0.00E+00	0.00E+00	0.00	0.00
1.41	0.12	0.11	0.11	179	1.81	0.23	483	0.79	7.56E-02	6.00E-02	-0.10	2.75	1.09	0.00	0.00E+00	0.00E+00	0.00E+00	0.00	0.00
1.41	0.11	0.10	0.10	180	1.78	0.22	478	0.79	7.44E-02	5.84E-02	-0.04	2.81	1.07	0.00	0.00E+00	0.00E+00	0.00E+00	0.00	0.00
1.48	0.11	0.10	0.11	177	1.83	0.22	488	0.81	7.15E-02	5.76E-02	-0.05	2.84	1.06	0.00	0.00E+00	0.00E+00	0.00E+00	0.00	0.00
1.56	0.12	0.11	0.11	176	1.83	0.22	485	0.80	7.18E-02	5.73E-02	-0.01	2.73	1.10	0.00	0.00E+00	0.00E+00	0.00E+00	0.00	0.00
1.63	0.13	0.12	0.11	176	1.84	0.23	489	0.80	7.29E-02	5.86E-02	-0.08	2.82	1.06	0.00	0.00E+00	0.00E+00	0.00E+00	0.00	0.00
1.63	0.18	0.15	0.12	169	1.93	0.24	501	0.83	7.06E-02	5.84E-02	-0.16	2.83	1.06	0.00	0.00E+00	0.00E+00	0.00E+00	0.00	0.00
1.70	0.13	0.12	0.11	175	1.84	0.22	488	0.80	7.12E-02	5.72E-02	-0.02	2.75	1.09	0.00	0.00E+00	0.00E+00	0.00E+00	0.00	0.00
1.77	0.13	0.12	0.11	172	1.90	0.23	499	0.82	6.86E-02	5.65E-02	-0.04	2.72	1.10	0.00	0.00E+00	0.00E+00	0.00E+00	0.00	0.00
1.84	0.15	0.14	0.11	172	1.90	0.23	499	0.82	6.81E-02	5.57E-02	0.04	2.76	1.09	0.00	0.00E+00	0.00E+00	0.00E+00	0.00	0.00
1.98	0.15	0.14	0.11	170	1.91	0.23	498	0.82	6.87E-02	5.63E-02	-0.02	2.73	1.10	0.00	0.00E+00	0.00E+00	0.00E+00	0.00	0.00
1.98	0.22	0.19	0.12	164	2.00	0.24	511	0.84	6.69E-02	5.64E-02	-0.17	2.72	1.10	0.00	0.00E+00	0.00E+00	0.00E+00	0.00	0.00
2.13	0.18	0.16	0.11	169	1.93	0.23	503	0.83	6.79E-02	5.61E-02	-0.08	2.62	1.14	0.00	0.00E+00	0.00E+00	0.00E+00	0.00	0.00
2.13	0.16	0.15	0.11	168	1.96	0.24	507	0.84	6.70E-02	5.61E-02	0.00	2.65	1.13	0.00	0.00E+00	0.00E+00	0.00E+00	0.00	0.00
2.27	0.18	0.16	0.11	167	1.95	0.23	504	0.83	6.68E-02	5.54E-02	0.02	2.67	1.12	0.00	0.00E+00	0.00E+00	0.00E+00	0.00	0.00
2.48	0.20	0.19	0.12	163	2.01	0.24	515	0.85	6.55E-02	5.54E-02	-0.06	2.46	1.22	0.00	0.00E+00	0.00E+00	0.00E+00	0.00	0.00
2.56	0.20	0.18	0.12	162	2.01	0.24	514	0.84	6.57E-02	5.55E-02	-0.05	2.60	1.15	0.00	0.00E+00	0.00E+00	0.00E+00	0.00	0.00
2.84	0.23	0.22	0.12	159	2.08	0.25	524	0.86	6.40E-02	5.51E-02	-0.05	2.60	1.15	0.00	0.00E+00	0.00E+00	0.00E+00	0.00	0.00
2.84	0.21	0.20	0.12	160	2.07	0.24	522	0.86	6.25E-02	5.39E-02	-0.02	2.56	1.17	0.00	0.00E+00	0.00E+00	0.00E+00	0.00	0.00
2.84	0.31	0.27	0.13	153	2.15	0.26	532	0.88	6.05E-02	5.31E-02	-0.31	2.71	1.11	0.00	0.00E+00	0.00E+00	0.00E+00	0.00	0.00
3.19	0.25	0.22	0.12	157	2.09	0.25	525	0.86	6.25E-02	5.39E-02	-0.08	2.51	1.20	0.00	0.00E+00	0.00E+00	0.00E+00	0.00	0.00
3.55	0.29	0.27	0.12	168	1.95	0.22	506	0.83	6.14E-02	5.10E-02	-0.20	2.49	1.21	0.00	0.00E+00	0.00E+00	0.00E+00	0.00	0.00
3.55	0.26	0.24	0.13	152	2.18	0.26	538	0.89	5.92E-02	5.25E-02	-0.18	2.53	1.19	0.00	0.00E+00	0.00E+00	0.00E+00	0.00	0.00
3.90	0.30	0.27	0.13	151	2.18	0.26	536	0.88	5.98E-02	5.26E-02	-0.15	2.51	1.20	0.00	0.00E+00	0.00E+00	0.00E+00	0.00	0.00

Table C.5: FPG 16-Sample Raw Data (cont')

y (mm)	y/δ_u	y/δ_M	$-u'v'/u^2$	$-u'v'/u_e^2$	$-\rho u'v'/\tau_w$	R_w	TKE/u_e^2	Δu (m/s)	u_{eff}/u^*	y^+	ρ/ρ_e
0.57	0.05	0.04	0.00E+00	0.00E+00	0.00E+00	0.00	2.55E-03	48.69	17.09	50.72	0.43
0.64	0.05	0.04	0.00E+00	0.00E+00	0.00E+00	0.00	2.52E-03	44.78	16.78	58.17	0.43
0.64	0.07	0.06	0.00E+00	0.00E+00	0.00E+00	0.00	2.19E-03	46.66	17.83	58.56	0.45
0.71	0.06	0.05	0.00E+00	0.00E+00	0.00E+00	0.00	2.46E-03	12.05	17.79	63.40	0.46
0.78	0.06	0.05	0.00E+00	0.00E+00	0.00E+00	0.00	2.17E-03	11.33	17.55	71.10	0.44
0.78	0.09	0.07	0.00E+00	0.00E+00	0.00E+00	0.00	2.08E-03	8.43	18.27	71.58	0.47
0.85	0.07	0.06	0.00E+00	0.00E+00	0.00E+00	0.00	2.16E-03	11.62	18.46	76.08	0.48
0.92	0.07	0.06	0.00E+00	0.00E+00	0.00E+00	0.00	2.18E-03	9.67	18.01	84.02	0.45
0.99	0.08	0.08	0.00E+00	0.00E+00	0.00E+00	0.00	1.70E-03	11.36	18.95	88.76	0.49
0.99	0.11	0.09	0.00E+00	0.00E+00	0.00E+00	0.00	2.02E-03	8.16	18.80	91.10	0.48
1.06	0.08	0.07	0.00E+00	0.00E+00	0.00E+00	0.00	1.89E-03	9.45	18.42	96.95	0.46
1.13	0.09	0.09	0.00E+00	0.00E+00	0.00E+00	0.00	2.55E-03	10.10	19.49	101.44	0.51
1.20	0.09	0.08	0.00E+00	0.00E+00	0.00E+00	0.00	1.82E-03	14.45	18.76	109.88	0.47
1.20	0.13	0.11	0.00E+00	0.00E+00	0.00E+00	0.00	1.94E-03	11.08	19.25	110.62	0.50
1.27	0.10	0.10	0.00E+00	0.00E+00	0.00E+00	0.00	2.29E-03	10.96	19.56	114.13	0.51
1.27	0.10	0.09	0.00E+00	0.00E+00	0.00E+00	0.00	2.22E-03	30.00	18.54	112.92	0.49
1.34	0.10	0.09	0.00E+00	0.00E+00	0.00E+00	0.00	2.27E-03	16.46	19.71	122.80	0.50
1.34	0.15	0.13	0.00E+00	0.00E+00	0.00E+00	0.00	2.47E-03	12.50	20.01	123.64	0.52
1.41	0.12	0.11	0.00E+00	0.00E+00	0.00E+00	0.00	2.43E-03	12.19	20.14	126.80	0.53
1.41	0.11	0.10	0.00E+00	0.00E+00	0.00E+00	0.00	2.30E-03	17.01	20.13	125.46	0.53
1.48	0.11	0.10	0.00E+00	0.00E+00	0.00E+00	0.00	2.24E-03	10.82	19.99	135.73	0.51
1.56	0.12	0.11	0.00E+00	0.00E+00	0.00E+00	0.00	2.25E-03	8.75	20.50	138.01	0.54
1.63	0.13	0.12	0.00E+00	0.00E+00	0.00E+00	0.00	2.33E-03	10.69	20.45	145.82	0.54
1.63	0.18	0.15	0.00E+00	0.00E+00	0.00E+00	0.00	2.40E-03	9.70	20.51	149.66	0.54
1.70	0.13	0.12	0.00E+00	0.00E+00	0.00E+00	0.00	2.24E-03	8.55	20.65	150.56	0.55
1.77	0.13	0.12	0.00E+00	0.00E+00	0.00E+00	0.00	2.18E-03	9.85	20.36	161.58	0.53
1.84	0.15	0.14	0.00E+00	0.00E+00	0.00E+00	0.00	2.19E-03	9.74	20.92	164.84	0.55
1.98	0.15	0.14	0.00E+00	0.00E+00	0.00E+00	0.00	2.21E-03	8.64	21.17	175.65	0.57
1.98	0.22	0.19	0.00E+00	0.00E+00	0.00E+00	0.00	2.29E-03	9.40	21.02	182.20	0.56
2.13	0.18	0.16	0.00E+00	0.00E+00	0.00E+00	0.00	2.30E-03	9.87	21.14	191.09	0.56
2.13	0.18	0.15	0.00E+00	0.00E+00	0.00E+00	0.00	2.17E-03	9.03	20.95	194.80	0.54
2.27	0.18	0.16	0.00E+00	0.00E+00	0.00E+00	0.00	2.17E-03	8.96	21.46	201.63	0.58
2.48	0.20	0.19	0.00E+00	0.00E+00	0.00E+00	0.00	2.15E-03	11.03	21.76	222.79	0.59
2.56	0.20	0.18	0.00E+00	0.00E+00	0.00E+00	0.00	2.18E-03	8.83	21.96	226.72	0.60
2.84	0.23	0.22	0.00E+00	0.00E+00	0.00E+00	0.00	2.17E-03	4.43	22.22	254.49	0.61
2.84	0.21	0.20	0.00E+00	0.00E+00	0.00E+00	0.00	2.09E-03	9.61	21.72	259.44	0.58
2.84	0.31	0.27	0.00E+00	0.00E+00	0.00E+00	0.00	2.08E-03	9.38	22.09	261.20	0.62
3.19	0.25	0.22	0.00E+00	0.00E+00	0.00E+00	0.00	2.10E-03	8.47	22.54	283.18	0.63
3.55	0.29	0.27	0.00E+00	0.00E+00	0.00E+00	0.00	1.95E-03	8.69	21.28	317.89	0.58
3.55	0.26	0.24	0.00E+00	0.00E+00	0.00E+00	0.00	2.02E-03	9.24	22.52	324.07	0.62
3.90	0.30	0.27	0.00E+00	0.00E+00	0.00E+00	0.00	2.03E-03	8.41	23.15	345.91	0.66

Table C.5: FPG 16-Sample Raw Data (cont')

y (mm)	y/δ_u	y/δ_M	ρ (kg/m ³)	T (K)	M	M'	u (m/s)	u/u_e	u/u	u/u_e	Sk_u	Fl_u	γ_u	v (m/s)	v/u_e	v/u	v/u_e	Sk_v	Fl_v
4.25	0.32	0.29	0.14	147	2.25	0.26	546	0.90	5.70E-02	5.13E-02	-0.23	2.54	1.18	32.77	5.41E-02	2.81E-02	2.53E-02	-0.21	5.28
4.25	0.47	0.40	0.15	138	2.37	0.26	558	0.92	4.94E-02	4.55E-02	-0.66	3.27	0.92	34.53	5.70E-02	2.67E-02	2.46E-02	-0.28	6.09
4.96	0.41	0.38	0.14	145	2.29	0.27	550	0.90	5.68E-02	5.13E-02	-0.34	2.54	1.18	35.62	5.85E-02	2.81E-02	2.54E-02	-0.06	3.36
4.96	0.38	0.35	0.14	144	2.28	0.27	548	0.90	5.62E-02	5.06E-02	-0.29	2.60	1.15	33.81	5.56E-02	2.83E-02	2.54E-02	-0.21	5.19
5.67	0.42	0.39	0.14	143	2.31	0.26	553	0.91	5.38E-02	4.91E-02	-0.32	2.62	1.15	35.63	5.88E-02	2.79E-02	2.54E-02	-0.16	4.97
6.38	0.53	0.48	0.15	135	2.45	0.28	567	0.93	5.06E-02	4.71E-02	-0.59	2.98	1.01	41.19	6.76E-02	2.38E-02	2.22E-02	0.03	3.14
6.38	0.49	0.45	0.15	137	2.39	0.27	560	0.92	5.06E-02	4.66E-02	-0.41	2.78	1.08	39.19	6.44E-02	2.64E-02	2.43E-02	-0.29	6.17
7.09	0.53	0.49	0.15	136	2.42	0.26	565	0.93	4.84E-02	4.51E-02	-0.50	2.81	1.07	40.75	6.73E-02	2.61E-02	2.43E-02	-0.38	6.91
7.09	0.78	0.67	0.19	119	2.72	0.20	592	0.98	2.90E-02	2.83E-02	-1.75	9.40	0.32	39.05	6.43E-02	1.99E-02	1.94E-02	-0.79	12.34
7.80	0.64	0.59	0.16	127	2.58	0.27	581	0.95	4.26E-02	4.06E-02	-0.90	4.48	0.67	46.28	7.60E-02	2.41E-02	2.30E-02	-1.32	17.35
7.80	0.60	0.54	0.16	130	2.52	0.26	573	0.94	4.47E-02	4.21E-02	-0.66	3.11	0.96	44.73	7.35E-02	2.44E-02	2.30E-02	-0.59	9.37
8.51	0.63	0.59	0.17	127	2.57	0.25	580	0.96	4.08E-02	3.91E-02	-0.84	3.50	0.86	46.27	7.64E-02	2.36E-02	2.25E-02	-0.60	9.73
9.21	0.71	0.64	0.17	123	2.63	0.25	584	0.96	3.82E-02	3.67E-02	-0.94	3.86	0.78	50.00	8.22E-02	2.16E-02	2.07E-02	-1.03	15.09
9.21	1.01	0.87	0.21	112	2.84	0.13	603	1.00	1.65E-02	1.65E-02	-4.06	51.41	0.06	40.51	6.69E-02	1.68E-02	1.67E-02	-1.33	25.11
9.92	0.73	0.68	0.18	122	2.66	0.23	589	0.97	3.43E-02	3.34E-02	-1.10	4.20	0.71	51.52	8.50E-02	1.98E-02	1.93E-02	-1.01	15.92
10.64	0.88	0.81	0.19	117	2.77	0.24	597	0.98	3.21E-02	3.15E-02	-2.19	12.98	0.23	57.09	9.38E-02	1.74E-02	1.70E-02	-1.72	29.27
10.64	0.82	0.74	0.18	118	2.73	0.22	593	0.97	3.10E-02	3.02E-02	-1.32	5.27	0.57	54.69	8.99E-02	1.89E-02	1.84E-02	-1.37	20.00
11.34	0.84	0.78	0.19	119	2.73	0.21	594	0.98	2.90E-02	2.84E-02	-1.32	5.05	0.59	55.83	9.21E-02	1.74E-02	1.70E-02	-1.40	22.43
11.34	1.24	1.07	0.23	110	2.88	0.11	606	1.00	1.35E-02	1.35E-02	-7.50	143.49	0.02	49.12	8.11E-02	1.47E-02	1.47E-02	-1.56	34.84
12.05	0.93	0.84	0.19	112	2.86	0.19	603	0.99	2.44E-02	2.41E-02	-1.98	11.18	0.27	62.24	1.02E-01	1.57E-02	1.56E-02	-2.44	43.58
12.40	1.02	0.94	0.20	110	2.90	0.16	607	1.00	1.97E-02	1.96E-02	-2.40	14.17	0.21	61.25	1.01E-01	1.45E-02	1.45E-02	-3.34	66.49
12.76	0.95	0.88	0.20	115	2.81	0.16	601	0.99	2.07E-02	2.06E-02	-2.04	12.27	0.24	60.26	9.95E-02	1.53E-02	1.52E-02	-2.93	53.98
12.76	1.40	1.21	0.23	111	2.87	0.11	604	1.00	1.35E-02	1.35E-02	-9.58	191.96	0.02	47.81	7.89E-02	1.58E-02	1.58E-02	-1.40	29.91
13.47	1.04	0.94	0.20	109	2.91	0.16	607	1.00	1.87E-02	1.87E-02	-3.04	28.73	0.10	66.38	1.09E-01	1.45E-02	1.44E-02	-4.55	84.10
14.17	1.17	1.08	0.21	109	2.92	0.12	609	1.00	1.44E-02	1.44E-02	-4.44	70.06	0.04	65.23	1.07E-01	1.20E-02	1.20E-02	-1.78	45.15
14.17	1.05	0.98	0.21	112	2.87	0.12	605	1.00	1.43E-02	1.43E-02	-2.31	17.52	0.17	63.69	1.05E-01	1.36E-02	1.36E-02	-4.71	90.76
14.89	1.15	1.04	0.20	108	2.94	0.12	608	1.00	1.37E-02	1.37E-02	-3.88	53.82	0.06	70.36	1.16E-01	1.60E-02	1.60E-02	-1.84	40.69
15.60	1.16	1.08	0.22	111	2.88	0.10	606	1.00	1.18E-02	1.18E-02	-6.23	133.30	0.02	66.17	1.09E-01	1.37E-02	1.37E-02	-7.46	142.93
15.95	1.31	1.21	0.21	110	2.92	0.09	609	1.00	1.04E-02	1.04E-02	-3.79	60.36	0.05	67.67	1.11E-01	1.20E-02	1.20E-02	-4.40	107.21
16.30	1.26	1.14	0.21	108	2.94	0.11	608	1.00	1.19E-02	1.19E-02	-7.06	159.68	0.02	73.59	1.21E-01	1.56E-02	1.56E-02	-9.85	171.35
17.01	1.26	1.17	0.22	112	2.87	0.09	605	1.00	1.02E-02	1.02E-02	-4.49	104.63	0.03	67.09	1.11E-01	1.58E-02	1.58E-02	-8.87	145.86
17.72	1.46	1.34	0.21	111	2.89	0.08	606	1.00	9.43E-03	9.39E-03	-8.81	311.73	0.01	67.85	1.11E-01	1.29E-02	1.29E-02	-5.29	114.06
17.72	1.37	1.24	0.21	108	2.93	0.10	607	1.00	1.11E-02	1.10E-02	-7.92	199.59	0.02	76.10	1.25E-01	1.37E-02	1.37E-02	-9.66	193.36

Table C.6: FPG 16-Sample Coincident Data

γ (mm)	γ/δ_u	γ/δ_M	ρ (kg/m ³)	T (K)	M	M'	u (m/s)	u/u_e	u'/u	u'/u_e	Sk_u	Fl_u	γ_u	ν (m/s)	ν/u_e	ν/u	ν/u_e
1.27	0.10	0.10	0.10	186	1.72	0.19	469	0.77	6.82E-02	5.25E-02	-0.02	2.69	1.11	21.07	3.46E-02	3.13E-02	2.41E-02
1.27	0.10	0.09	0.10	195	1.59	0.19	445	0.73	7.69E-02	5.63E-02	0.00	2.80	1.07	20.40	3.35E-02	3.44E-02	2.52E-02
1.34	0.10	0.09	0.11	180	1.80	0.22	482	0.80	7.21E-02	5.74E-02	-0.03	2.78	1.08	21.52	3.55E-02	2.94E-02	2.34E-02
1.34	0.15	0.13	0.11	174	1.86	0.23	490	0.81	7.36E-02	5.95E-02	-0.20	2.80	1.07	24.12	3.98E-02	3.10E-02	2.50E-02
1.41	0.12	0.11	0.10	181	1.77	0.21	478	0.79	7.30E-02	5.73E-02	-0.08	2.77	1.08	22.74	3.74E-02	3.18E-02	2.50E-02
1.41	0.11	0.10	0.10	180	1.78	0.22	478	0.79	7.42E-02	5.83E-02	-0.09	2.79	1.08	20.36	3.35E-02	3.01E-02	2.37E-02
1.48	0.11	0.10	0.11	177	1.83	0.22	488	0.80	6.96E-02	5.60E-02	-0.05	2.86	1.05	21.71	3.58E-02	2.94E-02	2.36E-02
1.56	0.12	0.11	0.11	177	1.82	0.22	485	0.80	7.05E-02	5.63E-02	0.02	2.67	1.12	20.68	3.40E-02	3.02E-02	2.41E-02
1.63	0.13	0.12	0.11	176	1.85	0.23	490	0.80	7.33E-02	5.90E-02	-0.27	2.93	1.02	23.50	3.86E-02	3.13E-02	2.51E-02
1.63	0.18	0.15	0.12	169	1.92	0.24	500	0.83	7.01E-02	5.79E-02	-0.19	2.87	1.04	25.63	4.23E-02	3.11E-02	2.56E-02
1.70	0.13	0.12	0.11	175	1.85	0.22	489	0.80	7.00E-02	5.62E-02	-0.01	2.70	1.11	21.50	3.53E-02	3.01E-02	2.42E-02
1.77	0.13	0.12	0.11	171	1.91	0.23	500	0.82	6.73E-02	5.55E-02	-0.07	2.71	1.11	23.25	3.84E-02	2.88E-02	2.38E-02
1.84	0.15	0.14	0.11	172	1.90	0.22	498	0.82	6.63E-02	5.42E-02	0.14	2.67	1.13	24.31	3.99E-02	2.90E-02	2.37E-02
1.98	0.15	0.14	0.11	170	1.91	0.23	498	0.82	6.83E-02	5.60E-02	-0.04	2.70	1.11	22.84	3.75E-02	3.02E-02	2.47E-02
1.98	0.22	0.19	0.12	164	1.99	0.24	510	0.84	6.67E-02	5.62E-02	-0.16	2.70	1.11	27.35	4.52E-02	3.04E-02	2.56E-02
2.13	0.18	0.16	0.11	170	1.93	0.22	502	0.82	6.45E-02	5.32E-02	-0.04	2.44	1.23	25.93	4.26E-02	2.85E-02	2.35E-02
2.13	0.16	0.15	0.11	168	1.95	0.24	506	0.84	6.79E-02	5.67E-02	0.05	2.67	1.13	24.48	4.04E-02	2.90E-02	2.42E-02
2.27	0.18	0.16	0.11	168	1.94	0.23	503	0.83	6.64E-02	5.49E-02	0.05	2.67	1.12	24.03	3.95E-02	2.94E-02	2.43E-02
2.48	0.20	0.19	0.12	163	2.02	0.24	516	0.85	6.50E-02	5.50E-02	0.03	2.65	1.13	26.66	4.38E-02	2.90E-02	2.46E-02
2.56	0.20	0.18	0.12	163	2.01	0.24	513	0.84	6.51E-02	5.49E-02	-0.05	2.58	1.16	25.50	4.19E-02	2.97E-02	2.50E-02
2.84	0.23	0.22	0.12	161	2.05	0.24	520	0.85	6.31E-02	5.39E-02	-0.07	2.44	1.23	27.84	4.57E-02	2.95E-02	2.52E-02
2.84	0.21	0.20	0.12	160	2.07	0.24	522	0.86	6.13E-02	5.29E-02	-0.02	2.57	1.17	27.60	4.55E-02	2.87E-02	2.47E-02
2.84	0.31	0.27	0.13	153	2.14	0.25	531	0.88	5.99E-02	5.25E-02	-0.29	2.73	1.10	31.05	5.13E-02	2.89E-02	2.53E-02
3.19	0.25	0.22	0.12	157	2.09	0.25	524	0.86	6.26E-02	5.39E-02	-0.08	2.51	1.20	27.73	4.56E-02	2.92E-02	2.51E-02
3.55	0.29	0.27	0.12	160	2.06	0.24	521	0.86	6.15E-02	5.26E-02	-0.09	2.71	1.11	31.82	5.23E-02	2.81E-02	2.40E-02
3.55	0.26	0.24	0.13	152	2.17	0.25	537	0.89	5.89E-02	5.22E-02	-0.14	2.57	1.17	29.82	4.92E-02	2.75E-02	2.43E-02
3.90	0.30	0.27	0.13	151	2.17	0.26	534	0.88	5.93E-02	5.21E-02	-0.12	2.54	1.18	30.72	5.05E-02	2.87E-02	2.52E-02
4.25	0.32	0.29	0.14	148	2.24	0.26	544	0.90	5.71E-02	5.13E-02	-0.20	2.55	1.18	33.12	5.47E-02	2.76E-02	2.48E-02
4.25	0.47	0.40	0.15	139	2.36	0.26	557	0.92	4.98E-02	4.58E-02	-0.62	3.14	0.95	35.24	5.82E-02	2.58E-02	2.37E-02
4.96	0.41	0.38	0.14	145	2.29	0.26	550	0.90	5.50E-02	4.97E-02	-0.38	2.65	1.13	36.14	5.94E-02	2.79E-02	2.52E-02
4.96	0.38	0.35	0.14	145	2.26	0.26	546	0.90	5.58E-02	5.01E-02	-0.26	2.55	1.17	34.21	5.62E-02	2.80E-02	2.51E-02
5.67	0.42	0.39	0.14	144	2.29	0.26	551	0.91	5.37E-02	4.88E-02	-0.24	2.51	1.19	35.98	5.94E-02	2.78E-02	2.53E-02

Table C.6: FPG 16-Sample Coincident Data (cont)

y (mm)	y/δ_u	y/δ_M	Sk_v	Fl_v	$-u^2/v^2$	$-u^2/v^2$	$-u^2/v^2$	R_{uv}	TKE/u_e^2	Δu (m/s)	u_{eff}/u^*	y^*
1.27	0.10	0.10	-0.19	3.09	7.21E-04	2.15E-04	3.66E-01	0.34	1.96E-03	47.11	16.65	133.27
1.27	0.10	0.09	0.06	3.19	6.42E-04	1.66E-04	2.78E-01	0.24	2.22E-03	30.00	15.86	131.86
1.34	0.10	0.09	-0.01	3.30	6.22E-04	1.97E-04	3.47E-01	0.29	2.19E-03	46.06	16.89	143.40
1.34	0.15	0.13	0.07	3.19	7.06E-04	2.36E-04	4.27E-01	0.31	2.40E-03	40.63	17.10	144.38
1.41	0.12	0.11	0.15	3.38	7.46E-04	2.37E-04	4.04E-01	0.32	2.26E-03	13.32	17.03	148.07
1.41	0.11	0.10	0.06	3.60	5.77E-04	1.87E-04	3.14E-01	0.26	2.26E-03	17.10	17.24	146.51
1.48	0.11	0.10	0.09	3.35	5.73E-04	1.89E-04	3.32E-01	0.28	2.13E-03	10.89	17.11	158.50
1.56	0.12	0.11	-0.05	4.45	5.29E-04	1.81E-04	3.02E-01	0.25	2.16E-03	8.74	17.55	161.16
1.63	0.13	0.12	-0.13	3.21	6.78E-04	2.34E-04	3.99E-01	0.30	2.37E-03	12.30	17.53	170.28
1.63	0.18	0.15	0.07	3.34	6.12E-04	2.21E-04	4.00E-01	0.28	2.33E-03	9.71	17.53	174.77
1.70	0.13	0.12	0.05	3.31	4.78E-04	1.67E-04	2.80E-01	0.23	2.16E-03	8.58	17.69	175.82
1.77	0.13	0.12	-0.09	3.47	3.79E-04	1.36E-04	2.40E-01	0.20	2.11E-03	9.71	17.62	188.69
1.84	0.15	0.14	-0.08	2.85	5.38E-04	1.97E-04	3.36E-01	0.28	2.03E-03	9.45	17.88	192.49
1.98	0.15	0.14	-0.14	4.41	3.81E-04	1.43E-04	2.40E-01	0.18	2.18E-03	8.44	18.12	205.12
1.98	0.22	0.19	0.02	3.22	4.82E-04	1.89E-04	3.41E-01	0.24	2.23E-03	9.39	17.96	212.76
2.13	0.18	0.16	0.06	3.11	4.12E-04	1.56E-04	2.66E-01	0.22	1.96E-03	10.36	18.07	223.15
2.13	0.16	0.15	-0.11	4.74	3.84E-04	1.45E-04	2.56E-01	0.20	2.20E-03	9.00	17.89	227.48
2.27	0.18	0.16	0.03	3.23	3.47E-04	1.35E-04	2.26E-01	0.18	2.10E-03	8.91	18.33	235.45
2.48	0.20	0.19	-0.08	3.09	3.06E-04	1.28E-04	2.19E-01	0.16	2.12E-03	10.27	18.67	260.16
2.56	0.20	0.18	-0.04	3.65	2.56E-04	1.08E-04	1.80E-01	0.13	2.14E-03	8.92	18.79	264.75
2.84	0.23	0.22	0.17	2.74	2.80E-04	1.21E-04	2.06E-01	0.15	2.09E-03	6.97	18.84	297.18
2.84	0.21	0.20	-0.10	3.61	2.21E-04	9.53E-05	1.68E-01	0.13	2.01E-03	9.65	18.61	302.96
2.84	0.31	0.27	-0.01	3.59	3.45E-04	1.61E-04	2.91E-01	0.20	2.02E-03	9.39	18.87	305.01
3.19	0.25	0.22	0.03	3.48	2.00E-04	9.13E-05	1.53E-01	0.11	2.08E-03	8.39	19.27	330.68
3.55	0.29	0.27	-0.19	3.17	1.51E-04	6.66E-05	1.14E-01	0.09	1.96E-03	9.16	18.90	371.22
3.55	0.26	0.24	0.06	3.22	9.96E-05	4.82E-05	8.48E-02	0.06	1.95E-03	9.06	19.24	378.43
3.90	0.30	0.27	0.05	3.28	1.21E-04	5.99E-05	1.00E-01	0.07	1.99E-03	8.34	19.76	403.94
4.25	0.32	0.29	0.04	3.28	7.52E-05	3.90E-05	6.86E-02	0.05	1.93E-03	7.90	19.59	453.90
4.25	0.47	0.40	0.02	3.59	1.43E-04	8.40E-05	1.52E-01	0.11	1.61E-03	9.14	20.06	456.99
4.96	0.41	0.38	-0.06	3.24	5.74E-05	3.19E-05	5.45E-02	0.04	1.87E-03	10.34	20.23	519.29
4.96	0.38	0.35	-0.02	3.47	2.48E-05	1.36E-05	2.27E-02	0.02	1.89E-03	8.39	20.30	513.82
5.67	0.42	0.39	-0.04	3.96	-2.87E-05	-1.60E-05	-2.82E-02	-0.02	1.83E-03	8.26	19.89	604.85

Table C.6: FPG 16-Sample Coincident Data (cont)

y (mm)	y/δ_u	y/δ_M	ρ (kg/m ³)	T (K)	M	M'	u (m/s)	w/u_e	u'/u	u'/u_e	Sk_u	Fl_u	γ_u	v (m/s)	v/u_e	v'/u	v'/u_e
6.38	0.53	0.48	0.15	134	2.45	0.27	568	0.93	4.80E-02	4.48E-02	-0.57	2.90	1.03	41.87	6.88E-02	2.23E-02	2.08E-02
6.38	0.49	0.45	0.14	138	2.38	0.27	559	0.92	5.06E-02	4.65E-02	-0.35	2.67	1.12	39.55	6.50E-02	2.60E-02	2.39E-02
7.09	0.53	0.49	0.15	137	2.41	0.26	564	0.93	4.91E-02	4.57E-02	-0.49	2.77	1.08	40.94	6.76E-02	2.56E-02	2.38E-02
7.09	0.78	0.67	0.19	119	2.71	0.20	592	0.98	2.87E-02	2.80E-02	-1.47	6.09	0.49	39.87	6.58E-02	1.91E-02	1.86E-02
7.80	0.64	0.59	0.16	128	2.56	0.26	579	0.95	4.30E-02	4.09E-02	-0.61	2.80	1.07	46.94	7.71E-02	2.30E-02	2.19E-02
7.80	0.60	0.54	0.16	131	2.50	0.26	572	0.94	4.53E-02	4.25E-02	-0.61	2.96	1.01	45.18	7.43E-02	2.36E-02	2.21E-02
8.51	0.63	0.59	0.17	128	2.56	0.25	579	0.96	4.07E-02	3.89E-02	-0.79	3.40	0.88	46.83	7.73E-02	2.25E-02	2.15E-02
9.21	0.71	0.64	0.17	124	2.62	0.25	583	0.96	3.84E-02	3.68E-02	-0.88	3.49	0.86	50.21	8.25E-02	2.10E-02	2.01E-02
9.21	1.01	0.87	0.21	112	2.84	0.12	603	1.00	1.44E-02	1.44E-02	-2.03	14.20	0.21	41.95	6.93E-02	1.63E-02	1.62E-02
9.92	0.73	0.68	0.18	123	2.66	0.23	588	0.97	3.43E-02	3.33E-02	-1.09	4.13	0.73	51.74	8.54E-02	1.91E-02	1.86E-02
10.64	0.88	0.81	0.19	117	2.76	0.22	597	0.98	3.06E-02	3.00E-02	-1.43	5.83	0.51	57.45	9.44E-02	1.57E-02	1.54E-02
10.64	0.82	0.74	0.18	119	2.72	0.22	592	0.97	3.14E-02	3.05E-02	-1.26	4.73	0.63	54.88	9.02E-02	1.79E-02	1.74E-02
11.34	0.84	0.78	0.19	119	2.72	0.21	593	0.98	2.95E-02	2.89E-02	-1.29	4.77	0.63	56.00	9.24E-02	1.63E-02	1.60E-02
11.34	1.24	1.07	0.23	110	2.89	0.10	606	1.00	1.15E-02	1.15E-02	-7.30	182.36	0.02	50.26	8.30E-02	1.44E-02	1.44E-02
12.05	0.93	0.84	0.19	112	2.86	0.19	603	0.99	2.45E-02	2.43E-02	-1.81	9.18	0.33	62.52	1.03E-01	1.48E-02	1.46E-02
12.40	1.02	0.94	0.20	111	2.89	0.16	607	1.00	1.97E-02	1.96E-02	-2.06	9.23	0.32	61.67	1.01E-01	1.38E-02	1.37E-02
12.76	0.95	0.88	0.20	115	2.81	0.16	601	0.99	2.05E-02	2.03E-02	-1.81	7.65	0.39	60.34	9.96E-02	1.42E-02	1.40E-02
12.76	1.40	1.21	0.24	111	2.87	0.08	605	1.00	9.66E-03	9.64E-03	-4.31	89.12	0.03	49.14	8.11E-02	1.55E-02	1.55E-02
13.47	1.04	0.94	0.20	109	2.91	0.15	606	1.00	1.79E-02	1.79E-02	-2.05	9.75	0.31	66.72	1.10E-01	1.26E-02	1.26E-02
14.17	1.17	1.08	0.21	109	2.92	0.12	609	1.00	1.38E-02	1.38E-02	-3.97	51.21	0.06	65.67	1.08E-01	1.14E-02	1.14E-02
14.17	1.05	0.98	0.21	112	2.86	0.11	604	1.00	1.40E-02	1.40E-02	-2.18	11.73	0.26	63.81	1.03E-01	1.14E-02	1.14E-02
14.17	1.55	1.34	0.24	112	2.85	0.07	603	1.00	8.63E-03	8.59E-03	-3.10	66.09	0.05	49.40	8.16E-02	1.55E-02	1.55E-02
14.89	1.15	1.04	0.20	108	2.94	0.11	608	1.00	1.24E-02	1.24E-02	-2.39	17.99	0.17	70.91	1.17E-01	1.10E-02	1.10E-02
15.60	1.16	1.08	0.22	111	2.88	0.08	606	1.00	9.51E-03	9.51E-03	-1.37	10.58	0.28	66.34	1.09E-01	1.12E-02	1.12E-02
15.95	1.31	1.21	0.21	110	2.92	0.08	609	1.00	9.19E-03	9.19E-03	-1.61	13.21	0.23	67.97	1.12E-01	1.23E-02	1.23E-02
16.30	1.26	1.14	0.21	108	2.94	0.10	608	1.00	1.04E-02	1.04E-02	-6.62	174.00	0.02	73.70	1.21E-01	1.31E-02	1.31E-02
17.01	1.26	1.17	0.22	112	2.87	0.07	605	1.00	8.53E-03	8.52E-03	-1.14	9.56	0.31	67.54	1.11E-01	1.14E-02	1.14E-02
17.72	1.46	1.34	0.21	111	2.89	0.07	606	1.00	7.32E-03	7.28E-03	-0.04	4.65	0.65	68.48	1.12E-01	1.27E-02	1.26E-02
17.72	1.37	1.24	0.21	108	2.93	0.08	607	1.00	8.53E-03	8.51E-03	-2.90	70.25	0.04	76.59	1.26E-01	1.02E-02	1.02E-02

Table C.6: FPG 16-Sample Coincident Data (cont)

y (mm)	y/δ_u	y/δ_M	Sk_v	Fl_v	$-u^2/v/u^2$	$-u^2/v/u^2$	$-u^2/v/u^2$	R_{uv}	TKE/u_e^2	Δu (m/s)	u_{eff}/u^*	y^+
6.38	0.53	0.48	0.08	3.31	2.73E-05	1.79E-05	3.05E-02	0.03	1.44E-03	9.70	21.12	668.40
6.38	0.49	0.45	-0.18	5.20	-4.46E-05	-2.74E-05	-4.59E-02	-0.03	1.65E-03	8.84	20.94	661.36
7.09	0.53	0.49	-0.26	5.32	-4.87E-05	-3.08E-05	-5.42E-02	-0.04	1.61E-03	9.45	20.49	756.86
7.09	0.78	0.67	-0.10	4.65	-1.31E-05	-1.10E-05	-1.99E-02	-0.02	7.40E-04	9.07	21.75	762.00
7.80	0.64	0.59	-0.29	3.49	-1.19E-04	-8.67E-05	-1.48E-01	-0.12	1.32E-03	9.47	21.64	816.47
7.80	0.60	0.54	-0.14	4.86	-6.63E-05	-4.57E-05	-7.64E-02	-0.06	1.39E-03	9.34	21.56	807.87
8.51	0.63	0.59	-0.34	7.19	-7.82E-05	-5.72E-05	-1.01E-01	-0.09	1.22E-03	9.81	21.24	907.81
9.21	0.71	0.64	-0.39	7.83	-6.71E-05	-5.15E-05	-8.61E-02	-0.08	1.08E-03	9.63	22.14	954.39
9.21	1.01	0.87	0.24	5.16	1.93E-05	1.88E-05	3.41E-02	0.08	3.66E-04	8.36	22.33	989.96
9.92	0.73	0.68	-0.28	6.63	-4.47E-05	-3.61E-05	-6.35E-02	-0.07	8.99E-04	9.50	21.69	1058.80
10.64	0.88	0.81	-0.07	3.69	-4.16E-05	-3.65E-05	-6.23E-02	-0.09	6.87E-04	10.32	22.56	1113.70
10.64	0.82	0.74	-0.44	8.16	-4.51E-05	-3.78E-05	-6.33E-02	-0.08	7.69E-04	10.08	22.60	1101.90
11.34	0.84	0.78	-0.12	3.79	-1.45E-05	-1.25E-05	-2.20E-02	-0.03	6.74E-04	9.79	21.94	1210.80
11.34	1.24	1.07	0.01	11.66	5.52E-06	5.84E-06	1.06E-02	0.03	2.74E-04	8.51	22.48	1219.00
12.05	0.93	0.84	-1.37	26.67	-1.64E-05	-1.54E-05	-2.57E-02	-0.05	5.09E-04	10.41	23.17	1248.40
12.40	1.02	0.94	-2.43	52.65	5.86E-06	5.76E-06	9.83E-03	0.02	3.81E-04	10.13	23.09	1298.70
12.76	0.95	0.88	-1.32	28.19	1.95E-06	1.83E-06	3.23E-03	0.01	4.03E-04	10.11	22.32	1361.70
12.76	1.40	1.21	-0.04	10.40	1.77E-06	1.91E-06	3.46E-03	0.01	2.85E-04	8.12	22.42	1371.00
13.47	1.04	0.94	-1.39	29.96	1.84E-06	1.81E-06	3.02E-03	0.01	3.17E-04	10.11	23.37	1395.00
14.17	1.17	1.08	-0.39	11.88	5.39E-06	5.54E-06	9.44E-03	0.03	2.25E-04	9.74	23.20	1483.80
14.17	1.05	0.98	-0.77	20.39	6.94E-06	6.91E-06	1.22E-02	0.04	2.27E-04	9.91	22.52	1512.70
14.17	1.55	1.34	0.68	4.61	4.70E-06	5.15E-06	9.33E-03	0.04	2.76E-04	8.34	22.32	1522.90
14.89	1.15	1.04	-2.73	70.92	5.82E-06	5.93E-06	9.92E-03	0.04	1.98E-04	10.16	23.48	1542.50
15.60	1.16	1.08	-4.05	100.41	3.94E-06	4.07E-06	7.17E-03	0.04	1.71E-04	9.67	22.60	1664.70
15.95	1.31	1.21	-5.75	144.91	9.70E-06	1.02E-05	1.74E-02	0.09	1.92E-04	9.57	23.19	1670.00
16.30	1.26	1.14	-9.69	206.40	2.68E-06	2.77E-06	4.64E-03	0.02	2.26E-04	10.08	23.48	1689.00
17.01	1.26	1.17	-5.46	122.47	5.11E-06	5.34E-06	9.41E-03	0.05	1.67E-04	9.71	22.54	1815.60
17.72	1.46	1.34	-4.73	103.48	8.81E-06	9.25E-06	1.58E-02	0.09	1.86E-04	9.79	23.06	1855.10
17.72	1.37	1.24	-5.15	147.20	8.27E-06	8.59E-06	1.44E-02	0.10	1.40E-04	10.41	23.40	1835.50

Table C.7: Flat Plate 8-Sample Raw Data

y (mm)	y/δ_u	y/δ_M	ρ (kg/m ³)	T (K)	M	M'	u (m/s)	u/u_e	u'/u	u'/u_e	Sk_u	Fl_u	γ_u	v (m/s)	v/u_e	v'/u	v'/u_e	Sk_v	Fl_v
1.20	0.16	0.10	0.17	183	1.71	0.29	467	0.79	1.05E-01	8.27E-02	-0.08	2.95	1.02	9.34	1.57E-02	4.77E-02	3.76E-02	-0.36	5.49
1.35	0.17	0.12	0.17	179	1.76	0.29	476	0.80	9.95E-02	7.97E-02	-0.18	2.93	1.02	9.07	1.53E-02	4.69E-02	3.75E-02	-0.32	5.40
1.50	0.19	0.13	0.17	176	1.80	0.29	482	0.81	9.70E-02	7.86E-02	-0.24	2.95	1.02	9.43	1.59E-02	4.72E-02	3.83E-02	-0.36	5.55
1.65	0.21	0.14	0.17	173	1.84	0.29	488	0.82	9.36E-02	7.68E-02	-0.31	3.00	1.00	9.06	1.52E-02	4.67E-02	3.83E-02	-0.31	5.40
1.80	0.23	0.15	0.18	171	1.87	0.30	493	0.83	9.26E-02	7.68E-02	-0.35	3.04	0.99	9.28	1.56E-02	4.72E-02	3.91E-02	-0.33	5.63
2.00	0.26	0.17	0.18	168	1.92	0.30	500	0.84	8.93E-02	7.51E-02	-0.41	3.05	0.98	8.85	1.49E-02	4.73E-02	3.98E-02	-0.34	5.77
2.50	0.32	0.21	0.19	160	2.03	0.30	516	0.87	8.05E-02	6.99E-02	-0.52	3.20	0.94	8.97	1.51E-02	4.47E-02	3.88E-02	-0.32	5.98
3.00	0.39	0.26	0.20	153	2.13	0.30	530	0.89	7.30E-02	6.50E-02	-0.68	3.65	0.82	8.26	1.39E-02	4.38E-02	3.90E-02	-0.40	6.77
3.50	0.45	0.30	0.21	147	2.21	0.30	541	0.91	6.89E-02	6.27E-02	-0.90	4.25	0.71	8.59	1.44E-02	4.18E-02	3.80E-02	-0.36	7.17
4.00	0.52	0.34	0.21	143	2.29	0.30	550	0.92	6.29E-02	5.81E-02	-1.04	4.93	0.61	7.67	1.29E-02	3.95E-02	3.65E-02	-0.46	7.64
4.50	0.58	0.38	0.22	137	2.37	0.29	559	0.94	5.77E-02	5.43E-02	-1.30	6.18	0.49	8.30	1.40E-02	3.58E-02	3.37E-02	-0.54	8.41
5.00	0.65	0.43	0.23	134	2.43	0.31	566	0.95	5.72E-02	5.44E-02	-1.88	9.80	0.31	8.97	1.51E-02	3.30E-02	3.15E-02	-0.49	9.18
5.50	0.71	0.47	0.23	130	2.49	0.29	573	0.96	5.08E-02	4.90E-02	-2.03	10.96	0.27	9.29	1.56E-02	3.15E-02	3.03E-02	-0.64	10.49
6.00	0.78	0.51	0.24	128	2.54	0.28	577	0.97	4.83E-02	4.70E-02	-2.42	14.14	0.21	9.74	1.64E-02	2.99E-02	2.91E-02	-0.84	11.98
7.00	0.91	0.60	0.25	122	2.65	0.26	588	0.99	3.98E-02	3.93E-02	-3.76	27.84	0.11	11.70	1.97E-02	2.68E-02	2.65E-02	-1.48	17.85
8.00	1.04	0.68	0.25	119	2.70	0.24	593	1.00	3.49E-02	3.48E-02	-4.94	43.15	0.07	13.93	2.34E-02	2.49E-02	2.48E-02	-1.86	21.74
9.00	1.17	0.77	0.25	123	2.64	0.28	587	0.99	4.25E-02	4.19E-02	-4.40	32.52	0.09	34.66	5.83E-02	2.64E-02	2.60E-02	-2.89	27.72
10.00	1.30	0.85	0.25	121	2.69	0.26	590	0.99	3.90E-02	3.87E-02	-5.03	40.33	0.07	34.84	5.86E-02	2.52E-02	2.51E-02	-3.33	33.03
11.00	1.43	0.94	0.25	120	2.71	0.27	592	1.00	3.98E-02	3.96E-02	-5.47	43.51	0.07	34.31	5.77E-02	2.41E-02	2.40E-02	-3.72	36.95
12.00	1.55	1.02	0.25	119	2.72	0.29	593	1.00	4.22E-02	4.22E-02	-5.70	44.14	0.07	33.16	5.58E-02	2.49E-02	2.49E-02	-4.11	38.60
13.00	1.68	1.11	0.26	118	2.73	0.30	594	1.00	4.34E-02	4.34E-02	-5.83	45.06	0.07	31.38	5.28E-02	2.34E-02	2.34E-02	-4.08	39.68

Table C.7: Flat Plate 8-Sample Raw Data (cont')

y (mm)	y/δ_u	y/δ_M	$-u^2v^2/u^2$	$-u^2v^2/\epsilon_w$	R_{uv}	TKE/u_e^2	Δu (m/s)	u_{eff}/u^*	y^+
1.20	0.16	0.10	0.00E+00	0.00E+00	0.00	8.84E-02	30.39	19.33	176.49
1.35	0.17	0.12	0.00E+00	0.00E+00	0.00	8.46E-02	8.32	19.73	198.55
1.50	0.19	0.13	0.00E+00	0.00E+00	0.00	8.33E-02	8.24	20.02	220.61
1.65	0.21	0.14	0.00E+00	0.00E+00	0.00	8.10E-02	8.40	20.33	242.67
1.80	0.23	0.15	0.00E+00	0.00E+00	0.00	8.07E-02	8.42	20.59	264.73
2.00	0.26	0.17	0.00E+00	0.00E+00	0.00	7.89E-02	8.65	20.93	294.14
2.50	0.32	0.21	0.00E+00	0.00E+00	0.00	7.24E-02	8.65	21.78	367.68
3.00	0.39	0.26	0.00E+00	0.00E+00	0.00	6.77E-02	8.25	22.48	441.21
3.50	0.45	0.30	0.00E+00	0.00E+00	0.00	6.42E-02	7.88	23.09	514.75
4.00	0.52	0.34	0.00E+00	0.00E+00	0.00	5.95E-02	7.84	23.56	588.29
4.50	0.58	0.38	0.00E+00	0.00E+00	0.00	5.43E-02	7.76	24.10	661.82
5.00	0.65	0.43	0.00E+00	0.00E+00	0.00	5.22E-02	7.45	24.46	735.36
5.50	0.71	0.47	0.00E+00	0.00E+00	0.00	4.78E-02	7.34	24.85	808.89
6.00	0.78	0.51	0.00E+00	0.00E+00	0.00	4.54E-02	7.23	25.13	882.43
7.00	0.91	0.60	0.00E+00	0.00E+00	0.00	3.88E-02	7.03	25.73	1029.50
8.00	1.04	0.68	0.00E+00	0.00E+00	0.00	3.50E-02	5.47	26.03	1176.60
9.00	1.17	0.77	0.00E+00	0.00E+00	0.00	4.00E-02	6.82	25.66	1323.60
10.00	1.30	0.85	0.00E+00	0.00E+00	0.00	3.74E-02	7.82	25.88	1470.70
11.00	1.43	0.94	0.00E+00	0.00E+00	0.00	3.71E-02	7.51	25.99	1617.80
12.00	1.55	1.02	0.00E+00	0.00E+00	0.00	3.89E-02	7.35	26.07	1764.90
13.00	1.68	1.11	0.00E+00	0.00E+00	0.00	3.86E-02	6.92	26.13	1911.90

Table C.8: Flat Plate 8-Sample Coincident Data

y (mm)	y/δ_u	y/δ_M	ρ (kg/m ³)	T (K)	M	M'	u (m/s)	w/u_e	u/u	u/u_e	Sk_u	Fl_u	γ_u	v (m/s)	v/u_e	v/u	v/u_e	Sk_v	Fl_v
1.20	0.16	0.10	0.17	183	1.71	0.29	467	0.79	1.05E-01	8.22E-02	-0.14	2.92	1.03	9.24	1.56E-02	4.62E-02	3.63E-02	-0.31	5.28
1.35	0.17	0.12	0.17	179	1.76	0.28	475	0.80	9.75E-02	7.80E-02	-0.29	2.79	1.08	9.30	1.56E-02	4.34E-02	3.47E-02	-0.06	4.23
1.50	0.19	0.13	0.17	176	1.80	0.29	482	0.81	9.63E-02	7.81E-02	-0.26	2.97	1.01	9.05	1.52E-02	4.68E-02	3.80E-02	-0.38	5.57
1.65	0.21	0.14	0.17	173	1.84	0.29	488	0.82	9.27E-02	7.60E-02	-0.35	2.92	1.03	9.38	1.58E-02	4.41E-02	3.62E-02	-0.17	4.94
1.80	0.23	0.15	0.18	171	1.87	0.29	494	0.83	9.16E-02	7.61E-02	-0.37	3.04	0.99	9.46	1.59E-02	4.61E-02	3.83E-02	-0.19	5.20
2.00	0.26	0.17	0.18	168	1.92	0.29	500	0.84	8.73E-02	7.34E-02	-0.43	2.94	1.02	9.70	1.63E-02	4.34E-02	3.65E-02	-0.10	4.66
2.50	0.32	0.21	0.19	159	2.03	0.29	517	0.87	7.79E-02	6.77E-02	-0.51	3.03	0.99	9.26	1.56E-02	4.10E-02	3.57E-02	-0.08	5.28
3.00	0.39	0.26	0.20	152	2.14	0.29	531	0.89	6.98E-02	6.24E-02	-0.64	3.43	0.88	8.66	1.46E-02	4.03E-02	3.60E-02	-0.21	6.30
3.50	0.45	0.30	0.21	146	2.23	0.30	542	0.91	6.63E-02	6.05E-02	-0.85	4.01	0.75	9.31	1.57E-02	3.79E-02	3.45E-02	-0.10	6.40
4.00	0.52	0.34	0.21	142	2.29	0.29	550	0.93	6.24E-02	5.77E-02	-1.01	4.76	0.63	7.95	1.34E-02	3.85E-02	3.56E-02	-0.38	7.67
4.50	0.58	0.38	0.22	137	2.38	0.28	561	0.94	5.47E-02	5.16E-02	-1.14	5.10	0.59	8.95	1.51E-02	3.29E-02	3.10E-02	-0.13	7.21
5.00	0.65	0.43	0.23	134	2.43	0.30	567	0.95	5.52E-02	5.26E-02	-1.79	9.48	0.32	9.35	1.57E-02	3.13E-02	2.98E-02	-0.25	7.78
5.50	0.71	0.47	0.23	130	2.50	0.27	573	0.96	4.73E-02	4.57E-02	-1.76	9.38	0.32	9.87	1.66E-02	2.85E-02	2.75E-02	-0.31	9.33
6.00	0.78	0.51	0.24	127	2.55	0.26	578	0.97	4.41E-02	4.29E-02	-2.12	12.47	0.24	10.63	1.79E-02	2.72E-02	2.64E-02	-0.44	10.22
7.00	0.91	0.60	0.25	121	2.66	0.21	589	0.99	3.26E-02	3.23E-02	-3.24	25.59	0.12	12.69	2.14E-02	2.23E-02	2.22E-02	-0.86	14.99
8.00	1.04	0.68	0.25	119	2.71	0.20	594	1.00	2.98E-02	2.97E-02	-5.27	55.65	0.05	14.26	2.40E-02	2.24E-02	2.24E-02	-2.01	23.89
9.00	1.17	0.77	0.25	121	2.67	0.20	589	0.99	2.98E-02	2.95E-02	-4.38	42.76	0.07	35.42	5.96E-02	2.16E-02	2.14E-02	-2.03	26.83
10.00	1.30	0.85	0.25	119	2.72	0.17	593	1.00	2.45E-02	2.45E-02	-5.09	62.37	0.05	35.29	5.94E-02	2.06E-02	2.05E-02	-2.59	32.38
11.00	1.43	0.94	0.26	118	2.74	0.17	595	1.00	2.32E-02	2.32E-02	-6.83	93.00	0.03	35.03	5.89E-02	1.86E-02	1.86E-02	-2.57	32.50
12.00	1.55	1.02	0.26	117	2.75	0.20	596	1.00	2.86E-02	2.87E-02	-7.37	81.32	0.04	34.11	5.74E-02	1.88E-02	1.88E-02	-2.97	39.56
13.00	1.68	1.11	0.26	117	2.76	0.21	597	1.00	2.88E-02	2.90E-02	-7.65	87.23	0.03	32.07	5.40E-02	1.88E-02	1.89E-02	-3.51	42.90

Table C.8: Flat Plate 8-Sample Coincident Data (cont)

y (mm)	y/δ_u	y/δ_M	$-u^2/v^2$	$-u^2/v^2$	$-u^2/v^2$	R_{uv}	TKE/u_e^2	Δu (m/s)	u_{eff}/u^*	y^+
1.20	0.16	0.10	5.15E-04	2.09E-04	0.26	0.11	8.72E-02	30.35	19.31	176.49
1.35	0.17	0.12	1.64E-03	7.02E-04	0.89	0.39	8.15E-02	8.59	19.70	198.55
1.50	0.19	0.13	6.63E-04	2.98E-04	0.38	0.15	8.26E-02	8.30	20.05	220.61
1.65	0.21	0.14	1.01E-03	4.69E-04	0.59	0.25	7.90E-02	8.43	20.32	242.67
1.80	0.23	0.15	3.51E-04	1.71E-04	0.22	0.08	7.95E-02	8.53	20.62	264.73
2.00	0.26	0.17	1.16E-03	5.90E-04	0.75	0.31	7.54E-02	8.73	20.93	294.14
2.50	0.32	0.21	1.05E-03	5.99E-04	0.76	0.33	6.87E-02	8.86	21.81	367.68
3.00	0.39	0.26	6.62E-04	4.17E-04	0.53	0.24	6.37E-02	8.39	22.55	441.21
3.50	0.45	0.30	6.13E-04	4.19E-04	0.53	0.24	6.03E-02	7.79	23.16	514.75
4.00	0.52	0.34	2.13E-04	1.54E-04	0.19	0.09	5.85E-02	7.82	23.58	588.29
4.50	0.58	0.38	4.21E-04	3.29E-04	0.42	0.23	5.07E-02	7.86	24.16	661.82
5.00	0.65	0.43	1.53E-04	1.25E-04	0.16	0.09	5.00E-02	7.43	24.50	735.36
5.50	0.71	0.47	2.12E-04	1.82E-04	0.23	0.16	4.40E-02	7.47	24.89	808.89
6.00	0.78	0.51	1.73E-04	1.55E-04	0.20	0.14	4.13E-02	7.40	25.18	882.43
7.00	0.91	0.60	7.13E-05	6.95E-05	0.09	0.10	3.21E-02	7.11	25.82	1029.50
8.00	1.04	0.68	1.12E-05	1.13E-05	0.01	0.02	3.08E-02	5.64	26.09	1176.60
9.00	1.17	0.77	8.15E-05	7.94E-05	0.10	0.13	3.02E-02	7.12	25.83	1323.60
10.00	1.30	0.85	2.34E-05	2.35E-05	0.03	0.05	2.69E-02	7.91	26.05	1470.70
11.00	1.43	0.94	7.35E-06	7.50E-06	0.01	0.02	2.48E-02	7.58	26.17	1617.80
12.00	1.55	1.02	6.07E-06	6.25E-06	0.01	0.01	2.76E-02	7.41	26.23	1764.90
13.00	1.68	1.11	-1.16E-05	-1.21E-05	-0.02	-0.02	2.77E-02	6.99	26.29	1911.90

Table C.9: FPG 16-Sample Coincident Data (x = 70.98 cm)

y (mm)	y/δ _u	y/δ _M	ρ (kg/m ³)	T (K)	M	M'	u (m/s)	u/u _e	u'/u	u'/u _e	Sk _u	Fl _u	γ _u	v (m/s)	v/u	v'/u _e	
1.98	0.23	0.22	0.12	164	2.01	0.25	516	0.84	6.65E-02	5.61E-02	-0.20	2.66	1.13	33.58	5.50E-02	3.04E-02	2.57E-02
2.84	0.32	0.31	0.13	153	2.16	0.26	535	0.88	6.08E-02	5.33E-02	-0.32	2.70	1.11	37.29	6.10E-02	2.96E-02	2.59E-02
4.25	0.49	0.46	0.15	139	2.39	0.27	562	0.92	5.09E-02	4.68E-02	-0.60	3.15	0.95	42.60	6.97E-02	2.64E-02	2.42E-02
7.09	0.81	0.77	0.19	116	2.79	0.21	600	0.98	2.83E-02	2.78E-02	-1.47	5.94	0.51	53.24	8.71E-02	1.72E-02	1.69E-02
9.21	1.05	1.00	0.21	110	2.91	0.14	609	1.00	1.62E-02	1.62E-02	-2.30	13.47	0.22	57.31	9.38E-02	1.42E-02	1.41E-02
11.34	1.30	1.23	0.22	110	2.92	0.09	611	1.00	1.07E-02	1.07E-02	-1.37	10.93	0.27	59.02	9.66E-02	1.33E-02	1.33E-02
12.76	1.46	1.39	0.22	111	2.90	0.08	609	1.00	9.43E-03	9.40E-03	-0.70	10.89	0.28	60.58	9.92E-02	1.32E-02	1.31E-02
14.17	1.62	1.54	0.22	112	2.87	0.07	606	0.99	8.33E-03	8.27E-03	0.00	3.84	0.78	59.82	9.79E-02	1.28E-02	1.27E-02

y (mm)	y/δ _u	y/δ _M	Sk _v	Fl _v	-u'v/u ²	-u'v/u _e ²	-ρu'v/τ _w	R _{wv}	TKE/u _e ²	Δu (m/s)	u _{eff} /u [*]	y ⁺
1.98	0.23	0.22	-0.09	4.05	4.92E-04	2.01E-04	0.26	0.24	5.60E-02	9.85	18.47	209.34
2.84	0.32	0.31	-0.13	4.98	3.79E-04	1.83E-04	0.24	0.21	5.22E-02	9.83	19.35	300.10
4.25	0.49	0.46	-0.49	8.73	1.82E-04	1.10E-04	0.14	0.14	4.46E-02	9.86	20.57	449.63
7.09	0.81	0.77	-0.44	10.29	2.40E-05	2.10E-05	0.03	0.05	2.63E-02	10.18	22.47	749.73
9.21	1.05	1.00	-1.95	33.44	1.56E-05	1.55E-05	0.02	0.07	1.82E-02	9.41	22.96	974.02
11.34	1.30	1.23	-2.90	59.96	2.94E-05	3.09E-05	0.04	0.21	1.53E-02	9.09	23.02	1199.40
12.76	1.46	1.39	-4.63	99.45	2.10E-05	2.24E-05	0.03	0.17	1.48E-02	8.93	22.93	1348.90
14.17	1.62	1.54	-1.10	26.49	1.22E-05	1.31E-05	0.02	0.11	1.41E-02	9.14	22.80	1498.40

Table C.10: FPG 16-Sample Coincident Data (x = 70.44 cm)

y (mm)	y/δ _u	y/δ _M	ρ (kg/m ³)	T (K)	M	M'	u (m/s)	w/u _e	u'/u	u'/u _e	Sk _u	Fl _u	γ _u	v (m/s)	v/u _e	v'/u	v'/u _e
1.34	0.15	0.14	0.11	174	1.88	0.24	495	0.81	7.47E-02	6.05E-02	-0.13	2.63	1.14	18.57	3.04E-02	3.24E-02	2.62E-02
1.63	0.18	0.17	0.11	170	1.93	0.24	503	0.82	7.17E-02	5.90E-02	-0.15	2.60	1.15	19.74	3.23E-02	3.18E-02	2.62E-02
1.98	0.22	0.20	0.12	165	2.00	0.25	514	0.84	6.85E-02	5.76E-02	-0.19	2.59	1.16	20.99	3.43E-02	3.19E-02	2.68E-02
2.84	0.32	0.29	0.13	154	2.14	0.26	533	0.87	6.22E-02	5.42E-02	-0.32	2.63	1.14	23.35	3.82E-02	3.02E-02	2.64E-02
4.25	0.48	0.44	0.15	140	2.37	0.26	561	0.92	5.07E-02	4.65E-02	-0.63	3.11	0.96	27.45	4.49E-02	2.67E-02	2.45E-02
7.09	0.80	0.73	0.19	118	2.76	0.21	599	0.98	2.96E-02	2.90E-02	-1.55	6.57	0.46	36.48	5.96E-02	1.78E-02	1.75E-02
9.21	1.04	0.95	0.21	111	2.90	0.13	610	1.00	1.54E-02	1.53E-02	-1.69	8.27	0.36	42.15	6.89E-02	1.38E-02	1.38E-02
11.34	1.28	1.17	0.22	110	2.92	0.09	612	1.00	1.07E-02	1.07E-02	-1.20	10.66	0.28	46.11	7.54E-02	1.35E-02	1.35E-02
12.76	1.44	1.32	0.22	110	2.91	0.08	611	1.00	9.10E-03	9.09E-03	-1.33	25.35	0.12	47.97	7.84E-02	1.19E-02	1.19E-02
14.17	1.60	1.46	0.23	110	2.91	0.07	610	1.00	8.45E-03	8.43E-03	-0.23	4.37	0.69	50.54	8.26E-02	1.13E-02	1.13E-02

y (mm)	y/δ _u	y/δ _M	Sk _v	Fl _v	-u'v/u ²	-ρu'v/τ _w	R _{uv}	TKE/u _e ²	Δu (m/s)	u _{eff} /u*	γ ⁺
1.34	0.15	0.14	-0.10	3.93	7.24E-04	2.52E-04	0.33	6.20E-02	40.50	17.50	142.57
1.63	0.18	0.17	-0.02	3.31	6.52E-04	2.41E-04	0.31	5.98E-02	8.98	17.85	172.59
1.98	0.22	0.20	-0.05	3.81	5.80E-04	2.33E-04	0.30	5.80E-02	8.83	18.30	210.11
2.84	0.32	0.29	0.05	3.38	3.83E-04	1.80E-04	0.23	5.34E-02	8.83	19.17	301.20
4.25	0.48	0.44	-0.02	4.42	2.05E-04	1.22E-04	0.16	4.47E-02	8.76	20.43	451.28
7.09	0.80	0.73	-0.13	5.73	2.07E-05	1.78E-05	0.02	2.75E-02	8.99	22.32	752.48
9.21	1.04	0.95	-0.71	14.64	3.18E-06	3.17E-06	0.00	1.76E-02	8.36	22.91	977.59
11.34	1.28	1.17	-3.63	74.33	1.10E-05	1.16E-05	0.02	1.55E-02	8.18	22.98	1203.80
12.76	1.44	1.32	-1.02	24.90	2.58E-05	2.78E-05	0.04	1.36E-02	8.20	22.94	1353.80
14.17	1.60	1.46	-1.70	36.87	2.28E-05	2.51E-05	0.03	1.28E-02	8.48	22.91	1503.90

Bibliography

1. Anderson, D., et al. *Computational Fluid Mechanics and Heat Transfer*. Series in Computational Methods in Mechanics and Thermal Sciences, New York: Hemisphere Publishing Corporation, 1984.
2. Anderson, J. *Fundamentals of Aerodynamics* (Second Edition). New York: McGraw-Hill, Inc., 1991.
3. Bendat, J. and Piersol, A. *Random Data Analysis and Measurement Procedures* (Second Edition). New York: John Wiley and Sons, 1986.
4. Beran, P. "Aero624 Class Notes," Air Force Institute of Technology, Wright-Patterson AFB, OH, 1995.
5. Beran, P. "Aero752 Class Notes," Air Force Institute of Technology, Wright-Patterson AFB, OH, 1995.
6. Bowersox, R.D.W. "Aero827 Class Notes," Air Force Institute of Technology, Wright-Patterson AFB, OH, 1995.
7. Bowersox, R.D.W. *Compressible Turbulence in a High-Speed High-Reynolds Number Mixing Layer*. PhD Dissertation, Virginia Polytechnic Institute and State University, VA, 1992.
8. Bowersox, R.D.W. "Thermal Anemometry," *Handbook of Fluid Dynamics and Fluid Machinery*, John Wiley and Sons, 1995.
9. Bowersox, R.D.W. et al. "Technique For Direct Measurement Of Skin Friction In High-Enthalpy Scramjet Flowfields," *AIAA Journal*, 33(7):1286-1291 (July 1995).
10. Dantec Measurement Technology A/S. "User's Guide: 57N20/57N35 BSA Enhanced." Skovlunde, Denmark: Dantec, Inc.
11. Dantec Measurement Technology A/S. "User's Guide: 60X Series FiberFlow." Skovlunde, Denmark: Dantec, Inc.
12. Dantec Measurement Technology A/S. "Burstware 2.0[®] User's Manual." Skovlunde, Denmark: Dantec, Inc.
13. Dotter, J. "Compressible Turbulence Measurements in a Supersonic Flow With Adverse Pressure Gradient." Master's Thesis, Air Force Institute of Technology, Wright-Patterson AFB, OH.
14. Durst, F., et al. *Principles and Practice of Laser-Doppler Anemometry* (Second Edition). London: Academic Press, 1976.
15. Elena, M. "LDA in Supersonic Flows: Problems of Seeding and Angular Bias." *AGARDograph-AG-315*, ch 7, AGARD, 1989.

16. Elena, M. and LaCharme, J. "Experimental Study of a Supersonic Turbulent Boundary Layer Using a Laser Doppler Anemometer," *Journal of Theoretical and Applied Mechanics*, 7(2):175-190 (1988).
17. Fick, E. "Numerical Simulation of Supersonic Turbulent Boundary Layer Flow Under the Influence of Mild Pressure Gradients." Master's Thesis, Air Force Institute of Technology, Wright-Patterson AFB, OH, 1995.
18. Hale, C. "Experimental Investigation of a Supersonic Turbulent Boundary Layer with Adverse Pressure Gradient." Master's Thesis, Air Force Institute of Technology, Wright-Patterson AFB, OH, 1995.
19. Johnson, A.W. "Laminarization and Re-transition of Laminar Boundary Layers in Supersonic Flow," PhD dissertation, Yale University, New Haven, CT, 1993.
20. Johnson, D. "Laser Doppler Anemometry." *AGARDograph-AG-315*, ch 6, AGARD, 1989.
21. Johnson, D. and Rose, W. "Laser Velocimeter and Hot-Wire Anemometer Comparison in a Supersonic Boundary Layer," *AIAA Journal*, 13(4):512-515 (April 1975).
22. Kistler, A. "Fluctuation Measurements in a Supersonic Turbulent Boundary Layer," *The Physics of Fluids*, 2(3):3:290-296 (1959).
23. Klebanoff, P. "Characteristics of Turbulence in a Boundary Layer with Zero Pressure Gradient," *Report 1247, National Committee for Aeronautics*, (NASA TN 3178) (July 1954).
24. Kreysig, E. *Advanced Engineering Mathematics* (Seventh Edition). New York: John Wiley and Sons, Inc., 1993.
25. Lewis, J.C., et al. "An Experiment on the Adiabatic Compressible Turbulent Boundary Layer in Adverse and Favorable Pressure Gradients," *Journal of Fluid Mechanics*, 51(4):657-672 (1972).
26. Miller, R. "Compressible Turbulence Measurements in a Supersonic Boundary Layer Including Favorable Pressure Gradient Effects." Master's Thesis, Air Force Institute of Technology, Wright-Patterson Air Force Base, OH (1994).
27. Miller, R., et al. "Compressible Turbulence Measurements in Supersonic Boundary Layers with Favorable and Adverse Pressure Gradients," *FED-Vol 224, Transitional and Turbulent Compressible Flows*, ed. L. Kral et al. Presented at the 1995 ASME/JSME Fluids Engineering and Laser Anemometry Conference and Exhibition, Aug 13-18 1995, Hilton Head, SC.
28. Morkovin, M. "Effects of Compressibility on Turbulent Flows," in *The Mechanics of Turbulence*, 367-380. New York: Gordon and Breach, 1964.
29. Patel, V. and Richmond, M. "Pressure Gradient and Surface Curvature Effects in Turbulent Boundary Layers," *AIAA Paper*, (87-1301) (1987).

30. Robinson, S., et al. "Hot-Wire and Laser Doppler Anemometer Measurements in a Supersonic Boundary Layer," *AIAA Paper*, (83-1723) (1983).
31. Settles, G. and Dodson, L. "Supersonic and Hypersonic Shock/Boundary-Layer Interaction Database," *AIAA Journal*, 32(7):1377-1383 (July 1994).
32. Smith, D. and Smits, A. "The Effects of Streamline Curvature and Pressure Gradient on the Behavior of Turbulent Boundary Layers in Supersonic Flow," *AIAA Paper*, (94-2227) (1994).
33. Spina, E., et al. "The Physics of Supersonic Turbulent Boundary Layers," *Annual Review of Fluid Mechanics*, 26:287-319 (1994)
34. TSI, Inc. "Model 9306 Six-Jet Atomizer Instruction Manual." 1983.
35. Van Driest, E. "Turbulent Boundary Layers in Compressible Fluids," *Journal of the Aeronautical Sciences*, 18(3):145-160 (March 1951).
36. White, F. *Viscous Fluid Flow* (Second Edition). New York: McGraw-Hill, Inc., 1991.
37. Wilcox, D. *Turbulence Modeling for CFD*. Glendale, CA: DCW Industries, Inc., 1993.

VITA

Lieutenant Joel J. Luker ~~was born on 04 November 1968 in New Ulm, Minnesota.~~ He graduated from New Ulm Senior High School in 1989 and went on to the University of Minnesota, Minneapolis Campus. He graduated in March 1994 with high distinction, earning a Bachelor of Science in Aerospace Engineering and Mechanics. He was also a distinguished graduate of the Air Force ROTC program at the University of Minnesota and was commissioned a Second Lieutenant in the United States Air Force on 26 March 1994. Lieutenant Luker was admitted into the University of Minnesota Graduate Studies program immediately upon receiving his Bachelor's degree and began pursuit of a Master's degree in aerospace engineering. However, in June of 1994 he was called onto active duty in order to attend the Air Force Institute of Technology, where he is currently pursuing his Master's degree in aerospace engineering. He plans to graduate on 19 Dec 95 and will be stationed at Wright Laboratories, WPAFB, as a follow-on assignment.

~~Permanent Address
30044-Gunt
New Ulm, Minnesota~~

VITA-1

Job 5569 Fiche 2 04/26/96 ADA86AM51
Operator ID: Machine ID: COM_1 Job Name: zik0zj81.0

Main Table: DTIC.MPT

Break Table:

Reel: 1 File: 0 Block: 1413 Offset: 64123

M T C IDSCOM 1.0 Version 3.1A7 Feb 07 1995

REPORT DOCUMENTATION PAGE

Form Approved
OMB No. 0704-0188

Public reporting burden for this collection of information is estimated to average 1 hour per response, including the time for reviewing instructions, searching existing data sources, gathering and maintaining the data needed, and completing and reviewing the collection of information. Send comments regarding this burden estimate or any other aspect of this collection of information, including suggestions for reducing this burden, to Washington Headquarters Services, Directorate for Information Operations and Reports, 1215 Jefferson Davis Highway, Suite 1204, Arlington, VA 22202-4302, and to the Office of Management and Budget, Paperwork Reduction Project (0704-0188), Washington, DC 20503.

1. AGENCY USE ONLY (Leave blank)		2. REPORT DATE December 1995	3. REPORT TYPE AND DATES COVERED Master's Thesis	
4. TITLE AND SUBTITLE EXPERIMENTAL INVESTIGATION OF A SUPERSONIC TURBULENT BOUNDARY LAYER INCLUDING FAVORABLE PRESSURE GRADIENT EFFECTS			5. FUNDING NUMBERS	
6. AUTHOR(S) Joel J. Luker				
7. PERFORMING ORGANIZATION NAME(S) AND ADDRESS(ES) Air Force Institute of Technology, WPAFB OH 45433-6583			8. PERFORMING ORGANIZATION REPORT NUMBER AFIT/GAE/ENY/95D-16	
9. SPONSORING/MONITORING AGENCY NAME(S) AND ADDRESS(ES) Dr. James McMichael AFOSR/NA 110 Duncan Ave, Suite B115 Bolling AFB, Washington, D.C. 20332-0001			10. SPONSORING/MONITORING AGENCY REPORT NUMBER	
11. SUPPLEMENTARY NOTES				
12a. DISTRIBUTION/AVAILABILITY STATEMENT Distribution Unlimited			12b. DISTRIBUTION CODE	
13. ABSTRACT (Maximum 200 words) This study used advanced laser Doppler velocimetry techniques to measure the turbulence intensities and Reynolds shear stresses in Mach 2.8 turbulent flat plate and Mach 2.9 favorable pressure gradient (FPG) boundary layers. The FPG was generated using a convex curved wall and had a strength of $\beta = 0.1$, where β is Clauser's equilibrium parameter. The maximum magnitude of the "extra" strain rates normalized by the main strain rates was 0.1, which meant the FPG was considered to be a strong pressure gradient. The flat plate results indicated that the LDV procedures used in this experiment prevented angular biasing of the velocity measurements reported in the literature. Analysis of the LDV system settings also showed that this biasing, which has been attributed in the past to the angular alignment of the lasers, may have actually been caused, at least in part, by the choice of record interval used during data collection. Measurements in the FPG test section demonstrated that the stabilizing effect of the FPG reduced the turbulence intensities below the location $y/\delta \leq 0.5$. Near the wall, the u-turbulence intensity was found to be reduced to 70% of the flat plate value. In addition, the FPG reduced the magnitude of the incompressible Reynolds shear stresses ($-\overline{p'u'v'}$) by approximately 75%. Comparison of the LDV data to hot-wire data collected in the same facilities showed that the assumption of $p' = 0$, used in the reduction of the hot-wire data, was valid in the flat plate region but not the FPG region. The increase in the magnitude of p' was likely due to the streamline curvature associated with the generation of the FPG and the resulting pressure difference across the boundary layer.				
14. SUBJECT TERMS Turbulence, Compressible, Favorable Pressure Gradient Boundary Layers, Laser Doppler Velocimetry			15. NUMBER OF PAGES 196	
			16. PRICE CODE	
17. SECURITY CLASSIFICATION OF REPORT UNCLASSIFIED	18. SECURITY CLASSIFICATION OF THIS PAGE UNCLASSIFIED	19. SECURITY CLASSIFICATION OF ABSTRACT UNCLASSIFIED	20. LIMITATION OF ABSTRACT UL	

GENERAL INSTRUCTIONS FOR COMPLETING SF 298

The Report Documentation Page (RDP) is used in announcing and cataloging reports. It is important that this information be consistent with the rest of the report, particularly the cover and title page. Instructions for filling in each block of the form follow. It is important to *stay within the lines* to meet *optical scanning requirements*.

Block 1. Agency Use Only (Leave blank).

Block 2. Report Date. Full publication date including day, month, and year, if available (e.g. 1 Jan 88). Must cite at least the year.

Block 3. Type of Report and Dates Covered. State whether report is interim, final, etc. If applicable, enter inclusive report dates (e.g. 10 Jun 87 - 30 Jun 88).

Block 4. Title and Subtitle. A title is taken from the part of the report that provides the most meaningful and complete information. When a report is prepared in more than one volume, repeat the primary title, add volume number, and include subtitle for the specific volume. On classified documents enter the title classification in parentheses.

Block 5. Funding Numbers. To include contract and grant numbers; may include program element number(s), project number(s), task number(s), and work unit number(s). Use the following labels:

C - Contract	PR - Project
G - Grant	TA - Task
PE - Program Element	WU - Work Unit Accession No.

Block 6. Author(s). Name(s) of person(s) responsible for writing the report, performing the research, or credited with the content of the report. If editor or compiler, this should follow the name(s).

Block 7. Performing Organization Name(s) and Address(es). Self-explanatory.

Block 8. Performing Organization Report Number. Enter the unique alphanumeric report number(s) assigned by the organization performing the report.

Block 9. Sponsoring/Monitoring Agency Name(s) and Address(es). Self-explanatory.

Block 10. Sponsoring/Monitoring Agency Report Number. (If known)

Block 11. Supplementary Notes. Enter information not included elsewhere such as: Prepared in cooperation with...; Trans. of...; To be published in.... When a report is revised, include a statement whether the new report supersedes or supplements the older report.

Block 12a. Distribution/Availability Statement. Denotes public availability or limitations. Cite any availability to the public. Enter additional limitations or special markings in all capitals (e.g. NOFORN, REL, ITAR).

DOD - See DoDD 5230.24, "Distribution Statements on Technical Documents."

DOE - See authorities.

NASA - See Handbook NHB 2200.2.

NTIS - Leave blank.

Block 12b. Distribution Code.

DOD - Leave blank.

DOE - Enter DOE distribution categories from the Standard Distribution for Unclassified Scientific and Technical Reports.

NASA - Leave blank.

NTIS - Leave blank.

Block 13. Abstract. Include a brief (*Maximum 200 words*) factual summary of the most significant information contained in the report.

Block 14. Subject Terms. Keywords or phrases identifying major subjects in the report.

Block 15. Number of Pages. Enter the total number of pages.

Block 16. Price Code. Enter appropriate price code (*NTIS only*).

Blocks 17. - 19. Security Classifications. Self-explanatory. Enter U.S. Security Classification in accordance with U.S. Security Regulations (i.e., UNCLASSIFIED). If form contains classified information, stamp classification on the top and bottom of the page.

Block 20. Limitation of Abstract. This block must be completed to assign a limitation to the abstract. Enter either UL (unlimited) or SAR (same as report). An entry in this block is necessary if the abstract is to be limited. If blank, the abstract is assumed to be unlimited.